



HAL
open science

Highly selective, active and stable Fischer-Tropsch catalyst using entrapped iron nanoparticles in silicalite-1

Joffrey Huve

► **To cite this version:**

Joffrey Huve. Highly selective, active and stable Fischer-Tropsch catalyst using entrapped iron nanoparticles in silicalite-1. Catalysis. Université de Lyon, 2017. English. NNT : 2017LYSE1042 . tel-01721319

HAL Id: tel-01721319

<https://theses.hal.science/tel-01721319>

Submitted on 2 Mar 2018

HAL is a multi-disciplinary open access archive for the deposit and dissemination of scientific research documents, whether they are published or not. The documents may come from teaching and research institutions in France or abroad, or from public or private research centers.

L'archive ouverte pluridisciplinaire **HAL**, est destinée au dépôt et à la diffusion de documents scientifiques de niveau recherche, publiés ou non, émanant des établissements d'enseignement et de recherche français ou étrangers, des laboratoires publics ou privés.



N°d'ordre NNT : 2017LYSE1042

THESE de DOCTORAT DE L'UNIVERSITE DE LYON

opérée au sein de
l'Université Claude Bernard Lyon 1

Ecole Doctorale ED206
École doctorale de Chimie

Spécialité de doctorat :
Discipline : Chimie

Soutenue publiquement le 20/03/2017, par :
Joffrey Huve

Highly selective, active and stable Fischer-Tropsch catalyst using entrapped iron nanoparticles in silicalite-1

Devant le jury composé de :

| | | |
|-------------------------|---|-----------------------|
| Fongarland, Pascal | Professeur, Université Lyon 1, LGPC | Président |
| Griboval-Constant, Anne | Maître de Conférences, CNRS, UCCS | Rapporteuse |
| Rønning, Magnus | Professeur, Norway University of Science and Technology, NTNU, Norway | Rapporteur |
| Galameau, Anne | Directeur de Recherche, CNRS, ICGM | Examinatrice |
| Decottignies, Dominique | Ingénieur de Recherche, IFP Energies nouvelle | Examinatrice |
| Kapteijn, Freek | Professeur, Delft University of Technology, TUDelft, Netherlands | Examineur |
| Farrusseng, David | Directeur de Recherche, CNRS, IRCELYON | Directeur de thèse |
| Schuurman, Yves | Directeur de Recherche, CNRS, IRCELYON | Co-directeur de thèse |

UNIVERSITE CLAUDE BERNARD - LYON 1

Président de l'Université

Président du Conseil Académique

Vice-président du Conseil d'Administration

Vice-président du Conseil Formation et Vie
Universitaire

Vice-président de la Commission Recherche

Directeur Général des Services

M. le Professeur Frédéric FLEURY

M. le Professeur Hamda BEN HADID

M. le Professeur Didier REVEL

M. le Professeur Philippe CHEVALIER

M. Fabrice VALLÉE

M. Alain HELLEU

COMPOSANTES SANTE

Faculté de Médecine Lyon Est – Claude Bernard

Directeur : M. le Professeur J. ETIENNE

Faculté de Médecine et de Maïeutique Lyon Sud
– Charles Mérieux

Directeur : Mme la Professeure C. BURILLON

Faculté d'Odontologie

Directeur : M. le Professeur D. BOURGEOIS

Institut des Sciences Pharmaceutiques et
Biologiques

Directeur : Mme la Professeure C. VINCIGUERRA

Institut des Sciences et Techniques de la
Réadaptation

Directeur : M. X. PERROT

Département de formation et Centre de
Recherche en Biologie Humaine

Directeur : Mme la Professeure A-M. SCHOTT

COMPOSANTES ET DEPARTEMENTS DE SCIENCES ET TECHNOLOGIE

Faculté des Sciences et Technologies

Directeur : M. F. DE MARCHI

Département Biologie

Directeur : M. le Professeur F. THEVENARD

Département Chimie Biochimie

Directeur : Mme C. FELIX

Département GEP

Directeur : M. Hassan HAMMOURI

Département Informatique

Directeur : M. le Professeur S. AKKOUCHE

Département Mathématiques

Directeur : M. le Professeur G. TOMANOV

Département Mécanique

Directeur : M. le Professeur H. BEN HADID

Département Physique

Directeur : M. le Professeur J-C PLENET

UFR Sciences et Techniques des Activités
Physiques et Sportives

Directeur : M. Y. VANPOULLE

Observatoire des Sciences de l'Univers de Lyon
Polytech Lyon

Directeur : M. B. GUIDERDONI

Ecole Supérieure de Chimie Physique
Electronique

Directeur : M. le Professeur E. PERRIN

Directeur : M. G. PIGNAULT

Institut Universitaire de Technologie de Lyon 1

Directeur : M. le Professeur C. VITON

Ecole Supérieure du Professorat et de
l'Education

Directeur : M. le Professeur A. MOUGNIOTTE

Institut de Science Financière et d'Assurances

Directeur : M. N. LEBOISNE

Acknowledgments

This study has been supported by the European Union Seventh Framework Program FP7-NMP-2013, under Grant Agreement n° 604277 (acronym FASTCARD).



I would like to thank the partners of the FASTCARD WP2 for their help and sharing of scientific knowledge.



Ce projet de thèse a été réalisé au sein de l'équipe Ingénierie (ING) de l'Institut de Recherches sur la Catalyse et l'Environnement de Lyon (IRCELYON), UMR 5256, CNRS, Université Claude Bernard Lyon 1, France.



Institut de recherches sur la catalyse et l'environnement de Lyon



Mes premiers remerciements vont à mes directeurs de thèse, David Farrusseng et Yves Schuurman pour m'avoir donné l'opportunité de réaliser ce projet de recherche au sein de leur équipe. Leurs conseils, leur confiance, leur patience et leur soutien tout au long de ces trois années de thèse m'ont été d'une grande aide. J'ai particulièrement apprécié toutes nos discussions techniques et les connaissances scientifiques qu'ils m'ont apportées. Leur amitié a été pour moi un encouragement précieux.

J'aimerais également témoigner ma reconnaissance à Alain Tuel pour avoir partagé son savoir sur les synthèses de zéolithes et à Jean-Marc Millet pour son expertise et son aide en spectroscopie Mössbauer.

Mes remerciements vont également aux rapporteurs et aux membres de mon jury de thèse qui ont examiné, évalué mes travaux et engagé des discussions scientifiques pertinentes lors de la soutenance. Un grand merci à Anne Griboval-Constant, Magnus Rønning, Dominique Decottignies, Anne Galarneau, Freek Kapteijn et Pascal Fongarland.

Ma gratitude va également à Siddardha Koneti et Lucian Roiban pour leur amitié et leur magnifique travail en TEM-tomographie. Je remercie aussi le Centre Lyonnais de Microscopie (Clym) pour m'avoir donné accès à l'ETEM TITAN 80-300 keV.

Je n'oublie pas Diego Pena Zapata, Andrea Cognigni et Magnus Rønning pour toute l'aide qu'ils m'ont apportée pour les analyses au synchrotron et, leur amitié et leurs conseils. J'en profite pour remercier l'équipe du Swiss-Norwegian Beamlines (SNBL) de l'European Synchrotron Radiation Facility (ESRF) pour leur expertise technique et leur assistance.

La formation à l'utilisation du microscope électronique en transmission (TEM) prodiguée avec patience par Laurence Burel et Mimoun Aouine s'est avérée très bénéfique au déroulement de mon travail.

J'aimerais également remercier les services scientifiques, plus particulièrement Noëlle Cristin et Pascale Mascunan pour les analyses élémentaires.

Les conseils avisés d'Edouard Rebmann au début de ma thèse, sa gentillesse ainsi que le temps qu'il a consacré à m'aider à résoudre les nombreux problèmes du bâtiment Z m'ont permis de prendre confiance et démarrer mes recherches sur de bonnes bases. Merci à Davide Lorito, mon collègue de bureau, pour son aide, son amitié et pour avoir pris la relève.

Je remercie Shiwen Li de m'avoir formé aux synthèses de zéolites, pour son aide précieuse, son amitié, et le partage de ses connaissances scientifiques.

Les très nombreux échanges scientifiques partagés avec David Laprune au cours de ces trois ans restent des moments privilégiés. Son aide, ses conseils et nos discussions ont été particulièrement constructifs. David, merci pour ton amitié et ton soutien.

Les trois années passées près d'Anaëlle Paredes-Nuñez, ma chère collègue de bureau, ont été ponctuées par sa gentillesse, sa bonne humeur, et de nombreuses discussions animées. Merci pour ton soutien.

Que tous les membres de l'équipe ingénierie que j'ai côtoyés pendant ces trois années, Anaëlle Paredes-Nuñez, Edouard Rebmann, Davide Lorito, David Laprune, Mathilde Luneau, Laurent Gueudré, Alexandre Margeriat, Alejandra Bueno, Linh Ho, Shiwen Li, Alexandre Legrand, Jérémy Dhainaut, Yoldes Khabzina, Ana-Rita Morgado, Céline Pagis, Alina Moscou, Florian Chapon, Youmin Guo, Florian Wisser, Caroline Urmès, Elise Bernoud, Yann Chapellière, Katia Barbera, Medhi Bessaa, Cindy Aquino, Marie Rochoux, Elia Gianotti, Mathieu Balas, York Mohr, Christina Theodoridi, Nargiz Novruzova, Audrey Valette, Xavier Besse, Jonathan Bonnefoy, David Farrusseng, Yves Schuurmann, Jérôme Canivet, Alain Tuel, Emmanuel Landrison, Cécile Daniel, Nolven Guillaume, Frédéric Meunier, Claude Mirodatos, Franck Morfin, Jean-Luc Rousset soient remerciés.

De même que les membres de l'institut, Sébastien Albert, Anne-Marie Grézaud, Narayman El-Jerrari, Marie-Laure Venditti, Christine Babolat, Géraldine Chapuis trouvent ici ma reconnaissance.

Et puisque cette liste n'est probablement pas exhaustive, je remercie toutes les personnes qui ont participé de près ou de loin à la réussite de cette thèse.

Résumé

L'intérêt pour la synthèse de Fischer-Tropsch (FTS) est d'actualité. Elle permet la conversion de matière première (biomasse) en combustible liquide. Comparés aux catalyseurs à base de cobalt, ceux à base de fer présentent une désactivation rapide, une activité et une sélectivité faibles en produisant une quantité non désirable de CO₂. Après plusieurs décennies d'études, l'origine de ces défauts reste méconnue. Les catalyseurs classiques sont généralement fortement chargés en fer (> 70 %wt) et composés de nombreuses phases empêchant l'établissement d'une relation structure-activité. Il est nécessaire de développer des catalyseurs contenant du fer plus actifs, plus sélectifs et plus stables par une approche rationnelle.

La synthèse de nanoparticules de taille contrôlée (3.5 nm) encapsulées dans les murs d'une silicalite-1 creuse (Fe@hollow-silicalite-1) est présentée. L'encapsulation empêche le frittage pendant la synthèse de Fischer-Tropsch, permettant de garder une bonne dispersion du fer. Contrairement aux autres catalyseurs, le catalyseur Fe@hollow-silicalite-1 actif ne produit pas de CO₂. L'hydrophobicité de la silicalite-1 est très certainement à l'origine de la non-production de CO₂ par inhibition de la réaction directe du gaz à l'eau. Afin d'établir une relation structure-activité, des catalyseurs à base de fer de taille bien contrôlée sont synthétisés et caractérisés (MET, in-situ XANES, in-situ Mössbauer).

Abstract

Fischer-Tropsch synthesis (FTS) is gaining renewed interests as it allows converting alternative feedstocks (biomass) into liquid fuels. Compared to Co-based catalysts, state of the art Fe catalysts show lower activity, faster deactivation and lower selectivity as it produces an undesirable amount of CO₂. Despite decades of studies, the origins of low activity and selectivity and fast deactivation are still unclear. Typical Fe based catalysts are highly metal loaded (> 70 %wt) and composed of many different phases, which strongly impedes the establishment of structure-activity relationships. There is a need to develop more active, more selective and more stable iron FTS catalysts by rational approaches.

The synthesis of well-controlled 3.5 nm iron nanoparticles encapsulated in the walls of a hollow-silicalite-1 zeolite (Fe@hollow-silicalite-1) is presented. The encapsulation prevents particle sintering under FTS conditions leading to a high and stable Fe dispersion. The catalyst Fe@hollow-silicalite-1 is active and highly selective in FTS. Most importantly, Fe@hollow-silicalite-1 does not produce CO₂ in contrast to all other Fe-based catalysts. The strong hydrophobicity of the silicalite-1 is likely the origin of the lack of CO₂ production by inhibition of the forward WGS reaction. In order to establish a structure-activity relationship, a series of Fe-based catalysts with well-controlled particle sizes were synthesized and characterized (TEM, in-situ XANES, in-situ Mössbauer, XRD).

Table of content

| | |
|---|------------------|
| Acknowledgments | <i>i</i> |
| Résumé | <i>iv</i> |
| Abstract | <i>v</i> |
| Table of content | <i>vi</i> |
| General introduction | 1 |
| I. Motivation | 1 |
| II. Objectives | 1 |
| III. Thesis outline | 3 |
| Chapter 1 - State of the art - A review | 5 |
| I. Context of the work | 6 |
| I.1. Introduction to FASTCARD | 6 |
| I.2. FASTCARD project – CO ₂ tolerant Fischer-Tropsch (WP2)..... | 9 |
| II. State of the art | 10 |
| II.1. Fischer-Tropsch synthesis (FTS)..... | 10 |
| II.1.1. A brief history of the Fischer-Tropsch synthesis | 10 |
| II.1.2. X-to-Liquid technologies (XtL) | 12 |
| II.1.3. General reaction during Fischer-Tropsch synthesis | 17 |
| II.1.4. Product distribution and selectivity | 18 |
| II.2. Iron-based FTS catalysts..... | 20 |
| II.2.1. Activity of Fe-based catalysts for FTS..... | 21 |
| a. FTS and WGS activity | 21 |
| b. Iron phases influence on activity during the Fischer-Tropsch synthesis | 22 |
| c. Particle size influence on activity..... | 25 |
| II.2.2. Selectivity of Fe-based catalysts for FTS..... | 26 |
| a. Product selectivity of Fe-based catalyst during FTS | 26 |
| b. Promoters influence (K, Cu, Mn) | 27 |
| c. Particle size influence on selectivity..... | 27 |
| II.2.3. Deactivation of iron based catalysts | 28 |
| a. Iron phases transformations | 29 |
| b. Deposition of carbonaceous compounds | 29 |
| c. Sintering and loss of catalytic surface area | 30 |
| d. Poisoning..... | 31 |
| II.2.4. Conclusion..... | 32 |
| II.3. Effect of CO ₂ -containing syngas mixture over Fe-based catalysts in FTS | 33 |
| III. Fe-zeolite core-shell system for Fischer-Tropsch synthesis | 35 |

| | |
|--|-----------|
| Chapter 2 - Experimental procedure..... | 39 |
| I. Catalyst preparation | 40 |
| I.1. Silicalite-1 synthesis..... | 40 |
| I.2. Impregnation of silicalite-1 by incipient wetness..... | 41 |
| I.3. Preparation of Fe@hollow-silicalite-1 | 41 |
| I.4. Reduction procedure of Fe@hollow-silicalite-1 | 42 |
| II. Characterization techniques for catalyst analysis | 43 |
| II.1. Powder X-ray Diffraction (XRD)..... | 43 |
| II.2. Elementary Analysis (ICP-OES)..... | 44 |
| II.3. N ₂ adsorption/desorption..... | 45 |
| II.4. Transmission Electronic Microscopy (TEM)..... | 45 |
| II.4.1. Sample preparation..... | 45 |
| II.4.2. Transmission Electronic Microscopy apparatus | 45 |
| II.4.3. Energy Dispersive X-ray spectroscopy | 47 |
| II.4.4. Study of nano-particles with TEM | 47 |
| II.5. Environmental Transmission Electronic Microscopy (E-TEM)..... | 48 |
| II.6. Mössbauer spectroscopy..... | 49 |
| II.6.1. Ex-situ Mössbauer | 49 |
| II.6.2. In-situ Mössbauer..... | 52 |
| II.7. Magnetic measurements | 53 |
| II.7.1. Theory of magnetism..... | 53 |
| II.7.2. Experimental setup | 58 |
| II.8. Synchrotron: In-situ X-ray powder diffraction (XRDP) and X-ray absorption spectroscopy (XAS) | 59 |
| II.8.1. Experimental setup | 59 |
| II.8.2. Methodology of measurements | 61 |
| III. Catalytic reactions and data processing | 62 |
| III.1. Fischer-Tropsch synthesis – setup and processing..... | 62 |
| III.1.1. Experimental setup | 62 |
| III.1.2. Analytical setup..... | 63 |
| III.1.3. Catalytic data treatment and calculation..... | 66 |
| III.2. Water-gas-shift testing setup | 69 |
| III.3. Labelled ¹³ C ₂ MS and GC-MS experimental setup..... | 70 |
| Chapter 3 - Characterization of iron-based catalysts | 71 |
| Introduction..... | 73 |
| I. Characterization of a state of the art catalyst: Commercial catalyst..... | 75 |
| I.1. Study of the commercial catalyst before FTS | 75 |
| I.1.1. Transmission electron microscopy (TEM) | 75 |
| I.1.2. Powder X-ray diffraction (XRD) | 75 |
| I.1.3. Magnetism analysis..... | 76 |
| I.1.4. Iron phases determination by ⁵⁷ Fe Mössbauer spectroscopy | 77 |
| I.2. Study of the commercial catalyst after FTS | 78 |
| I.2.1. Transmission electron microscopy (TEM) | 78 |
| I.2.2. Iron phases determination by powder X-ray diffraction (XRD) | 79 |
| I.2.4. Magnetism analysis..... | 80 |
| I.2.3. Iron phases determination by ⁵⁷ Fe Mössbauer spectroscopy | 81 |
| Conclusion..... | 83 |
| II. Characterization of a Fe@hollow-silicalite-1 catalyst..... | 84 |

| | |
|--|------------|
| II.1. Preparation of Fe@hollow-silicalite-1 catalyst..... | 84 |
| II.1.1 Post-impregnation of hollow-silicalite-1..... | 84 |
| II.1.2. Impregnation followed by the formation of the hollow-silicalite-1..... | 85 |
| II.1.3. Control of the loading of iron in hollow-silicalite-1..... | 87 |
| II.1.4. Promoters addition to the iron in hollow-silicalite-1..... | 87 |
| II.2. Study of the Fe@hollow-silicalite-1 before FTS..... | 88 |
| II.2.1. High resolution transmission electron microscopy and tomography..... | 88 |
| II.2.2. Nitrogen adsorption/desorption isotherms..... | 90 |
| II.2.3. Powder X-ray diffraction (XRD)..... | 91 |
| II.2.4. Iron phases determination by ⁵⁷ Fe Mössbauer spectroscopy..... | 92 |
| II.3. Study of the Fe@hollow-silicalite-1 during FTS..... | 96 |
| II.3.1. Iron phases determination by <i>in-situ</i> XRD and <i>in-situ</i> Xanes..... | 96 |
| a. Iron phases determination by <i>in-situ</i> XRD..... | 96 |
| b. Iron phases determination by <i>in-situ</i> Xanes..... | 97 |
| II.3.2. Iron phases determination by <i>in-situ</i> ⁵⁷ Fe Mössbauer spectroscopy..... | 98 |
| II.4. Study of the Fe@hollow-silicalite-1 after FTS..... | 101 |
| II.4.1. Transmission electron microscopy (TEM)..... | 101 |
| II.4.2. Iron phases determination by XRD..... | 102 |
| II.4.3. Iron phases determination by ⁵⁷ Fe Mössbauer spectroscopy..... | 102 |
| Conclusion..... | 106 |
| III. Characterization of a Fe/hollow-silicalite-1 catalyst..... | 108 |
| III.1. Study of the Fe/hollow-silicalite-1catalyst before FTS..... | 109 |
| III.1.1. Transmission electron microscopy (TEM)..... | 109 |
| III.1.2. Powder X-ray diffraction (XRD)..... | 109 |
| III.1.3. Iron phases determination by ⁵⁷ Fe Mössbauer spectroscopy..... | 110 |
| III.2. Study of the Fe/hollow-silicalite-1catalyst after FTS..... | 114 |
| III.2.1. Transmission electron microscopy (TEM)..... | 114 |
| III.2.2. Powder X-ray diffraction (XRD)..... | 114 |
| III.2.3. Iron phases determination by ⁵⁷ Fe Mössbauer spectroscopy..... | 115 |
| Conclusion..... | 118 |
| IV. Characterization of a Fe/SiO₂ catalyst..... | 119 |
| IV.1. Study of the Fe/SiO ₂ catalyst before FTS..... | 119 |
| IV.1.1. Transmission electron microscopy (TEM)..... | 119 |
| IV.1.2. Powder X-ray diffraction (XRD)..... | 120 |
| IV.1.3. Iron phases determination by ⁵⁷ Fe Mössbauer spectroscopy..... | 121 |
| IV.2. Study of the Fe/SiO ₂ catalyst post FTS..... | 122 |
| IV.2.1. Transmission electron microscopy (TEM)..... | 122 |
| IV.1.3. Powder X-ray diffraction (XRD)..... | 123 |
| IV.2.4. Iron phases determination by ⁵⁷ Fe Mössbauer spectroscopy..... | 124 |
| Conclusion..... | 125 |
| V. Characterization of a nano-structured α-Fe₂O₃ catalyst..... | 127 |
| V.1. Preparation of nano-structured α-Fe ₂ O ₃ catalyst..... | 127 |
| V.1.1. Preparation of SBA-15 support..... | 127 |
| V.1.2. Preparation of nanostructured α-Fe ₂ O ₃ | 127 |
| V.2. Study of the nano-structured α-Fe ₂ O ₃ catalyst before FTS..... | 128 |
| V.2.1. Transmission electron microscopy (TEM)..... | 128 |
| V.2.2. Powder X-ray diffraction (XRD)..... | 129 |
| V.2.3. Iron phases determination by ⁵⁷ Fe Mössbauer spectroscopy..... | 130 |
| V.3. Study of the nano-structured α-Fe ₂ O ₃ catalyst during FTS..... | 131 |
| V.3.1. Iron phases determination by <i>in-situ</i> XRD..... | 131 |
| V.3.2. Iron phases evolution by <i>in-situ</i> XANES..... | 132 |

| | |
|---|------------|
| V.4. Study of the nano-structured α -Fe ₂ O ₃ catalyst after FTS | 133 |
| V.4.1. Transmission electron microscopy after FTS | 133 |
| V.4.2. Determination of iron phases after FTS by <i>ex-situ</i> XRD | 133 |
| V.4.3. Iron phases determination by ⁵⁷ Fe Mössbauer spectroscopy..... | 134 |
| Conclusion..... | 139 |
| Conclusion | 140 |
| Chapter 4 - Study of the Fischer-Tropsch synthesis on iron-based catalysts. 145 | |
| Introduction..... | 146 |
| I. Catalytic testing on the iron co-precipitated commercial catalyst..... | 147 |
| I.1. Fischer-Tropsch synthesis catalytic study..... | 147 |
| I.1.1. Validation of rig test..... | 147 |
| I.1.2. Fischer-Tropsch synthesis study at a CO conversion of 20 % | 149 |
| I.1.3. Conclusion..... | 151 |
| I.2. Water-gas-shift testing of the commercial catalyst..... | 151 |
| II. Catalytic testing on the Fe@hollow-silicalite-1 catalyst | 153 |
| II.1. Fischer-Tropsch synthesis catalytic study..... | 153 |
| a. Effect of temperature on Fe@hollow-silicalite-1 during FTS | 153 |
| b. Effect of GHSV on Fe@hollow-silicalite-1 during FTS..... | 155 |
| c. Effect of Promoters on Fe@hollow-silicalite-1 during FTS..... | 157 |
| d. Conclusion..... | 158 |
| II.2. Fischer-Tropsch synthesis catalytic study: stoichiometry conditions H ₂ :CO:CO ₂ = 2:0.8:0.2 | 159 |
| II.3. Water-gas-shift catalytic testing of Fe@hollow-silicalite-1 material..... | 161 |
| III. Fischer-Tropsch catalytic testing on the other iron-based catalysts | 162 |
| Conclusion | 164 |
| Chapter 5 - Study of the Fe@hollow-silicalite-1 catalyst: Determination of the relationship between structural features and catalytic performances | 167 |
| Introduction..... | 168 |
| I. Study of the stability of iron-based catalysts | 168 |
| II. Study of the activity and selectivity of the iron-based catalysts | 175 |
| II.1. Activity, dispersion and structure sensitivity of iron catalyst | 175 |
| II.2. Study of the effects of the iron phases on the activity | 180 |
| II.3. Study of the effects of iron phases on the CO ₂ selectivity..... | 183 |
| III. Effect of the hydrophobicity of silicalite-1 on the selectivity and especially on CO₂.185 | |
| III.1. Hydrophobicity of silicalite-1 | 185 |
| III.2. Hydrocarbons adsorption properties of silicalite-1 | 189 |
| III.3. Relation between silicalite-1 hydrophobicity and FTS performances | 191 |
| III.3.1. Behavior of the catalyst at the nano-scale..... | 191 |
| III.3.2. Behavior of the catalyst at the reactor scale..... | 195 |
| IV. Study of the CO₂ transformation mechanism using labelled ¹³CO₂, MS and GC-MS analysis. | 198 |
| IV.1. Testing conditions and analytical apparatus | 198 |
| IV.2. ¹³ C analysis by mass spectrometer | 199 |

| | |
|--|------------|
| Overall conclusion and perspectives..... | 203 |
| Appendix | 205 |
| 1) Mössbauer spectroscopy of FeCuK@hollow-silicalite-1 catalyst..... | 205 |
| 2) Olefin to paraffin ratio..... | 206 |
| 3) Determination of the water-gas-shift reaction equilibrium..... | 207 |
| a) If the WGS is at equilibrium..... | 207 |
| b) If the WGS is not at equilibrium | 209 |
| 4) ¹³ C analysis by gas chromatography coupled with mass spectrometer | 210 |
| Bibliography..... | 213 |

General introduction







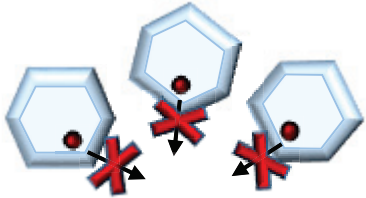
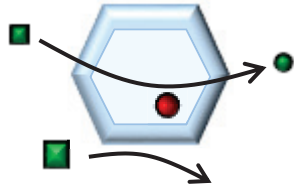

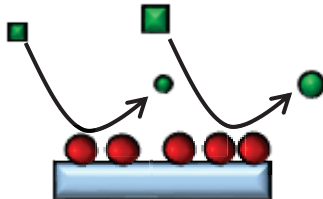
I. Motivation

Although already applied at industrial scale about one century ago, the Fischer-Tropsch process is gaining renewed interests as it is a key step for converting alternative feedstocks, including biomass to transportation fuels. For example, currently 140 kbarrels/day of synthetic transportation fuels are produced by Fischer-Tropsch process at PEARL (Qatar), on a Co-based catalyst. Because of the high price of Co, iron-based Fischer-Tropsch catalysts are increasingly reinvestigated. Compared to Co-based catalysts, state of the art Fe catalysts show lower activity (per volume), lower selectivity as it produces a significant and undesirable quantity of CO₂ and much faster deactivation. Unfortunately, the origin of low selectivity and fast deactivation is still unclear. Typical Fe based catalysts have high metal loadings (> 70 %wt) and contain many different phases, strongly limiting the establishment of structure-activity relationships. Therefore, there is a need to develop more active, more selective and more stable Fe Fischer-Tropsch Synthesis (FTS) catalysts using rational approaches.

II. Objectives



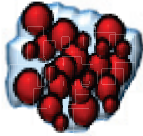
The major aim of this thesis is to design a more active, selective and stable iron-based catalyst for the Fischer-Tropsch synthesis (FTS). In this study, the concept used is the encapsulation of well-controlled iron nanoparticles inside a silicalite-1 material (**Table 1**). It requires the synthesis of well-dispersed iron nanoparticles and a good control of the particles size distribution. A good control of the iron nanoparticles size should enhance the activity of the catalyst by providing a higher active surface. In addition, the use of the silicalite-1 material, as a protection around the particles, shall help to prevent or at least reduce the sintering or coalescence of particles. Furthermore, the use of silicalite-1 with a well-defined porous network shall play a role in reactants and products traffic close to the catalytic site and shall impact on Fischer-Tropsch synthesis selectivity.

Table 1 | Concept of this work and comparison with conventional catalyst (adapted from [1])

|  Encapsulated iron nanoparticles in silicalite-1  Conventional catalyst  Small reactant  Small product  Large reactant  Large product | |
|---|--|
| Stability and particle size control | Selectivity |
|  <p>Stable catalyst, no sintering or coalescence, reusable, no activity loss, particle size controlled</p> |  <p>Selectivity controlled</p> |
|  <p>Not stable, sintering, coalescence, loss of activity</p> |  <p>No selectivity controlled</p> |

To perfectly understand the behavior and catalysis of this newly designed iron-based catalyst, the **fresh** and **spent** catalyst shall thoroughly be studied and characterized. In addition, several type of iron-based catalysts shall be studied and compared with the new catalyst. The iron-based catalysts studied in this work fall into three categories: encapsulated, supported and bulk-type catalysts (**Table 2**).

Table 2 | Iron-based catalyst types studied in this work

| | | |
|---|--|--|
|  Encapsulated catalyst |  Supported catalyst |  Bulk-type catalyst |
|---|--|--|

Each catalyst shall be systematically characterized to get a precise knowledge of their structure, iron phases and morphology. Furthermore, activity, selectivity and deactivation studies shall be carried out to allow catalysts to be compared.

This study is expected to improve the understanding of iron-based catalysts and to open new pathway in rational design of iron-based catalysts for the near future.

III. Thesis outline

This thesis consists of five chapters. There is a degree of repetition in the experimental work and characterization description in each chapter. However, this should help to strengthen the reader's understanding of the work.

Chapter 1 describes the basic information and knowledge needed for a better understanding and comprehension of this study. The Fischer-Tropsch synthesis, as well as, the basic knowledge on iron-based catalysts is described.

Chapter 2 gives the general experimental procedures and equipment used all along this study. The FTS setup and calculation formula are incorporated in this chapter.

Chapter 3 aims to describe the in-depth characterization of a certain number of iron-based catalysts references as well as the newly designed iron catalyst. The synthesis processes of the newly iron-based catalyst are described in this chapter. The characterization of the fresh and spent catalysts by various techniques such as transmission electron microscopy, X-ray diffraction, Mössbauer spectroscopy and in-situ XANES are needed to get a full understanding of the iron phases, particles size and dispersion.

Chapter 4 deals with the evolution of the different iron-based catalysts during the Fischer-Tropsch synthesis. Several FTS conditions are investigated, such as temperature, GHSV, promoters and CO₂ addition in the feed. Also, additional water-gas-shift (WGS) tests are conducted for a better understanding of the iron-catalyst's behavior.

Chapter 5 aims to discuss the data of chapter 3 and chapter 4. The objective is to relate the iron phases, particles size and dispersion of the iron-based catalysts with the Fischer-Tropsch reaction data to get a full understanding of the relationship between the structural features of the new iron-based catalyst and its catalytic performances.

Chapter 1 - State of the art - A review

| | |
|--|-----------|
| Chapter 1 - State of the art - A review..... | 5 |
| I. Context of the work..... | 6 |
| I.1. Introduction to FASTCARD..... | 6 |
| I.2. FASTCARD project – CO ₂ tolerant Fischer-Tropsch (WP2)..... | 9 |
| II. State of the art..... | 10 |
| II.1. Fischer-Tropsch synthesis (FTS)..... | 10 |
| II.1.1. A brief history of the Fischer-Tropsch synthesis..... | 10 |
| II.1.2. X-to-Liquid technologies (XtL)..... | 12 |
| II.1.3. General reaction during Fischer-Tropsch synthesis..... | 17 |
| II.1.4. Product distribution and selectivity..... | 18 |
| II.2. Iron-based FTS catalysts..... | 20 |
| II.2.1. Activity of Fe-based catalysts for FTS..... | 21 |
| a. FTS and WGS activity..... | 21 |
| b. Iron phases influence on activity during the Fischer-Tropsch synthesis..... | 22 |
| c. Particle size influence on activity..... | 25 |
| II.2.2. Selectivity of Fe-based catalysts for FTS..... | 26 |
| a. Product selectivity of Fe-based catalyst during FTS..... | 26 |
| b. Promoters influence (K, Cu, Mn)..... | 27 |
| c. Particle size influence on selectivity..... | 27 |
| II.2.3. Deactivation of iron based catalysts..... | 28 |
| a. Iron phases transformations..... | 29 |
| b. Deposition of carbonaceous compounds..... | 29 |
| c. Sintering and loss of catalytic surface area..... | 30 |
| d. Poisoning..... | 31 |
| II.2.4. Conclusion..... | 32 |
| II.3. Effect of CO ₂ -containing syngas mixture over Fe-based catalysts in FTS..... | 33 |
| III. Fe-zeolite core-shell system for Fischer-Tropsch synthesis..... | 35 |

I. Context of the work

I.1. Introduction to FASTCARD

This PhD is sponsored by the FAST industrialization by Catalyst Research and Development (FASTCARD, [2]) project, a Large Scale Collaborative Project supported by the European Commission in the 7th Framework Programme (GA no 604277) [3].

Nowadays Europe is facing some major energy challenges. Europe desires to focus more efficiently on increasing the part of the Biomass used in bio-based economy. In 2008, the European commission presented new targets for the members of the European Union directing on emission cuts, renewables and energy efficiency, called the “three 20 targets” and a reduction of greenhouse gas emission by 80 - 95 % as targeted in the European Energy Roadmap 2050.

An important component to achieve the new targets set by EU is the conversion of Biomass into advanced fuels, as bio-fuels by the mean of catalysis.

Heterogeneous catalysis has already a crucial role in the conversion of fossil resources into energy and transportation fuels, for example synthetic diesel is produced by Fischer-Tropsch (~210 000 bpd Gas-to-Liquid (GtL) in Middle East and 170 000 bpd Coal-to-Liquid (CtL) in South Africa) while fluid catalytic cracking (FCC) produces gasoline from heavy fossil oils in Europe (European FCC capacity: 132 million tons).

However, the new demand from Europe for transformation of bio-resources (biomass) into liquid bio-fuels has generated new challenges in catalyst development that have so far hindered the implementation of industrial pilot-plants and facilities. Actual catalyst developments are severely hindered by increasing costs and risks when going from laboratory scale to pilot plant-level and from pilot plant to industrial-scale, constituting real barriers and increasing the time for industrialization and commercial implementation. Nevertheless the development of successful catalysts for biomass conversion is a challenging but sustainable and environmentally desirable outcome.

To increase by 20 % the share of renewable energy and, at the same time, to reduce by 20 % greenhouse gas emissions, the substitution of traditional feedstocks by biomass is one of the

major possible ways. However, new challenges arise in terms of catalyst development. Undeniably, catalytic conversion of biomass compared to fossil oil, coal and natural gas is highly complex due to its large amount of oxygen, nitrogen and sulfur containing molecules and its huge variability depending on its origin (waste, paper, wood, grass and straw). This level of complexity strengthens the need to design new, more flexible, robust and reliable catalysts before going to industrial scale.

When compared to classical feedstocks, like fossil oils and natural gas, biomass is generally more reactive towards catalytic conversion and thus required additional pre-treatment/catalytic steps for conditioning and stabilization. The gasification of biomass produces hydrocarbons (methane, C₂ and C₃ hydrocarbons and single/multi-ring aromatics) representing some 50 % of the energy within the feedstocks, which would be wasted if not converted to useful fuels [2]. The liquefaction of biomass through pyrolysis leads to very unstable sugar and oxygenated aromatics containing liquids that must be stabilized to an optimal level by hydro-treatment before post-processing [2]. Therefore to achieve the 20 % increase in energy efficiency, it is important to deal with these critical pre-treatment steps to increase the overall energy efficiencies of the value chains from biomass to biofuels and, in the end, achieving a low carbon footprint.

FASTCARD brings more knowledge and better technical performance of the catalysts, hence decreasing technological risk and consequently reducing costs and time needed for further industrialization. To meet short term European 20-20-20 objectives and long term targets of European Energy Roadmap 2050, FASTCARD aims at two major value chains for the catalytic conversion of biomass into advanced biofuels (**Figure 1**).

- **The pyrolysis liquid value chain:** Hydro-treating of pyrolysis oil and co-fluid catalytic cracking (co-FCC) processing.
- **The gasification gas value chain:** Hydrocarbon reforming and CO₂ tolerant Fischer-Tropsch (CO₂-FTS) synthesis.

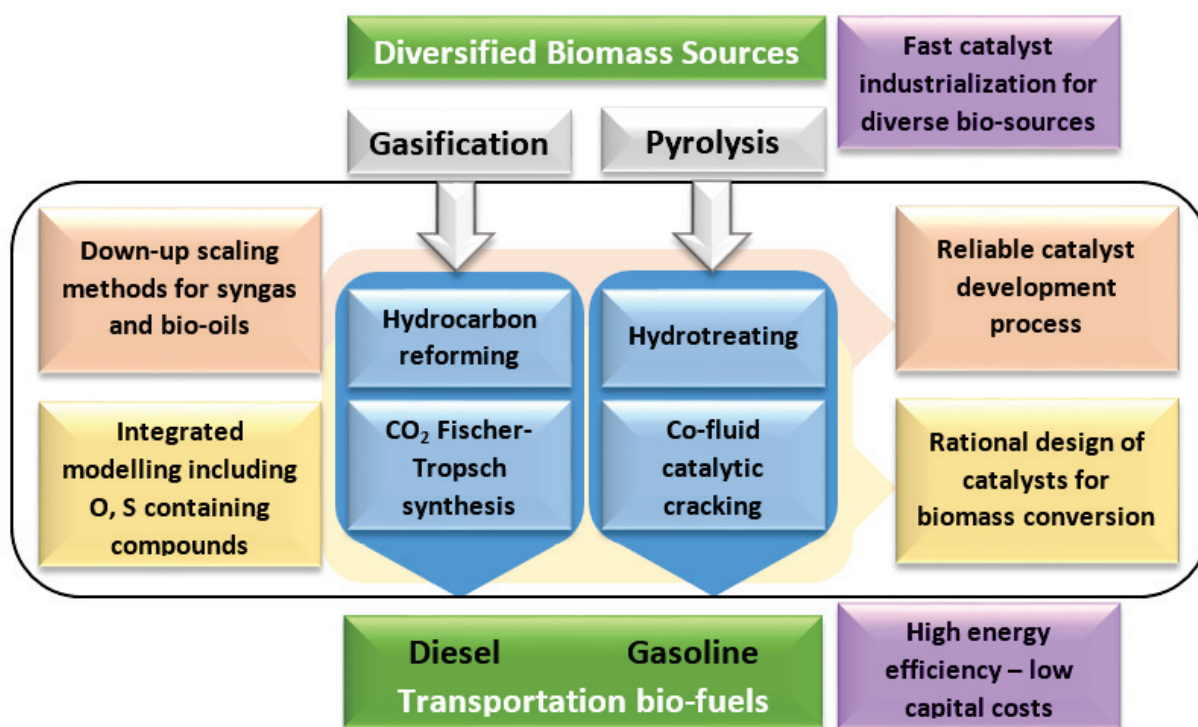


Figure 1 | FASTCARD concept [3].

FASTCARD focuses on four key catalytic steps for these two major pathways to advanced bio-fuels:

- **Hydrocarbon reforming (WP1)** – The objective is to develop steam reforming catalysts either in a single step or in a two-step catalytic reforming process. The development of sulphur-resistant and sintering-resistant noble metal nano-catalysts is one of the major objective of this work package.
- **CO₂ tolerant Fischer-Tropsch (WP2)** – Development of the next generation of iron-supported Fischer-Tropsch catalysts. The challenges to address are performance robustness with respect to higher temperatures, for the diverse feedstocks with significant CO₂ levels, and improved durability. Therefore as activity is controlled at the nano-particle scale, the nano-catalyst design approach allows the differentiation between active sites, helping to improve selectivity and to reduce deactivation.
- **Hydrotreating (WP3)** – Development of the next generation catalysts for the key two levels of hydrotreating (HT), i.e. 1) bio-oil stabilization and 2) further upgrading by hydrodeoxygenation (HDO), to produce high quality co-feed to bio-FCC plants at a minimum level of treatment. Challenges to address are robustness of performance with respect to

requirements of hydrogen consumption and pressure, improved durability, and control of selectivity at varying depth of oxygen removal.

- **Co-Fluid catalytic cracking (WP4)** - The high content of oxygen-containing compounds in the bio-oil (more than 10 %wt vs. << 1 %wt for common FCC feed [2]) and the lack of hydrothermal stability of the types of catalysts of interest for the catalytic co-processing of bio-oil are the main issues. Therefore, the development of advanced nano-porous structured catalysts aiming at radically improving the catalytic performance as well as the stability of these materials in the upgrading of bio-oil is crucial and the main objectives of this package.

I.2. FASTCARD project – CO₂ tolerant Fischer-Tropsch (WP2)

The main objective of the WP2 of FASTCARD is to develop the next generation of iron-supported Fischer-Tropsch catalysts to match the requirements of small delocalized 500 to 3000 bpd Biomass-To-Liquid (BTL) industrial plants. This part of the project regroups several industrial and academic partners each of them having different tasks to fulfill (**Figure 2**).

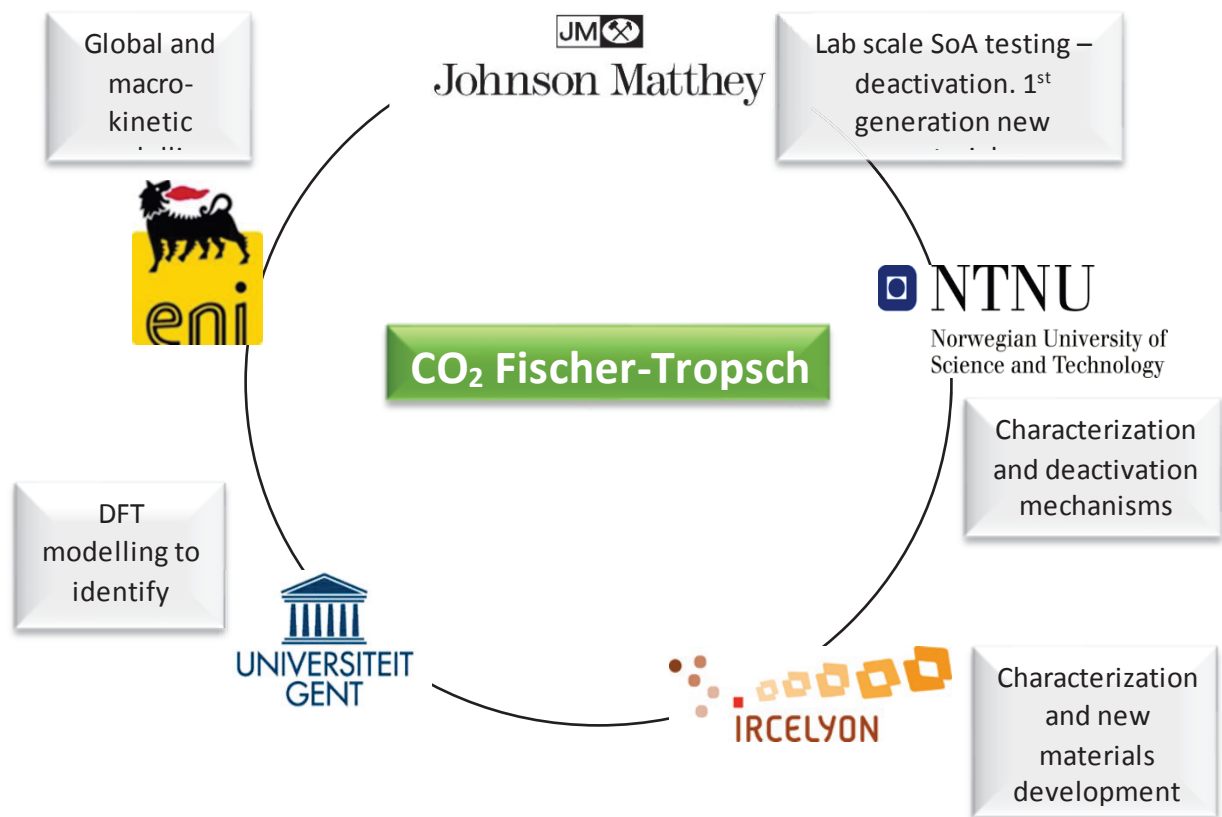


Figure 2 | WP2 FASTCARD members [3].

The general aims of the CO₂-tolerant Fischer-Tropsch work package are the following:

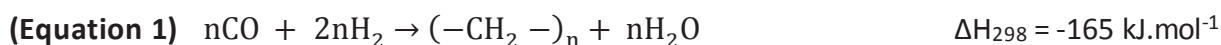
- To develop new catalysts operating at higher temperatures conditions (> 250 °C) with a higher carbon efficiency, i.e. higher C₅₊ selectivity. Furthermore, the new catalysts should also improve the process efficiency and robustness to both stoichiometric and sub-stoichiometric syngas ratios.
- To develop catalysts capable of benefiting from the utilization of the reverse water-gas-shift reaction in CO₂ rich feeds. The aim here is to reduce the process complexity by avoiding CO₂ capture up-stream of the Fischer-Tropsch reactor.
- To improve catalyst durability under each and every reaction conditions to avoid the need for replacement/regeneration every few months, a common feature with conventional Fe-containing Fischer-Tropsch catalysts. This will require developing a detailed understanding of the degradation/deactivation mechanisms.
- To improve the new catalyst selectivity to produce optimum diesel/gasoline type hydrocarbons, allowing downstream upgrading processes to be removed or simplified.
- To demonstrate that the novel catalysts can be produced using scalable industrial processes.

II. State of the art

II.1. Fischer-Tropsch synthesis (FTS)

II.1.1. A brief history of the Fischer-Tropsch synthesis

The Fischer-Tropsch (FT) reaction is the chemical heart of the gas-to-liquid technology (GtL). This highly exothermic reaction converts synthesis gas into a large range of linear hydrocarbons, which is represented as followed:



The Fischer-Tropsch process was first reported by Franz Fischer and Hans Tropsch ninety years ago [4]. They discovered the process in 1923 by converting a mixture of hydrogen and carbon monoxide into hydrocarbons and water using an iron catalyst. Their work was derived from the work of Sabatier and Senderens back in 1902 when they first produced methane from a mixture of carbon monoxide and hydrogen on a nickel-based catalyst [5, 6]. In 1913, Mittasch

and Schneider from BASF were the first to roughly define what is called nowadays the Fischer-Tropsch synthesis [7]. In an US patent, they reported the syngas conversion over cobalt catalysts at a pressure above 5 atmospheres and temperature between 200 °C and 500 °C [8]. However the reaction was reported to be non-selective and to produce a complex mixture (aqueous solution, aldehyde, organic phases, saturated and unsaturated hydrocarbons). Due to this, the newly discovered reaction did not catch the attention of industrials who preferred to stay focused on pure and valuable products such as methanol and ammonia.

Therefore it was only after Franz Fischer and Hans Tropsch, from the Kaiser Wilhelm Institute, pioneering work in the 1920's and 1930's that this process became interesting from a commercial point of view [9]. Later on, the most promising and efficient metallic catalyst for Fischer-Tropsch were determined, the most active metals known for the Fischer-Tropsch synthesis were ruthenium, iron, cobalt and nickel [10,11]. Iron and nickel were reported as highly effective for carbon monoxide hydrogenation with a high methane selectivity in the case of nickel [12]. Cobalt appeared to be the most efficient active phase for long chain production [13, 14]. Furthermore promoters were identified and added in the catalyst formula [15-19]. The hydrocarbon product mixture obtain after the Fischer-Tropsch process is called synthetic crude oil. It consists mostly of linear hydrocarbon chains (olefins and paraffins) with a wide boiling range. Absence of sulphur and nitrogen contaminant is generally observed.

The first industrial Fischer-Tropsch plant was operated with cobalt at low temperature in Oberhausen, Germany by Ruhrchemie AG in 1936 [20]. Later on in the 1950's, Sasol built the next generation of Fischer-Tropsch plant in South Africa centered on iron based catalysts [21]. During the last century, many industrial companies started to be involved in this promising energy field (Shell, Sasol, Statoil, BP, ExxonMobil, PetroSA, Ras Laffan Qatar, Velocys, Rentech...) [22, 23]. However due to the process complexity, many companies stopped their Fischer-Tropsch R&D activities at an early stage. Today Fischer-Tropsch synthesis plants are located in Qatar, South Africa, Nigeria and Malaysia (**Figure 3**). Two large projects were issued lately Oryx GtL in 2008 (Sasol/Qatar Petroleum) and Pearl GtL in 2011 (Shell).

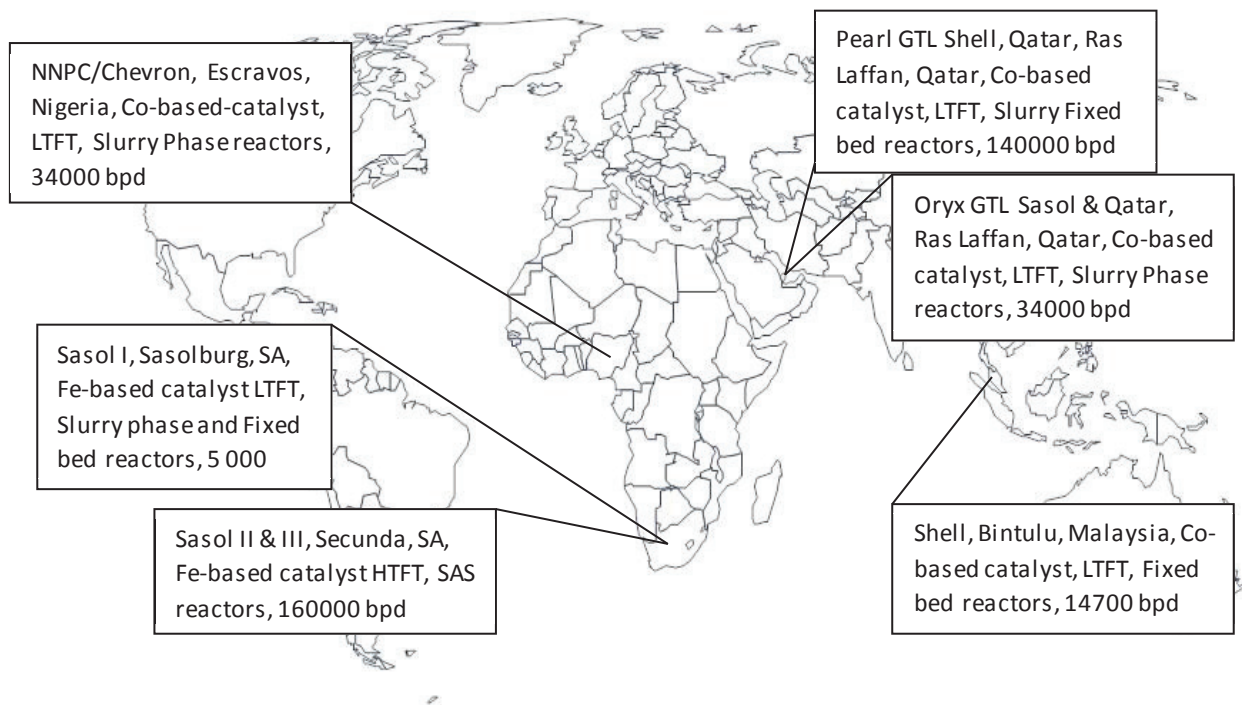


Figure 3 | World map of larger commercial Fischer-Tropsch plants.

II.1.2. X-to-Liquid technologies (XtL)

XtL technologies are refinery processes (GtL, CtL, BtL, WtL...) composed of a group of technologies converting solid or gaseous carbon-based sources into products that can be useful as chemicals and fuels (naphtha, gasoline, kerosene, diesel, waxes...). A variety of carbon-based sources most commonly called feedstocks, are used. The most common one are coal (CtL), natural gas (GtL) and biomass (BtL). From **Figure 4** we can see that other types of feedstock can be converted into syngas such as waste (WtL) and shale oil. The transformation of these feedstocks by XtL processes leads firstly to the production of a mixture called syngas a mixture of hydrogen (H_2) and carbon monoxide (CO). Following the nature of the feedstock, several processes are being used in the industry, from the gasification of solid sources (biomass, waste...) to the reforming or partial oxidation of natural gas [24, 25]. Usually the syngas mixture is converted into the so-called syncrude, before being upgraded in very specific valuable products such as fuel gas, diesel, kerosene... (**Figure 4**).

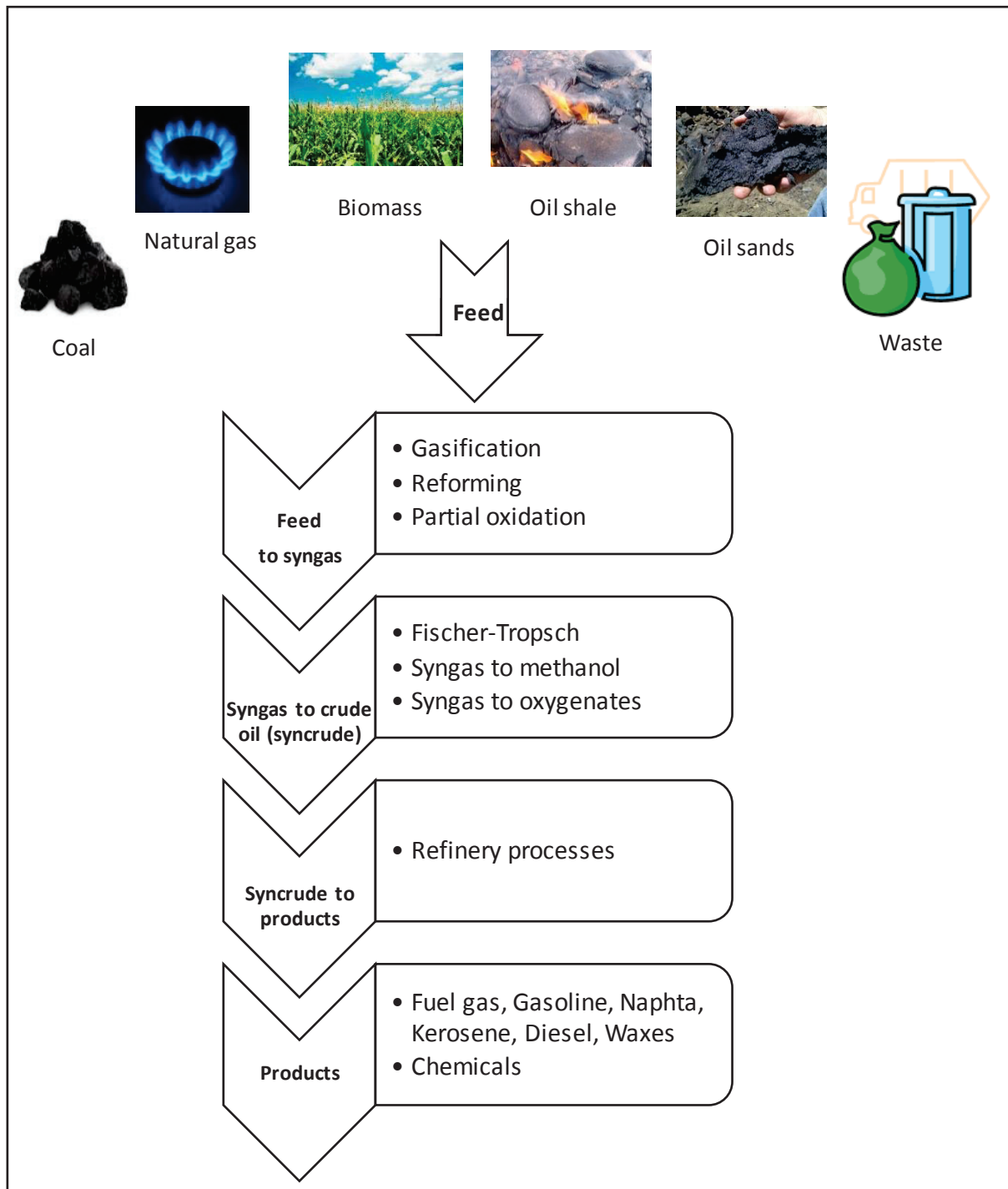


Figure 4 | Simplified XtL processes from feedstock to upgraded products.

The second step of this process consists in converting the syngas mixture into a syncrude (synthetic crude oil). It is generally done by the so called Fischer-Tropsch synthesis (FTS). However the Fischer-Tropsch synthesis is not the only possible process that can do it, together with the syngas-to-methanol processes, they are the most relevant one [25]. The Fischer-

Tropsch synthesis lies at the heart of the XtL process, however it is actually only a small part of the overall process (Figure 5).

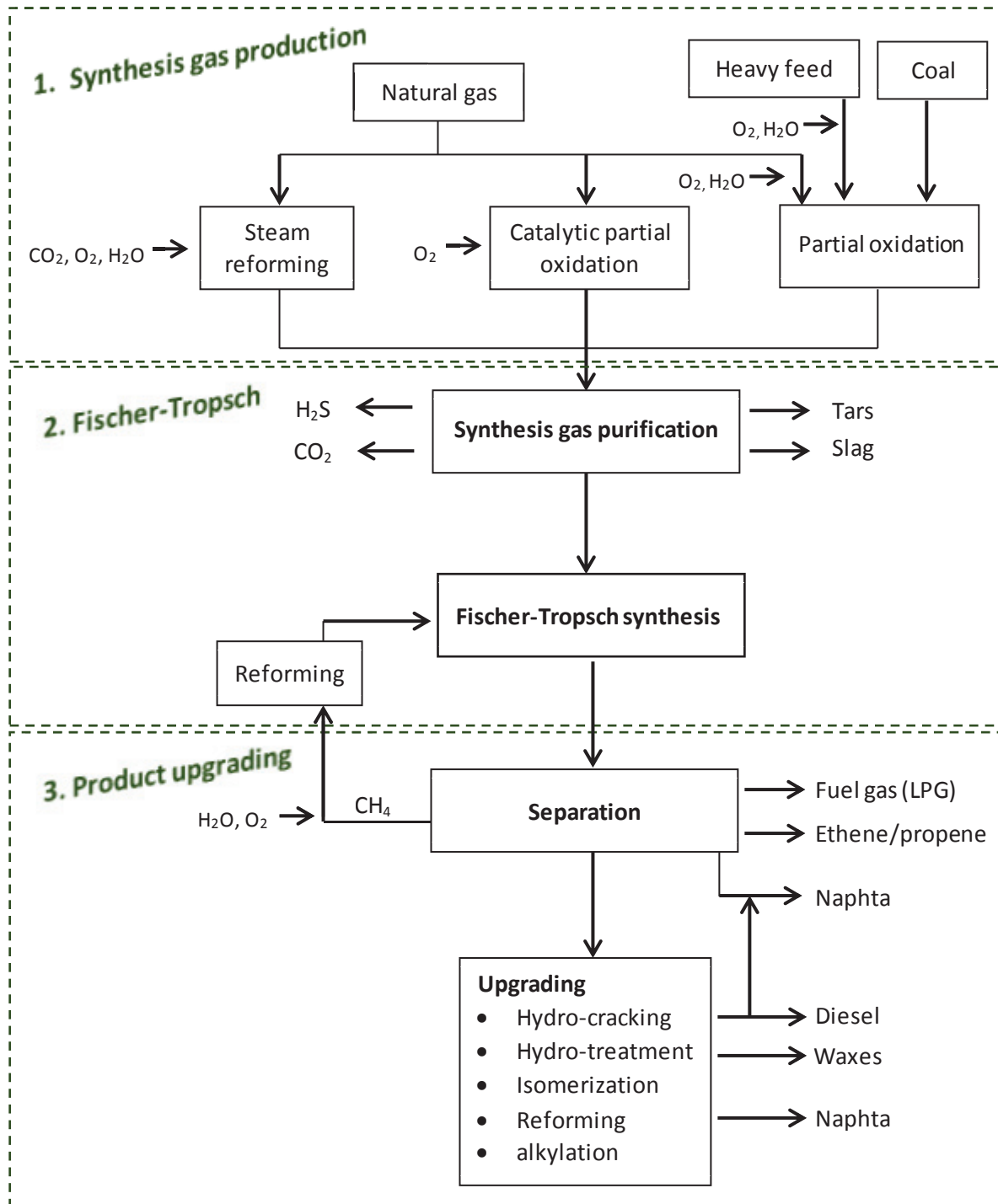
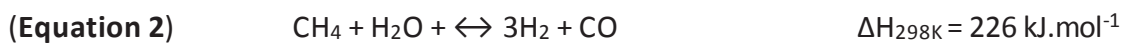


Figure 5 | Schematic representation of a Fischer-Tropsch process [22, 23, 26].

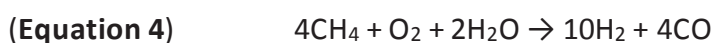
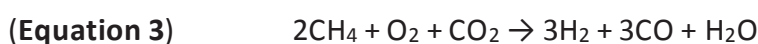
The XtL process is a complex process with several steps:

➤ **Gasification:** This step consists of transforming the different feedstocks (coal, natural gas and biomass) into synthesis gas called syngas ($H_2 + CO$). For that, different technologies are used depending of the nature of the initial feedstock. Synthesis gas can be obtained from reforming of natural gas with either steam or carbon dioxide, or by partial oxidation:

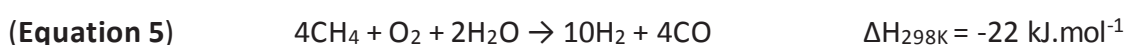
- **Steam reforming (SR):** this highly endothermic process is the most commonly based method to produce H_2 and CO . At high temperature ($700 - 1100\text{ }^\circ C$) and in presence of a metallic catalyst (generally nickel-based), steam reacts with methane to form syngas.



- **Autothermal reforming (ATR):** Oxygen and carbon dioxide or steam are used in a reaction with methane to produce syngas. The exothermic reaction generally takes place in a single chamber where the methane is partially oxidized. Different syngas ratios can be obtained following the type of gases used in the process carbon dioxide gives a H_2/CO ratio of 1:1 meanwhile steam gives a H_2/CO ratio of 2.5:1. The reactions are described as follows: (Equation 3) and (Equation 4) using CO_2 and steam, respectively:



- **Partial oxidation (POX) and catalytic partial oxidation (CPOX):** In POX and CPOX, the feed stream (mainly methane, CH_4) is mixed with oxygen and steam and fed to a high temperature flame between 1573 and 1773 K (Equation 5). The feed is then partially combusted. The syngas produced has a H_2/CO ratio close to 2, which is attractive for several chemical syntheses like direct methanol synthesis or Fischer-Tropsch synthesis.



➤ **Syngas processing:** Purification of the syngas to get rid of undesired compounds such as chlorine, sulfurous compounds...

➤ **Fischer-Tropsch synthesis:** The Fischer-Tropsch synthesis is the chemical heart of the gas-to-liquid process. The highly exothermic FTS reaction converts synthesis gas into a wide

range of hydrocarbons. FT synthesis is basically a catalytic reaction and the active and selective catalysts for the FT reaction are mainly based on cobalt or iron. Main products of the FT synthesis are linear paraffins and α -olefins. There are several types of Fischer-Tropsch reactors in commercial use: slurry phase reactor, tubular fixed-bed reactor and fluidized-bed reactor [27, 28]. Generally multi-tubular fixed bed and slurry phase reactors are used for low-temperature FTS (between 220 and 250 °C) to obtain long-chain hydrocarbons. High-temperature FTS (between 320 and 350 °C) is mostly being done with a two-phase fluidized systems with Fe-based catalysts to obtain short-chain hydrocarbons. In **Figure 6** an example of multi-tubular fixed bed reactor for the Fischer-Tropsch synthesis is given.

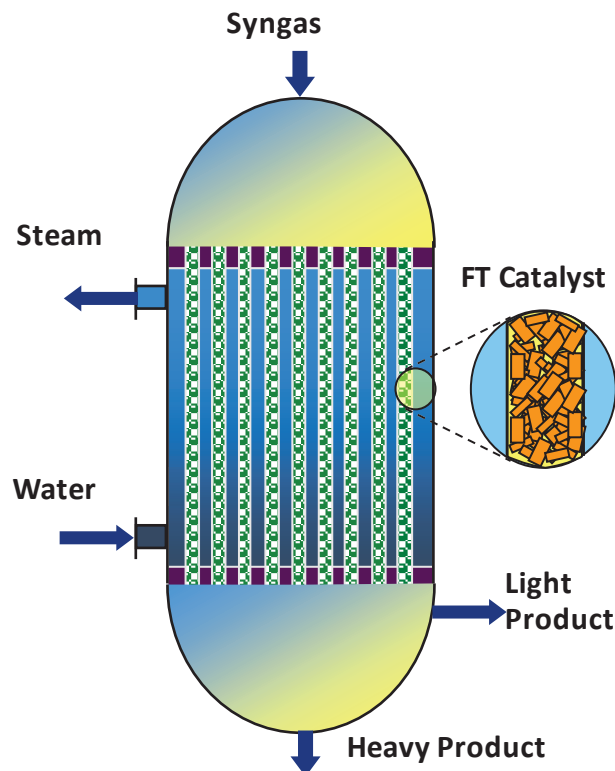


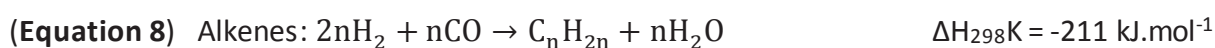
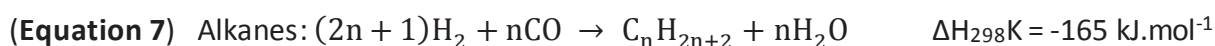
Figure 6 | Schematic representation of a multi-tubular fixed bed reactor.

- **Refining and Upgrading:** The hydrocarbon product mixture obtained by the Fischer-Tropsch reactor is referred to as synthetic crude oil. Fischer-Tropsch waxes consist mostly of linear hydrocarbon chains over a large boiling range and has a zero-level of S- or N-contaminants and aromatics. High selectivities towards fuels are obtained by hydrocracking the waxes (hydrocarbons chains higher than C₂₀). Hydrocracking is a

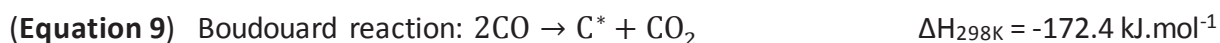
selective process, which converts heavy hydrocarbons into the C₄-C₁₂ range with low selectivities to C₁-C₃. This directly produces a high quality gasoil (high cetane index, low sulfur content, low aromatics) and kerosene (high paraffin content). The octane number of the hydrocracked wax is improved by processes such as isomerization, catalytic reforming, alkylation, and oligomerization.

II.1.3. General reaction during Fischer-Tropsch synthesis

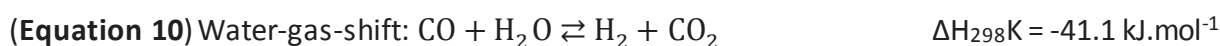
The Fischer-Tropsch synthesis (FTS) is a heterogeneous catalytic process and a non-selective polymerization reaction. It converts synthesis gas, called syngas (carbon monoxide (CO) and hydrogen (H₂)), into a large variety of products (a mixture of linear alkanes, alkenes, alcohols, aldehydes, ketones, carboxylic acids and water) for transportation fuels (diesel, gasoline) and petrochemical substituents. The purpose of this process is to produce long hydrocarbons chain without aromatics and sulphur species in order to comply with the most constraining legislations defining suitable and proper fuels. Alkanes and alkenes are the target products for FT synthesis. The Fischer-Tropsch process generally includes the following reactions:



In addition to the formation of these hydrocarbons, competing reactions may form organic oxygenates hydrocarbons, alcohols and carboxylic acids. Another side reaction called the Boudouard reaction may occur [11]:



Another reaction called the water-gas shift (WGS) reaction may happen during the FT process, especially in the case of Fe-based catalyst, this reaction is reversible [11, 28, 29]:



II.1.4. Product distribution and selectivity

Fischer-Tropsch synthesis is kinetically controlled and follows a polymerization mechanism, in fact CH₂ group polymerizes on the catalyst surface. The product selectivities are determined by the capacity of a catalyst to catalyze the chain propagation instead of the termination reactions. Therefore the product selectivities of Fischer-Tropsch synthesis can be described with a simple statistical distribution, better known as the Anderson-Schulz-Flory (ASF) distribution [31]. When considering the ideal case, the chain growth probability (α) is independent of carbon chain length. α can be expressed by two parameters, the rate of propagation or rate of chain growth (r_p , allowing the growth of C_nH_{2n} by addition of a CH₂ monomer) and the rate of chain termination (r_t , termination reaction leading to the final product) which gives the following formula for a given chain length n:

$$\text{(Equation 11)} \quad \alpha_n = \frac{r_{p,n}}{r_{p,n} + r_{t,n}}$$

The mole fraction (M_n) of a hydrocarbon (C_n) which has a chain length of n carbon is expressed as followed:

$$\text{(Equation 12)} \quad M_n = (1 - \alpha)\alpha^{n-1}$$

The weight percent (W_n) of a C_n product containing n carbon is derived by this equation:

$$\text{(Equation 13)} \quad W_n = \frac{n \cdot m \cdot \alpha^{n-1} (1-\alpha)}{\sum_{n=1}^p n \cdot m \cdot \alpha^{n-1} (1-\alpha)} = \frac{n \cdot \alpha^{n-1} (1-\alpha)}{1 - \alpha + 2\alpha(1-\alpha) + \dots + p\alpha^{n-1}(1-\alpha)} = \frac{n\alpha^{n-1}(1-\alpha)}{1/(1-\alpha)}$$

$$W_n = n(1 - \alpha)^2\alpha^{n-1}$$

With m representing the monomer's mass considered, n is the unit number of monomer used (in the case of a -(CH₂)- monomer, n represent the carbon number in the chain). This equation is used to determine the experimental growth probability α . We finally obtain the following equation:

$$\text{(Equation 14)} \quad \log\left(\frac{W_n}{n}\right) = n * \log(\alpha) + \log\left(\frac{(1-\alpha)^2}{\alpha}\right)$$

The ASF plot of $\log\left(\frac{W_n}{n}\right) = f(n)$ is used to determine the slope equal to $\log(\alpha)$ at high n values by least square adjustment.

However the ideal ASF curve has never been observed. Generally several α are needed to describe the ASF distribution [5, 6]. In non-ideal cases, CH_4 proportion is much more important. **Figure 7** displays the predicted ASF distribution for the range of products. For high α values the product selectivity is shifted toward the high chain products whereas at low α values, the selectivity tends to produce smaller molecules [32].

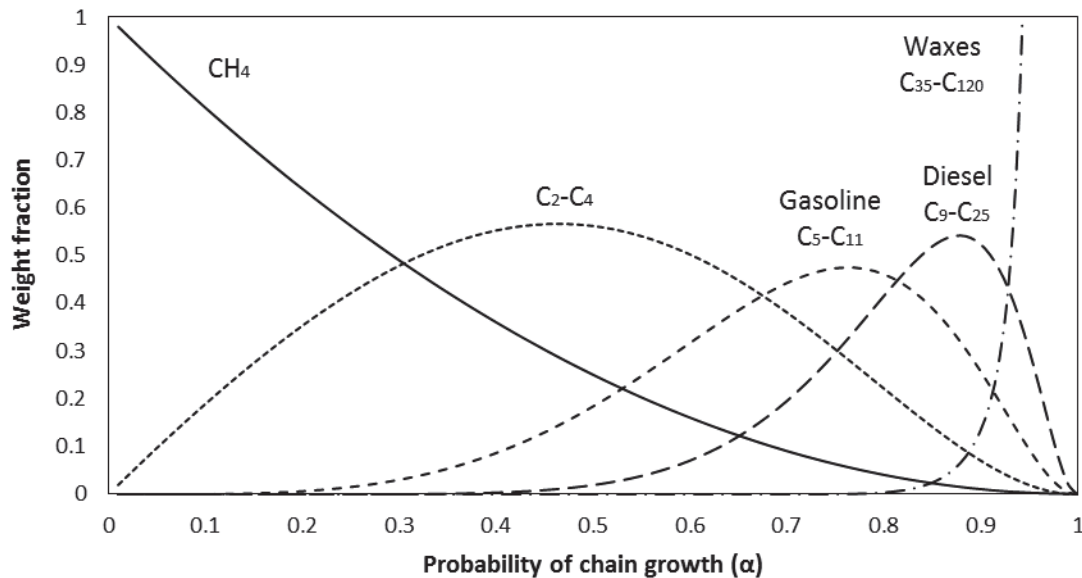


Figure 7 | Example of ASF curve to determine the chain growth probability factor α . Product distribution in FTS as a function of the chain growth probability α .

Besides, it is essential to realize that the chain growth probability can be affected by the catalyst and the process operating conditions (temperature, pressure, H_2/CO ratio...). Selectivity in methane, and other products also depends on these conditions.

To conclude, the Fischer-Tropsch synthesis is a multifaceted and difficult process to understand, many variables can modify and enhance the FTS selectivities and activities of the reaction. Depending on the desired products, conditions need to be carefully adapted.

II.2. Iron-based FTS catalysts

Although already applied at industrial scale about one century ago, the Fischer-Tropsch process is gaining renewed interests as it is a key step for converting alternative feedstocks, including biomass to transportable fuels. Ruthenium, nickel, cobalt and iron are all catalytically active in Fischer-Tropsch synthesis, though mainly cobalt and iron are used in the gas-to-liquid process (GtL) [10]. Nickel shows undesirably high methane selectivity, while ruthenium resources are scarce and expensive, and therefore both elements are not commonly used.

Owing to its high activity for Fischer-Tropsch synthesis, its good stability towards deactivation, its high selectivity to linear products, and its low water-gas-shift (WGS) activity, cobalt remained the preferred catalyst for Fischer-Tropsch synthesis [28, 33, 34]. However due to the higher price of Co compared to Fe, iron-based Fischer-Tropsch catalysts are increasingly reinvestigated [11]. In addition to its relatively cheap price and availability (4th most abundant element in the earth's crust), iron-based catalyst have additional advantages on cobalt: it is less impacted by operating conditions (pressure, temperature), it is less sensitive towards sintering, the product spectrum can be tuned to a wider range (alcohols, alkenes,...) and under high temperature the product spectrum is more directed to short-unsaturated hydrocarbons chain [35]. Also iron-based catalysts are known to be active toward the water-gas-shift reaction. This reaction consumes CO and water formed during FTS reaction to produce additional hydrogen and carbon dioxide (CO₂). This particular aspect of iron-based catalysts is important when syngas with a non-stoichiometric amounts of hydrogen is used. WGS helped to counter-balance the lack or excess of hydrogen in the feed. Therefore, WGS can become a major advantage for iron catalysts when used appropriately.

Nevertheless state of the art iron catalysts show lower activity (per volume), lower selectivity as they produce a significant and undesirable quantity of CO₂, and show a much faster deactivation [36]. A comparison of the main characteristics of the four metals discussed above are shown in **Table 3**.

Table 3 | Overview of the main characteristics of Ni-, Fe-, Co- and Ru-based FT catalysts [37]

| Active metal | Price | FT activity | WGS activity | Hydrogenation activity |
|------------------|----------|-------------|--------------|------------------------|
| Nickel (Ni) | ++++ | + | +/- | +++++ |
| Iron (Fe) | + | + | +++ | + |
| Cobalt (Co) | +++ | +++ | +/- | +++ |
| Ruthenium (Ru) | +++++ | +++++ | +/- | +++ |

II.2.1. Activity of Fe-based catalysts for FTS

a. FTS and WGS activity

Several parameters can influence the activity or FTS reaction rate, for instance, temperature, H₂/CO ratio and/or partial pressure. Temperature is likely the most important parameters in FTS. Using their predicting model, Botes et al. [28] show the temperature effect of cobalt and iron, at a constant CO and H₂ partial pressures, on the FTS reaction rate (**Figure 8**).

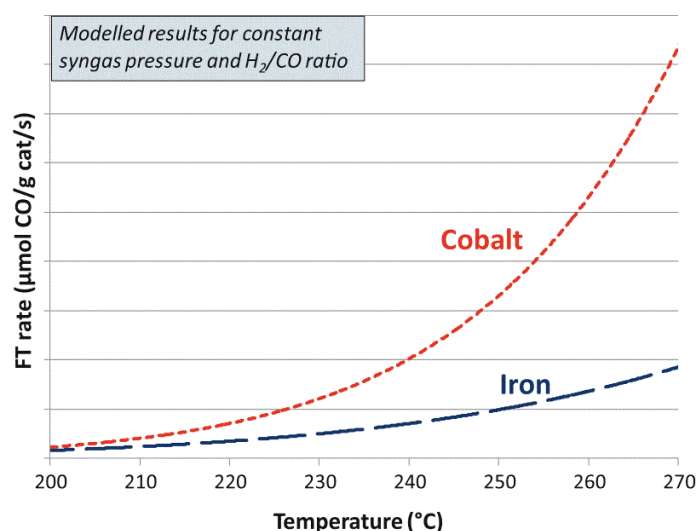
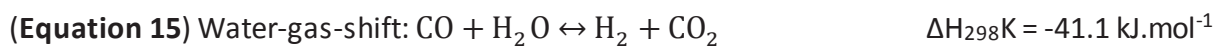


Figure 8 | Effect of temperature on FTS reaction rate of Co- and Fe-based catalyst [28].

Even though a cobalt-based catalyst shows a better activity/FT reaction rate than an iron-based catalyst for a given temperature, cobalt catalysts are more sensitive to FT operating conditions such as pressure and H₂/CO ratio, whereas iron-based catalysts are more tolerant to varying H₂/CO ratios and operating conditions.

Besides having lower FT activity than cobalt-based catalysts, iron-based catalysts are known to be very active towards the water-gas-shift reaction (WGS), a reaction that is very limited in the case of cobalt:



One of the main (by-)products of the FT synthesis is water. The amount of water present in the reactor during FT depends on various parameters such as conversion, reactor system and catalyst. For iron it has been shown that water and CO may oxidize iron during FT synthesis [11]. Furthermore it is well known that magnetite (Fe_3O_4) catalyzes the water-gas-shift reaction [30]. Therefore researchers consider that magnetite may be the phase responsible for the WGS activity of iron catalysts during FTS. However magnetite co-exists with other iron phases during FTS, thus it remains difficult to determine the exact impact of all phases on the activity and selectivity of the catalyst. Furthermore in literature, it is generally accepted that WGS and FTS reaction are taking place on different types of active sites and iron phases, oxides for WGS and carbides/metallic iron for FTS [38, 39, 40, 41, 42].

b. Iron phases influence on activity during the Fischer-Tropsch synthesis

Generally the main challenge in designing iron-based FTS catalyst lies in developing a more active and more stable iron Fischer-Tropsch synthesis catalysts. Typical Fe based catalysts have high metal loadings (>70 %wt.) and contain many different phases, strongly limiting the establishment of structure-activity relationships. During FTS, a complex mixture of iron phases is formed. Through the different reaction steps of the Fischer-Tropsch synthesis (activation, deactivation...), metallic iron, iron oxides (hematite $\alpha\text{-Fe}_2\text{O}_3$, maghemite $\gamma\text{-Fe}_2\text{O}_3$, magnetite Fe_3O_4 , wüstite FeO ...) and iron carbides (cementite Fe_3C , Hägg's-carbides $\chi\text{-Fe}_5\text{C}_2$) are believed to coexist [11, 43]. Even though in literature carbides iron species are believed to be the active phases for FTS, the exact role of each phases in the activation and deactivation of iron-based catalyst materials is still highly disputed and remained controversial [11]. In the following part each family of iron phases will be described and their known role in the FTS reaction explained.

Iron oxides are the most commonly found iron phases in nature. Small iron oxide crystallites, either present as hematite ($\alpha\text{-Fe}_2\text{O}_3$), goethite ($\alpha\text{-FeO(OH)}$) or magnetite (Fe_3O_4), may constitute the fresh FTS catalyst, however $\alpha\text{-Fe}_2\text{O}_3$ is generally the main constituent of the

fresh catalyst. There are sixteen iron oxides in total [43] which include also iron hydroxides and iron oxide hydroxides. All of them are reported in the following table (**Table 4**). The most commonly found iron oxides during Fischer-Tropsch synthesis are α -Fe₂O₃, γ -Fe₂O₃, Fe₃O₄, FeO and FeO(OH). α -Fe₂O₃ is generally the starting material for iron-based catalysts. In H₂ atmosphere the α -Fe₂O₃ is reduced in Fe₃O₄, FeO and metallic Fe [44, 45, 46]. The reduced Fe₃O₄ is transformed continually to FeO phase, or reduced directly to metallic iron, thus we generally have Fe₂O₃ -> Fe₃O₄ -> FeO -> Fe. Under CO or syngas atmosphere these reduced iron species could be converted into different types of iron carbides (such as χ -Fe₅C₂, ϵ -Fe_{2.2}C, and θ -Fe₃C). Chen et al. [47] indicated in their work that magnetite (Fe₃O₄) is first reduced into metallic Fe before being transformed into carbides Fe₃O₄ -> Fe -> Fe_xC_y whereas Li et al. [48] reported that Fe₃O₄ is directly transformed into iron carbides without intermediary iron phases. In syngas mixture atmosphere it is believed that a mixture of oxides, carbides and metallic iron coexist [49].

Table 4 | Iron oxides and hydroxides [11]

| Oxides | Hydroxides | Oxide hydroxides |
|--|---|---|
| Magnetite Fe ₃ O ₄ | Fe(OH) ₂ | Goethite α -FeO(OH) |
| Wüstite FeO | Ferrihydrite Fe ₅ HO ₈ .4H ₂ O | Lepidocrocite γ -FeO(OH) |
| Hematite α -Fe ₂ O ₃ | Bernalite Fe(OH) ₃ | Akageneite β -FeO(OH) |
| Maghemite γ -Fe ₂ O ₃ | | Feroxyhyte δ -FeO(OH) |
| β -Fe ₂ O ₃ | | δ' -FeO(OH) |
| ϵ -Fe ₂ O ₃ (Fe(III)) | | Schwertmannite Fe ₁₆ O ₁₆ (OH) _y (SO ₄) _z .nH ₂ O High pressure FeO(OH) |

As explain earlier, iron oxides and especially magnetite (Fe₃O₄) are known to be particularly WGS active. The other iron phases roles in the FTS reaction are still either not understood or unclear.

Metallic iron can never be found in nature, as it is not stable in air. There are two forms of metallic iron, the first one can be found at low or moderate temperature (< 900 °C) and is called ferrite or α -Fe, the second one, austenite, or γ -Fe is only formed and stable at high temperature (> 900 °C). They have a body centered cubic (bcc) and face centered cubic (fcc) crystal structure, respectively. During FTS reaction, α -Fe is generally the only seen metallic

iron species as FTS is generally done at a temperature range lower than the temperature of formation of austenite. α -Fe is generally formed during the reduction of the fresh catalyst (mainly α -Fe₂O₃) in reductive atmosphere. Metallic iron just like metallic cobalt is known for its ability to adsorb on its active surface sites and dissociate CO. This is generally leading to its transformation into various kind of carbides phases by incorporation of the carbon into the crystal interstices. Yet the exact role of metallic iron in FTS is still highly disputed [16, 19].

Iron carbides: Carbides are generally formed during FTS by incorporation of carbon in the metallic iron crystal interstice. Iron carbides can assume many structures classified according to the sites occupied by the carbon atoms meaning structures with carbon atoms in trigonal prismatic interstices and structures with carbon atoms in octahedral interstices. Cementite (θ -Fe₃C), Hägg carbide (χ -Fe₅C₂) and Eckstrom-Adcock (Fe₇C₃) carbides are the most known one [36, 46, 50, 51]. However during FTS many additional carbides were observed such as ϵ -Fe₂C, ϵ' -Fe_{2.2}C... [52, 53, 54, 55]. Most of them are reported in the following table (**Table 5**).

Table 5 | Iron carbides and their crystal structures [11]

| Carbides | Atomic ratio (C:Fe) | Crystal lattice | Interstitial occupation of carbon atom |
|--|---------------------|-------------------|--|
| Cementite θ -Fe ₃ C | 0.33 | Orthorhombic | Trigonal prismatic |
| Hägg carbide χ -Fe ₅ C ₂ | 0.40 | Monoclinic | Trigonal prismatic |
| Eckstrom-Adcock carbide Fe ₇ C ₃ | 0.43 | Orthorhombic | Trigonal prismatic |
| Hexagonal carbide ϵ -Fe ₂ C | 0.50 | hcp to monoclinic | Octahedral |
| Hexagonal carbide ϵ' -Fe _{2.2} C | 0.45 | hcp | Octahedral |

Carbides are formed during activation treatment or directly under FTS reaction conditions. In Fischer-Tropsch the precise role of each iron carbide phases and the hydrocarbons production in the catalytic reaction remain largely unclear. Even though authors claim that iron carbides are absolutely necessary for a FTS catalyst to be active, it is still disputed by others.

c. Particle size influence on activity

The effect of crystallite size on the Fischer-Tropsch synthesis has been investigated so far mostly on the Cobalt catalyst [56, 57, 58]. Fe did not receive as much attraction as Co. In the case of cobalt recent studies have shown a decreasing activity when the particle size decreases below 6 nm [56, 57, 58]. Also the turnover frequency (TOF) evolution can be seen for Co particle sizes below 6 - 10 nm and then remain constant for bigger sizes.

In the case of Fe-based catalyst, a size dependency of the activity has been found, but less research on the subject has been carried out and published. Amongst the few, Mabaso et al. have shown in their work that small iron particles (< 7 - 9 nm) supported on carbon nanotubes were less active and had a higher methane selectivity compared to bigger crystallites sized catalysts [59]. Also recent studies by Park et al. showed an optimum Fe particle size of 6.1 nm in the case of Fe supported on Al₂O₃ catalysts (**Figure 9**) [60].

It has been shown that catalysts containing very small iron crystallites are not as active for the Fischer-Tropsch synthesis as catalysts containing larger crystallites [59, 60]. Nevertheless, it is not clear yet whether this is caused by a decrease in the intrinsic activity due to the diminution in size of iron crystallites or whether the size dependency comes from the size-dependent phase transformation (iron phases are more or less reducible and sensible to FTS conditions depending on the particle size, therefore modifying the activity of the catalyst).

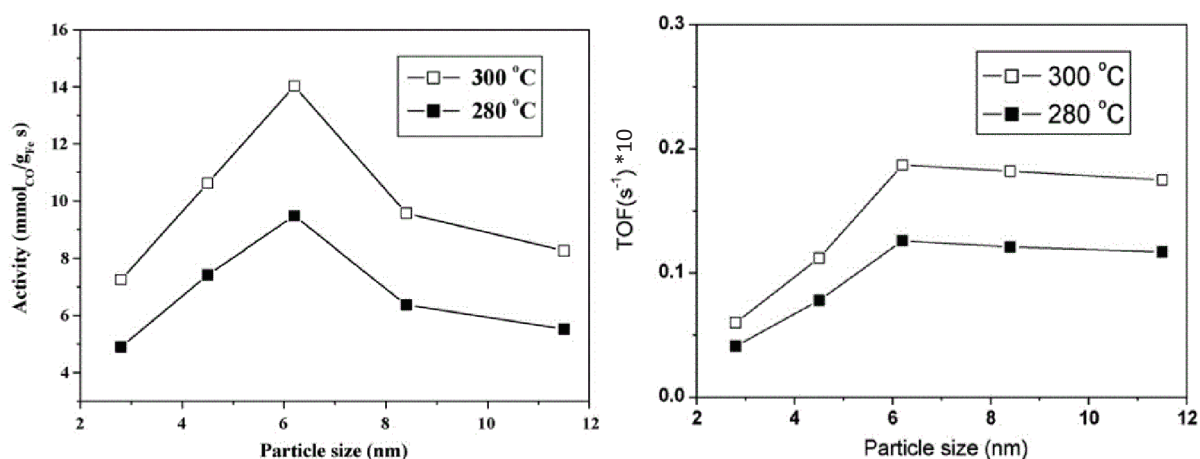


Figure 9 | The influence of iron particle size on activity (left) and the influence of iron particle size on the TOF (right) (280 °C and 300 °C, Space velocity = 3600 L.kg_{cat}⁻¹.h⁻¹, H₂:CO:Ar = 63.2:31.3:5.5, 10 bar) [60].

II.2.2. Selectivity of Fe-based catalysts for FTS

a. Product selectivity of Fe-based catalyst during FTS

The following table reports some Fe-based catalysts that can be found in literature (**Table 6**).

Table 6 | Selectivity of Fe-based catalyst

| Catalysts | Conditions of operation | | | Conversion | Selectivity | | Reference |
|--|-------------------------|----------------|--------------------|------------|---------------------|---------------------|-----------|
| | Temperature (°C) | Pressure (bar) | H ₂ /CO | CO (%) | CO ₂ (%) | C ₅₊ (%) | |
| Commercial cat.* | 230 | 20 | 2 | 29 | 14 | 77 | This work |
| Commercial cat.* | 250 | 20 | 2 | 44 | 19 | 72 | This work |
| FeCuK/ZSM-5 | 300 | 10 | 2 | 81 | 36 | 34 | [61] |
| FeCuK/SiO ₂ | 300 | 10 | 2 | 37 | 16 | 59 | [62] |
| FeCuK/γ-Al ₂ O ₃ | 300 | 10 | 2 | 96 | 38 | 48 | [63] |
| Fe/α-Al ₂ O ₃ | 300 | 20 | 1 | 49 | 39 | 37 | [63] |
| BFe (bulk-Fe) | 265 | 19 | 2 | 32 | 17 | 47 | [64] |
| SFeZ4 | 265 | 19 | 2 | 23 | 7 | 47 | [64] |
| Fe/SBA-15 | 300 | 10 | 1 | 68 | 37 | 51 | [65] |
| 25-Fe@C | 270 | 13 | 1 | 72 | 45 | - | [66] |
| 38-Fe@C | 340 | 30 | 1 | 77 | 46 | - | [66] |

*78.4%Fe₂O₃, 3.4%CuO, 2.6%K₂O, 0.04%Na₂O, 15%SiO₂

Even though the literature FT tests were conducted under a variety of operating conditions (feed composition, temperature and pressure) and over different catalytic systems, CO₂ generally represents a large fraction of the total selectivity of a Fe catalyst.

b. Promoters influence (K, Cu, Mn)

To improve the selectivity of iron-based catalysts, chemical promoters such as K, Cu, Mn, Zn, Cr... have been integrated into iron-based catalyst [43–52]. K and Cu are the most commonly used chemical promoters for iron-based FTS catalysts. Extensive studies have been conducted to discover the exact role of these promoters in the FTS reaction [43–46, 49, 51–53].

It is acknowledged that Cu can facilitate reduction of Fe oxides at low temperature and promote the formation of the active phase [43, 52, 54, 55]. While the role of Cu in facilitating catalyst reduction has been widely accepted, its influence on the FTS product distribution has not been well addressed. Some found that Cu has no effect on selectivity whereas others found that selectivity was improved or suppressed.

Several promoters like alkali metal promoters (Li, Na, K) were reported to influence the catalytic performances of iron-based FTS catalyst. K, the most widely studied promoter, is known to decrease or suppress the methane formation, to improve the olefin selectivity and shift selectivity to higher hydrocarbons chains. It also improves the dissociative adsorption of CO, strengthens the Fe-C bonds, and facilitates carbon deposition and catalyst deactivation [43, 45, 46, 49, 51, 56].

c. Particle size influence on selectivity

The different studies on effect of crystallite size on the Fischer-Tropsch synthesis revealed that the catalyst activity (**c. Particle size influence on activity**) was dependent of size. The same observations were made for the selectivity. In the case of iron-based catalysts, limited studies have been carried out on the subject, still Park et al. [60] reported the same kind of observation on a Fe/Al₂O₃ catalyst. Indeed they showed that CH₄ and C₂-C₄ selectivity decreases with increasing particle size from 2 to 12 nm, therefore a C₅+ selectivity increase with increasing particle size.

II.2.3. Deactivation of iron based catalysts

The principal challenge for iron-based catalysts in FTS reaction is to overcome their notorious high deactivation rates. Compared to cobalt-based catalysts, iron-based catalysts are known to deactivate rather quickly [11]. From an industrial or commercial point of view, the cost for replacement and/or regeneration of a catalyst is relatively high and is not something wanted. Generally catalysts are losing their activity with time on stream. There exist many ways for a catalyst to deactivate, however the use of promoters or some supports can delay or lessen the deactivation rate [11, 36, 76]. Eliason and Bartholomew reported their studies on unpromoted and promoted Fe catalyst [36]. **Figure 10** shows that the temperature do have an effect on the deactivation rate of the Fe catalyst, indeed it is clear when studying these graphs that an increase in temperature drastically increases the deactivation rate of the catalyst. For example, at 250 °C, the activity of the unpromoted Fe catalyst decreases by 30 % in 24 h, meanwhile at 280 °C, it decreases by 90% over the same period of time on stream. Also when comparing the promoted and unpromoted Fe catalysts, it is clearly visible that the promoted one deactivates slower than the unpromoted one.

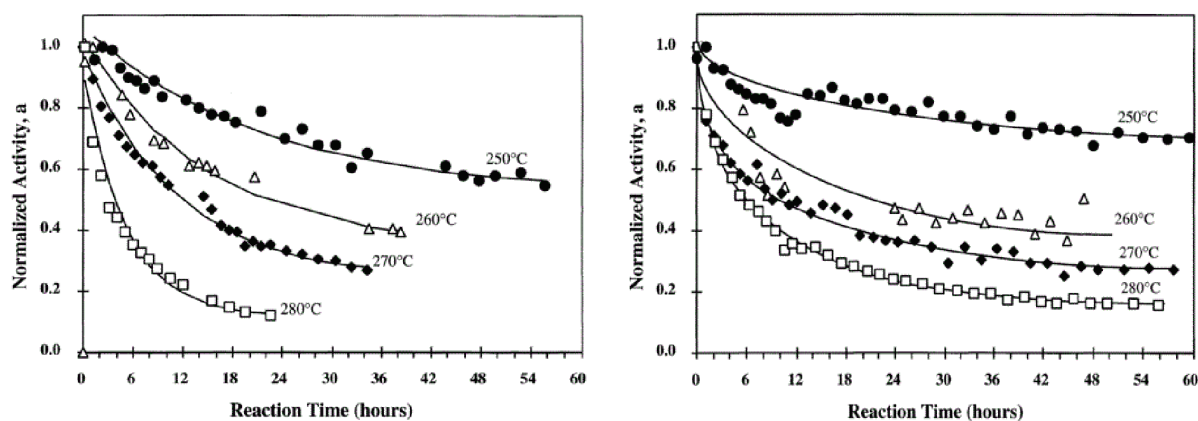


Figure 10 | Normalized activity of unpromoted Fe (left) and promoted Fe (right) at $P_{H_2}^0 = 1.2$ atm, $P_{CO}^0 = 0.8$ atm, 10 atm total pressure and reaction temperatures of 250 - 280°C [36].

Origins of the catalyst deactivation are numerous, scientists generally agreed on four main deactivation routes: phase transformation, sintering, deposition of carbonaceous compounds, and poisoning [11]. Those four possible causes are explained below.

a. Iron phases transformations

The first route for catalyst deactivation is believed to be the active phases (certain carbides and α -Fe, **(b. Iron phases influence on activity during the Fischer-Tropsch synthesis)** transformations into less active or inert phases (oxides and different carbides phases). In literature, it is acknowledged that the active phase progressively oxidized to less FTS active phases such as magnetite (Fe_3O_4) believed to be FTS inactive and more WGS active. Also some are considering that the deactivation may come from the transformation of carbides phases into other carbides less FTS active [36, 77, 78, 79, 80, 81, 82] **(Figure 11)**.

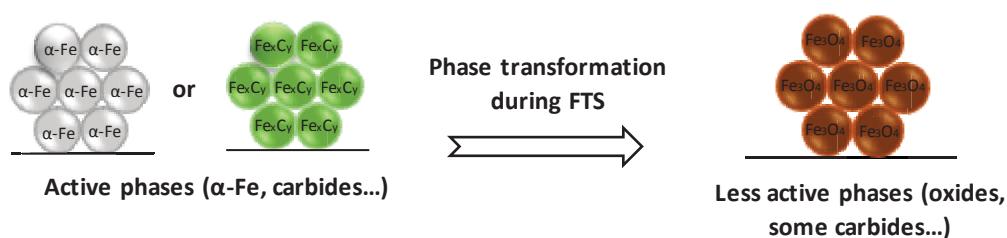
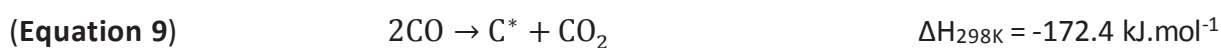


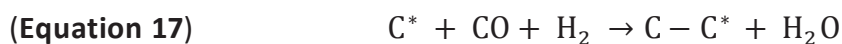
Figure 11 | Schematic illustration of the deactivation by phase transformation during FTS reaction.

As already indicated water is the main (by-)product of the FTS reaction and also one of the main reason of the phases deactivation by transformation into less active phases [80, 81]. Indeed, water strongly oxidizes metallic iron into iron oxides. Iron carbides however is known to be more resistant to oxidation by water [11].

b. Deposition of carbonaceous compounds

The second route for catalyst deactivation is believed to be the deposition of carbonaceous compounds [11], either by formation of polymeric or graphitic carbon or by carbidic carbon. The active surface sites of the FTS catalyst can be blocked or fouled by carbon poisoning. Under typical FTS conditions, hydrocarbons, waxes and insoluble carbonaceous compounds are formed, those carbon species lower the catalyst activity, partially block the catalyst pores, and thus limit the access to the active sites **(Figure 12)**. Carbonaceous compounds deposition permanently block the access to active sites leading to a decrease of activity and an increase of CH_4 production. The carbon deposition onto the catalyst active site can be described by the following reaction:





When temperature increases the rate of carbon deposition increases, meaning that carbon deposition is temperature sensitive. At high temperature, graphitic carbon formation is favored, leading to coke deposition. The catalyst pretreatment conditions plays an important role. Indeed, pre-reduced catalysts tend to be more prone to carbon deposition compared to fully carburized catalysts. Also it is known that carbides are progressively converted into carbon deposits [81, 83, 84].

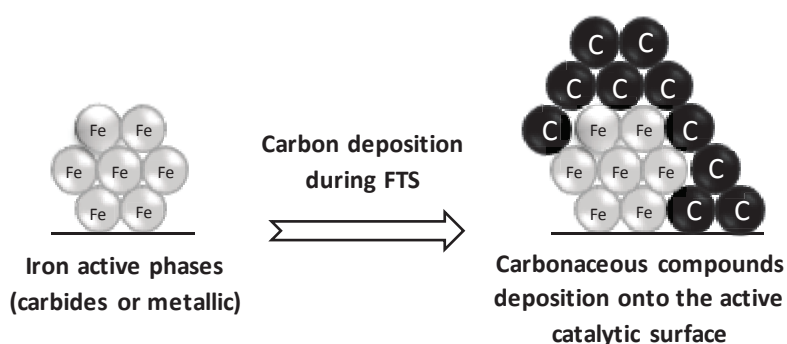


Figure 12 | Schematic illustration of the deactivation by carbon deposition onto the active catalytic surface.

c. Sintering and loss of catalytic surface area

The third cause for catalyst deactivation is believed to be sintering or thermal deactivation. Iron catalysts can deactivate by loss of active surface due to sintering of the active phase. To be more exact, the small crystallites composing the active phase tend to grow into larger crystallites (**Figure 13**) [11, 85, 86].

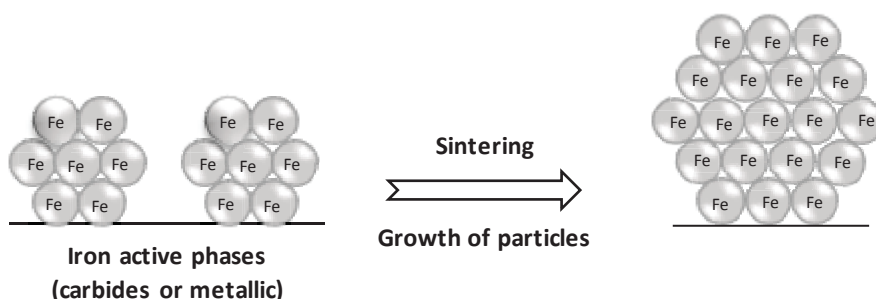


Figure 13 | Schematic illustration of the deactivation by particles sintering.

Duvenhage et al. [86] reported that high partial pressure of water in the catalyst bed reactor could be one of the cause of particles sintering and, therefore catalyst deactivation. Two mechanisms for sintering were proposed by scientists, namely the particle migration and coalescence (PMC) and the Ostwald ripening (OR) (**Figure 14**). PMC implicates particles mobility and diffusion in a Brownian-like motion on the catalyst surface, following by coalescence, which leads to the particles growth when they come in close proximity with each other. Ostwald ripening implicates migration and transport of ad-atoms and/or molecular species with larger particles growing at the expense of smaller particles due to surface free energy differences (large particles possess a lower free energy than small particles).

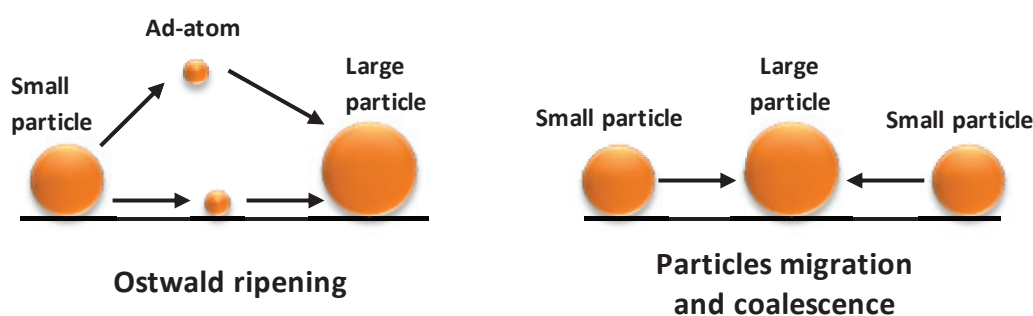


Figure 14 | Schematic illustration of Ostwald ripening and particles migration followed by coalescence.

According to literature, Datye et al. [87] and other work [88, 89], suggested that, in the case of a well particles dispersed material, the Ostwald ripening seems to occur first when mostly very small particles are present. Larger particles are therefore formed, and thus are more effectively mobile and migrate on the surface to sinter together.

d. Poisoning

The last possible route for catalyst deactivation is by poisoning [11, 90, 91]. Chemical poisoning consists of strong chemisorption of reactants, products or impurities on the catalyst available active sites (**Figure 15**). A species is considered as a poison if it competes for catalytic active sites with other species, subsequently having a stronger adsorption, preventing reactant species to adsorb on the sites and carrying out the reaction. Most well-known poisons species are oxygen, chlorine, bromine and sulfur. Sulfur species especially is known for its capacity, at

high concentration, to lower the catalyst activity during FTS, and, at low concentration, to enhance the olefin selectivity and catalyst reducibility [66, 67, 71, 91]. Poison species are generally part of the feedstock at the beginning of the entire process, several steps of cleaning and treatments of the syngas is done before the FTS reactor, however a few ppm of those species can still be leftover, leading nevertheless to the catalyst deactivation.

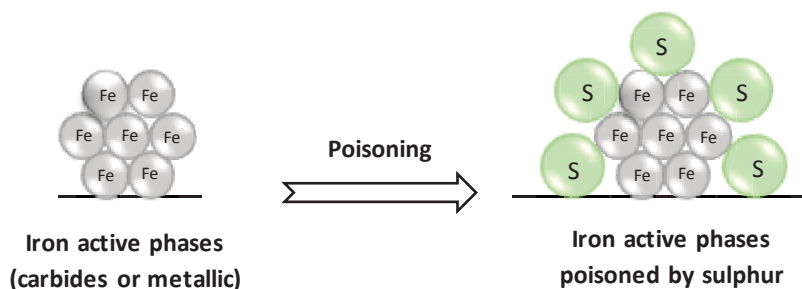


Figure 15 | Schematic illustration of the deactivation by poisoning.

II.2.4. Conclusion

Iron has unlike features, compared to cobalt or ruthenium, which can impact activity, selectivity and deactivation of the catalyst. FTS and WGS activities are controlled by the different iron phases that constitute the catalyst, however the exact role of each of these phases remain uncertain. Even though authors are still disputing the possible roles of the various phases, one's can agree that some phases tend to be more active for FTS (like metallic Fe or carbides) and for WGS (like oxides, Fe_3O_4). Furthermore, activity of iron-based FTS catalysts is dependent upon many different factors like FT operating condition parameters (temperature, pressure, gas partial pressure...) and particles size. The complexity of the FTS reaction combined with the complex behavior of iron phases make the study and development of iron catalysts for FTS really challenging to fully apprehend.

Furthermore the parallel reaction called the water-gas-shift reaction is happening at the same time as FTS, changing the gases partial pressure (CO , H_2 , CO_2 , H_2O) in the reactor leading to a modification of the selectivity (high CO_2 selectivity). Selectivity of iron-based FTS catalysts is dependent upon various factors such as FT operating condition parameters (temperature, pressure, gas partial pressure...), promoters inferences and particles size. Nevertheless, water-gas-shift reaction is intrinsic to iron-based catalyst.

Finally, iron-based FTS catalysts are well-known for their quick and high deactivation rates, compared to other metallic catalysts such as cobalt or ruthenium based ones. Although scientists tend to agree that there exist four main deactivation pathways responsible for the catalyst deactivation, i.e. phases transformations, sintering, carbon deposition and poisoning, the lack of knowledge and understanding in the field make the study of iron catalysts quite challenging.

II.3. Effect of CO₂-containing syngas mixture over Fe-based catalysts in FTS

Synthesis gas or syngas derived from coal, natural gas or biomass is generally a mixture of H₂, CO, CH₄ and CO₂. Most of the time, CO₂ is a significant component in the syngas mixture, therefore it requires expensive purification steps which increases the cost of the overall XtL process. However, due to depletion of crude oil resources, there is a need to improve the carbon utilization efficiency. Therefore, using CO₂, instead of removing it, as reactant for the FTS (by adding it to the feed or by replacing directly CO) is attracting attention. Recent studies have discussed the potential advantage if CO₂ is not removed before the FTS synthesis takes place. The idea being the hydrogenation of CO₂ along with CO in the Fischer-Tropsch reactor [92].

In the case of cobalt-based catalyst for the Fischer-tropsch reaction, CO₂ is believed by many researchers to act as an inert diluent [91–96] at low temperature. Riedel et al. [97] noted that increasing the CO₂ content (while decreasing the CO, to maintain the total pressure and inlet flow rate), shifted the usual FT product distribution toward the exclusive production of methane. They concluded that CO₂ acted as a diluent for the FT reaction while it is a reactant for the methanation reaction. In the same order of idea, Zhang et al. [96] concluded from the product distributions that the CO₂ and CO hydrogenation appears to follow different reaction pathways. More recently, Yao et al. [92] said that CO₂ and CO mixtures can be used as feed for cobalt catalyst. They claimed that CO₂ is not an inert gas but can possibly be converted into hydrocarbons products using a syngas with high CO₂ content. However the exact role of CO₂ on the cobalt-based catalysts FTS reaction remains controversial. Furthermore, the reason of the different reactivity of CO and CO₂ on cobalt-based catalyst is still debated [91,92].

Not only iron catalysts are known to be low cost catalysts, but they also demonstrate high activity for both FT and water-gas shift (WGS) reactions, which make them good candidates

for syngas with low H₂/CO ratios. Compared to cobalt-based catalysts, iron-based catalysts are good candidates for CO₂ co-feeding or hydrogenation. This is principally due to either the intrinsic WGS (R-WGS) reaction of iron-based catalyst [94, 96, 99, 100] or the direct hydrogenation of CO₂ to hydrocarbons [101]. The formation of CO₂ by the water-gas shift (WGS) reaction limits carbon utilization efficiency. Therefore, there is a need to control the WGS and to understand the impact of CO₂ onto the FTS reaction. Iglesia et al. [99] explained that as the WGS reaction is a reversible reaction, the CO₂ formed during this reaction can be minimized by increasing the rate of the R-WGS reaction, with the possible addition of CO₂. The presence of CO₂ inhibits the neat rate of WGS during FTS on iron-based catalysts. He explains that CO₂ addition in the feed results in the reduction of CO₂ formation during FTS and that oxygen is preferentially removed as H₂O via the WGS reaction. Furthermore, the reduction of CO₂ formation lowers the H₂/CO ratio in the reactor which in return gives a higher C₅₊ and olefins selectivity in the products. Therefore, Iglesia et al. [99] claim that recycling CO₂ formed during FTS can be used to improve carbon efficiency. Others research by Xu et al. [102] and Yao et al. [92] established that CO₂ is hydrogenated only at low CO partial pressure due to a relevant contribution of the R-WGS under these conditions. However, when CO₂ is converted, the selectivity to methane suddenly rises up with a diminution of the C₂₊ hydrocarbons selectivity [92]. Other researchers have found that a comparison of the product selectivity between CO and CO₂ hydrogenation on iron-based catalysts shows that CO₂ hydrogenation has a higher selectivity for light hydrocarbon products with a low alpha distribution. Most of the literature on the subject report that CO₂ can be effectively hydrogenated at low CO partial pressure [94, 96, 99, 98]. Others claim different effects of the presence of CO₂ on CO conversion and product distribution. Chun et al. [103] observe an inhibition of the hydrocarbon yield by the CO₂, also they report that the product distribution and the olefin to paraffin ratio is not affected by CO₂ presence in the feed. Fletcher J. [104] carried out isotopic experiments, switching between a mixture of H₂/CO/¹²CO₂ and a mixture of H₂/CO/¹³CO₂ once steady state is achieved. His objective was to determine if CO₂ can be directly hydrogenated to hydrocarbons or if CO₂ first reacts to CO in the gas phase before adsorbing on FT catalytic sites for hydrocarbons formation. In the end, no direct CO₂ hydrogenation was found, therefore he proposed that the CO₂ is first transformed into CO before it can be incorporated into CH₄ and any other hydrocarbons products of the FT synthesis. Further works need to be done on the exact role of the CO₂ during FTS on iron-based catalysts.

III. Fe-zeolite core-shell system for Fischer-Tropsch synthesis

The concept of coating FTS catalyst particles with zeolites to tune the product selectivity [65, 105, 106, 107, 108, 109] was first introduced by Tsubaki and co-workers [105]. A catalyst in the form of a capsule catalyst was prepared by coating an acidic H-ZSM5 zeolite on a pre-shaped Co/SiO₂ catalyst pellet (**Figure 16**). The cobalt catalyst was tested under Fischer-Tropsch conditions. The catalyst exhibits excellent selectivity for light chains hydrocarbons, especially for isoparaffins, while suppressing totally the long chained hydrocarbons. Tsubaki et al. use H-ZSM-5 as a coating membrane due to its molecular diffusion rate in the pores, its shape selectivity, as well as for its acidic properties. In more details, the syngas (H₂ and CO) diffused inside the micropores system and reacts onto the Co/SiO₂ pellet. Hydrocarbons are formed and diffused back into the H-ZSM-5 membrane, where they are cracked and isomerized by the acidic sites inside the zeolite. The low diffusion rate of long chain hydrocarbons in the zeolite membrane makes them stay in the membrane layer longer, having a higher possibility of isomerization and cracking reaction inside the zeolite.

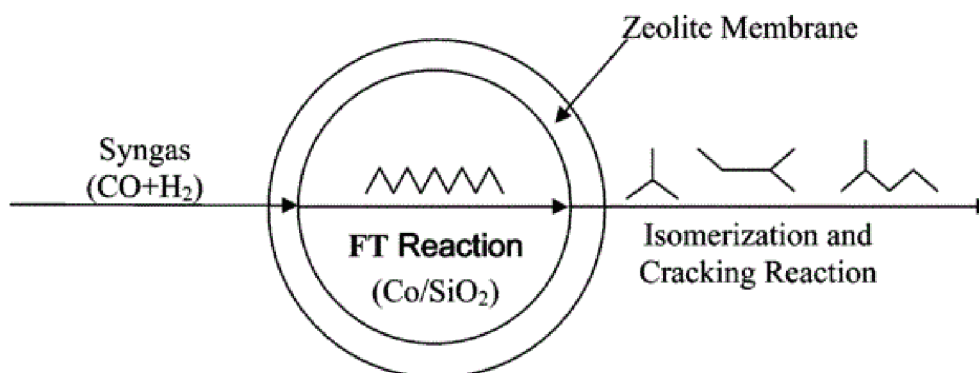


Figure 16 | Catalytic process over bifunctional core-shell catalyst (H-ZSM-5 coated on Co/SiO₂ particles) during FTS [taken from ¹⁰⁵].

Kapteijn et al. [107] designed a catalyst combining the acid functionality of H-ZSM-5 and the FTS active properties of a Co/SiO₂ material. The MFI was used as a coating layer over Co agglomerates. Silica from Co/SiO₂ particles (300 - 500 μm) was transformed into zeolite via hydrothermal synthesis, resulting in the enwrapping or encapsulation of Co agglomerates. The FTS on H-ZSM-5 coated Co/SiO₂ revealed that the membrane coating results in a mass transport resistances, as well as a lower productivity and CO conversion compared to Co supported on H-ZSM-5.

Recently, Tsubaki et al. designed an **iron-based** micro-capsule catalyst with Fe/silica as the core and acidic H-ZSM-5 as the shell [65]. This iron-based catalyst was designed for the Fischer-Tropsch synthesis, more especially for isoparaffins synthesis. The micro-capsule catalyst is synthesized via in-situ crystallization route of Fe/SBA-15 by using steam-assisted crystallization (SAC) process. The overall synthesis process used here is presented on **Figure 17**.

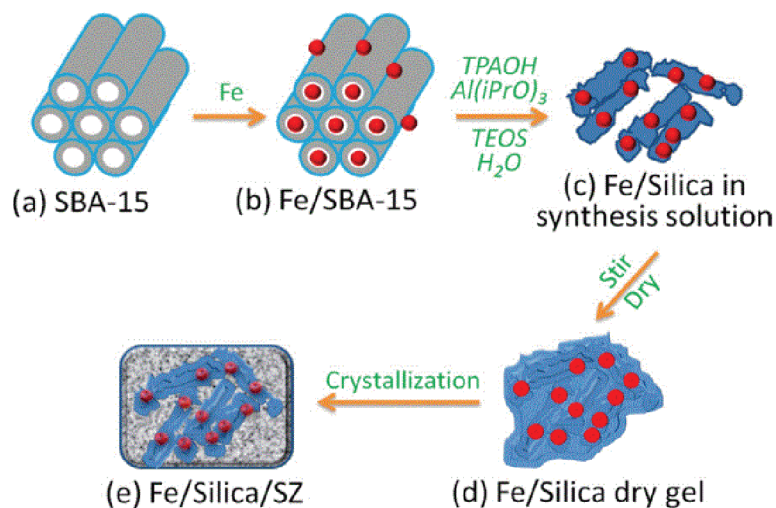


Figure 17 | Synthesis schematic route of iron-based micro-capsuled catalyst established by Tsubaki et al. (taken from [65]).

Characterization of the iron-based micro-capsuled catalyst shows a size of micro-capsule of about 1 - 2 μm (**Figure 18**). The iron catalyst should in principle operate in the same way as the coated Co/SiO₂ presented before. The mesoporous pores and channels of the micro-capsuled iron-based catalyst core offer a high diffusion rate of reactants and products, while the H-ZSM-5 micropores shell with acidic sites affords to hydrocrack and isomerize long chain hydrocarbons. The spatial confinement effect of the H-ZSM-5 zeolite shell acted as an important factor in the improvement of isoparaffin selectivity.

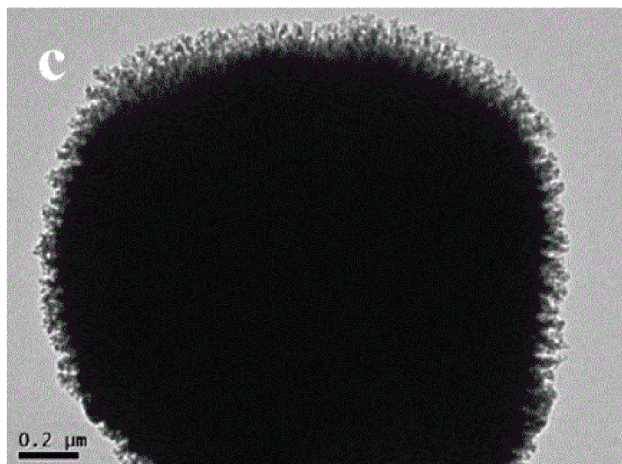


Figure 18 | TEM images of the micro-capsuled iron-based catalyst (taken from [65]).

No precise information is given on the particle size distribution and morphology of the micro-capsuled iron-based catalyst. In addition, no iron phase characterization was carried out in this work.

In this study, we aim at developing an iron-based catalyst with high dispersion and good control on the particles size. The size of our Fe particles encapsulated in zeolite is estimated at 3.5 nm in average, whereas for Tsubaki et al. no such information can be obtained. Also, the size of the zeolite system in our study is of 200 to 100 nm while Tsubaki designed a system 10 times larger (1 - 2 μm). Furthermore, the use of non-acidic silicalite-1 zeolite, instead of H-ZSM-5, will prevent cracking and other interferences from the zeolite onto the reaction process, making the Fischer-Tropsch performances easier to link with the iron particle phase. Consequently, the novel designed iron-based catalyst developed in our study differs from the ones that can be found in the literature, especially by the dimension of the system.

Chapter 2 - Experimental procedure

| | |
|---|-----------|
| Chapter 2 - Experimental procedure..... | 39 |
| I. Catalyst preparation | 40 |
| I.1. Silicalite-1 synthesis..... | 40 |
| I.2. Impregnation of silicalite-1 by incipient wetness | 41 |
| I.3. Preparation of Fe@hollow-silicalite-1..... | 41 |
| I.4. Reduction procedure of Fe@hollow-silicalite-1 | 42 |
| II. Characterization techniques for catalyst analysis | 43 |
| II.1. Powder X-ray Diffraction (XRD)..... | 43 |
| II.2. Elementary Analysis (ICP-OES) | 44 |
| II.3. N ₂ adsorption/desorption | 45 |
| II.4. Transmission Electronic Microscopy (TEM) | 45 |
| II.4.1. Sample preparation | 45 |
| II.4.2. Transmission Electronic Microscopy apparatus..... | 45 |
| II.4.3. Energy Dispersive X-ray spectroscopy..... | 47 |
| II.4.4. Study of nano-particles with TEM | 47 |
| II.5. Environmental Transmission Electronic Microscopy (E-TEM) | 48 |
| II.6. Mössbauer spectroscopy..... | 49 |
| II.6.1. Ex-situ Mössbauer | 49 |
| II.6.2. In-situ Mössbauer..... | 52 |
| II.7. Magnetic measurements | 53 |
| II.7.1. Theory of magnetism..... | 53 |
| II.7.2. Experimental setup | 58 |
| II.8. Synchrotron: In-situ X-ray powder diffraction (XRDP) and X-ray absorption spectroscopy (XAS)..... | 59 |
| II.8.1. Experimental setup | 59 |
| II.8.2. Methodology of measurements | 61 |
| III. Catalytic reactions and data processing | 62 |
| III.1. Fischer-Tropsch synthesis – setup and processing..... | 62 |
| III.1.1. Experimental setup | 62 |
| III.1.2. Analytical setup | 63 |
| III.1.3. Catalytic data treatment and calculation..... | 66 |
| III.2. Water-gas-shift testing setup | 69 |
| III.3. Labelled ¹³ C O ₂ MS and GC-MS experimental setup | 70 |

I. Catalyst preparation

The synthesis of iron nanoparticles encapsulated in silicalite-1 catalyst is a multi-step process (**Figure 19**). This synthesis has been adapted from a previous study by Tuel, A. et al. [¹¹⁰, ¹¹¹] on noble metal. This catalyst will be denoted all along this work as Fe@hollows-silicalite-1, with @ meaning “encapsulated in”, while the use of / in the name of a catalyst means “supported on”. Briefly, the silicalite-1 is impregnated with an iron aqueous solution, then a dissolution-recrystallization treatment with TPAOH is carried out, finally a calcination followed by a reduction is done.

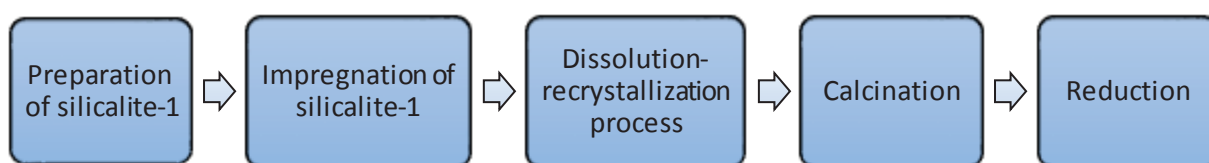


Figure 19 | Multi-step process diagram for the iron nanoparticles encapsulated in silicalite-1 catalyst synthesis.

The following parts described more accurately the different required steps for the synthesis of the iron nanoparticles encapsulated in silicalite-1 catalyst.

I.1. Silicalite-1 synthesis

Silicalite-1 nanocrystals are prepared from the crystallization of a clear gel containing 1M tetrapropylammonium hydroxide solution (TPAOH), tetraethyl orthosilicate (TEOS) and water. In a typical preparation 140 mL of TEOS (0.62 mol) are dispersed in 250 mL of TPAOH (alkali-free, 1 M solution) under stirring. After a few minutes for homogenization, 200 ml of distilled water is added to the mixture, then the mixture is heated to 80 °C for 3 h and vigorously stirred to remove the alcohol formed by hydrolysis of TEOS. The resulting gel with the following composition in mole, 1 SiO₂ : 0.4 TPAOH : 35 H₂O, is transferred into a Teflon-lined stainless steel autoclave and heated in an oven at 170 °C under static conditions for 3 d. The autoclave is then cooled down to room temperature and the solid is recovered by centrifugation, washed several times with distilled water until reaching a neutral pH. Finally the solid is dried

at 90 °C overnight. The dried-solid is crushed and calcined at 550 °C in air for 6 h to remove the organic template. Silicalite-1 nano-crystals with a uniform size of ca. 100 to 250 nm are obtained (**Figure 20**). Generally 30 g of Silicalite-1 are synthesized in one synthesis.

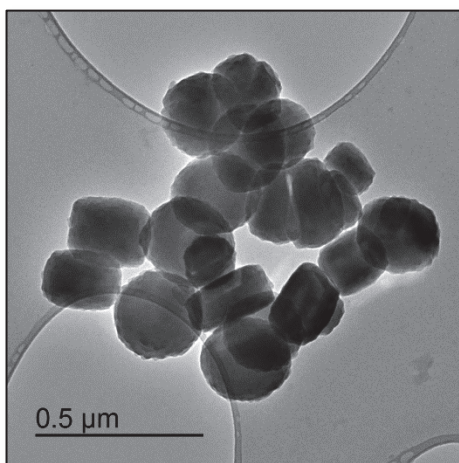


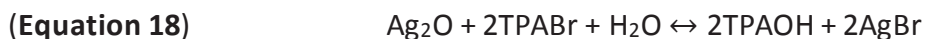
Figure 20 | TEM pictures of silicalite-1 nano-crystals.

I.2. Impregnation of silicalite-1 by incipient wetness

Fe/silicalite-1 samples are prepared by following the incipient-wetness impregnation method. The pre-degassed silicalite-1 is impregnated with an aqueous solution of the metal salt iron (II) sulfate heptahydrate ($\text{Fe(II)SO}_4 \cdot 7\text{H}_2\text{O}$, Fluka 99.5%). Additives like Cu and K ($\text{Cu(NO}_3)_2 \cdot 3\text{H}_2\text{O}$, KNO_3) can also be added to the impregnation solution. In a typical wet impregnation, 1 g of silicalite-1 is impregnated with 1 ml of iron precursor aqueous solution. The mixture is stirred at 50 °C until evaporation of water is completed. The obtained solid is dried at 90 °C overnight. The exact concentration of the impregnated solution is indicated in the synthesis description in **Chapter 3**.

I.3. Preparation of Fe@hollow-silicalite-1

An alkali-free TPAOH solution with a concentration of 1M is prepared by exchange of 66.6 g of TPABr with 29 g Ag_2O in 250 ml water for 10 min in complete absence of light (**Equation 18**). The AgBr precipitate is separated by filtration on a Büchner.



Fe@hollow-silicalite-1 is prepared by a dissolution-recrystallization process in the presence of TPAOH at 170 °C as previously established in our team by Tuel, A. et al. [110, 111]. 1 g of the previously calcined Fe/silicalite-1 is dispersed in a solution containing 4.15 mL 1M free-alkali TPAOH and 3.32 mL water. The mixture is transferred in a Teflon-lined stainless steel autoclave in an oven at 170 °C for 24 h. During this process, the highly defective core of the silicalite-1 crystal is preferentially dissolved and silica species recrystallize on the outer surface in the presence of TPA⁺ cations (**Figure 21**). The autoclave is then cooled down to room temperature and the solid is recovered by centrifugation, washed several times with water until reaching a neutral pH, crushed and dried at 90 °C overnight. The dried solid is calcined at 550 °C in air to remove the TPAOH template.

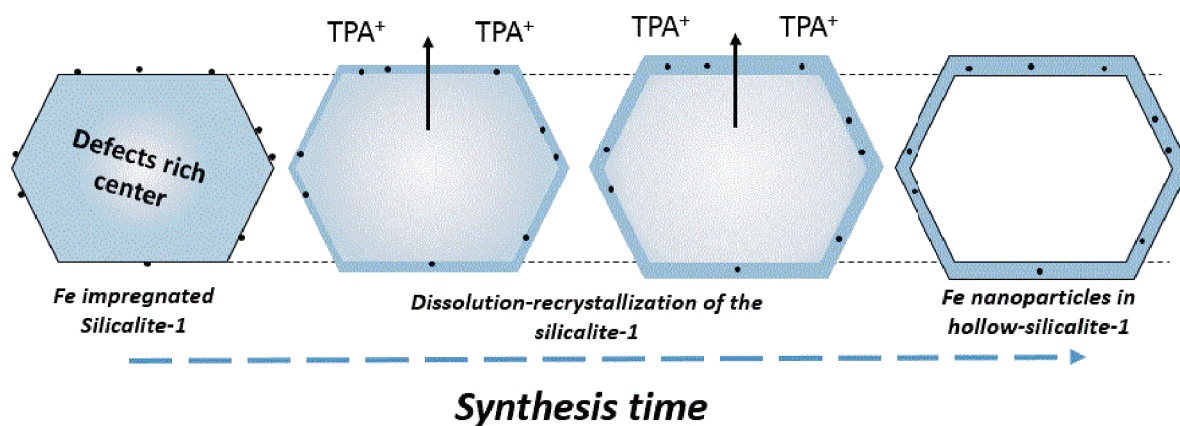


Figure 21 | Dissolution-recrystallization process of the Fe@silicalite-1 in presence of TPAOH.

I.4. Reduction procedure of Fe@hollow-silicalite-1

The synthesized Fe@hollow-silicalite-1 is reduced under hydrogen at high temperature to form the metallic nanoparticles. Typically the sample is inserted into a quartz reactor which is then fixed in an oven. Approximately 40 mL/min hydrogen is used for the reduction of the iron. The oven is brought at 750 °C in 3 h and stay at this temperature for 3 more hours. This procedure is applied also in the case of copper dopant.

II. Characterization techniques for catalyst analysis

II.1. Powder X-ray Diffraction (XRD)

Powder X-ray diffraction spectroscopy is a technique used to determine the structure of a crystal and/or solid, in other word, the different phases contained in a sample. Furthermore, by using the Debye-Scherrer equation, the mean particle size of crystallites can be estimated. X-ray diffraction (XRD) patterns of the solid were recorded on a Bruker D8 Advance diffractometer using CuK α radiation (**Figure 22**). Diffraction patterns were collected between 4 and 80° (2 θ) with steps of 0.02° and 1 s per step.

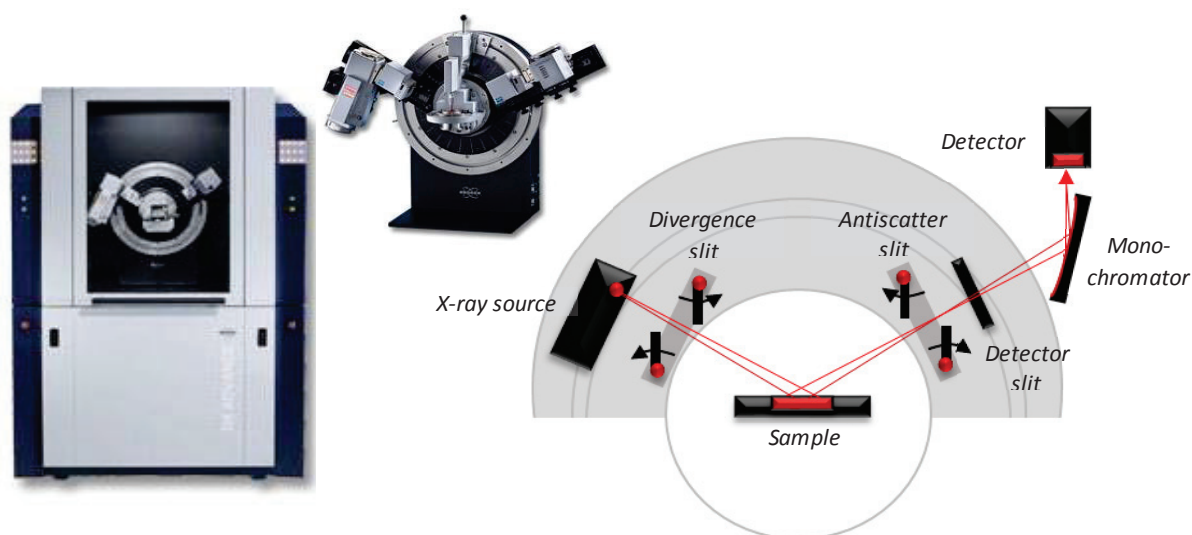


Figure 22 | Bruker D8 advance pictures and scheme of the overall setup.

When the incident beam of monochromatic X-ray emitted by the X-ray source enter in contact with the material, the beam is scattered. In a crystalline structure the scattered beam undergo constructive and destructive interference. This process is called diffraction. Diffraction of X-rays by a crystal is described by Bragg's law:

(Equation 19)
$$n\lambda = 2d_{hkl} \sin \theta$$

λ is the wavelength of the incident beam ($\lambda=1.54184 \text{ \AA}$), n is a positive integer, θ is the scattering angle and d_{hkl} is the interplanar distance (distance between two crystallographic planes). Size and shape of the unit cell, as well as the arrangement of atoms in a crystal structure, can change the directions of diffraction and the intensity of the diffracted beam. In a powder, several small crystallites domains randomly orientated coexist, therefore the

incident X-ray beam can see all the interatomic planes by varying the incident angle θ by moving the source, in the end all possible diffraction peaks will be detected. The beam is deflected following a 2θ angle (**Figure 23**).

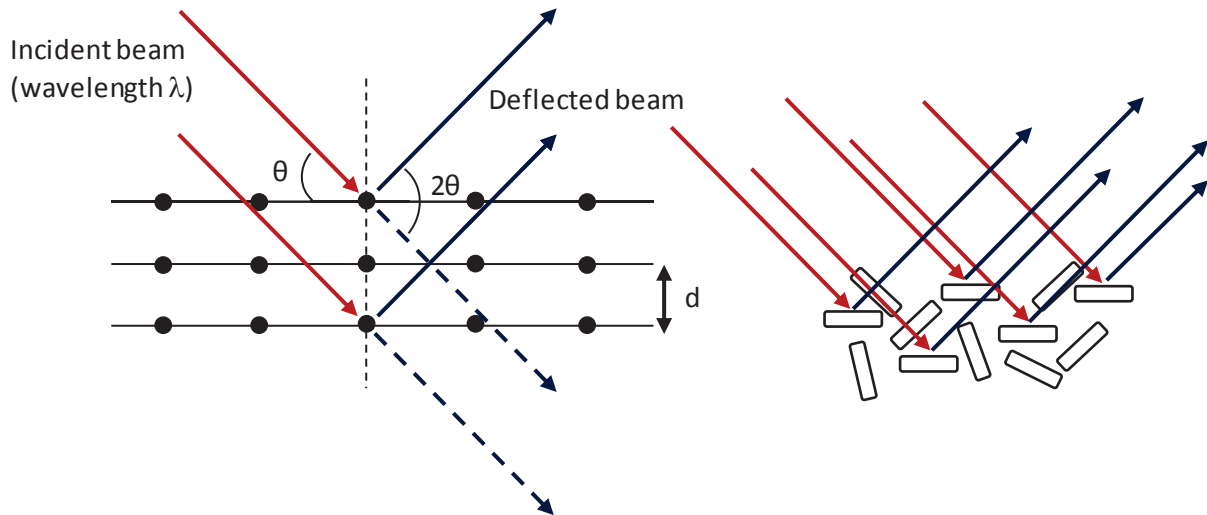


Figure 23 | Bragg's diffraction (left) and X-ray incident beam on randomly orientated crystallites (right).

X-ray diffraction can be used to estimate the mean particle size of crystallites in a domain between 1 to 100 nm by applying the Scherrer method:

(Equation 20)

$$d_{\text{crystallite}} = \frac{K \cdot \lambda}{B(2\theta) \cdot \cos\theta}$$

K is the Scherrer constant, λ is the wavelength of the apparatus, θ is the diffraction angle and $B(2\theta)$ the peak width (FWHM).

II.2. Elementary Analysis (ICP-OES)

Elemental analysis (EA) gives information about the loading of iron in the zeolite. EA is carried out by Inductively-Coupled Plasma Optical Emission Spectroscopy (HORIBA Jobin Yvon Activa ICP-OES). The samples are first dissolved in an acid solution (mixture of HF, H₂SO₄ and HNO₃ solutions), which is then introduced into the spectrometer. Excited atoms and ions produced from each element emit a characteristic radiation whose intensity is measured. This intensity is then correlated to the amount of each element.

II.3. N₂ adsorption/desorption

N₂ adsorption and desorption isotherms give information on the material pores and mesoporous/microporous volume. N₂ adsorption and desorption isotherms are measured on an ASAP 2020 from a Micromeritics apparatus. Samples are first pretreated by calcination under vacuum (10⁻⁹ bar) at 300 °C. After the pretreatment, the cell is put under N₂ and placed under vacuum between 10⁻⁷ - 10⁻⁸ bar at the liquid nitrogen temperature (77 K). The nitrogen pressure is then increase at different P/P₀ until it comes closer to P/P₀ = 1.

Apparent surface area is calculated using the BET method and the microporous volume estimated from the t-plot curve. The y-intercept of the extrapolation of the t-plots curves to x = 0 is used to determine the presence of micropores and/or mesopores in the materials.

II.4. Transmission Electronic Microscopy (TEM)

Transmission electronic microscopy gives tremendous information on the structure, morphology and localization of particles in a material. Particle size distribution and dispersion can be derived from TEM images.

II.4.1. Sample preparation

The sample is prepared first by grinding the catalyst in a mortar with a small amount of ethanol. The ethanol solution with catalyst suspension is then place for a few minutes in an ultrasonic bath in order to get a homogeneous suspension and break agglomerated particles. A drop of this solution is deposited on a holey carbon film Cu grid. The grid is dried at room temperature.

II.4.2. Transmission Electronic Microscopy apparatus

TEM images were taken using a Jeol 2010 LaB6 microscope operating at 200 kV. The resolution of electron microscopy is much higher than the optical ones due to the very short De Broglie wavelength of electrons (resolution of 0.19 nm). The photo and schematic of the TEM

equipment is showed in **Figure 24**. At the top of the microscope an electron beam is emitted by an electron gun containing the emission source LaB_6 single crystal. The emission source is connected to a high voltage source of 200 kV under vacuum. The beam emitted by the source is focused by various electromagnetic lenses such as the condenser, the objective and projector lenses. The first one, the condenser, is in charge of focusing the beam onto the sample. While passing through the sample, the electron beam collided with the sample's atoms which result in scattering the electrons. The scattered beam is thereafter refocused by the objective lens in order to form the sample's images. The projector lens helped to magnify the images and project them on an imaging device, here a CCD camera. Afterwards the images are recorded via a Digital Micrograph software. The contrast observed are due to the absorption of electrons by the material, and depend also of the thickness and composition of the sample.

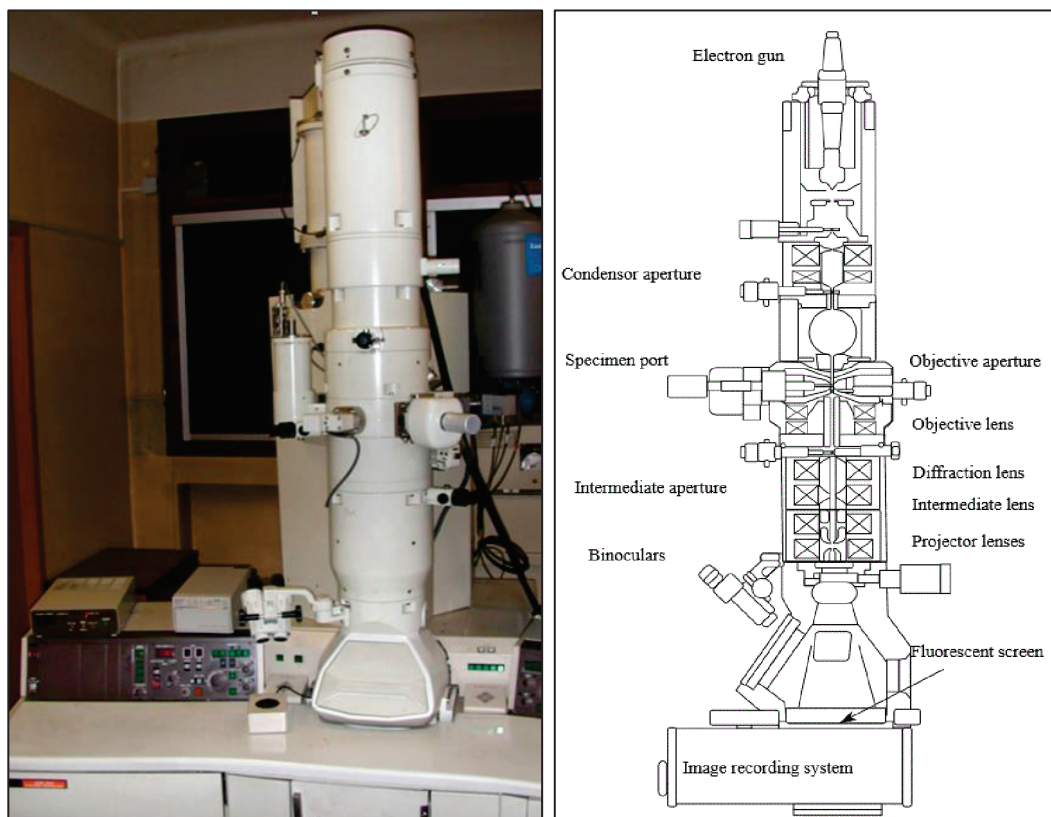


Figure 24 | Scheme (right) and photo (left) of the JEOL 2010 apparatus.

In this work, the TEM was an essential technique to verify the shape of our material as well as the localization of our particles. Most materials observed were in the range of nanometer.

II.4.3. Energy Dispersive X-ray spectroscopy

The microscope is equipped with an EDX Link ISIS analyzer from Oxford Instruments. It is possible with EDX to identify the elements present in the sample. When the electron beam passes through the sample, X-ray is emitted by the material. X-rays can be detected and measured, then it is compared with the characteristic spectrum of each element. Furthermore the number of photons emitted by the species in the material is proportional to the mass concentration of these species. Therefore this techniques can be correlated with the ICP-OES elemental analysis even though being less accurate. EDX is hence used to provide the constitution of particular area in the sample or the constitution of a particles itself, in the case of alloy or bi-metallic particles.

II.4.4. Study of nano-particles with TEM

In this work, with TEM images, the size distribution and dispersion of our particles were obtained by counting around 500 particles with the help of Image J software. Two different methods of calculation of the metal particles dispersion are used here, either by following the Handbook method [112] using the average diameter to make the calculation (not a very accurate method) or by using the method of Van Hardeveld and Hartog [113]. This last one is estimated from the size distribution using a cub-octahedral model and by considering the percentage of surface atoms among the overall atoms in each metal particle.

- Handbook model [112]: with TEM images the diameter of 500 particles is calculated, therefore an average value of the diameter can be calculated (this method can be use if the size distribution is quite narrow otherwise it will not be accurate). Then the dispersion can be calculated by the following formula:

(Equation 21)
$$D (\%) = 6 * \frac{V_m}{A_m} * \frac{1}{d_a}$$

D is the metal particle dispersion in %, V_m is the volume occupied by an atom in bulkmetal in \AA^3 , A_m is the area occupied by a surface atom in \AA^2 and d_a is the mean particle size in \AA . The value for V_m and A_m are taken from the table of the Handbook.

- Van Hardeveld and Hartog model [113]: As explained above, this method consists of considering a cub-octahedral model and by using the Cardan method to solve third-order equation, the number of surface atoms in each metal particles can be calculated and therefore we can calculate the dispersion.

II.5. Environmental Transmission Electronic Microscopy (E-TEM)

To investigate particles localization in a material, tomography 3D reconstruction was performed with the Environmental Transmission Electron Microscope (Cs-corrected TITAN ETEM G2 FEI, 80 - 300 kV) at CNRS (**Figure 25**). The objective was to obtain a three-dimensional spatial image of our material.

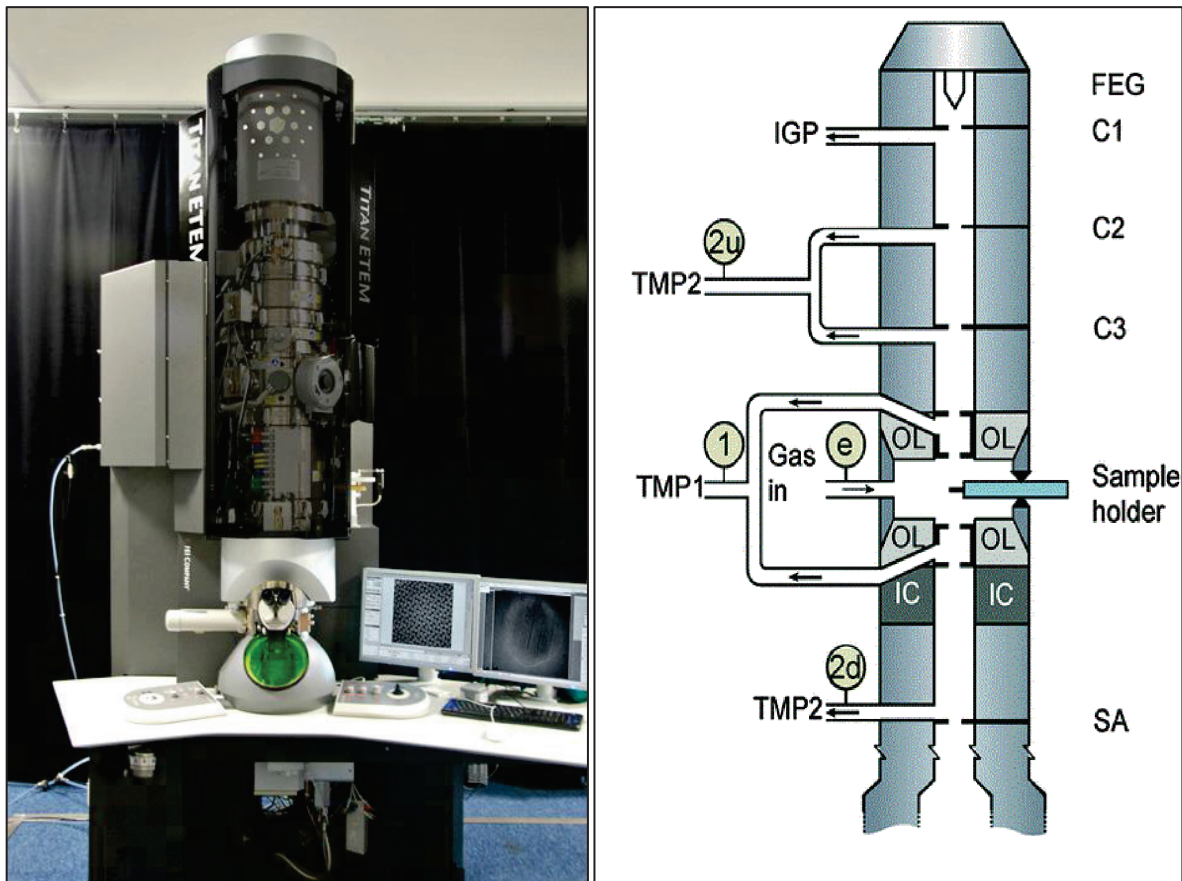


Figure 25 | Photo (left) and scheme (right) of the Cs-corrected TITAN ETEM G2 FEI apparatus. Vacuum system highlighting the pressure-limiting apertures at the stages of the objective lens (OL), the condenser lenses (first (C1), second (C2) and third (C3)) and the selected area (SA) aperture. Also the image corrector (IC) and field emission gun (FEG) positions are indicated. The first and second stages are pumped by turbo-molecular pump units (TMP1 and TMP2).

Electron tomography was performed using a FEI ETEM Titan 80-300 keV in bright field mode. The sample was tilted from 74° to -74° with a step of 2° degree in Saxton mode [] by using the TIA software. It was recorded a tilt series of 113 projections with a resolution of 2048x2048 having the pixel size of 0.25 nm. The alignment was performed using the IMOD software [] and the volume reconstruction was performed using 15 iterations of ART algorithm implemented in the TOMOJ software []. The volume rendering was calculated using the 3D Slicer software ([], URL: <http://www.slicer.org/>).

II.6. Mössbauer spectroscopy

Mössbauer spectroscopy was carried out to identify and quantify the different iron phases present in the samples. This technique is very sensitive to iron environment and thus provides very valuable information on the environment and oxidation state of the Fe species.

A ⁵⁷Co/Rh γ -ray source and a conventional constant acceleration Mössbauer spectrometer were used for spectra collection. The integrated areas under individual de-convoluted peaks have been used to obtain the relative populations of the different iron species. Isomer shifts (IS) are given with respect to α -Fe and are calculated as quadrupole splitting (QS) with a precision of about 0.02 mms⁻¹. Hyperfine field relative intensity: 0.1 T. The relative areas of observed spectral components have been used to quantitatively evaluate the relative amounts of the iron species present in the catalysts. This has been done by assuming equal recoil-free fractions for all Fe species.

II.6.1. Ex-situ Mössbauer

Mössbauer spectroscopy was carried out on the fresh and spent iron catalyst directly in air. The schematic of the setup build for the ex-situ experiment is represented in **Figure 26**. A Mössbauer spectrometer system consists of a γ -ray source that is oscillated toward and away from the sample by a Mössbauer drive, a collimator to filter the γ -rays, the sample, and a detector.

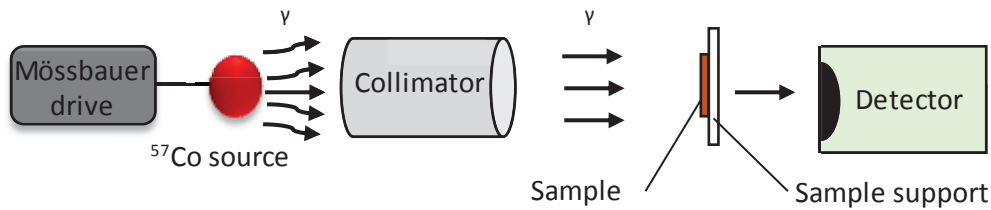


Figure 26 | Schematic setup of the Mössbauer for ex-situ experiments.

Integrated areas under individual de-convoluted peaks were used to obtain the relative populations of different iron species, assuming an equal recoil-free fraction for all iron species. The parameters characterizing a Mössbauer spectrum were determined by least-squares fitting and minimizing the χ^2 quadratic function:

(Equation 22)

$$\chi^2 = \sum_i \frac{(y_{i,th} - y_{i,exp})^2}{y_{i,exp}} * \frac{1}{N-K}$$

N is the number of measured points, K the number of the parameters to be determined, $y_{i,exp}$ and $y_{i,th}$ respectively measured and calculated spectral values in velocity for each point i. The calculations were made using pure Lorentzian functions.

Mössbauer spectroscopy probes transition between energy states of the Fe nucleus and allows obtaining information about the atom and its surroundings owing to the existence of hyperfine interactions. These hyperfine interactions characterize each iron species and allow identifying and quantifying the iron compounds. These hyperfine interactions are three:

1) The isomer shift (IS):

The isomer shift (δ) measures the difference in electron density at the nucleus in the studied absorbing sample and that at the nucleus of an atom of the source. Because all sources may be different, the isomer shift calculated is expressed related to a reference compound, in our case metallic iron. This shift in the energy levels is related to the interaction between the nucleus and s electrons which wave function overlaps the nucleus. It can be expressed by:

(Equation 23)

$$\delta = \frac{1}{4\pi\epsilon_0} * \frac{Ze^2}{R} * 4\pi R^2 \Delta R * \left[|\Psi_a(0)|^2 - |\Psi_q(0)|^2 \right]$$

Where Z is the atomic charge number and e the elementary charge. We have for the potential of the nuclear charge at the distance R from the center of the sphere: $U = eZ/4\pi\epsilon_0R$. When increasing R by ΔR the volume of the sphere is increased by $4\pi R^2\Delta R$. With $\Psi(0)$ as normalized wave function of the s -electron (dimension: $m^{-3/2}$) within the nuclear sphere, we get for the absolute value of the charge density of the electrons $e: |\Psi(0)|^2$. Subscripts “ q ” and “ a ” denote source and absorber, respectively.

2) The electric quadrupole splitting (QS):

The ^{57}Fe nucleus has a positive electrical quadrupole moment. Consequently in the presence of an electric field gradient (EFG) a splitting of the excited state will occur. This splitting is proportional to the magnitude of the EFG. This EFG is due to charges arising from the asymmetrically distributed electrons in incompletely filled shells of the iron atom and to charges on neighboring atoms in the crystal lattice. The quadrupolar splitting can be expressed by:

(Equation 24)
$$E_q(I, m_i) = \frac{eQV_{zz}}{4I(2I-1)} * [3m_i^2 - I(1 - I)] \left(1 + \frac{\eta^2}{3}\right)^{1/2}$$

Where eQ is the electric quadrupole moment, V_{zz} the main tensor component, η the asymmetry parameter ($\eta=(V_{xx}-V_{yy})/V_{zz}$), m_i the magnetic spin quantum moment and I the nuclear state.

3) The magnetic hyperfine splitting:

The magnetic hyperfine splitting also called Zeeman splitting arises from the interaction between the nuclear magnetic dipole moment and the magnetic field H at the nucleus. It leads to the splitting of both the ground state level and the two excited states. This leads to eight possible transitions among which, only those corresponding to a change in magnetic number is 0 or +1 are allowed. There are thus six transitions and the spectrum consists of six lines often called a sextet or sextuplet.

The calculated internal magnetic field is expressed in Tesla (1 T=10 kOe).

A metallic iron foil sample is used to calibrate the apparatus, the Mössbauer spectrum is given in **Figure 27** and the Mössbauer parameters (Isomeric shift (IS, mm.s^{-1}), quadrupolar splitting (QS, mm.s^{-1}), hyperfine field (T) and relative intensity (%)) are given in **Table 7**.

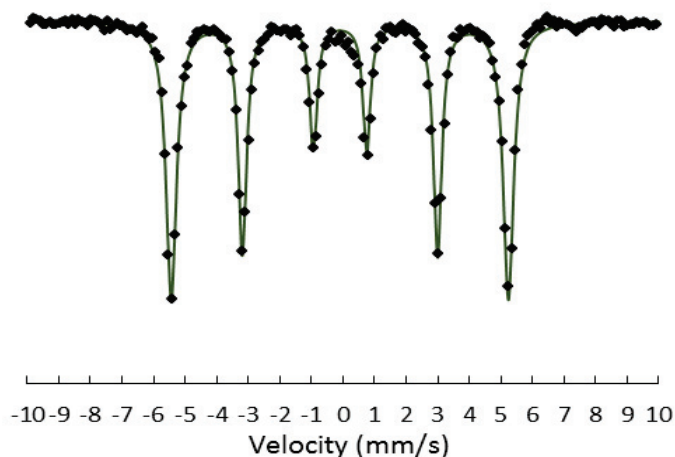


Table 7 | ^{57}Fe Mössbauer parameters of the $\alpha\text{-Fe}$ foil sample

| | |
|---------------------------|--------------------|
| Species | $\alpha\text{-Fe}$ |
| IS (mm.s^{-1}) | -0.00 |
| QS (mm.s^{-1}) | 0.00 |
| Hyperfine field (T) | 33.0 |
| Relative intensity (%) | 100 |

Figure 27 | ^{57}Fe Mössbauer spectrum of the calibration sample: Experimental spectrum (black dot) and reference $\alpha\text{-Fe}$ fit (green line).

Ex-situ Mössbauer permits to have a better signal and is easier to perform unlike in-situ Mössbauer. However the spent iron catalyst is partially re-oxidized in air, meaning that the different phases observed might not be representative of the iron phases present during and after the FTS reaction in the reactor.

II.6.2. In-situ Mössbauer

In-situ Mössbauer spectroscopy was also carried out for a more accurate characterization of the iron phases. The schematic of the setup build for the in-situ experiment is represented in **Figure 28**. The sample is placed on a heating support inside a Mössbauer cell. The sample support can be heated up to the desired temperature. Cooling water is going through the walls of the Mössbauer cell to prevent damaging the cell and the kapton windows which allow the γ -rays to pass through the cell and the sample. Two cylinders, one containing a mixture of H_2/CO of ratio 2 and another with N_2 are connected to the cell. However pressure cannot be applied inside the cell, therefore all in-situ experiments were carried out at atmospheric pressure.

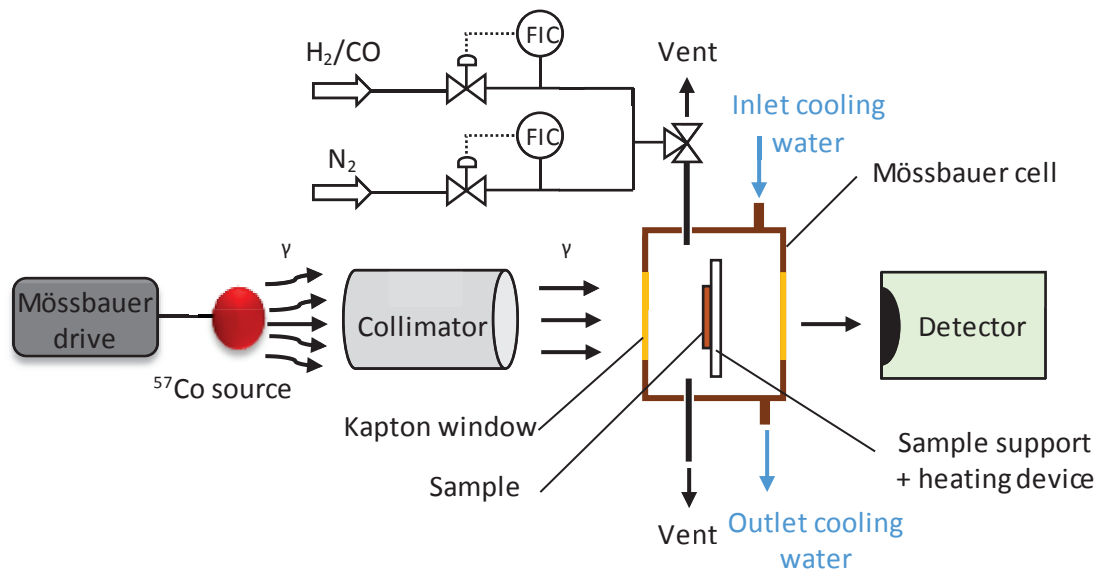


Figure 28 | Schematic setup of the Mössbauer for in-situ experiments.

II.7. Magnetic measurements

II.7.1. Theory of magnetism

Magnetism is a physical phenomenon ruled by magnetic fields which can be characterized by repulsive and attractive forces of an object on another. Magnetism comes from two sources, the electric current (or electric magnetic moment) and the spin magnetic moments of elementary particles. Also every material can be influenced to some extent by a magnetic field. When a material is subject to a magnetic field, the material will most likely be oriented or moved depending of the force or direction of the field.

Moreover magnetic state of a material depends on various parameters such as temperature, pressure and the applied magnetic field. Furthermore magnetic behavior of a material depends also of its structure, more particularly its electron configuration. A material may display more than one form of magnetism as these variables change. There exist several type of magnetism:

Diamagnetism (DM): this type of magnetism appears in mostly all kind of materials. It is characterized by the tendency to oppose the applied magnetic field (**Figure 29**), and therefore being repelled by this last one. In a diamagnetic material, there are no unpaired electrons.

Nonetheless in a material containing paramagnetic and diamagnetic properties, the paramagnetic behavior is dominant.

Paramagnetism (PM): this magnetism is characterized by a material with unpaired electron in atomic or molecular orbitals. Thus unpaired electron is free to align its magnetic moment in any direction. When an external magnetic field is applied to such material, those magnetic moments will tend to align in the same direction as the applied field and consequently strengthen it (**Figure 29**).

Ferromagnetism (FM): In a ferromagnetic material, there are unpaired electrons. Alike a paramagnetic material, magnetic moments tends to be align in the same direction of the applied magnetic field, furthermore there is also a tendency for the magnetic moments to orient parallel to each other to maintain a lowered-energy state. Consequently even in the lack of an applied field, the magnetic moments in the material spontaneously line up parallel to one another (**Figure 29**). Also a ferromagnetic material has its own temperature, called the Curie temperature (or Curie point, T_c), which is the temperature above which the material lose its ferromagnetic properties. The most common ferromagnetic materials are cobalt, nickel, iron and their alloys.

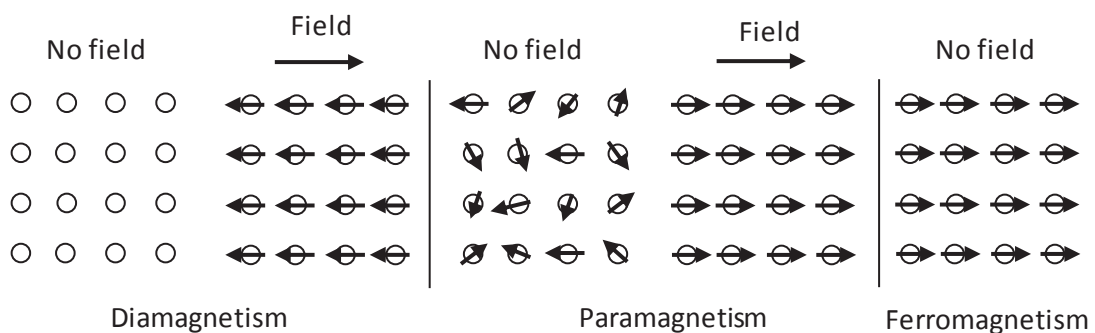


Figure 29 | Magnetic dipole and behavior in the presence or absence of external magnetic field.

Antiferromagnetism: In this sort of magnetism, intrinsic magnetic moments of valence electrons tend to orient themselves in opposite directions. Antiferromagnetic materials have a zero net magnetic moment meaning no field is induced by them (**Figure 30**). This type of magnetism is less common and is mainly observed at low temperature.

Ferrimagnetism: alike ferromagnetic materials, ferromagnetic materials keep their magnetization in the absence of a magnetic field. Furthermore they look alike antiferromagnetic materials and have the magnetic moments of neighboring pairs of valence electrons point in opposite direction. However the intensity of magnetic moment in one of the direction is more important than the ones pointing in the other (**Figure 30**).

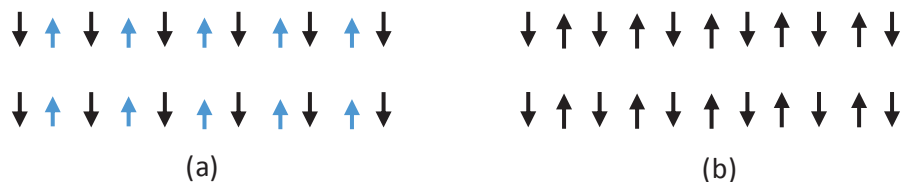


Figure 30 | Difference between spin ordering in a ferrimagnetic material (a) and an antiferromagnetic material (b).

Superparamagnetism (SPM): this type of magnetism is typically characteristic of small ferromagnetic and ferrimagnetic nanoparticles. This implies sizes from a few nanometers to a couple of tenth nanometers depending on the material. Moreover these nanoparticles are made of a single domain particles, which mean that the total magnetic moment of the nanoparticle can be regarded as one giant magnetic moment. In the absence of an external field, the net moment is zero. However as soon as an external magnetic field is applied, the nanoparticles are magnetized and behave similarly as a paramagnetic material with the exception that their magnetic susceptibility is much larger.

The magnetic measurement is based on the superparamagnetic particles theory. The behavior of a set of superparamagnetic particles is given by the orientation of the magnetic moment μ of a particle. The magnetic moment is proportional to the volume of the particles, thus the magnetic response becomes dependent on the particle size distribution of superparamagnetic particles. The macroscopic magnetization is given by the following equation:

(Equation 25)
$$M(H, T) = M_s \int_0^\infty L(T, H, D) * f_v(D) * dD$$

M is the magnetization (cgs) dependent of the magnetic field H (T or Oe) and the temperature T (°C). M_s is the saturation magnetization (cgs or emu.g^{-1} or A.m^{-1}), L is the Langevin function, D is the particle size diameter and f_v is the particle size distribution.

The behavior of superparamagnetic particles is described by the Langevin function:

(Equation 26)
$$L(H, T, D) = L(x) = \tanh(x) - \frac{1}{x}$$

With x being the following equation:

(Equation 27)
$$x = \frac{\pi\rho\sigma_s H}{6kT} * D^3$$

ρ is the specific volume of the material ($\text{kg}\cdot\text{m}^{-3}$), σ_s is the specific magnetization at saturation ($\text{emu}\cdot\text{kg}^{-1}$), H is the magnetic field (emu) and D the particle diameter (m). emu stands for electromagnetic unit and cgs for centimeter-gram-second unit system.

In this work the magnetization is measured at constant temperature but at variable external magnetic field. Generally materials contain various particles sizes, therefore the magnetic moment of those diverse particles do not orient themselves the same way in the presence of an external field, i.e. large particles first orient themselves, then by increasing the external field, the smallest ones start to align too, until the saturation magnetization M_s (**Figure 31**).

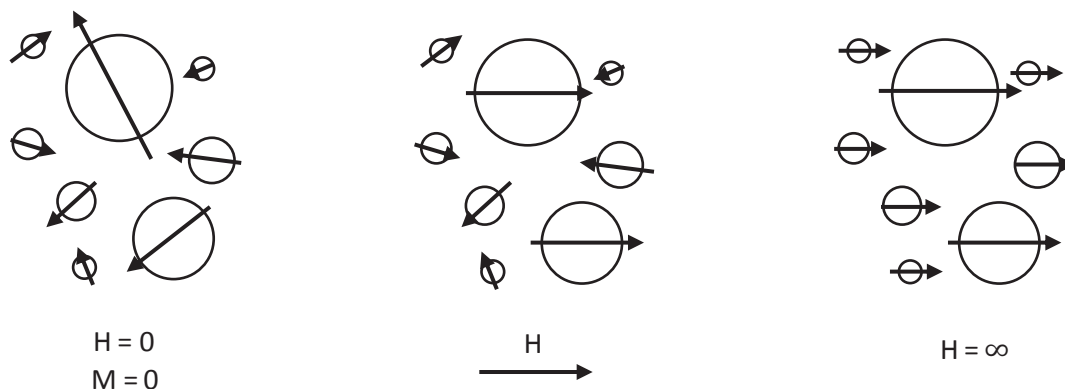


Figure 31 | Magnetization as function of external magnetic field and particle size .

All those types of magnetism show different behaviors of the magnetization M (cgs) when varying the external magnetic field H (T). A comparison of those different magnetic materials is shown in **Figure 32**:

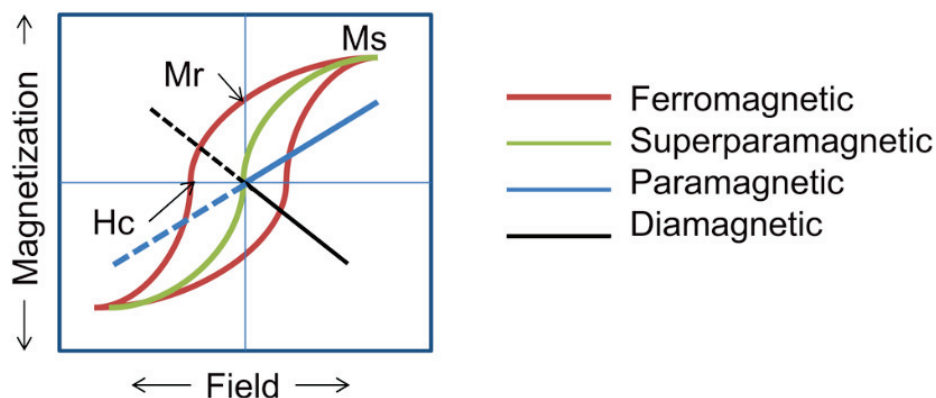


Figure 32 | This figure shows the schematic behavior of diamagnetic, paramagnetic, ferromagnetic and superparamagnetic materials in an external magnetic field. Where M_s is the saturation magnetization, M_r the remanent magnetization and H_c the coercivity.

Magnetic curves of the material are obtained by varying the external magnetic field H from -0.1 T to 2 T at room temperature. During the experiment the obtained signal correspond to a tension U (V), which can be related to the magnetization M by the following formula:

(Equation 28)
$$M = U * C$$

M is the magnetization of the material in cgs, U is the tension in V and C is a constant coming from the apparatus (this constant is determined from a metallic nickel sample, here = 4300 cgs.V⁻¹)

During an experiment, the magnetic behavior (depending of the particles size) is characterized as a function of the magnetic field. From the measured magnetization from 1.5 T to 2 T, the saturation magnetization can be calculated by plotting $M = f(\frac{1}{H})$, and by extrapolating at infinite field ($H = \infty$) we can determined the M_s (cgs). That way it is possible to determine **the reduction degree of the catalyst**, for that the following formula is used:

(Equation 29)
$$\%red = \frac{M_s}{M_{sp}(x) * m(x)} * 100$$

$M_{sp}(x)$ is the specific magnetization of the element x considered and m is the mass of this element in the sample in g. In the case of iron $M_{sp}(Fe) = 218 \text{ cgs.g}^{-1}$.

From the measured magnetization from -0.1 T to 0.2 T, the remanent magnetization M_r can be determined. The remanent magnetization is associated to the magnetization left behind in

a ferromagnetic material after the external field is removed. M_r is determined by the intersection of the magnetization curve with the y axis therefore solving the equation $M = M_r = f(H = 0)$. If M_r is inferior to 5 - 10% of M_s then we can correctly apply the Langevin equation to determine **the quantity of ferromagnetic material** which is calculated with the following formula:

(Equation 30)
$$\% \text{ferromagnetic} = 2 * \frac{M_r}{M_s}$$

This give also information on the sintering of the catalyst, as an increase in ferromagnetic material can be attributed to sintering of smaller particles.

Finally the magnetization measurement can help estimating the average diameter size of the large (D_1) and small particles (D_2). For low and high magnetic fields, the reduced Langevin's equation can be used. At low magnetic field (H tends to 0) the average large particle size diameter can be determined by the following equation:

(Equation 31)
$$D_1 = 93.4 * \left(\frac{T}{\sigma_s * \rho * M_s} * \left(\frac{M}{H} \right)_{H \rightarrow 0} \right)$$

At high magnetic field ($1/H$ tends to 0) the average small particle size diameter can be determined by the following equation:

(Equation 32)
$$D_2 = 3 * \left(\frac{T}{\sigma_s * \rho} * \left(\frac{M_s}{M_s - M_{H=10^4}} \right) \right)$$

II.7.2. Experimental setup

Magnetic measurement are being done with the Weiss extraction method, hence the sample is placed in a quartz tube which can moved up and down (with a pneumatic jack) in the uniform magnetic field induced by two electromagnets (from -0.1 T to 2 T). During the experiment an electrical voltage is created and measured with an integrated measuring coil (**Figure 33**). Magnetic measurement are carried out at room temperature.

The quartz reactor can be connected to different gases such as CO, H₂ and Ar in order to do in-situ Fischer-Tropsch on the sample. An oven can be installed on top of the electromagnet and be heated up to 400 °C. That way FTS can be carried out at high temperature under H₂/CO

ratio 2:1 before being cooled down, then magnetic measurement can be made. Thus this technique help to follow the evolution of magnetic properties of the catalyst during FTS.

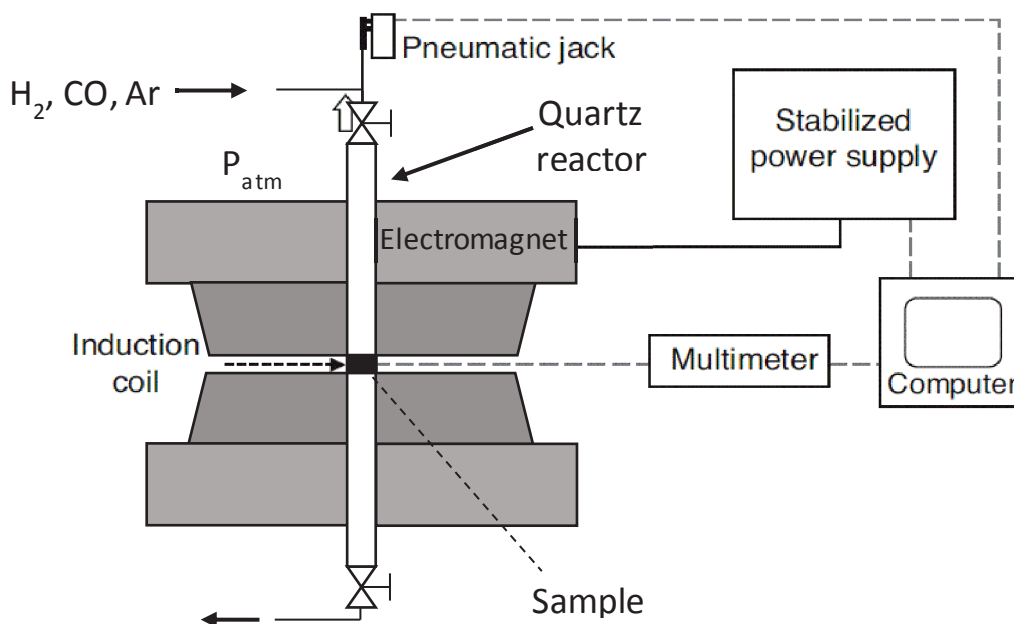


Figure 33 | Scheme of the magnetic measurement setup.

II.8. Synchrotron: In-situ X-ray powder diffraction (XRDP) and X-ray absorption spectroscopy (XAS)

II.8.1. Experimental setup

In-situ measurements were carried out at the European Synchrotron Radiation Facility (ESRF) in Grenoble, France. More precisely at the Swiss-Norwegian beam lines BM01. The data analysis and treatment were carried out by our partner NTNU (Norwegian University of Science and Technology). These in-situ experiments are used to correlate the different iron phases with the catalytic performances of a catalyst using different kinds of characterization techniques:

- X-ray powder diffraction (XRPD): a bulk analysis technique.
- X-ray absorption spectroscopy (XAS): a bulk analysis technique.
- A mass spectrometer (MS): on-line analytical device to monitor the evolution of various species during FTS (CO, H₂, CH₄ and CO₂).

For an experiment, approximately 5 - 6 mg of sample are placed in the middle of a quartz capillary reactor (catalyst bed size \approx 1 cm) and fixed with glass wool on both side. The reactor is mounted on a stainless steel bracket support and secured on both side with a glue resistant to high temperatures. The bracket is thereafter screwed onto an in-situ cell which has an inlet and an outlet opening for gases (**Figure 34**).

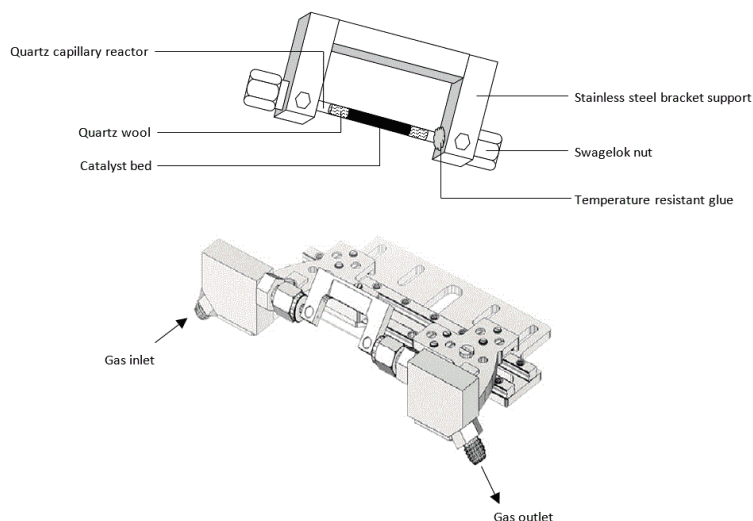


Figure 34 | Experimental setup of the synchrotron apparatus, stainless steel bracket maintaining the glass reactor (up) and in-situ cell (down).

The cell is then connected to the full setup, constituted of a feed system, with different gases, and the analysis system (XRPD, XAS and MS) (**Figure 35**). The heating system is placed right below the catalyst bed.

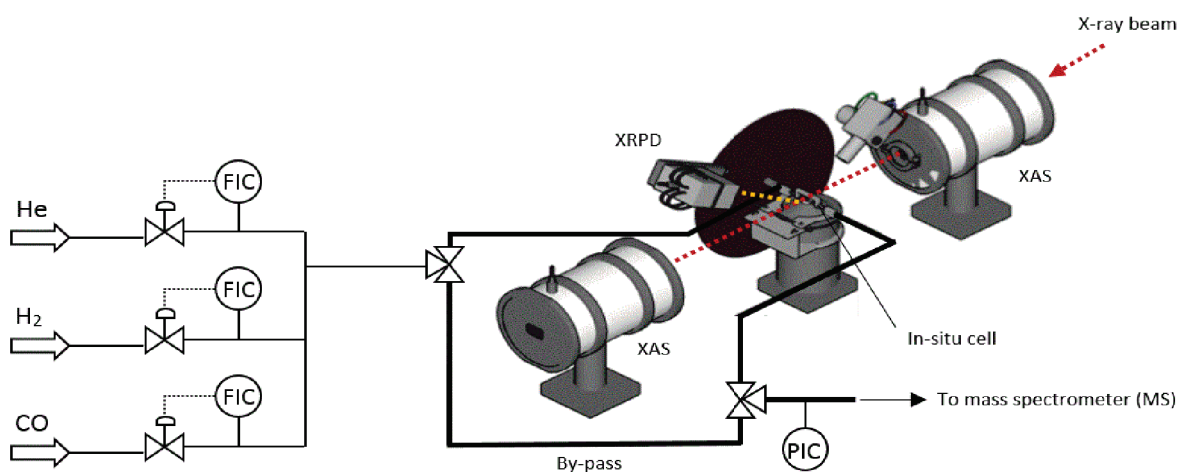


Figure 35 | Experimental setup of the synchrotron apparatus, XRPD (X-Ray powder diffraction), XAS (X-ray Absorption spectroscopy), FIC (flow rate indicator/controller), PIC (Pressure indicator/controller).

II.8.2. Methodology of measurements

First of all XRPD and XAS measurement scans are conducted on the fresh catalyst. Helium is first introduced into the system in order to reach a pressure of 18 bars, then the syngas mixture ($H_2/CO = 2$ and $GHSV \approx 15000 \text{ L.kg}_{\text{cat}}^{-1}.\text{h}^{-1}$) is introduced. The glass reactor temperature is first increased up to $230 \text{ }^\circ\text{C}$ with a ramp of $5 \text{ }^\circ\text{C}/\text{min}$. Approximately 5 cycles of measurements (1 cycle = 1 XRPD and 6 XAS scans) were collected during this isothermal step (6 h) as explain in **Figure 36**. The temperature is then increased to the next operating temperature and the same procedure is repeated.

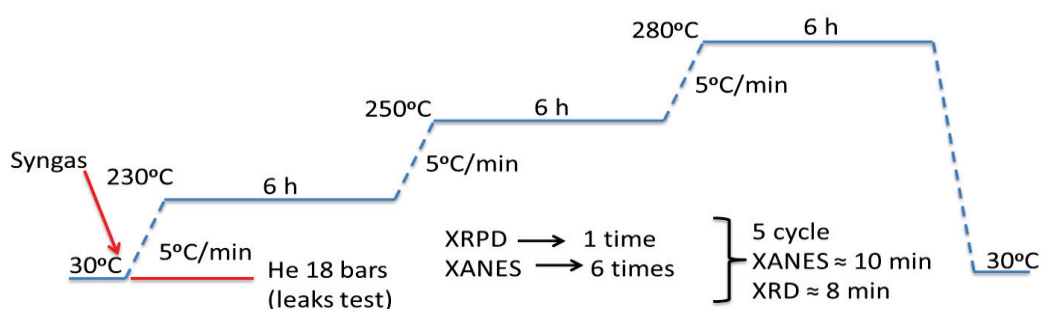


Figure 36 | Experimental procedure measurements for synchrotron.

The XAS data is divided in two regions, X-ray Absorption Near-Edge structure (XANES) and Extended X-ray Absorption Fine Structure (EXAFS), both regions were collected but the EXAFS data showed a lot of noise, consequently data treatment was focused on XANES region. The iron phases references data used for the linear combination are shown in **Figure 37**.

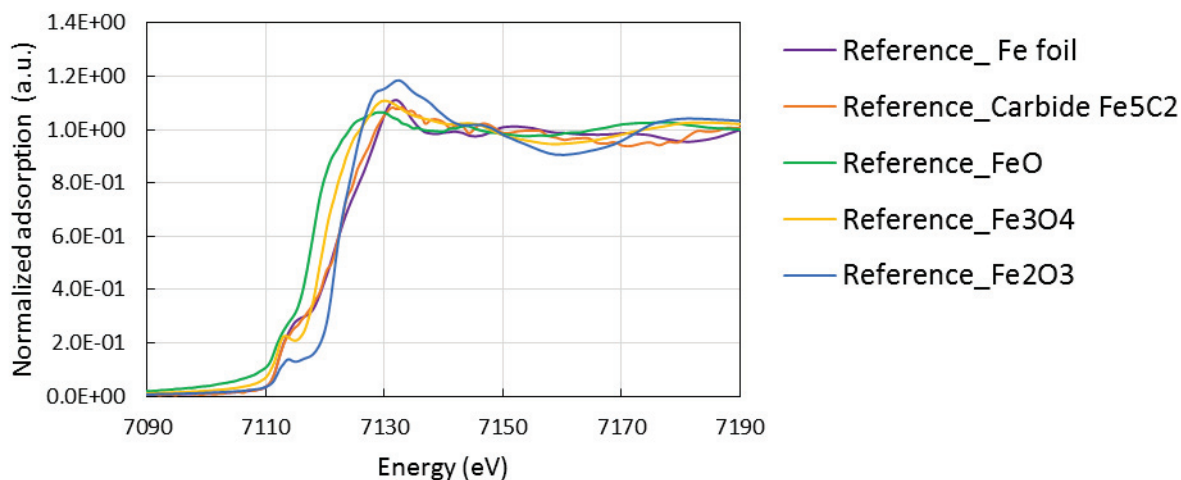


Figure 37 | Iron phases references for the linear combination.

III. Catalytic reactions and data processing

III.1. Fischer-Tropsch synthesis – setup and processing

III.1.1. Experimental setup

The global scheme of the experimental Fischer-Tropsch setup is represented in **Figure 38**. A stainless-steel reactor 30 cm long with an internal diameter of 4 mm is used. SiC (>200 μm) and quartz wool are placed on both side of the reactor to maintain the catalysts bed at the center of the reactor. The catalyst bed length depend on the quantity of catalyst used for the reaction. A thermocouple is placed inside the catalyst bed to acquire the exact temperature in the catalyst bed. A temperature profile for the entire bed can be determined by pulling the thermocouple step by step upward. The reactor setup is positioned in an oven heated (hot box) at 150 °C. A hot trap maintained at 120 °C is used to collect the heavy product fraction (mainly waxes), whereas the cold trap is maintained at around 10 °C for the collection of water and light fraction. An online-GC is positioned after the two traps to analyze the gas fraction (CO, H₂, CO₂, CH₄ and C₂ to C₉).

To start the experiment, a flow of H₂/CO/N₂ in the desired proportion is sent to the reactor. The temperature is then rose up to the desired temperature of operation. Then, the pressure is applied in the system thanks to a back pressure regulator, fixed to attain 20 bars. When the desired pressure is stable, the test starts and the analysis by GC-online is started. The test is then carried on for a period of 100 hours. To stop the catalytic test, the flow of H₂/CO is stopped, only the flow of N₂ remains to purge the system. At the same time the back pressure regulator is closed, permitting to the pressure to drop step by step until reaching the atmospheric pressure. The system is kept at the temperature of operation for two days to fully evacuate the waxes outside the catalytic bed. The temperature of the rig and hot box is then after stopped and the all setup is cooled down. When cold, the reactor can be disconnected from the setup and open to retrieve the catalyst. The catalyst is then taken to the various analytical techniques to fully characterize it.

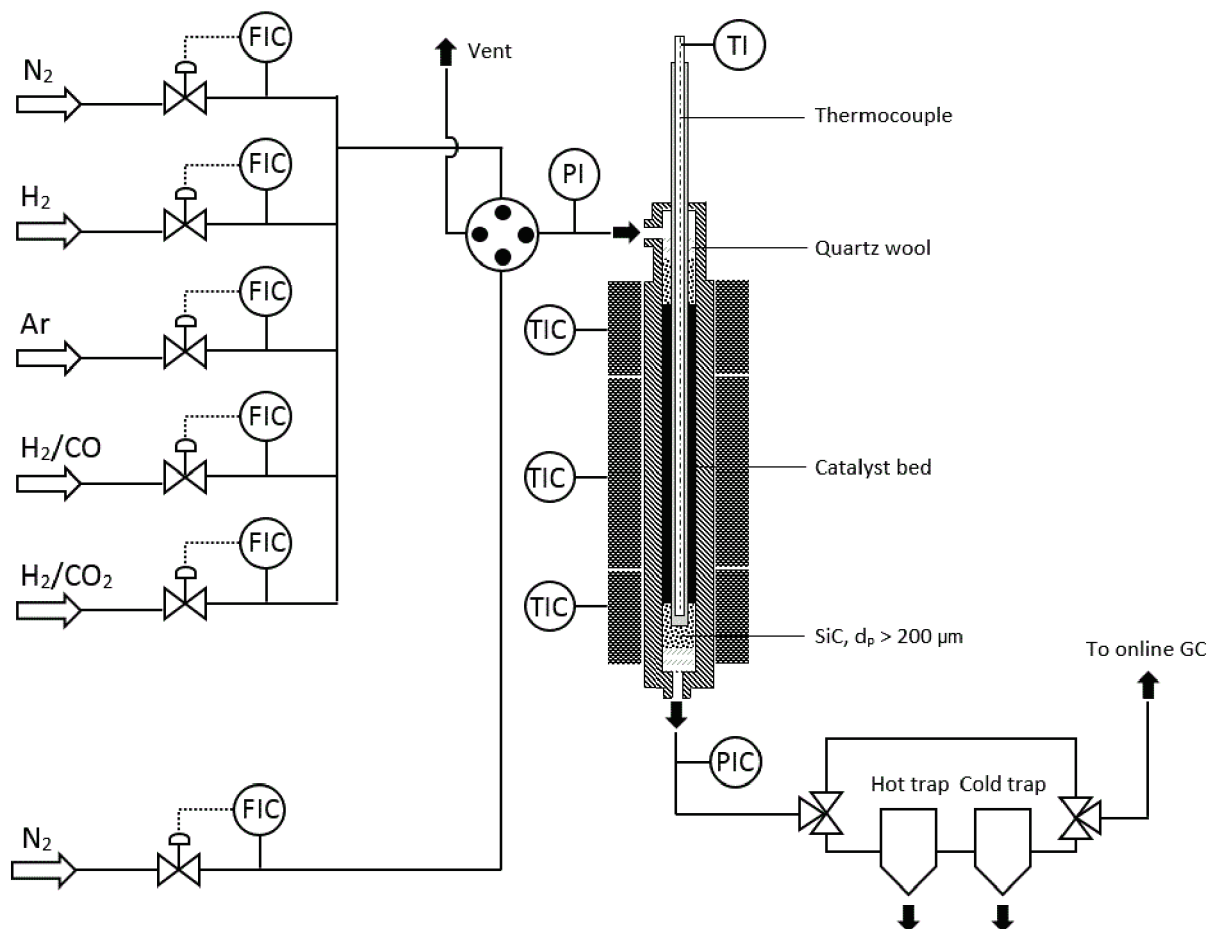


Figure 38 | Experimental setup, FIC (flow rate indicator/controller), TIC (Temperature indicator/controller), TI (Temperature indicator), PIC (Pressure indicator/controller), PI (Pressure indicator).

In the case of bulk-type catalysts (the JM commercial catalyst and the nano-structured α -Fe₂O₃ catalyst), waxes are trapped in the hot trap set at 120 °C. As this type of catalyst produces large quantity of waxes, it is necessary to use the two traps. However, in the case of the supported catalysts and encapsulated one (Fe/hollow-silicalite-1, Fe/SiO₂ and Fe@hollow-silicalite-1), the traps are not used. They produce so little waxes that the traps are bypassed. The overall flow/products are sent to the GC-online.

III.1.2. Analytical setup

Gas chromatography (GC) is an analytical techniques that allows a qualitative and quantitative analysis of gaseous and liquids compounds. Online gas analysis is performed during FTS using an Agilent gas chromatograph (GC) thus the activity of the catalyst and the selectivity of the

gaseous phase can be estimated. Detailed information concerning the columns, carrier gas and oven temperature program is given in **Table 8**). All analysis lines and valves were heated (150 °C) to prevent possible condensation of the products before entering the gas chromatograph.

Table 8 | Characteristics of the GC employed

| On-line GC | Agilent |
|--------------------------|---|
| Detector 1 | FID, 325 °C |
| Column 1 | DP-1 pona ($T_{\max} = 300$ °C), 100 m* 250 μm *0.5 μm nominal |
| Sample valve temperature | 250 °C |
| Mode | Split |
| Carrier gas | He |
| Oven temperature program | Hold at -60 °C for 3 min, heat to 50 °C at 3 °C/min, heat to 270 at 4 °C/min (Run time 123 min) |
| Product analysis | C ₁ - C ₉ |
| Detector 2 | TCD, 150 °C |
| Column 2 | Agilent J&W DB-1 ($T_{\max} = 300$ °C), 30 m* 530 μm *1.5 μm nominal |
| Sample valve temperature | 180 °C |
| Mode | Split |
| Carrier gas | Ar |
| Oven temperature program | Hold at -60 °C for 3 min, heat to 50 °C at 3 °C/min, heat to 270 at 4 °C/min (Run time 123 min) |
| Product analysis | H ₂ , CO, N ₂ , CH ₄ , CO ₂ |

Carbon monoxide (CO), carbon dioxide (CO₂), methane (CH₄), nitrogen (N₂) and hydrogen (H₂) were analyzed on an Agilent J&W DB-1 column equipped with a TCD (**Figure 39**). N₂ was used as an internal standard.

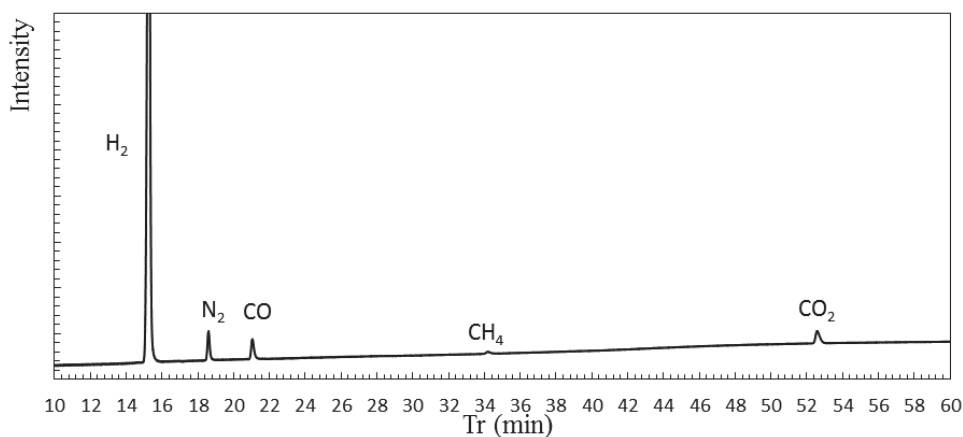


Figure 39 | TCD chromatogram of calibration mixture.

Methane and C₂ to C₉ light hydrocarbons were separated with a DP-1 pona column and analyzed with an FID detector (**Figure 40**). The different compounds shown in **Figure 40** are indicated in **Table 9**.

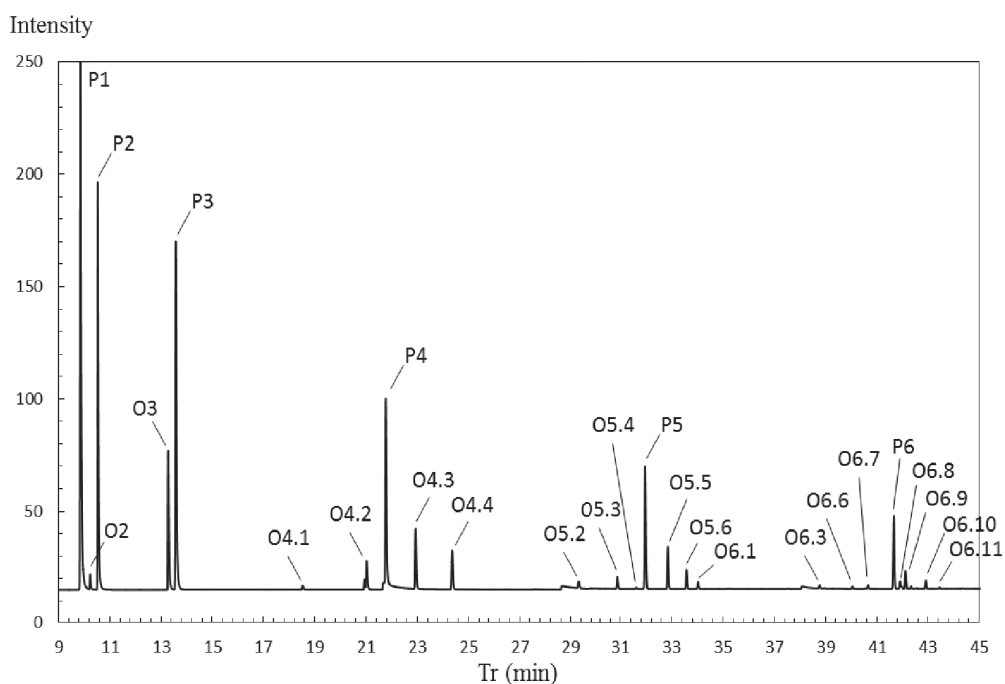


Figure 40 | Typical FID chromatogram of FTS test with corresponding compounds (Table 9).

Table 9 | Summary of the compounds analyzed by on-line GC

| Compounds | Tr : retention time (min) | Peak indicator |
|---|---------------------------|----------------|
| Methane | 9.95 | P1 |
| Ethylene | 10.3 | O2 |
| n-Ethane | 10.6 | P2 |
| Propene | 13.37 | O3 |
| n-Propane | 13.70 | P3 |
| Iso-butylene | 18.75 | O4.1 |
| 1-Butene | 21.07 | O4.2 |
| n-Butane | 22.05 | P4 |
| 2-Butene (E) | 23.2 | O4.3 |
| 2-Butene (Z) | 24.5 | O4.4 |
| 3-Methyl-1-butene | 27.9 | O5.1 |
| 2-Methyl-butane | 29.7 | O5.2 |
| 1-Pentene | 31.15 | O5.3 |
| 3-Methyl-butene | 31.85 | O5.4 |
| n-Pentane | 32.32 | P5 |
| 2-Pentene (E) | 33.1 | O5.5 |
| 2-Pentene (Z) | 33.75 | O5.6 |
| 2-Methyl-2-butene | 34.3 | O6.1 |
| 3-Methyl-1-pentene + 4-Methyl-1-pentene | 37.8 | O6.2 |
| 2-Methyl-pentane | 38.94 | O6.3 |
| 3-Methyl-2-pentene | 39.24 | O6.4 |
| 3-Methyl-pentane | 40.26 | O6.5 |
| 2-Methyl-1-pentene | 40.66 | O6.6 |
| 1-Hexene | 40.99 | O6.7 |
| n-Hexane | 42.01 | P6 |
| 3-Methyl-2-pentene | 42.25 | O6.8 |
| 2-Hexene (E) | 42.46 | O6.9 |
| 4-Methyl-2-pentene (E) | 42.77 | O6.10 |
| 2-Hexene (Z) | 43.25 | O6.11 |

P : paraffins, O : olefins

Diesel and waxes fractions are recovered with a hot and cold traps and analyzed off-line on another gas chromatograph GC SIMDIS analyzer.

III.1.3. Catalytic data treatment and calculation

A calibration mixture with the main gases (H₂, CO, N₂, Ar, CO₂, CH₄...) is used to calibrate the different gases we will use and form during FTS. Even though the gases are delivered in Nml/min in the rig, the calculation are done in standard conditions for temperature and pressure. Therefore for the calculation the Nml/min is converted in ml/min.

N₂ is used as an inert reference gas to calculate conversions and selectivities, based on a flow rate in vs. out basis. The N₂ areas are calculated by comparing the N₂ responses before and during Fischer-Tropsch reaction with that of a calibrated N₂ response. Thus the total flow at the outlet ($F_{\text{tot,out}}$ in mL/min) of the reactor is given by:

$$\text{(Equation 33)} \quad F_{\text{tot,out}} \text{ (mL/min)} = \frac{A_{\text{N}_2,\text{in}}}{A_{\text{N}_2,\text{out}}} * F_{\text{tot,in}}$$

Where $F_{\text{tot,in}}$ (mL/min) is the total flow at the inlet of the reactor, $A_{\text{N}_2,\text{in}}$ and $A_{\text{N}_2,\text{out}}$ are respectively the area of N₂ before the reactor and the area of N₂ after the reactor calculated with the GC-TCD analysis. In our case the total flow in ($F_{\text{tot,in}}$) represents the syngas flow (H₂ + CO) and the internal standard N₂, whilst the total flow in ($F_{\text{tot,out}}$) represents the unconverted (H₂ + CO), N₂ and any other gaseous products (CH₄, CO₂, C₂ to C₉). Normally the total gas flow out should be lower than the total gas flow in, as we are making heavier product during FTS.

The flow for each of the different gases being analyzed by GC is given by the following formula:

$$\text{(Equation 34)} \quad F_{x,\text{out}} \text{ (mL/min)} = \%M_x * F_{\text{tot,out}}$$

x is a given molecule, $F_{x,\text{out}}$ and $F_{\text{tot,out}}$ are respectively the flow out for x and the total flow out. $\%M_x$ is the molar concentration of x in the flow.

The gas hourly space velocity, better known as GHSV, is defined as follows:

$$\text{(Equation 35)} \quad \text{GHSV (L. kg}_{\text{cat}}^{-1} \cdot \text{h}^{-1}) = \frac{F_{\text{in,syngas}}}{m_{\text{cat}}}$$

$F_{\text{in,syngas}}$, is the total flow of syngas (H₂ + CO + CO₂) at the reactor inlet and m_{cat} is the mass of catalyst in the reactor.

The conversion of CO (%) is given by:

$$\text{(Equation 36)} \quad \text{CO (\%)} = \frac{F_{\text{CO,in}} - F_{\text{CO,out}}}{F_{\text{CO,in}}} * 100$$

$F_{\text{CO,out}}$ and $F_{\text{CO,in}}$ are respectively the outlet CO flow and the inlet CO flow in ml/min. Hydrogen and CO₂ conversion can also be calculated using the same formula. The CO₂ conversion is only calculated when CO₂ is part or when it totally replaces the CO in the feed for the Water-Gas-Shift (WGS) experiments.

The selectivities (S_x , %) for the CO_2 and hydrocarbons gaseous products are given by the general following formula:

$$\text{(Equation 37)} \quad S_x (\%) = n * \frac{F_{x,\text{out}} - F_{x,\text{in}}}{F_{\text{CO},\text{in}} - F_{\text{CO},\text{out}}} * 100$$

x is a given molecule, $F_{x,\text{out}}$ and $F_{\text{tot},\text{out}}$ are respectively the flow out for x and the total flow out. n is the number of carbon in the molecule x . In this study we mainly focus on the selectivity calculation for CO_2 , CH_4 and $\text{C}_1\text{-C}_4$ products, the remaining products selectivity (S_{C_5+} , %) is calculated by the following expression:

$$\text{(Equation 38)} \quad S_{\text{C}_5+} = 1 - (S_{\text{CO}_2} + S_{\text{CH}_4} + S_{\text{C}_2\text{-C}_4})$$

The olefin-to-paraffin ratio is calculated by the following formula:

$$\text{(Equation 39)} \quad \text{O/P}_x = \frac{S_{x,\text{olefin}}}{S_{x,\text{paraffin}}}$$

$S_{x,\text{olefin}}$ is the olefin selectivity and $S_{x,\text{paraffin}}$ is the paraffin selectivity for component x .

The catalytic activities, expressed as iron time yield (FTY, in mol of CO converted to hydrocarbons per gram of catalyst per second) is calculated by the following formula:

$$\text{(Equation 40)} \quad \text{FTY (mol. g}_{\text{cat}}^{-1} * \text{s}^{-1}) = \frac{F_{\text{CO},\text{in}} - F_{\text{CO},\text{out}}}{V_m * m_{\text{cat}}}$$

V_m is the molar volume (L/mol), the volume occupied by one mole of a substance at a given temperature and pressure and m_{cat} the mass (g) of catalyst in the reactor. The FTY will be expressed as $\mu\text{mol}_{\text{CO}}.\text{g}_{\text{cat}}^{-1}.\text{s}^{-1}$. This formula can be extended to mole of CO converted to hydrocarbons per gram of Fe and mole of CO converted to hydrocarbons per gram of Fe at the surface of particles per second:

$$\text{(Equation 41)} \quad \text{FTY (mol. g}_{\text{fe}}^{-1} * \text{s}^{-1}) = \frac{F_{\text{CO},\text{in}} - F_{\text{CO},\text{out}}}{V_m * m_{\text{fe}}}$$

$$\text{(Equation 42)} \quad \text{FTY (mol. g}_{\text{fe,surface}}^{-1} * \text{s}^{-1}) = \frac{F_{\text{CO},\text{in}} - F_{\text{CO},\text{out}}}{V_m * m_{\text{fe,surface}}}$$

The site time yield (STY) was calculated with the following formulas:

$$\text{(Equation 43)} \quad \text{STY (s}^{-1}) = \frac{\text{FTY}}{n_{\text{fe,surf}}} = \frac{\frac{F_{\text{CO},\text{in}} - F_{\text{CO},\text{out}}}{V_m * m_{\text{cat}}}}{n_{\text{fe,surf}}}$$

With iron time yield FTY in $\text{mol}_{\text{CO}} \cdot \text{g}_{\text{cat}}^{-1} \cdot \text{s}^{-1}$ and $n_{\text{Fe,surf}}$, the number of mol of iron at the surface of a particle per gram of catalyst ($\text{mol}_{\text{CO}} \cdot \text{g}_{\text{cat}}^{-1}$). $n_{\text{Fe,surf}}$ was calculated with the following formula:

$$\text{(Equation 44)} \quad n_{\text{Fe,surf}} \text{ (mol.g}_{\text{cat}}^{-1}\text{)} = \frac{N_{\text{Fe,surf}}}{N_{\text{a}}} = \frac{N_{\text{Fe,tot}} \cdot D}{N_{\text{a}}}$$

$N_{\text{Fe,surf}}$ is the total number of iron atom at the surface of a particle per gram of catalyst ($\text{g}_{\text{cat}}^{-1}$), $N_{\text{Fe,tot}}$ is the total number of iron atom in a particle per gram of catalyst, N_{a} is Avogadro's constant (mol^{-1}) and D is the particle dispersion (%).

III.2. Water-gas-shift testing setup

The global scheme of the experimental Water-gas-shift setup is represented in the following figure (Figure 41):

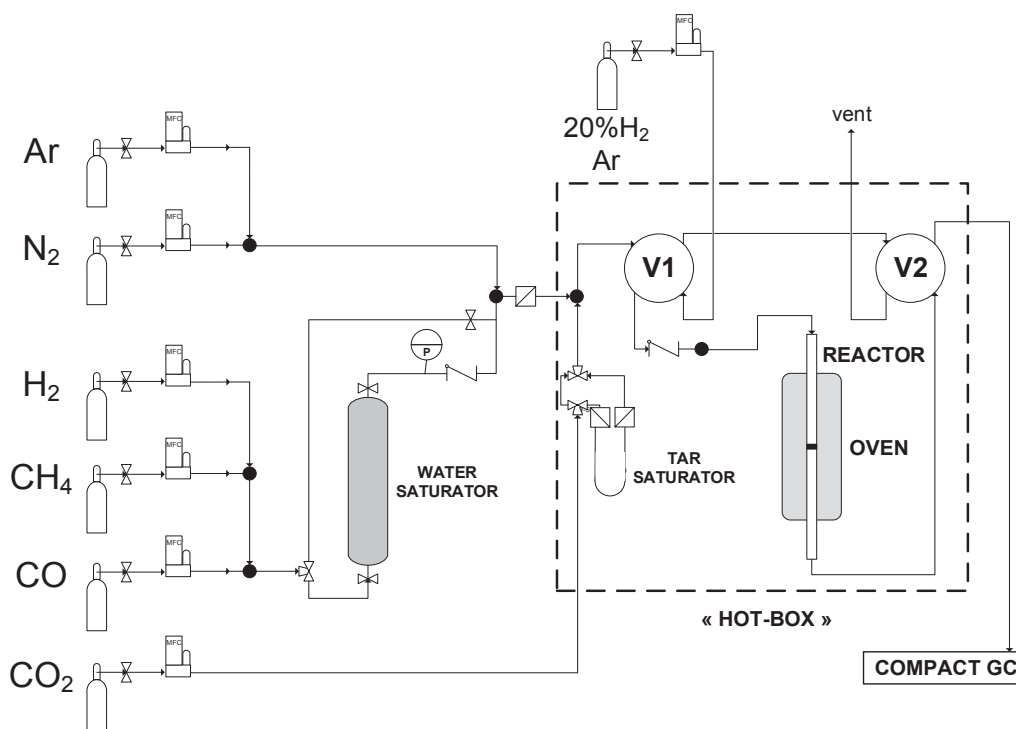
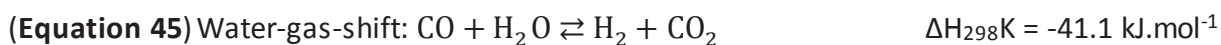


Figure 41 | Experimental setup for the water-gas-shift analysis tests.

This setup permits to get information on the water-gas-shift activity of a catalyst. To evaluate its capacity to produce CO_2 . The water-gas-shift reaction is indicated below:



A few mg of the catalyst is typically placed in a 4 mm ID fixed-bed continuous-flow quartz reactor. The catalyst is studied at 2.2 bar with a mixture of $\text{H}_2\text{O}/\text{CO}$ with a ratio of 1:2. N_2 was

is added in the feed as internal standard. Water was added to the feed via a water saturator. The flow of CO passes through the saturator and take the water to the reactor. The water-gas-shift reaction can be studied at various temperature within a range of 230 °C to 450 °C. A compact GC is installed at the outlet. Gases such as H₂, CO, N₂ and CO₂ can be analyzed and quantify.

III.3. Labelled ¹³CO₂ MS and GC-MS experimental setup

A simplified scheme of the experimental setup for labelled ¹³CO₂ experiments is represented in the following figure (Figure 36).

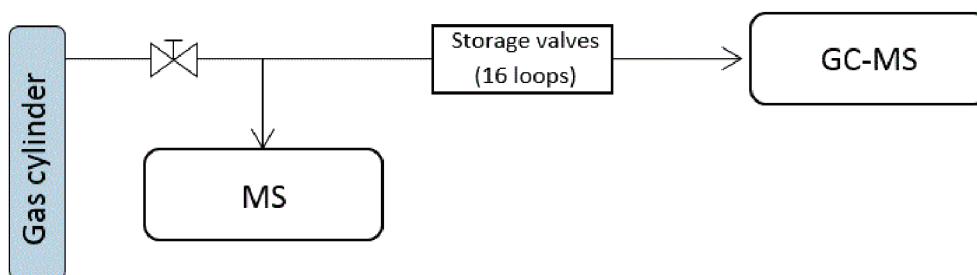


Figure 42 | Simplified experimental setup for the labelled ¹³CO₂ analysis by MS and GC-MS.

An empty cylinder is connected at the outlet of the Fischer-Tropsch setup presented earlier. The Fischer-Tropsch reaction is carried out at 20 bar pressure with a H₂:CO:¹²CO₂ ratio of 2:0.8:0.2 with a GHSV of 1.3 L.g_{cat}⁻¹.h⁻¹ syngas (H₂, CO, CO₂). The temperature of operation is ramped up to 250 °C and later on to 280 °C during the test. Argon (Ar) is used as an internal standard as the mass of N₂ is the same as of CO (m/z = 28), therefore differentiating the two with the mass spectrometer would be impossible. The reaction was carried on for 24 h under these conditions. Then, ¹³CO₂ was introduced in the reactor in place of the ¹²CO₂. The reactor was flushed for 2 h with the H₂/CO/¹³CO₂ mixture, to be sure all the ¹²CO₂ is replaced. The outlet gas mixture (reactants and products) are captured in the cylinder. The cylinder is then moved and connected to another setup where a MS and GC-MS are present. The cylinder is opened and the captured gas flowed into the setup. A storage valves is used to store the gas before being analysed one by one. The mass spectrometer is used to follow the ¹²CO, ¹³CO, ¹²CO₂, ¹³CO₂, ¹²CH₄ and ¹³CH₄. A GC-MS is also used to first separate the different products and then analyze them by MS. Labeled C₂, C₃ and C₄ were analyzed by this technique.

Chapter 3 - Characterization of iron-based catalysts

| | |
|--|------------|
| Chapter 3 - Characterization of iron-based catalysts..... | 71 |
| Introduction | 73 |
| I. Characterization of a state of the art catalyst: Commercial catalyst | 75 |
| I.1. Study of the commercial catalyst before FTS | 75 |
| I.1.1. Transmission electron microscopy (TEM) | 75 |
| I.1.2. Powder X-ray diffraction (XRD)..... | 75 |
| I.1.3. Magnetism analysis..... | 76 |
| I.1.4. Iron phases determination by ⁵⁷ Fe Mössbauer spectroscopy..... | 77 |
| I.2. Study of the commercial catalyst after FTS | 78 |
| I.2.1. Transmission electron microscopy (TEM) | 78 |
| I.2.2. Iron phases determination by powder X-ray diffraction (XRD)..... | 79 |
| I.2.4. Magnetism analysis..... | 80 |
| I.2.3. Iron phases determination by ⁵⁷ Fe Mössbauer spectroscopy..... | 81 |
| Conclusion..... | 83 |
| II. Characterization of a Fe@hollow-silicalite-1 catalyst..... | 84 |
| II.1. Preparation of Fe@hollow-silicalite-1 catalyst..... | 84 |
| II.1.1 Post-impregnation of hollow-silicalite-1 | 84 |
| II.1.2. Impregnation followed by the formation of the hollow-silicalite-1..... | 85 |
| II.1.3. Control of the loading of iron in hollow-silicalite-1..... | 87 |
| II.1.4. Promoters addition to the iron in hollow-silicalite-1..... | 87 |
| II.2. Study of the Fe@hollow-silicalite-1 before FTS | 88 |
| II.2.1. High resolution transmission electron microscopy and tomography | 88 |
| II.2.2. Nitrogen adsorption/desorption isotherms | 90 |
| II.2.3. Powder X-ray diffraction (XRD)..... | 91 |
| II.2.4. Iron phases determination by ⁵⁷ Fe Mössbauer spectroscopy..... | 92 |
| II.3. Study of the Fe@hollow-silicalite-1 during FTS..... | 96 |
| II.3.1. Iron phases determination by <i>in-situ</i> XRD and <i>in-situ</i> Xanes..... | 96 |
| a. Iron phases determination by <i>in-situ</i> XRD | 96 |
| b. Iron phases determination by <i>in-situ</i> Xanes..... | 97 |
| II.3.2. Iron phases determination by <i>in-situ</i> ⁵⁷ Fe Mössbauer spectroscopy..... | 98 |
| II.4. Study of the Fe@hollow-silicalite-1 after FTS..... | 101 |
| II.4.1. Transmission electron microscopy (TEM) | 101 |
| II.4.2. Iron phases determination by XRD..... | 102 |
| II.4.3. Iron phases determination by ⁵⁷ Fe Mössbauer spectroscopy..... | 102 |
| Conclusion..... | 106 |
| III. Characterization of a Fe/hollow-silicalite-1 catalyst..... | 108 |
| III.1. Study of the Fe/hollow-silicalite-1catalyst before FTS..... | 109 |

| | |
|---|------------|
| III.1.1. Transmission electron microscopy (TEM) | 109 |
| III.1.2. Powder X-ray diffraction (XRD)..... | 109 |
| III.1.3. Iron phases determination by ⁵⁷ Fe Mössbauer spectroscopy..... | 110 |
| III.2. Study of the Fe/hollow-silicalite-1catalyst after FTS..... | 114 |
| III.2.1. Transmission electron microscopy (TEM) | 114 |
| III.2.2. Powder X-ray diffraction (XRD)..... | 114 |
| III.2.3. Iron phases determination by ⁵⁷ Fe Mössbauer spectroscopy..... | 115 |
| Conclusion..... | 118 |
| IV. Characterization of a Fe/SiO₂ catalyst..... | 119 |
| IV.1. Study of the Fe/SiO ₂ catalyst before FTS..... | 119 |
| IV.1.1. Transmission electron microscopy (TEM)..... | 119 |
| IV.1.2. Powder X-ray diffraction (XRD)..... | 120 |
| IV.1.3. Iron phases determination by ⁵⁷ Fe Mössbauer spectroscopy | 121 |
| IV.2. Study of the Fe/SiO ₂ catalyst post FTS..... | 122 |
| IV.2.1. Transmission electron microscopy (TEM)..... | 122 |
| IV.1.3. Powder X-ray diffraction (XRD)..... | 123 |
| IV.2.4. Iron phases determination by ⁵⁷ Fe Mössbauer spectroscopy | 124 |
| Conclusion..... | 125 |
| V. Characterization of a nano-structured α-Fe₂O₃ catalyst..... | 127 |
| V.1. Preparation of nano-structured α-Fe ₂ O ₃ catalyst..... | 127 |
| V.1.1. Preparation of SBA-15 support..... | 127 |
| V.1.2. Preparation of nanostructured α-Fe ₂ O ₃ | 127 |
| V.2. Study of the nano-structured α-Fe ₂ O ₃ catalyst before FTS..... | 128 |
| V.2.1. Transmission electron microscopy (TEM) | 128 |
| V.2.2. Powder X-ray diffraction (XRD)..... | 129 |
| V.2.3. Iron phases determination by ⁵⁷ Fe Mössbauer spectroscopy | 130 |
| V.3. Study of the nano-structured α-Fe ₂ O ₃ catalyst during FTS..... | 131 |
| V.3.1. Iron phases determination by <i>in-situ</i> XRD..... | 131 |
| V.3.2. Iron phases evolution by <i>in-situ</i> XANES | 132 |
| V.4. Study of the nano-structured α-Fe ₂ O ₃ catalyst after FTS | 133 |
| V.4.1. Transmission electron microscopy after FTS..... | 133 |
| V.4.2. Determination of iron phases after FTS by <i>ex-situ</i> XRD | 133 |
| V.4.3. Iron phases determination by ⁵⁷ Fe Mössbauer spectroscopy | 134 |
| Conclusion..... | 139 |
| Conclusion | 140 |

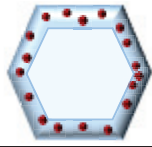


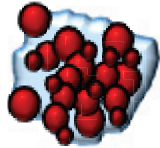
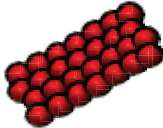
Introduction

This chapter deals with the characterization of a well-controlled iron-based catalyst. In addition, several iron-based catalysts will be characterized for comparison and better understanding.

A well-controlled iron catalyst was synthesized to understand the Fischer-Tropsch catalysis behavior of iron-based catalyst. The preparation of this iron-based model catalyst was adapted from a previous study from Li [114]. In this work, the concept of noble metal nanoparticles encapsulated in a single-crystal hollow zeolite shell developed by Li et al. [115–117] has been extended to iron nanoparticles. The zeolite shell protects the nanoparticles from sintering during Fischer-Tropsch synthesis. Morphology and particles size distribution are estimated by the mean of transmission electron microscopy. Dispersion of iron in the catalyst is derived from the particles size distribution using the method from Van Hardeveld and Hartog [113]. The iron phases are characterized by various techniques such as Mössbauer spectroscopy, X-ray diffraction and in-situ X-ray absorption near-edge structure spectroscopy. The objective is to understand the relationship between the structural features of this model catalyst and its Fischer-Tropsch catalytic performances.

To facilitate the understanding of the behavior of the well-controlled iron catalyst, several other iron-based catalysts will be used for comparison and better understanding. A commercial co-precipitate catalyst will be used as a benchmark catalyst. Other iron-based catalyst derived from the well-controlled catalyst will be investigated. More exactly, the well-controlled iron catalyst developed in this study will be denoted “**Fe@hollow-silicalite-1**”, with @ meaning “encapsulated in”. The iron catalyst derived from the well-controlled iron catalyst will be denoted as “**Fe/hollow-silicalite-1**”, with / standing for “supported on”. A classical iron supported on silica catalyst, denoted **Fe/SiO₂**, will be investigated. Two bulk-type catalysts are also proposed in this study, a benchmark catalyst denoted “**commercial catalyst**” and a nanostructured iron catalyst denoted as “**nanostructured α -Fe₂O₃ catalyst**”. All five catalysts will be studied and extensively characterized one after another.

Table 10 | Names and types of iron-based catalyst studied in this work

| Supported or encapsulated-type catalyst | |
|---|--|
|  | Fe@hollow-silicalite-1 catalyst |
|  | Fe/hollow-silicalite-1 catalyst |
|  | Fe/SiO ₂ catalyst |
| Bulk-type catalyst | |
|  | Commercial/benchmark catalyst (co-precipitated) |
|  | Nanostructured α -Fe ₂ O ₃ catalyst (well-ordered bulk catalyst) |

The first part of this chapter focuses on the iron commercial catalyst. It will help to fully understand the complexity and difficulty of characterizing properly a typical iron catalyst. Then, the encapsulated catalyst (Fe@hollow-silicalite-1) and the two iron supported catalysts (Fe/hollow-silicalite-1 and Fe/SiO₂) will be investigated. Lastly, the bulk nanostructured α -Fe₂O₃ catalyst, similar to the commercial catalyst, will be studied. A summary table is displayed at the end of the chapter for better comparison of all catalysts.

I. Characterization of a state of the art catalyst: Commercial catalyst

A commercial iron catalyst provided by our partner Johnson Matthey (JM) was chosen as the State of the Art catalyst (SoA). This co-precipitated catalyst contains 78.4 % Fe_2O_3 , 3.4 % CuO , 2.6 % K_2O , 0.04 % Na_2O and 15 % SiO_2 . The commercial catalyst is used as a benchmark catalyst in this study regarding Fischer-Tropsch performances.

I.1. Study of the commercial catalyst before FTS

I.1.1. Transmission electron microscopy (TEM)

The commercial catalyst transmission electron microscopy (TEM) images were taken with a Jeol 2010 LaB6 microscope. The images are shown in **Figure 43**.

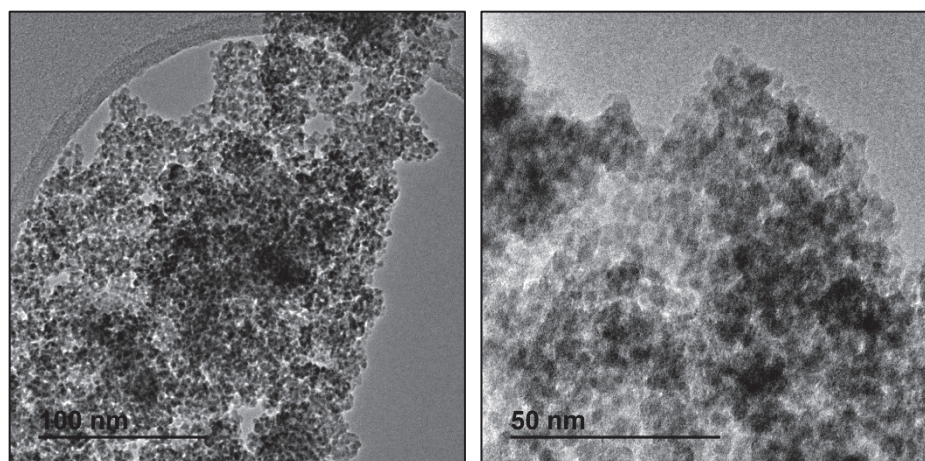


Figure 43 | TEM images of the commercial catalyst.

The commercial catalyst is a co-precipitated catalyst. We mainly observed what we can call iron bulk. It is difficult to distinguish particles with TEM images. Therefore determining a particle size distribution and thus a dispersion is impossible. When taking what looks like a particle at the surface of the bulk, a size between 2 to 5 nm is obtained. However these values are not representative of the overall sample. Other techniques (like XRD and magnetism) might be better for the determination of the dispersion.

I.1.2. Powder X-ray diffraction (XRD)

X-ray diffraction (XRD) patterns of the solid were recorded on a Bruker (Siemens) D5005 diffractometer using $\text{CuK}\alpha$ radiation. Diffraction patterns were collected between 4 and 80° (2θ) with steps of 0.02° and 1 s per step. The X-ray diffraction pattern of the commercial catalyst is displayed on **Figure 44**.

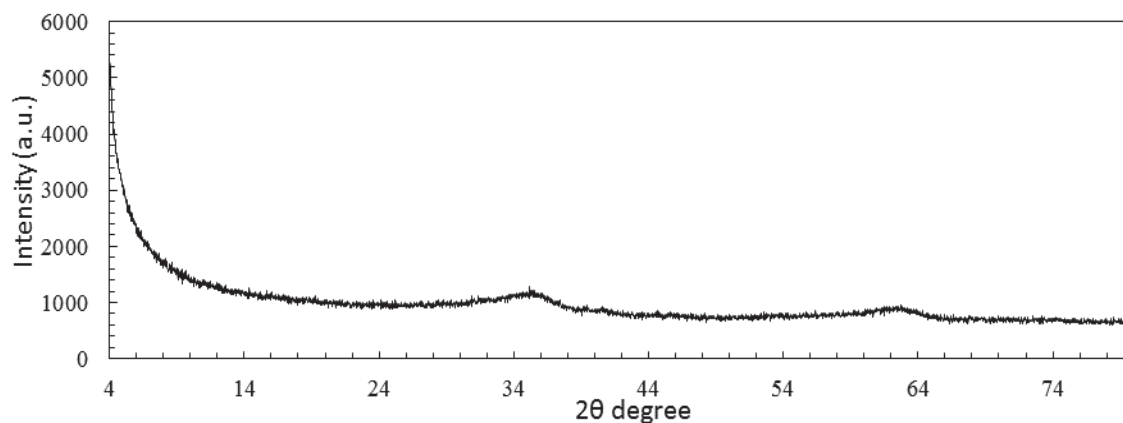


Figure 44 | X-ray diffraction spectrum of the commercial catalyst.

The XRD analysis of the commercial catalyst shows that the commercial catalyst is not crystallized. Again XRD is not useful for the calculation of the dispersion.

I.1.3. Magnetism analysis

Magnetism analysis have been performed on the commercial catalyst. The description of the technique is indicated in **Chapter 2 - Experimental procedure - Magnetic measurements**. The magnetic curve of the commercial catalyst is shown in **Figure 45**. When referring to the state of the art review presented in the previous chapter. It can be concluded clearly that the commercial catalyst has a paramagnetic magnetism behavior as the magnetic curve is a straight line. In other word, the M vs H curve does not saturate at high field. No hysteresis is observed.

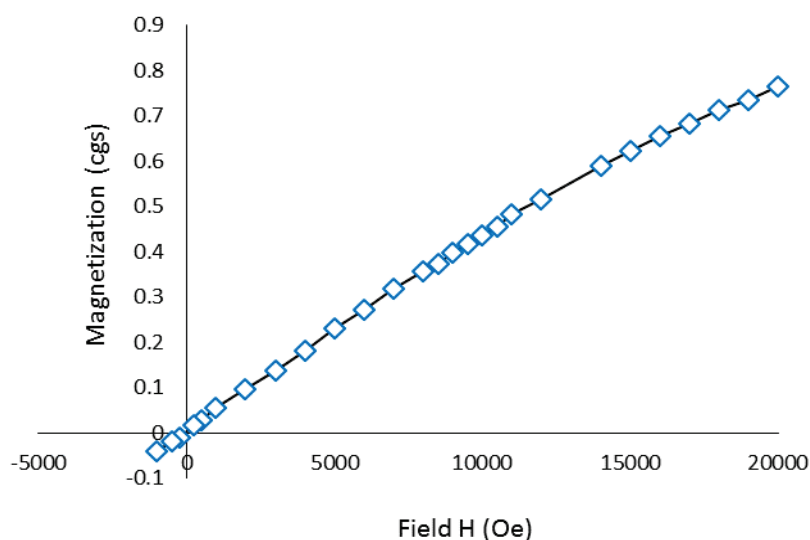


Figure 45 | Magnetic curve of the commercial catalyst.

Therefore, no ferromagnetic material is present in the sample. Consequently, calculating particles size with Langevin's equation is also not possible.

I.1.4. Iron phases determination by ^{57}Fe Mössbauer spectroscopy

Mössbauer spectroscopy was applied at room temperature to gain insight into the nature of the iron species present in the commercial catalyst. This technique permits to complete the observation made with X-Ray diffraction spectroscopy and to acquire full knowledge of the fresh catalyst before the Fischer-Tropsch reaction. The Mössbauer spectrum is given in **Figure 46** and the Mössbauer parameters (Isomeric shift (IS, $\text{mm}\cdot\text{s}^{-1}$), quadrupolar splitting (QS, $\text{mm}\cdot\text{s}^{-1}$), hyperfine field (T) and relative intensity (%)) calculated from its fit are given in **Table 11**.

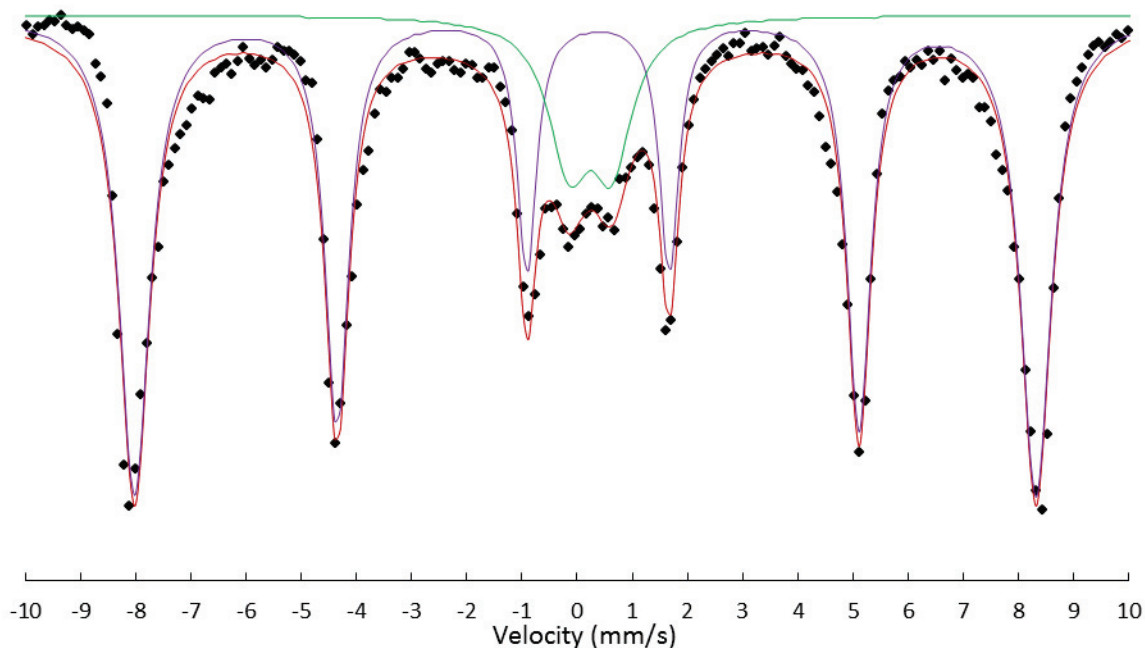


Figure 46 | ^{57}Fe Mössbauer spectrum of the fresh commercial catalyst: Experimental spectrum (black dot), experimental spectrum fit (red line), Fe_2O_3 (green line and purple line).

Two components can be distinguished in the spectrum for the fresh iron commercial catalyst: a magnetic sextet characterized by a magnetic field of 50.5 T (relative intensity 82 %) and a quadrupolar hyperfine doublet with a quadrupolar splitting $\text{QS} = 0.78 \text{ mm}\cdot\text{s}^{-1}$ (relative intensity 18 %). The isomer shifts of these two components are similar $\text{IS} = 0.33 \text{ mm}\cdot\text{s}^{-1}$ and $\text{IS} = 0.35 \text{ mm}\cdot\text{s}^{-1}$, which allows assigning these spectra to Fe^{3+} .

Table 11 | The Mössbauer fitted parameters for the fresh commercial catalyst

| Sample | Splitting | IS (mm.s ⁻¹) | QS (mm.s ⁻¹) | Hyperfine field (T) | Species | Relative intensity (%) |
|------------------------|-----------|-----------------------------|-----------------------------|------------------------|--------------------------------|---------------------------|
| Commercial catalyst | Sextet | 0.35 | -0.23 | 50.5 | Fe ₂ O ₃ | 82 |
| | Doublet | 0.33 | 0.78 | - | Fe ₂ O ₃ | 18 |

The sextet can be attributed without ambiguity to antiferromagnetic hematite α -Fe₂O₃ in relatively large particles (bigger than about 30 nm) [19]. The doublet with an isomeric shift of 0.78 mm.s⁻¹ is also attributed to α -Fe₂O₃ but under the form a small superparamagnetic oxide [19]. The fresh catalyst is thus only composed of one iron phase, α -Fe₂O₃. The spectrum is not perfectly fitted. As a matter of fact it could have been fitted with a distribution of sextets rather than only one sextet. This distribution would arise from a relatively wide range of particles size. Nevertheless, the interpretation would not have changed.

I.2. Study of the commercial catalyst after FTS

I.2.1. Transmission electron microscopy (TEM)

TEM images taken with the Jeol 2010 LaB6 microscope of the spent commercial catalyst are shown in **Figure 47**. After FTS testing, the spent catalyst was recovered from the reactor. Therefore, the spent catalyst was in contact with air, meaning that the catalyst most likely re-oxidized partially with the oxygen.

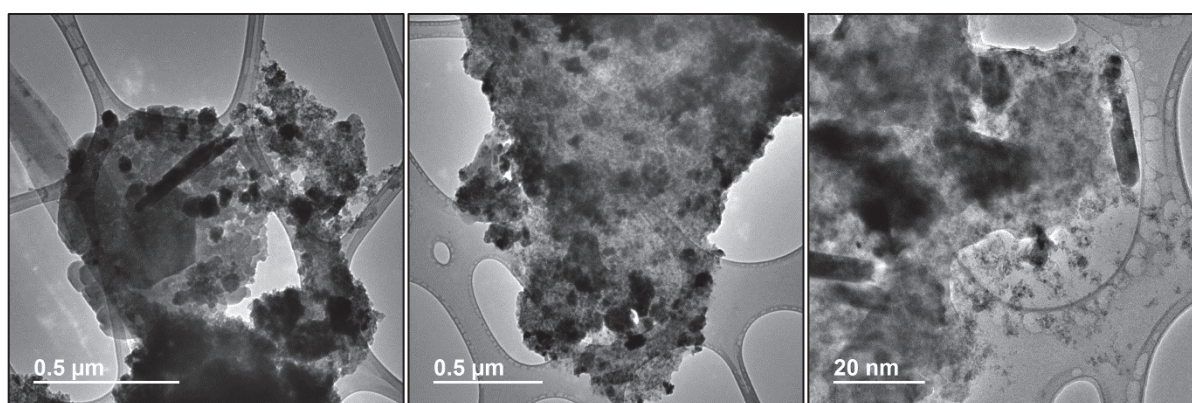


Figure 47 | TEM images of the commercial catalyst after FTS.

The commercial catalyst is strongly modified during the Fischer-Tropsch synthesis: the iron has sintered in large particles, and the structure seems more chaotic. Again, determining the

average particle size and dispersion of the commercial catalyst after Fischer-Tropsch is relatively complex.

I.2.2. Iron phases determination by powder X-ray diffraction (XRD)

The X-ray diffraction pattern of the spent commercial catalyst at 250 °C and 280 °C after 100 hours on stream are displayed respectively on **Figure 48** and **Figure 49**.

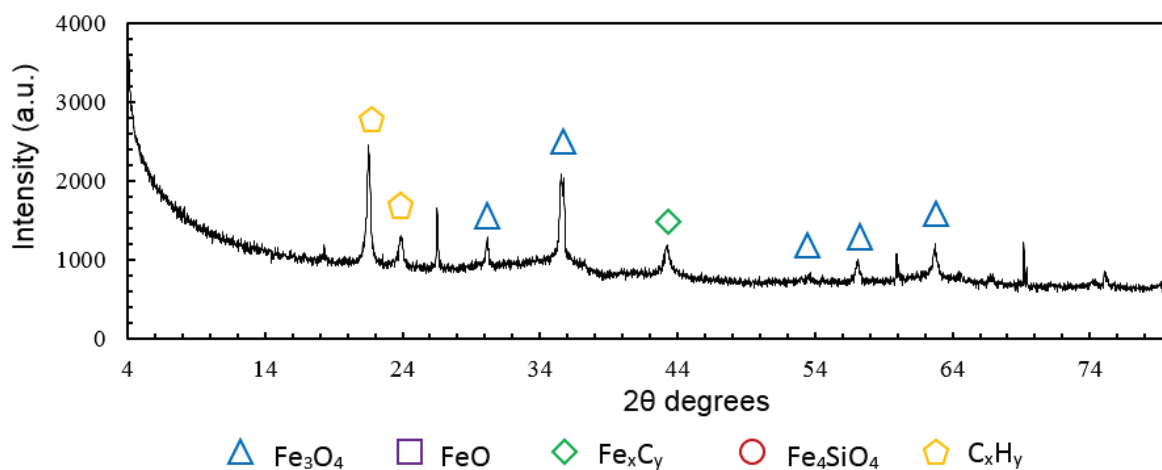


Figure 48 | X-ray diffraction spectrum of the spent commercial catalyst after FTS at 250 °C.

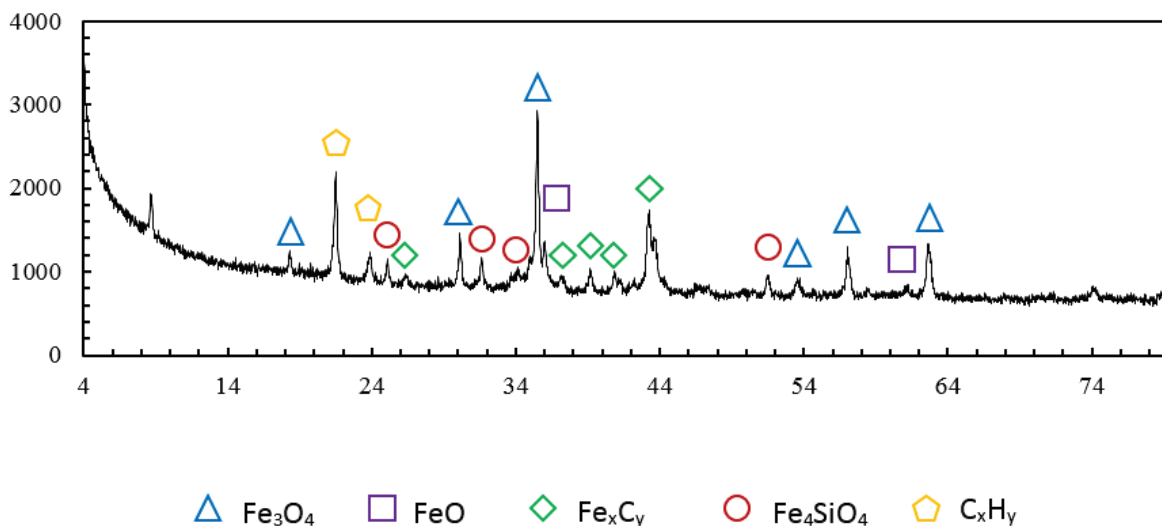


Figure 49 | X-ray diffraction spectrum of the spent commercial catalyst after FTS at 280 °C.

The phases obtained after Fischer-Tropsch are similar for both reaction temperatures, we mainly have magnetite (Fe_3O_4) and carbides (Fe_xC_y), yet at higher temperature small amounts

of ferrous oxide or wüstite (FeO) and iron silicate (Fe_4SiO_4) are identified. The commercial catalyst after Fischer-Tropsch reaction is a huge mixture of different iron phases. Therefore it makes its understanding and the establishment of structure-to-activity relationship quite challenging. This time the iron catalyst is crystallized, consequently, using the Debye-Scherrer equation to determine the particles size is possible (**Chapter 2 - Experimental procedure - II.1. Powder X-ray Diffraction (XRD)**). Following the Debye-Scherrer equation the average particle size based on the Fe_3O_4 peaks can be estimated. An average value of 24.6 nm is obtained, and using the handbook dispersion equation (**Chapter 2 - Experimental procedure - II.4.4. Study of nano-particles with TEM**) a dispersion around 4.7 % for the test performed at 280 °C can be derived.

I.2.4. Magnetism analysis

Magnetism analysis has been performed on the spent commercial catalyst. The description of the technique is given in **Chapter 2 - Experimental procedure - Magnetic measurements**. The magnetic curve of the commercial catalyst is shown in **Figure 50**. When referring to the state of the art presented in the previous chapter it can be clearly stated that the spent commercial catalyst has a ferromagnetic magnetism behavior.

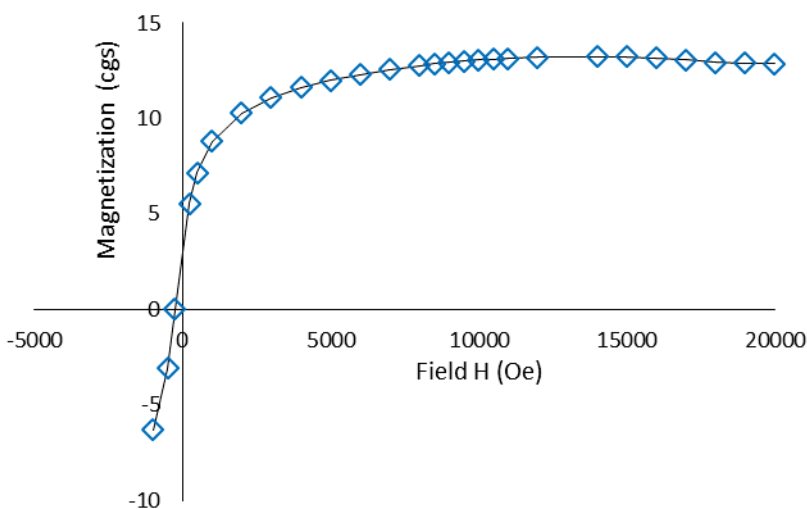


Figure 50 | Magnetic curve of the spent commercial catalyst.

The saturation magnetization (M_s), the remanent magnetization (M_r), the amount of ferromagnetic material in the sample, as well as the particle size diameter of small and large particles (respectively D_2 and D_1) can be calculated following the different formulas indicated

in **Chapter 2 - Experimental procedure - Magnetic measurements**. The different value are indicated in **Table 12**. It can be clearly seen that the catalyst became quite ferromagnetic during the Fischer-Tropsch synthesis (31 %).

Table 12 | The magnetism parameters for the spent commercial catalyst

| Sample | Ms (cgs) | Mr (cgs) | 2Mr/Ms (%) | D ₁ (nm) | D ₂ (nm) |
|-------------------------------|----------|----------|------------|---------------------|---------------------|
| Commercial catalyst after FTS | 13.7 | 2.1 | 31.1 | 129.3 | 5.0 |

I.2.3. Iron phases determination by ⁵⁷Fe Mössbauer spectroscopy

Mössbauer spectroscopy was applied at room temperature to gain insight into the nature of the iron species present in the commercial catalyst. This technique permits to complete the observation made with X-Ray diffraction spectroscopy and to acquire a quantification of the phases present in the spent catalyst after the Fischer-Tropsch reaction. After FTS testing, the spent catalyst was recovered from the reactor. Therefore, the spent catalyst was in contact with air, meaning that the catalyst most likely re-oxidized partially with the oxygen. The catalyst Mössbauer spectrum was taken after 100 hours on stream at 280 °C. The Mössbauer spectrum is given in **Figure 51** and the calculated hyperfine parameters are given on **Table 13**.

Seven components can be distinguished for the spent iron commercial catalyst after Fischer-Tropsch reaction at 280 °C. The Mössbauer spectrum is characterized by five well-defined magnetic sextets. Two of them are characterized by magnetic fields of 48.3 T and 45.1 T. (respective relative intensity 10 and 19 %) and are attributed to magnetite (Fe₃O₄) in relatively large particles [44]. The three other sextets with magnetic fields of 10.0, 18.3 and 22.0 T (respective relative intensity 9 , 8 and 11 %) are attributed to Hägg carbides (Fe₅C₂) [70, 118]. The spectrum is also characterized by two doublets with IS = 0.37 mm.s⁻¹ QS = 0.85 mm.s⁻¹ (relative intensity 29 %) and with IS = 1.12mm.s⁻¹, QS = 2.72 mm.s⁻¹ (relative intensity 14 %) can respectively be attributed to ferric (Fe³⁺) and ferrous (Fe²⁺) cations but it is not possible to make definitive assignments as to the exact nature of the species [44, 119], to do that we would need to carry out the Mössbauer analysis at low temperature.

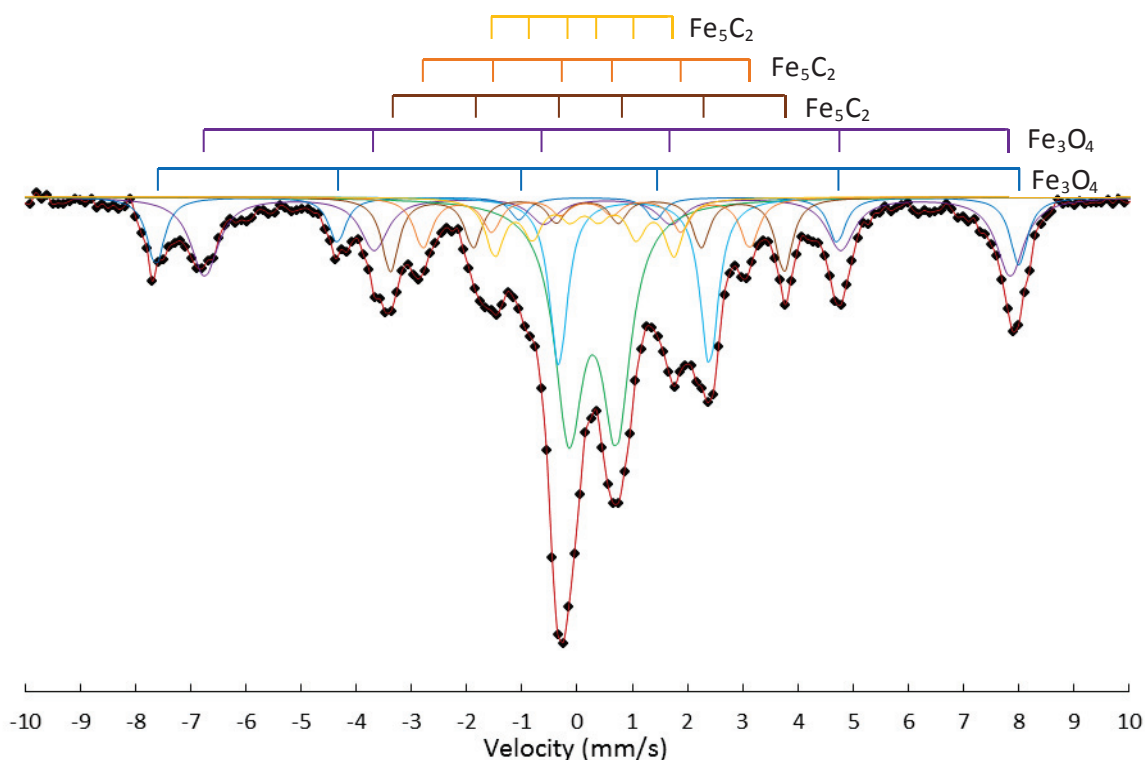


Figure 51 | ^{57}Fe Mössbauer spectrum of the commercial catalyst: Experimental spectrum (black dot), experimental spectrum fit (red line), Fe_3O_4 in large particles (blue line and purple line), Fe^{3+} (green line), Fe^{2+} (light blue line) and Fe_5C_2 carbides (brown, orange and yellow line).

However they could correspond to the phase Fe_{1-x}O detected by XRD. In comparison with the fresh catalyst, where only one iron phase was present, the $\alpha\text{-Fe}_2\text{O}_3$ oxides, the spent catalyst presents various iron phases (oxides and carbides) revealing the huge difficulty to understand the behavior of iron during Fischer-Tropsch synthesis and to determine the exact role of each phases for the establishment of a relationship between structure and activity.

Table 13 | The Mössbauer fitted parameters for the spent commercial catalyst

| Sample | Splitting | IS ($\text{mm}\cdot\text{s}^{-1}$) | QS ($\text{mm}\cdot\text{s}^{-1}$) | Hyperfine field (T) | Species | Relative intensity (%) |
|---|-----------|---|---|------------------------|-------------------------|---------------------------|
| Commercial catalyst after FTS at 280°C | Sextet | 0.27 | 0.04 | 48.3 | Fe_3O_4 | 10 |
| | Sextet | 0.64 | 0.01 | 45.1 | Fe_3O_4 | 19 |
| | Doublet | 0.37 | 0.85 | - | Fe^{3+} | 29 |
| | Doublet | 1.12 | 2.72 | - | Fe^{2+} | 14 |
| | Sextet | 0.22 | 0.00 | 10.0 | Fe_5C_2 | 9 |
| | Sextet | 0.25 | 0.00 | 18.3 | Fe_5C_2 | 8 |
| | Sextet | 0.27 | 0.00 | 22.0 | Fe_5C_2 | 11 |

Conclusion

The co-precipitated iron commercial catalyst is mainly composed of iron oxide (78.4 %) even though some silica (15 %) is present. This bulk-type catalyst is particularly hard to characterize properly. No particle size distribution or dispersion could be calculated for the fresh catalyst due to hardly identifiable particles with TEM analysis. XRD proved to be useless as well because the material is non-crystallized. However, Mössbauer confirmed the existence of iron in the form of α -Fe₂O₃. During Fischer-Tropsch synthesis the co-precipitated iron commercial catalyst structure is completely transformed. Mössbauer spectroscopy and X-ray diffraction confirm the existence of several iron species as oxides (Fe₃O₄, FeO and Fe₂O₃, 72 % in contribution) and carbides (Fe₅C₂, 28 % in contribution). Also, as the catalyst become crystalline, XRD is used to determine the particle size distribution and the dispersion using Debye-Scherrer equation. **Table 14** summarizes the essential information gained regarding the commercial catalyst.

Table 14 | Commercial catalyst information

| | Fresh catalyst | | | Spent catalyst | | |
|--------------------------|--------------------|----------------|--|--------------------|----------------|--|
| | Particle size (nm) | Dispersion (%) | Fe species | Particle size (nm) | Dispersion (%) | Fe species |
| TEM | - | - | - | - | - | - |
| Ex-situ XRD | - | - | - | 24.6 | 4.7 | Fe ₃ O ₄ , Fe ₅ C ₂ , FeO |
| Ex-situ Mössbauer | - | - | α-Fe₂O₃ | - | - | Fe ₃ O ₄ , Fe ₂ O ₃ , Fe ₅ C ₂ , Fe³⁺ , Fe ²⁺ |
| Magnetism | - | - | Paramagnetic phases | - | - | Ferromagnetic phases |

For ex-situ mössbauer: iron species in bold are in majority in the sample, iron species not in bold are in minority in the sample.

II. Characterization of a Fe@hollow-silicalite-1 catalyst

This part focuses on our own catalyst developed here at IRCElyon. The synthesis procedure by dissolution-recrystallization explained in **Chapter 2 - Experimental procedure - I.3. Preparation of Fe@hollow-silicalite-1** was used to develop a model iron catalyst called Fe@hollow-silicalite-1 catalyst. This new catalyst will be first characterized by various techniques such as Transmission electron microscopy, X-ray diffraction and Mössbauer spectroscopy to have an overall understanding of the fresh catalyst. The second part will focus on the study of the phase transformation during the Fischer-Tropsch synthesis by *in-situ* XRD, *in-situ* Xanes and *in-situ* Mössbauer. Finally the spent catalyst will be characterized.

II.1. Preparation of Fe@hollow-silicalite-1 catalyst

II.1.1 Post-impregnation of hollow-silicalite-1

1 g of hollow-silicalite-1 (**Chapter 2 - Experimental procedure - I.3. Preparation of Fe@hollow-1**) is impregnated with 1 ml of a 5 %wt Fe aqueous solution followed by a calcination in air at 550 °C for 4 h and a reduction under H₂ at 750 °C for 3 h. TEM images taken with the Jeol 2010 LaB6 microscope of Fe@hollow-silicalite-1 are shown in **Figure 52**. It can clearly be seen that the hollow-silicalite-1 is empty, no Fe is located inside. Instead huge Fe particles can be found outside the zeolite. The post-impregnation of the hollow-silicalite-1 did not work even after several trials. The post-impregnation method is therefore not further studied.

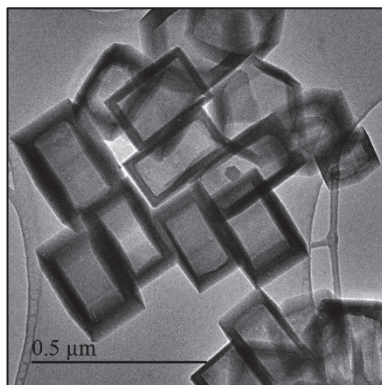


Figure 52 | TEM images of Fe@hollow-silicalite-1 synthesized by post-impregnation.

II.1.2. Impregnation followed by the formation of the hollow-silicalite-1

Another synthesis method is used to prepare the Fe@hollow-silicalite-1, as post-impregnation did not work. The synthesis method is detailed in **Chapter 2 - Experimental procedure - I.3. Preparation of Fe@hollow-silicalite-1**. Briefly silicalite-1 mono-crystals are impregnated with an aqueous Fe solution with a concentration such that the final yielding materials would give a 5 %wt Fe loading. The impregnated silicalite-1 is then treated to form the hollow-silicalite-1 followed by a calcination in air at 550 °C for 4 h and a reduction under H₂ at 750 °C for 3 h.

The synthesis proves to be more reliable and reproducible. **Figure 53** shows TEM images for three different samples (noted Fe@hollow-silicalite-1-A, -B and -C) with their respective particle size distribution. In all samples a particles size distribution between 1.5 nm to 7.5 nm with an average size of around 3.5 nm and 4.5 nm was founded, very few larges particles are observed inside and outside the zeolite.

The iron loading in these samples and the dispersion are indicated in **Table 15**, the dispersion is calculated following two different methods (**Chapter 2 - Experimental procedure - II.4.4. Study of nano-particles with TEM**). The Fe loading is in the same range for all samples. Most likely, some Fe is lost during the several washings after the dissolution-recrystallization in TPAOH as we should have obtained a loading close to 5 %wt.

Table 15 | Fe content and dispersion of several Fe@Hollow-silicalite-1 samples

| Sample | Fe loading (%wt) | Mean diameter (d _{va} , nm) | Dispersion Handbook model (%) | Dispersion Van Hardeveld and Hartog model (%) |
|---------------------------|------------------|--------------------------------------|-------------------------------|---|
| Fe@hollow-silicalite-1-A | 3.4 | 3.6 | 37.1 | 29.8 |
| Fe@hollow- silicalite-1-B | 2.5 | 4.5 | 25.8 | 24.0 |
| Fe@hollow- silicalite-1-C | 2.6 | 3.6 | 36.4 | 30.7 |

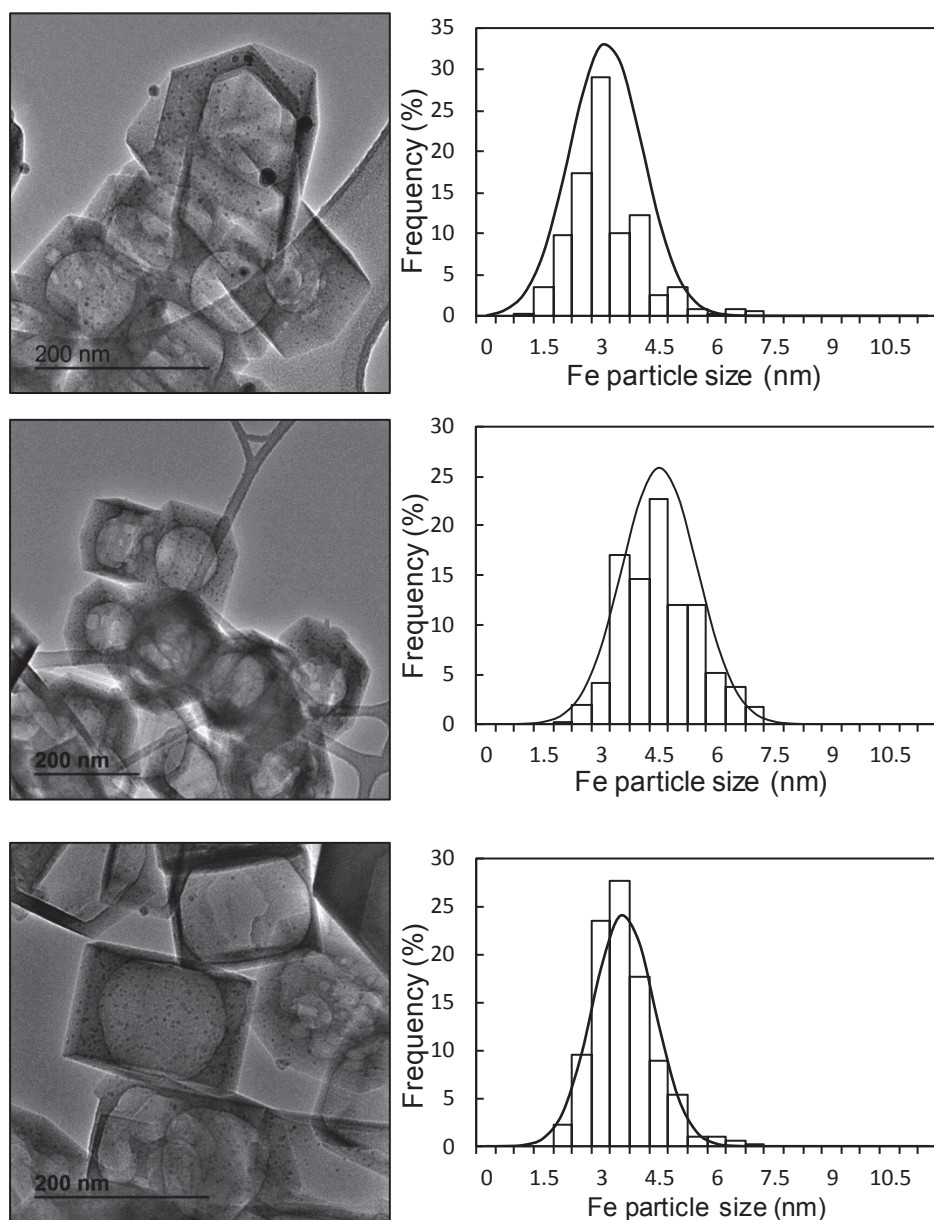


Figure 53 | TEM images and particle size distribution of Fe@hollow-silicalite-1-A (up), Fe@hollow-silicalite-1-B (middle) and Fe@hollow-silicalite-1-C (bottom).

In conclusion, the synthesis of Fe@hollow-silicalite-1 seems reproducible and reliable. Furthermore a good particles size distribution as well as a relatively high particle dispersion are obtained.

II.1.3. Control of the loading of iron in hollow-silicalite-1

In the synthesis method to prepare the Fe@hollow-silicalite-1, the bulk silicalite-1 crystal is generally impregnated with an aqueous solution with a Fe content of 5 %wt. At the end of the preparation a material with about 2.7 %wt Fe is obtained. Increasing the solution concentration to 10 %wt Fe did not improve the Fe loading of the catalyst, instead larger iron particles were formed outside the zeolite (**Figure 54**) resulting in a really wide range of Fe particles sizes ranging between 2 nm to 50 nm.

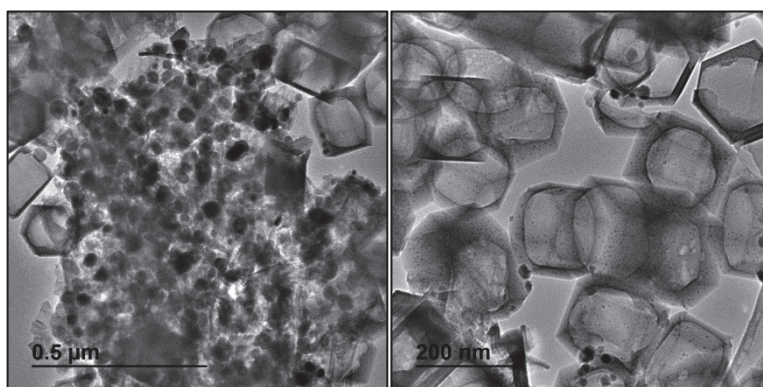


Figure 54 | TEM images of Fe@hollow-silicalite-1 when impregnating with a 10 %wt Fe solution.

Therefore no material with a Fe loading higher than 3.4 %wt could be prepared using this experimental protocol.

II.1.4. Promoters addition to the iron in hollow-silicalite-1

The synthesis protocol for the addition of promoters to the catalyst is reported in **Chapter 2 - Experimental procedure - I.1. Silicalite-1 synthesis**. TEM images of the promoted Fe@hollow-silicalite-1 (denoted as FeCuK@hollow-silicalite-1, with 2.8 %wt Fe, 0.08 %wt Cu and 0.03 %wt K) are obtained to see if promoters incorporation would have an influence on the particle size distribution. No difference are observed between the unpromoted and promoted catalyst (**Figure 57**).

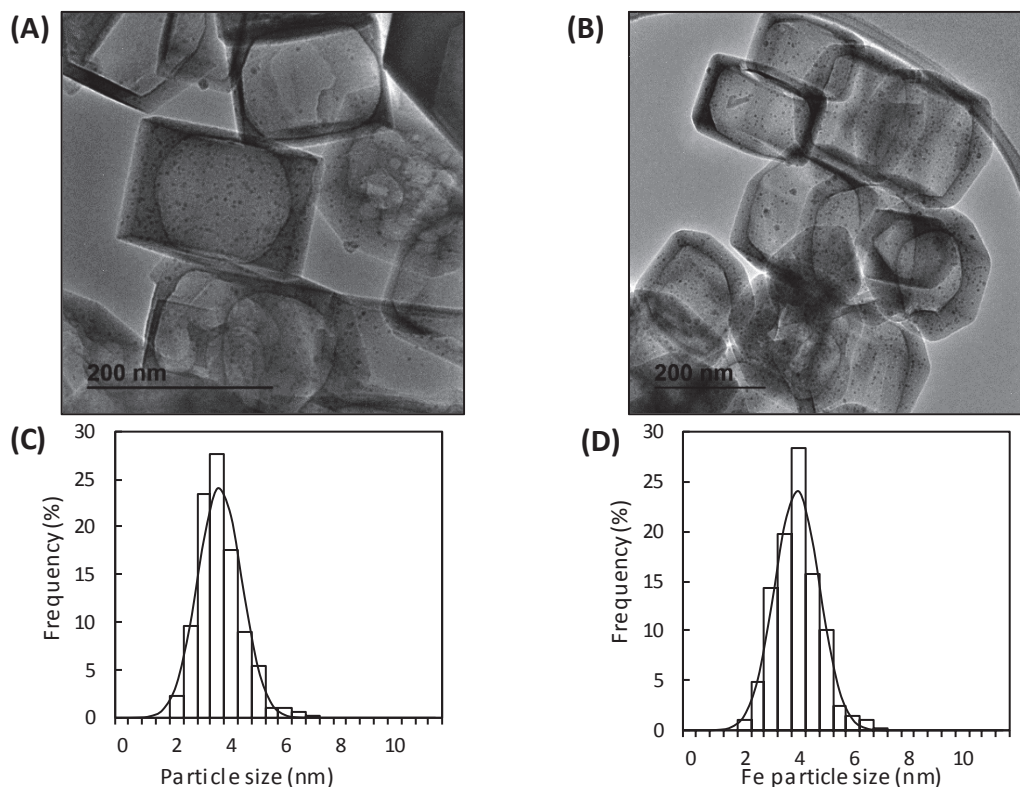


Figure 55 | Structural and morphologic features of (A) Fe@hollow-silicalite-1 and (B) FeCuK@hollow-silicalite-1 with their respective size distribution diagrams (C) and (D). Histograms are obtained from TEM analysis using at least 500 nanoparticles.

II.2. Study of the Fe@hollow-silicalite-1 before FTS

II.2.1. High resolution transmission electron microscopy and tomography

High resolution transmission electron microscopy (TEM) on the Fe@hollow-silicalite-1 catalyst shows a high degree of dispersion of iron nano particles confined within the hollow-silicalite-1 walls. However the exact localization of the iron particles remains unclear. TEM-tomography provided complementary information on the accurate localization of the iron particles. Tomography 3D reconstruction was performed on a Fe@hollow-silicalite-1 with the Environmental Transmission Electron Microscope (Cs-corrected TITAN ETEM G2 FEI, 80-300 kV). The objective was to obtain a three-dimensional spatial image of our material. Video frames of the sample under high vacuum at different slices are shown in (Figure 56) below.

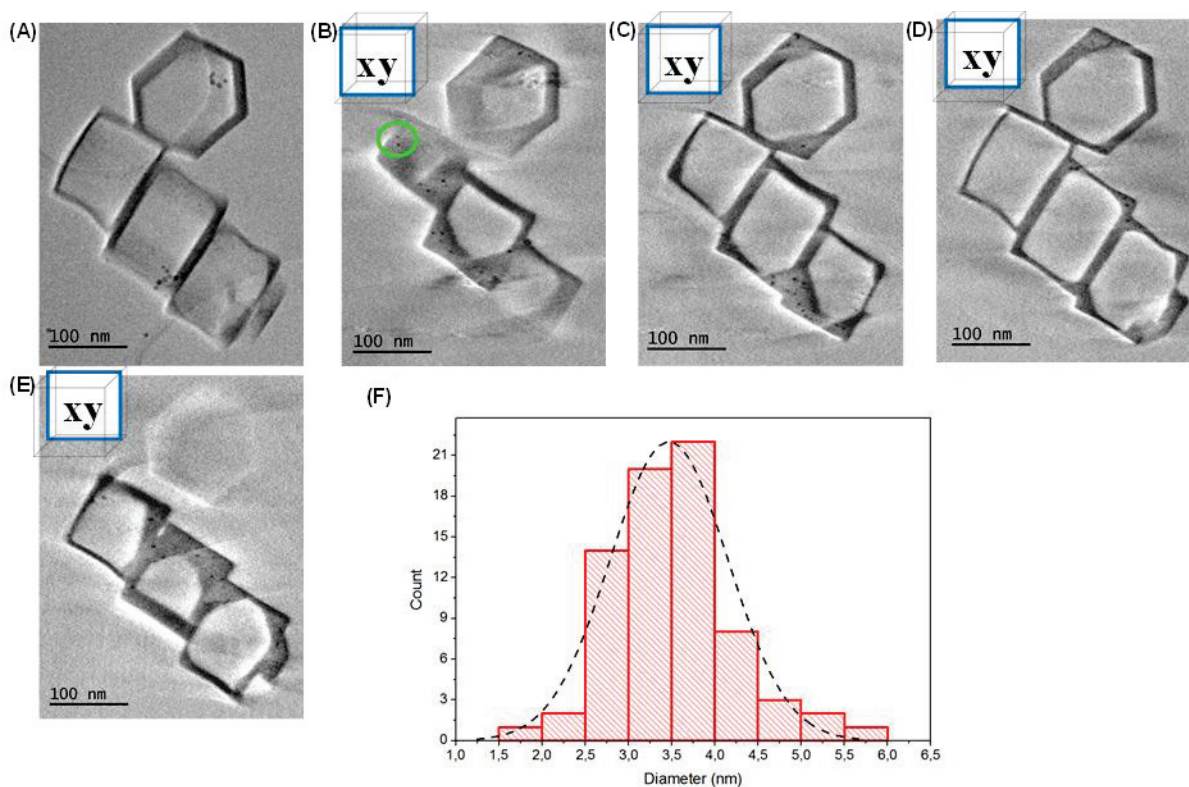


Figure 56 | Electron tomography analysis: (A) Projection at 0° tilt, (B-E) Cross section at different depths in the plane XY, the green circle show the Fe nanoparticles represented as black dots, it can be observed that de particles are in the wall of the silicalite-1, (F) the particles size distribution having an average size of 3.5 nm.

With the help of the TOMO video, the four boxes were reconstructed (**Figure 57**).

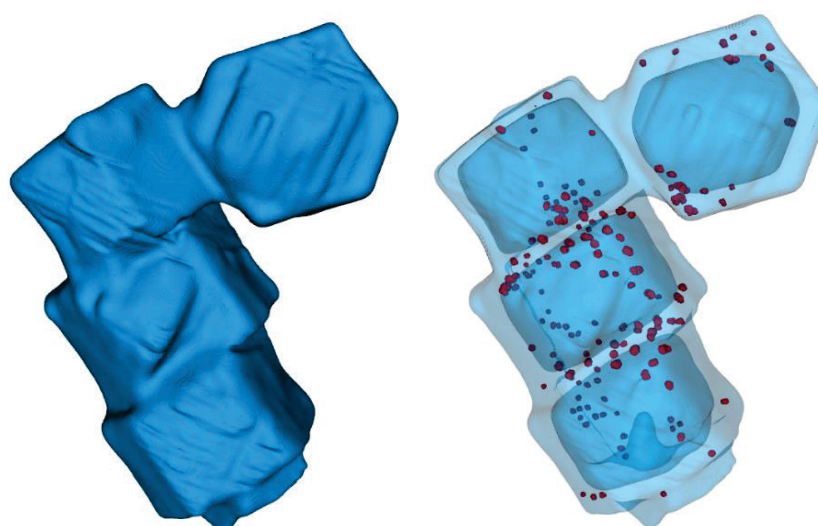


Figure 57 | Surface rendering obtained by reconstruction from the tomography video. Surface reconstruction of the material (left) and Inside of the material after turning outer surface opaque (right).

No particle on the outer surface of the materials is observed (**Figure 57**, left), iron particles are mostly located inside the walls of our materials (**Figure 57**, right) and perhaps on the inner walls. Tomography gave a more accurate iron particle size distribution, between 1.7 to 5.5 nm with a mean size around 3.5 nm (**Figure 57**, upper-right).

II.2.2. Nitrogen adsorption/desorption isotherms

Nitrogen adsorption/desorption isotherms at 77 K on bulk silicalite-1, metal-free hollow-silicalite-1 and Fe@hollow-silicalite-1 are reported in **Figure 58** with their respective TEM images.

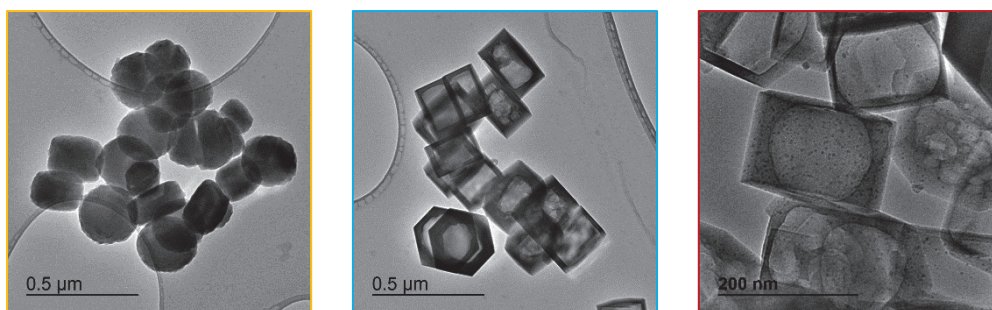
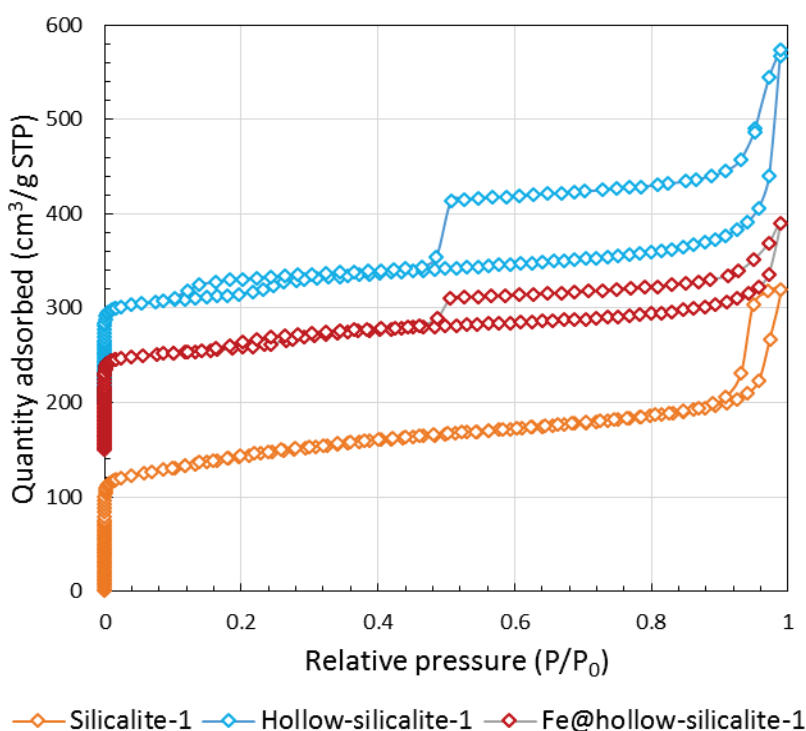


Figure 58 | N₂ adsorption/desorption isotherms for silicalite-1 (△), hollow-silicalite-1 (◇, with an offset of 150 cm³/g) and Fe@hollow-silicalite-1 (○, with an offset of 100 cm³/g) with their respective TEM images respectively from left to right.

The N₂ adsorption/desorption isotherms are of the type IV, it shows the presence of a H2 hysteresis loop with an abrupt step around $p/p_0 = 0.45 - 0.5$ in the desorption branch (**Figure 58**). H2-type hysteresis loop characterizes internal porosity connected to outer surface via entrances smaller than 4 nm. It can be used to estimate the volume of the cavities, assuming that the walls are exclusively microporous. The presence of a hysteresis loop is generally taken as an indication for the presence of cavities in the zeolite. The enhanced N₂ uptake at high P/P_0 is associated with capillary condensation of nitrogen within the large cavities of the zeolite nano-crystals. The calculated specific surface area (S_{BET}) and pore volume of the silicalite-1, hollow-silicalite-1 and Fe@hollow-silicalite-1 are listed in **Table 16**.

Table 16 | Textural properties of silicalite-1, hollow-silicalite-1 and Fe@hollow-silicalite-1

| Sample | S_{BET} (m ² /g) ^a | S_{micro} (m ² /g) ^b | S_{meso} (m ² /g) ^b | V_{micro} (cm ³ /g) ^b |
|-------------------------------|---|---|--|--|
| Silicalite-1 | 516 | 421 | 94 | 0.197 |
| Hollow- silicalite-1 | 430 | 349 | 80 | 0.167 |
| Fe@hollow-silicalite-1 | 407 | 352 | 55 | 0.168 |

^a Calculated using the BET method
^b Microporous volume (V_{micro}), Microporous surface area (S_{micro}) mesoporous surface area (S_{meso}) estimated from the t-plot

The loss of specific surface area between parent silicalite-1 and hollow-silicalite-1 is mainly due to the formation of the huge cavity in the middle of the zeolite.

II.2.3. Powder X-ray diffraction (XRD)

The XRD patterns of the Fe@hollow-silicalite-1 catalyst after reduction under H₂ at 750 °C and of the parent silicalite-1 are compared in **Figure 59**.

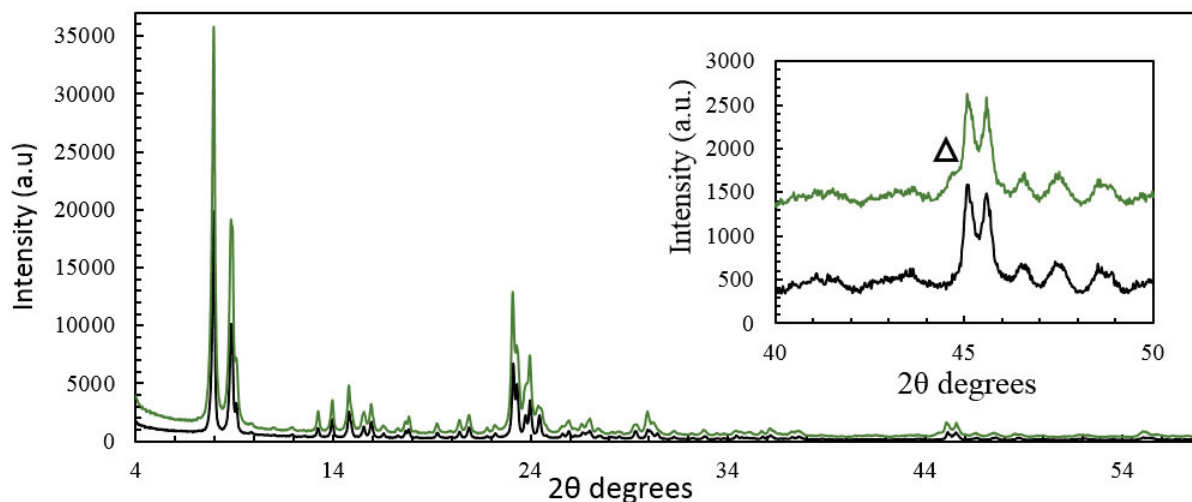


Figure 59 | X-ray diffraction spectrum of parent zeolite silicalite-1 (black line) and Fe@hollow-silicalite-1 (green line).

Only a small peak ($2\theta = 45^\circ$, Δ) corresponding to the reduced Fe into metallic α -Fe species can be detected in the catalyst after reduction. Oxide and/or carbides are hardly detectable, if any, as the amount of iron is quite low. Also it is of note that XRD only detects crystalline materials and that amorphous phases are not observable.

II.2.4. Iron phases determination by ^{57}Fe Mössbauer spectroscopy

Mössbauer spectroscopy was applied to gain insight into the nature of the iron species formed after reduction under H_2 at 750°C . After reduction, the catalyst was brought back to air, therefore the catalyst most likely re-oxidized partially in air. This technique allows completing the observation made with XRD spectroscopy and acquiring full knowledge of the fresh catalyst characteristics before the Fischer-Tropsch synthesis. Mössbauer spectroscopy has been carried out on the Fe@hollow-silicalite-1 catalyst described in **Figure 53**. Two different types of spectrum were recorded.

- The first kind of spectrum, is exemplified on **Figure 60** and the hyperfine interaction parameters calculated from the spectrum are summarized in **Table 17**.

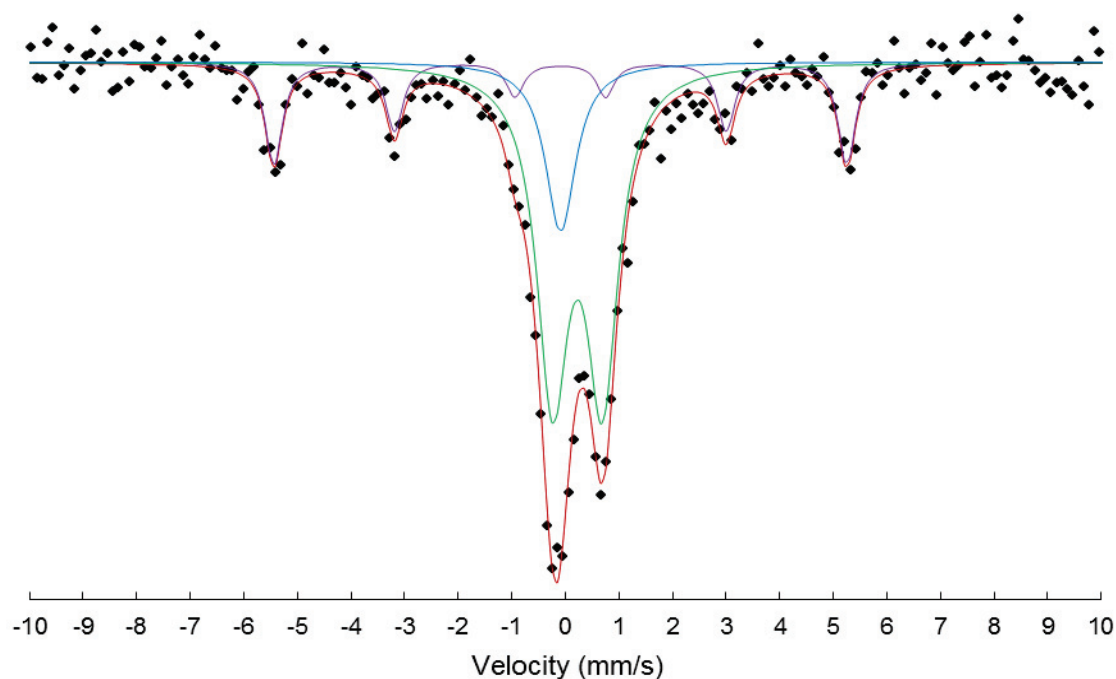


Figure 60 | ^{57}Fe Mössbauer spectrum of the Fe@hollow-silicalite-1: Experimental spectrum (black dot), experimental spectrum fit (red line), $\alpha\text{-Fe}$ (purple line), iron oxide Fe^{3+} (green line) and metallic $\alpha\text{-Fe}$ (blue line).

Three components can be distinguished for the fresh catalyst spectrum after reduction under H_2 at $750\text{ }^\circ\text{C}$: a magnetic hyperfine sextet with narrow lines and a hyperfine field of 33.0 T (relative intensity 22%), a quadrupolar hyperfine doublet with $\text{IS} = 0.32\text{ mm.s}^{-1}$ and $\text{QS} = 0.93\text{ mm.s}^{-1}$ (relative intensity 62%) and a hyperfine singlet (relative intensity 16%). The sextet can unambiguously be assigned to larger metallic iron particles [^{120, 119, 121}]. The singlet is assigned to the small superparamagnetic metallic iron nanoparticles ($\alpha\text{-Fe}$) [¹¹⁹] and the doublet to Fe^{3+} species probably formed at the surface of the iron nanoparticles (the center being metallic $\alpha\text{-Fe}$) [^{122, 123}] when the catalyst was in contact with air after the reduction reaction, when the sample was recovered at room temperature.

Table 17 | The Mössbauer fitted parameters for the fresh Fe@hollow-silicalite-1

| Sample | Splitting | IS (mm.s^{-1}) | QS (mm.s^{-1}) | Hyperfine field (T) | Species | Relative intensity (%) |
|------------------------|-----------|------------------------------|------------------------------|------------------------|--------------------|---------------------------|
| Fe@hollow-silicalite-1 | Doublet | 0.32 | 0.93 | - | Fe^{3+} | 62 |
| | Sextet | 0.00 | 0.00 | 30.3 | $\alpha\text{-Fe}$ | 22 |
| | Singlet | 0.01 | 0.00 | - | $\alpha\text{-Fe}$ | 16 |

- The second type of spectrum is exemplified in **Figure 61** and the hyperfine interaction parameters are summarized in **Table 18**.

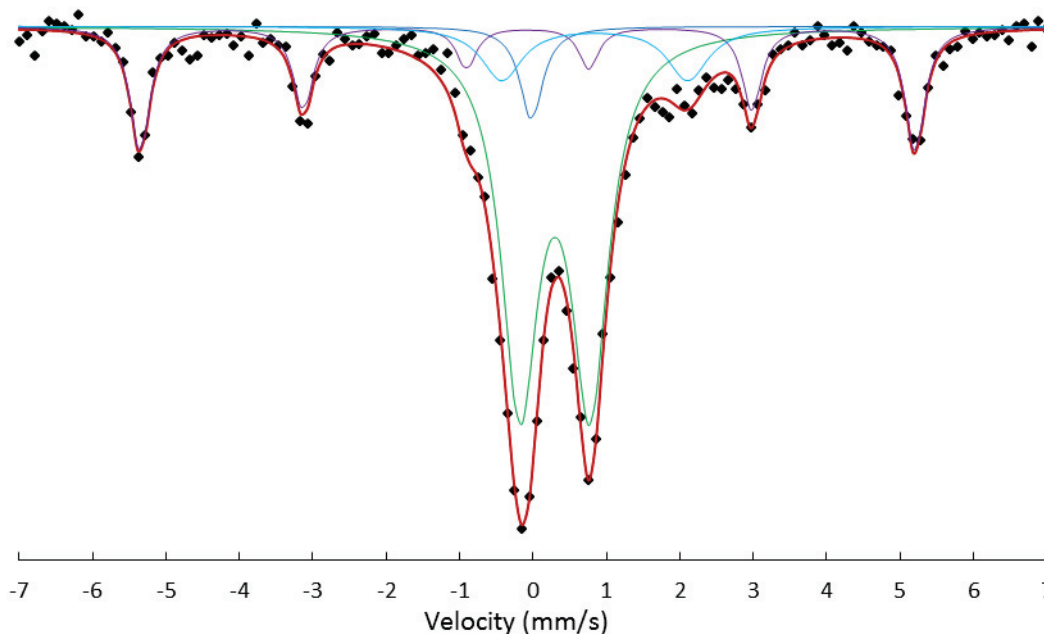


Figure 61 | ^{57}Fe Mössbauer spectrum of the Fe@hollow-silicalite-1: Experimental spectrum (black dot), experimental spectrum fit (red line), $\alpha\text{-Fe}$ (purple line), iron oxide Fe^{3+} (green line), Fe^{2+} (blue line) and metallic $\alpha\text{-Fe}$ (blue line).

Four components can be identified: a magnetic hyperfine sextet with a hyperfine magnetic field of 32.6 T (relative intensity 23 %), two quadrupolar hyperfine doublets with a $\text{IS} = \text{mm}\cdot\text{s}^{-1}$ and $\text{QS} = 0.95 \text{ mm}\cdot\text{s}^{-1}$ (relative intensity 62 %), and $\text{IS} = \text{mm}\cdot\text{s}^{-1}$ and $\text{QS} = 2.52 \text{ mm}\cdot\text{s}^{-1}$ (relative intensity 10 %) and a hyperfine singlet (relative intensity 5 %).

Table 18 | The Mössbauer fitted parameters for the fresh Fe@hollow-silicalite-1

| Sample | Splitting | IS ($\text{mm}\cdot\text{s}^{-1}$) | QS ($\text{mm}\cdot\text{s}^{-1}$) | Hyperfine field (T) | Species | Relative intensity (%) |
|------------------------|-----------|---|---|------------------------|--------------------|---------------------------|
| Fe@hollow-silicalite-1 | Doublet | 0.38 | 0.95 | - | Fe^{3+} | 62 |
| | Doublet | 0.93 | 2.52 | - | Fe^{2+} | 10 |
| | Sextet | 0.02 | 0.00 | 32.6 | $\alpha\text{-Fe}$ | 23 |
| | Singlet | 0.07 | 0.00 | - | $\alpha\text{-Fe}$ | 5 |

The same attribution can be made as for the first kind. In this case, the nanoparticles are much more oxidized and practically all converted into oxide characterized by the presence of both ferric and ferrous cations. This higher reduction may be indicative of a small size for the nanoparticles formed.

The two Mössbauer spectra are nearly similar in terms of iron phases (metallic and iron oxides), furthermore we have nearly the same Relative intensity for the Fe^{3+} (~62 %) and $\alpha\text{-Fe}$ (~23 %) phases. The difference between the two types of spectrum is centered on the apparition, in some cases of a Fe^{2+} phase. Nevertheless this does not change the interpretation regarding the fresh catalyst. The main information to remember here is the presence of principally iron oxides (> 60 %) and some metallic iron (< 40 %).

- Finally, promoted (Cu, K) Fe@gollow-silicalite-1 catalyst was studied with Mössbauer, the mössbauer spectrum and the hyperfine interaction parameters can be found in **Appendix 1**.

II.3. Study of the Fe@hollow-silicalite-1 during FTS

II.3.1. Iron phases determination by *in-situ* XRD and *in-situ* Xanes

The *in-situ* measurements were carried out at the European Synchrotron Radiation Facility (ESRF) in Grenoble France, more precisely at the Swiss-Norwegian beam lines BM01. The aim of the experiments was to understand the evolution of the iron phases during FTS using two types of characterization, a surface (XRD) technique and a bulk (XAS) technique. The reduced Fe@hollow-silicalite-1 catalyst was tested under FTS conditions ($H_2:CO = 2:1$, 18 bars) at different temperatures (230 °C, 250 °C and 280 °C, 6 h each).

a. Iron phases determination by *in-situ* XRD

Figure 62 below displays the evolution of the XRD spectrum of the Fe@hollow-silicalite-1 catalyst with time.

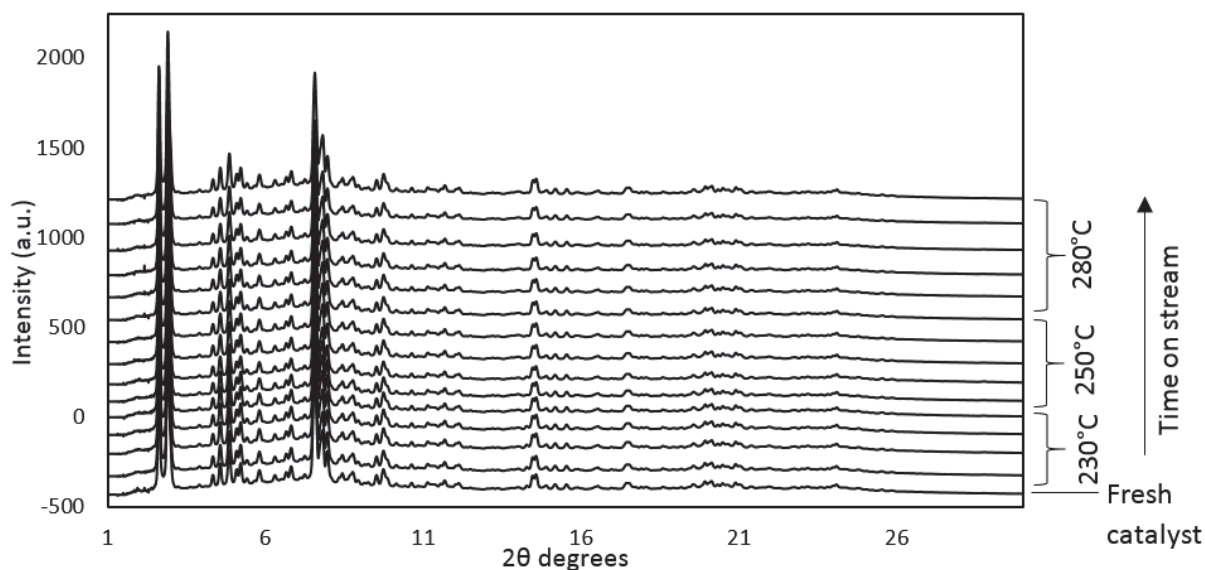


Figure 62 | Evolution of the iron phases with time and at different temperature (°C) by *in-situ* XRD.

Due to the really low amount of Fe present in the sample (< 3.4 %wt), no relevant phases transformation was observed. We observe mainly the silicalite-1 peaks, no iron phases peaks can be observed. Unfortunately, no significant information was acquired with *in-situ* XRD.

b. Iron phases determination by *in-situ* Xanes

Figure 63 below displays the *in-situ* XANES data-set evolution and the linear combination fitting results.

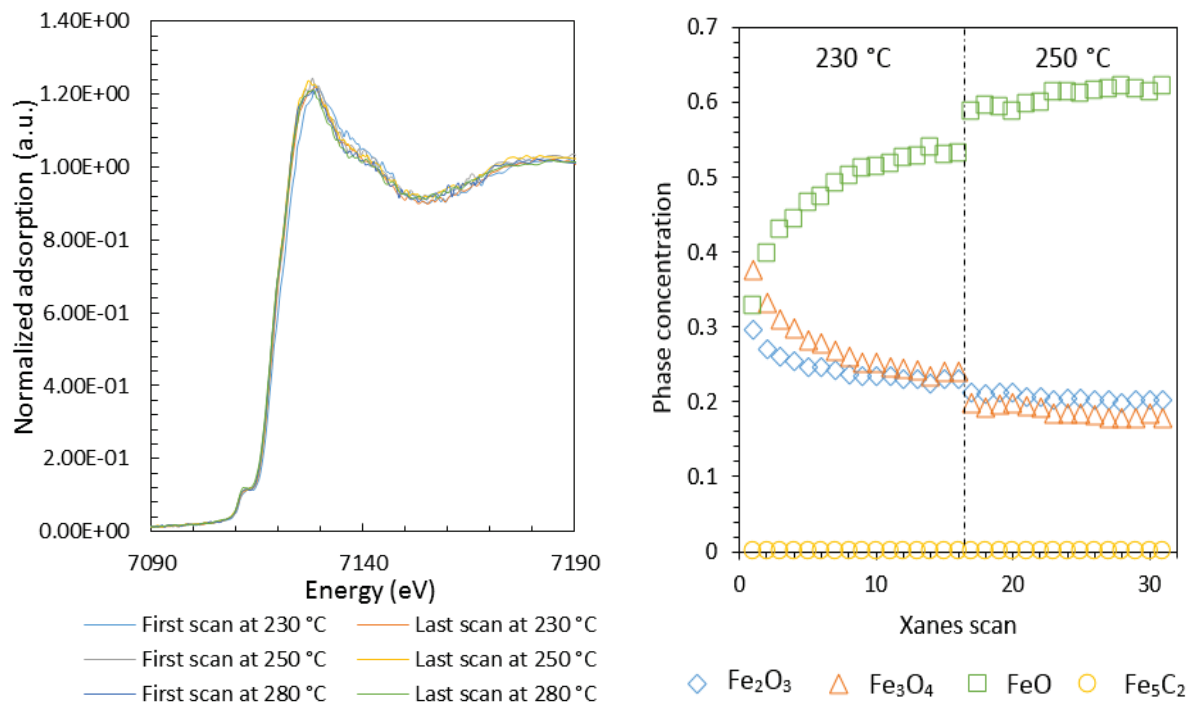


Figure 63 | *In-situ* Xanes evolution (left) and linear combination fitting of iron phases in time (right).

Hardly visible modifications in the pre-edge and white line (main absorption shoulder) during the FTS can be observed (**Figure 63**, left). The linear combination fitting at the beginning indicated the presence of three species Fe₂O₃, Fe₃O₄ and FeO. These observations are not fully in agreement with the other techniques used for the characterization of the sample. Indeed Mössbauer and XRD show the presence of metallic iron in the catalyst (between 20 to 40 % in proportion). There are some discrepancies between the two characterization methods. Getting a good linear combination with Xanes is quite difficult, especially in our case where no visible modification of the Xanes spectrum is discernable. The Mössbauer spectroscopy might be more accurate for iron phases characterization.

II.3.2. Iron phases determination by *in-situ* ^{57}Fe Mössbauer spectroscopy

In-situ measurements were carried out at IRCElyon using homemade *in-situ* cell. The aim of the experiments was to study the catalyst directly in reaction conditions without having to bring back the spent catalyst to air after testing. The reaction conditions were those used for the catalytic testing except that the total pressure was only 1 bar. 20 mg of sample of the reduced Fe@hollow-silicalite-1 catalyst were beforehand analyzed at 25 °C in air (**Figure 64 - a**). The temperature was ramped up to 250 °C and 280 °C under $\text{H}_2/\text{CO} = 2:1$ (**Figure 64 - b and c**). After several days of testing and data acquisition, the temperature was cooled down back to 25 °C and the catalyst brought back to air. A final spectrum was then recorded. (**Figure 64-d**). The hyperfine interaction parameters calculated from the spectra are summarized in **Table 19**.

Table 19 | The *in-situ* Mössbauer fitted parameters for Fe@hollow-silicalite-1 catalyst

| Sample | Splitting | IS (mm.s^{-1}) | QS (mm.s^{-1}) | Hyperfine field (T) | Species | Relative intensity (%) |
|---------------------------------|-----------|------------------------------|------------------------------|------------------------|-------------------------|---------------------------|
| Air, 25 °C | Doublet | 0.36 | 0.93 | - | Fe^{3+} | 59 |
| | Doublet | 1.21 | 1.75 | - | Fe^{2+} | 18 |
| | Sextet | 0.00 | 0.00 | 32.9 | $\alpha\text{-Fe}$ | 14 |
| | Singlet | 0.00 | 0.00 | - | $\alpha\text{-Fe nano}$ | 9 |
| H_2/CO , 250 °C | Doublet | 0.25 | 1.03 | - | Fe^{3+} | 29 |
| | Doublet | 1.00 | 1.27 | - | Fe^{2+} | 36 |
| | Singlet | 0.07 | 0.00 | - | $\alpha\text{-Fe nano}$ | 35 |
| H_2/CO , 280 °C | Doublet | 0.27 | 1.11 | - | Fe^{3+} | 8 |
| | Doublet | 0.96 | 1.24 | - | Fe^{2+} | 54 |
| | Singlet | 0.06 | 0.00 | - | $\alpha\text{-Fe nano}$ | 38 |
| Air, 25 °C | Doublet | 0.32 | 1.07 | - | Fe^{3+} | 49 |
| | Doublet | 1.25 | 1.48 | - | Fe^{2+} | 30 |
| | Singlet | 0.01 | 0.00 | - | $\alpha\text{-Fe nano}$ | 21 |

Four components were distinguished in the fresh catalyst spectrum (**Figure 64 - a**): a magnetic hyperfine sextet with a hyperfine magnetic field of 32.9 T (relative intensity 14 %), two quadrupolar hyperfine doublets with $\text{IS} = \text{mm.s}^{-1}$ and $\text{QS} = 0.93 \text{ mm.s}^{-1}$ (relative intensity 59 %), and $\text{IS} = \text{mm.s}^{-1}$ and $\text{QS} = 1.75 \text{ mm.s}^{-1}$ (relative intensity 18 %) and a hyperfine singlet (relative intensity 9 %). The sextet can unambiguously be assigned to larger metallic iron

particles [119, 120, 121]. The singlet is assigned to the small superparamagnetic metallic iron nanoparticles (α -Fe) [119] and the doublets respectively to Fe^{3+} and Fe^{2+} species probably formed at the surface of the iron nanoparticles [122, 123] when the catalyst was in contact with air after the reduction reaction, when it was recovered at room temperature.

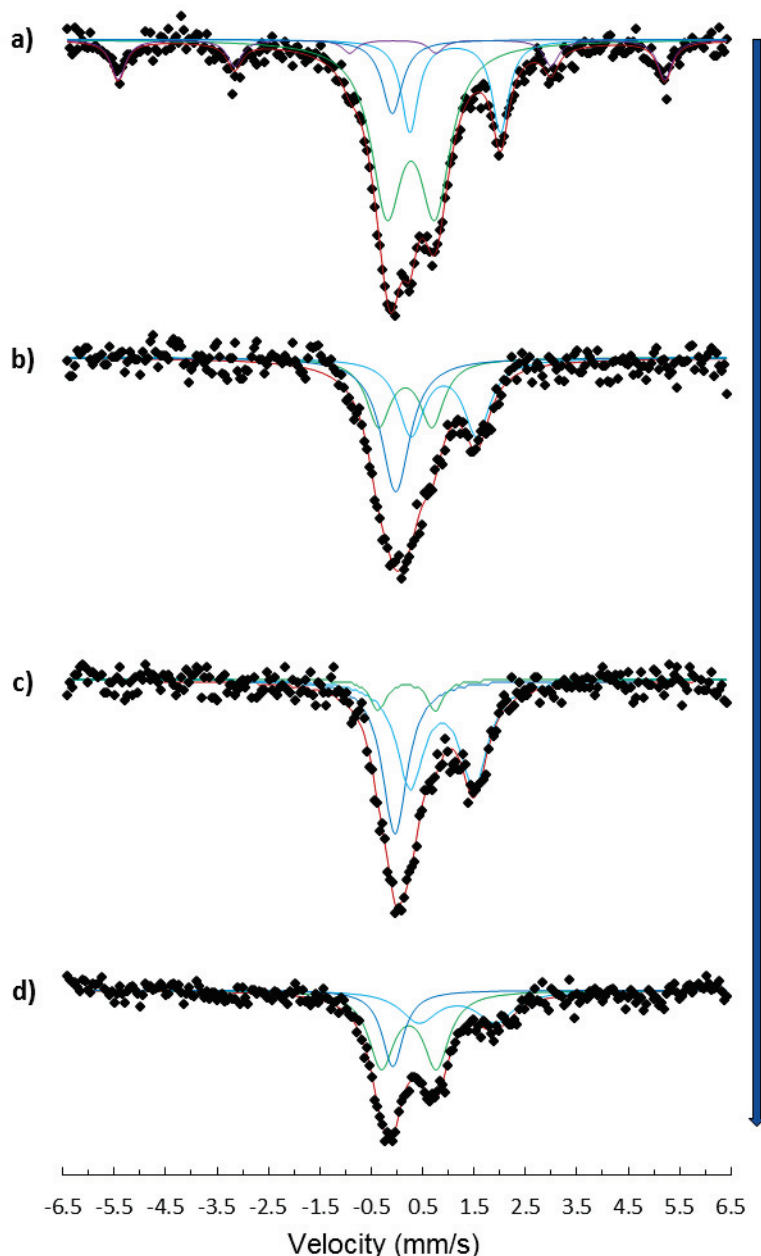


Figure 64 | In-situ ^{57}Fe Mössbauer spectrum of the Fe@hollow-silicalite-1 catalyst after FTS: a) In air at 25 °C, b) In H_2/CO at 250 °C, c) in H_2/CO at 280 °C, d) back to air at 25 °C. Experimental spectrum (black dot), experimental spectrum fit (red line), α -Fe in large particles (purple line), metallic α -Fe (blue line), Fe^{3+} (green line) and Fe^{2+} (blue line).

The catalyst was then studied in-situ under H_2/CO flow at 250 and 280 °C. Already at 250 °C, the α -Fe hyperfine sextet, corresponding to large particles, completely disappeared. These particles should most likely be oxidized by the reaction products with formation of Fe^{3+} and Fe^{2+} species. The oxidation reaction being limited by diffusion through the oxides layer. A metallic central core remains, which could explain the increase of the metallic singlet intensity observed at 250 °C. In the same time the small particles (singlet), which were largely oxidized are reduced by the reactants. This manifests itself with the increase of both total Fe^0 and Fe^{2+} spectral intensities. Both types of particles equilibrated thus in an opposite way in the redox atmosphere of catalysis. When the temperature was increased from 250 to 280 °C the catalytic redox is activated and the catalyst is more reduced, both total Fe^0 and Fe^{2+} spectral intensities increasing. Upon return to ambient temperature and atmosphere, the unstable iron nanoparticles are strongly oxidized as it could be expected. The relative intensity of the Fe^{3+} species rise up from 8 to 49 %, while the relative intensity of the Fe^{2+} species goes down from 54 to 30 % and the Fe^0 species down from 38 to 21 %.

The spectra obtained in-situ therefore appear to differ from the spectra obtained after catalytic testing so that no carbide has been detected. However it can be observed from the in situ experiments that the iron species evolve during the Fischer-Tropsch reaction both in terms of particle size and oxidation state. The absence of carbides may be linked to the fact that experiments were carried out at atmospheric pressure instead of 20 bars, which may limit the production of heavy FTS products that are efficient reactant for the formation of coke and carbides.

II.4. Study of the Fe@hollow-silicalite-1 after FTS

II.4.1. Transmission electron microscopy (TEM)

The evolution of the particles size during the Fischer-Tropsch synthesis was investigated. As explained in the state of the art chapter (**Chapter 1 - State of the art - A review - II.2.3. Deactivation of iron based catalysts - c. Sintering and loss of catalytic surface area**), sintering is one of the main way of deactivation of a catalyst. Therefore determining accurately the evolution of the particles size is indispensable for characterizing fully a catalyst. Consequently, transmission electron microscopy (TEM) was carried out on the Fe@hollow-silicalite-1 catalyst at different time on stream (**Figure 65**).

The average size of particles is increasing with time. By comparing the distribution at 100 hours and 1 month duration on stream the two distributions is nearly the same for particles of 2 to 8 nm, yet some bigger particles between larger than 12 nm can be seen after 1 month. When observing carefully the TEM images, it seems that mainly the particles inside the big cavity and outside the silicalite-1 is growing with time. The smallest particles located in the walls seems to grow to a certain size until 100 hours and then remained unchanged. Finally, the catalyst can be described as relatively stable has it keeps a good dispersion, although a few large particles are observed after 1 month of reaction.

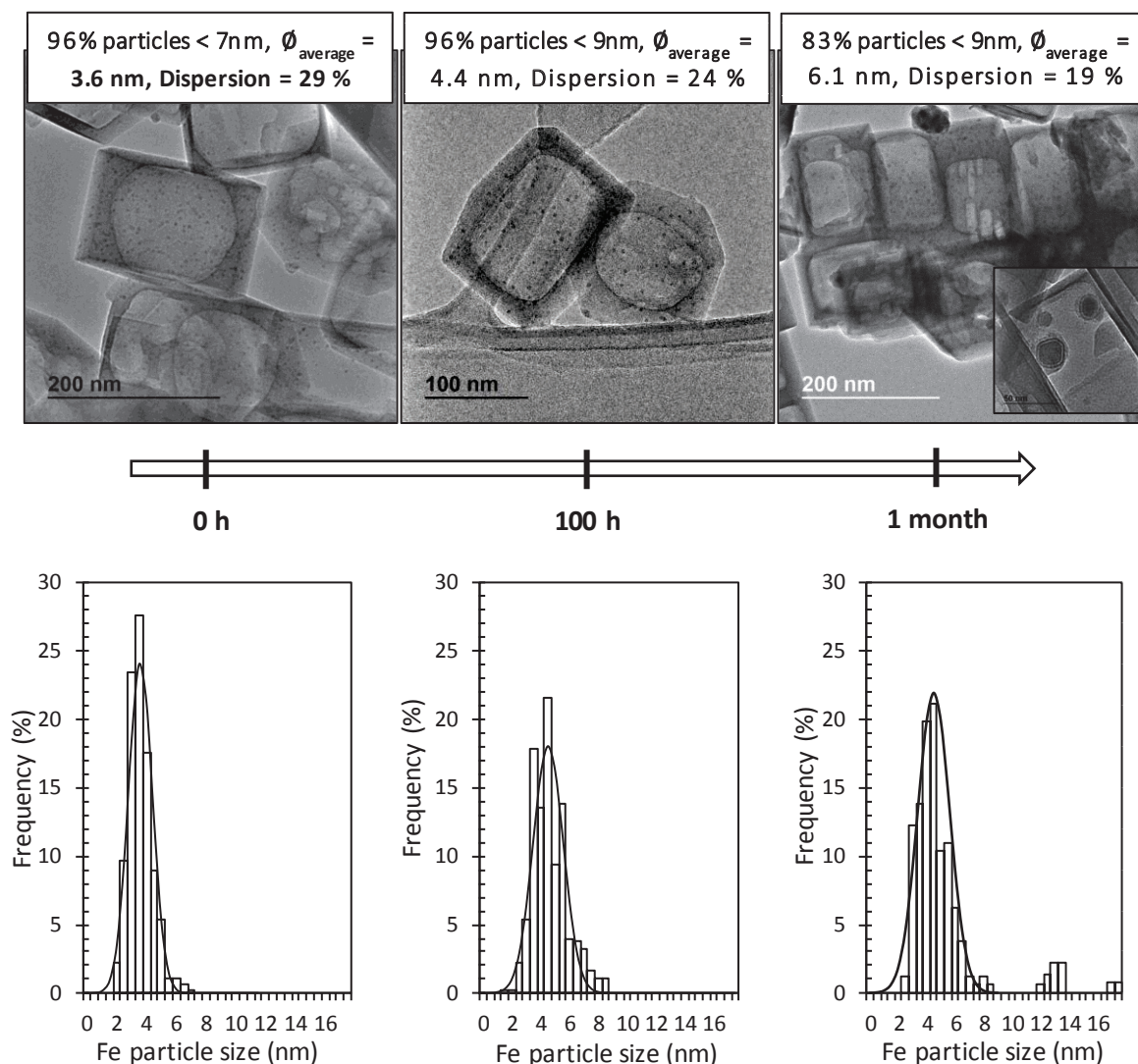


Figure 65 | Evolution of the particle size distribution at different time on stream. Fresh catalyst (left TEM images and histogram), at 100 hours on stream (middle TEM image and histogram) and after one month on stream (right TEM image and histogram).

II.4.2. Iron phases determination by XRD

Due to the really small amount of iron content, no iron phase could be seen with XRD. Therefore only Mössbauer will be of some help to determine the phases.

II.4.3. Iron phases determination by ^{57}Fe Mössbauer spectroscopy

Since XRD analysis did not give any significant information about iron phases, it was crucial to use Mössbauer spectroscopy to characterize the spent catalyst. After FTS testing, the spent catalyst was recovered from the reactor. Therefore, the spent catalyst was in contact with air,

meaning that the catalyst most likely re-oxidized partially with the oxygen. The catalyst Mössbauer spectrum was taken after 100 hours on stream at 280 °C. Again two different types of spectrum were observed after test.

- The first type of Mössbauer spectrum, corresponding to the first fresh catalyst Mössbauer spectrum studied above, is shown on **Figure 66** and its hyperfine interaction parameter are summarized in **Table 20**.

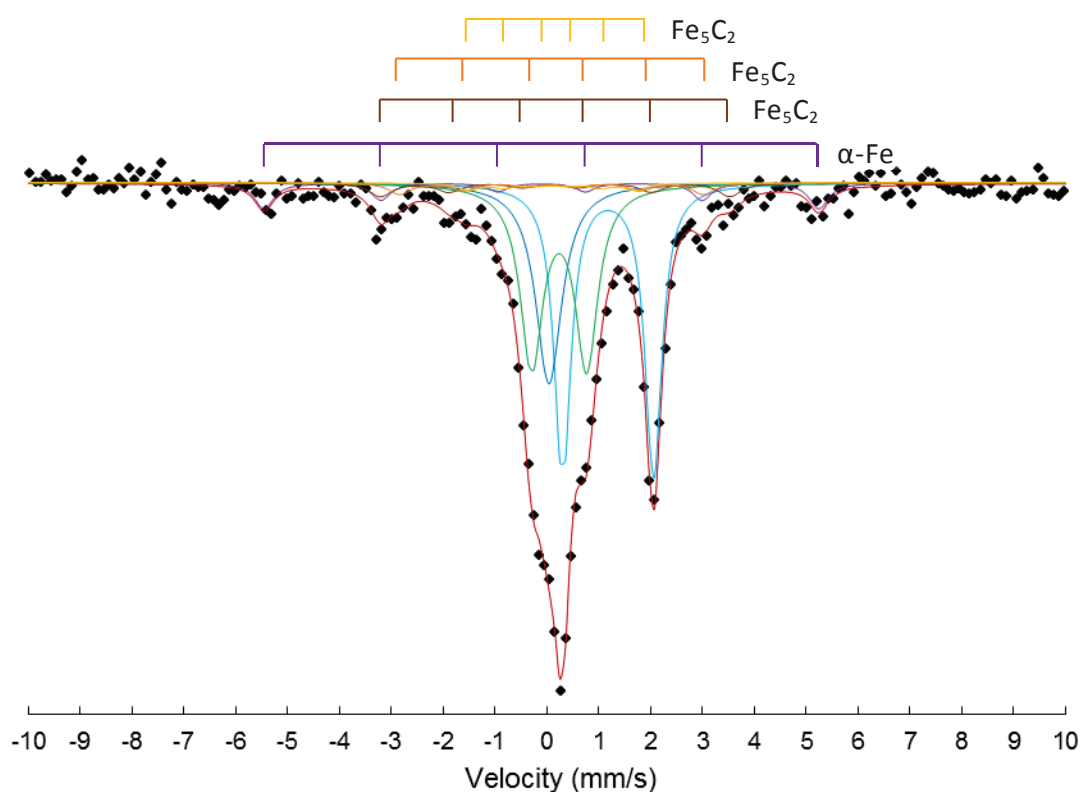


Figure 66 | ^{57}Fe Mössbauer spectrum of the Fe@hollow-silicalite-1 catalyst after FTS: Experimental spectrum (black dot), experimental spectrum fit (red line), $\alpha\text{-Fe}$ in large particles (purple line), metallic $\alpha\text{-Fe}$ (blue line), Fe^{3+} (green line), Fe^{2+} (blue line) and Fe_5C_2 carbides (brown, orange and yellow line).

Seven components can be distinguished for the spent catalyst spectrum: a magnetic hyperfine sextet with narrow lines and a hyperfine field of 33.0 T (relative intensity 8 %) attributed to $\alpha\text{-Fe}$ [120, 119, 121], a hyperfine singlet (relative intensity 18 %) attributed to the small superparamagnetic metallic iron nanoparticles [119], two quadrupolar hyperfine doublets with $\text{IS} = \text{mm}\cdot\text{s}^{-1}$ and $\text{QS} = 1.74 \text{ mm}\cdot\text{s}^{-1}$ (relative intensity 35 %) and $\text{IS} = \text{mm}\cdot\text{s}^{-1}$ and $\text{QS} = 1.05 \text{ mm}\cdot\text{s}^{-1}$

¹ (relative intensity 29 %) attributed to ferric and ferrous species [¹²², ¹²³] probably arising from the oxidation of the nanoparticles, and three small sextets with a magnetic field of 10.0, 18.1 and 20.8 T (relative intensity respectively of 4 %, 4 % and 1 %) attributed to Hägg carbides (Fe₅C₂) [⁷⁰, ¹¹⁸].

Table 20 | The Mössbauer fitted parameters for the spent Fe@hollow-silicalite-1 catalyst

| Sample | Splitting | IS (mm.s ⁻¹) | QS (mm.s ⁻¹) | Hyperfine field (T) | Species | Relative intensity (%) |
|--|-----------|-----------------------------|-----------------------------|------------------------|--------------------------------|---------------------------|
| Fe@hollow- silicalite-1 catalyst | Doublet | 1.26 | 1.74 | - | Fe ²⁺ | 35 |
| | Doublet | 0.32 | 1.05 | - | Fe ³⁺ | 29 |
| | Singlet | 0.10 | 0.00 | - | α-Fe | 18 |
| | Sextet | -0.01 | 0.00 | 33.0 | α-Fe | 8 |
| | Sextet | 0.20 | 0.09 | 20.8 | Fe ₅ C ₂ | 4 |
| | Sextet | 0.18 | 0.00 | 18.1 | Fe ₅ C ₂ | 4 |
| | Sextet | 0.19 | 0.00 | 10.0 | Fe ₅ C ₂ | 2 |

The relative intensity of Fe³⁺ species seems to decrease with the Fischer-Tropsch synthesis. At first the relative intensity was > 60 % whereas after FTS the intensity drop to 30 %. On the contrary, the Fe²⁺ species tend to increase. Also the relative intensity of α-Fe decreases from around ~25 % to less than 10 %. However, the relative intensity of the singlet corresponding to really small iron particles shows no significant evolution. The apparition of the carbides phases (Fe₅C₂) can be noticed. Further discussion on the iron phase evolution will be added after the second type of Mössbauer spectrum description.

- The second type of Mössbauer spectrum, corresponding to the second fresh catalyst spectrum studied above, is shown on **Figure 67** and its hyperfine interaction parameters are summarized in **Table 21**.

Table 21 | The Mössbauer fitted parameters for the spent Fe@hollow-silicalite-1 catalyst

| Sample | Splitting | IS (mm.s ⁻¹) | QS (mm.s ⁻¹) | Hyperfine field (T) | Species | Relative intensity (%) |
|--|-----------|-----------------------------|-----------------------------|------------------------|------------------|---------------------------|
| Fe@hollow- silicalite-1 catalyst | Doublet | 1.12 | 2.17 | - | Fe ²⁺ | 7 |
| | Doublet | 0.32 | 1.13 | - | Fe ³⁺ | 49 |
| | Singlet | -00.5 | 0.00 | - | α-Fe | 4 |
| | Sextet | 0.09 | 0.00 | 18.4* | ? | 40 |

*Field distribution centered around 18.4 T

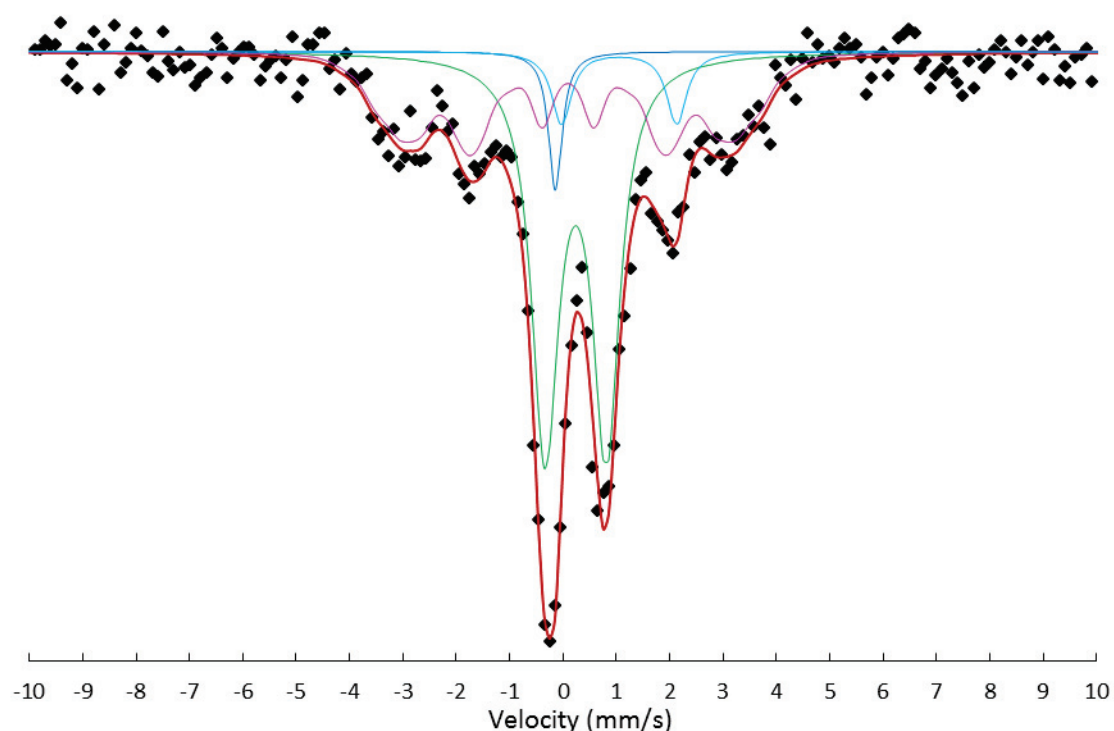


Figure 67 | ⁵⁷Fe Mössbauer spectrum of the Fe@hollow-silicalite-1 catalyst after FTS: Experimental spectrum (black dot), experimental spectrum fit (red line), αmetallic α-Fe (blue line), Fe³⁺ (green line), Fe²⁺ (blue line) and unknown phase (pink line).

Four components can be distinguished for the spent catalyst spectrum: Two quadrupolar hyperfine doublets with a quadrupolar splitting of $QS = 1.13 \text{ mm.s}^{-1}$ and $QS = 2.17 \text{ mm.s}^{-1}$ (with a relative intensity respectively of 49 % and 7 %), a hyperfine singlet (relative intensity 18 %) and a large sextet corresponding to a field distribution centered around 18.4 T.

Again, the two doublets with an isomer shift of $QS = 0.32 \text{ mm.s}^{-1}$ and $Qs = 1.12 \text{ mm.s}^{-1}$ can be assigned respectively to Fe^{3+} and Fe^{2+} species [122, 123]. The singlet is assigned to the small superparamagnetic metallic iron nano particles ($\alpha\text{-Fe}$) [119]. The wide sextet could not be assigned to any kind of iron phase. This large contribution seems to correspond to small metallic iron particles ($\alpha\text{-Fe}$) when considering its isomeric shift $\sim 0.09 \text{ mm.s}^{-1}$ (around 0.10 mm.s^{-1} in literature [119]) but also looks like carbides when considering its hyperfine field around $\sim 18.4 \text{ T}$ (between 10.0 T to 20.0 T in the literature [70, 118]). It could also correspond to metallic iron doped with C.

The relative intensity of Fe^{3+} species in this case seems to decrease slightly with the Fischer-Tropsch synthesis. It went from $\sim 60 \%$ to around $\sim 50 \%$ after Fischer-Tropsch synthesis. The relative intensity of Fe^{2+} species and small metallic particle (Fe^0) did not vary. The sextet corresponding to relatively large metallic iron particle has completely disappeared. Most of it might have been transformed into these wide sextet observed after Fischer-Tropsch synthesis. No carbides were observed.

In conclusion, in both cases, the relative intensity of Fe^{3+} species and $\alpha\text{-Fe}$ large particles is clearly decreasing during the Fischer-Tropsch synthesis. Fe^{2+} species are increasing whereas small $\alpha\text{-Fe}$ particles remain unchanged. Also carbides phases (Fe_5C_2) can be clearly identified after Fischer-Tropsch synthesis.

Fe^{3+} species can be assumed to be Fe_2O_3 and/or Fe_3O_4 oxides (the only way to be sure would be to analyze the sample at really low temperature [124, 125]). Part of Fe_2O_3 oxide might transformed into Fe_3O_4 and FeO species (corresponding to the increase of Fe^{2+} species), in-situ Xanes linear combination fitting seems to agree with this observation.

Conclusion

The promoted and unpromoted Fe@hollow-silicalite-1 are well-structured and show a well-defined particles size distribution as well as a relatively high particle dispersion ($> 30 \%$). Accurate localization of the iron particles inside the zeolite is permitted by TEM tomography. It reveals that the particles are located preferentially in the silicalite-1 walls. Mössbauer spectroscopy analysis reveals that the catalyst is principally a mixture of iron oxides (Fe^{3+} and

Fe²⁺) and metallic iron. In-situ characterizations lack accuracy due to the really low amount of iron contained in the catalyst. Finally, the Fe@hollow-silicalite-1 proves to be relatively stable during the Fischer-Tropsch synthesis. The average particles size slightly increases, but compared to the commercial catalyst, the growth is rather minor. The main technique of interest for iron phase characterization is the Mössbauer analysis. After Fischer-Tropsch, analysis three main phases can be identified, oxides phases (> 60 %) carbides (~10 %) and metallic iron (< 25 %). The Fe@hollow-silicalite-1 catalyst, even tough, well controlled in terms of structure and particles size, remains particularly tough to understand regarding the evolution of the iron phases, just like the commercial catalyst described previously. **Table 22** summarizes the essential information regarding the Fe@hollow-silicalite-1 catalyst.

Table 22 | Fe@hollow-silicalite-1 catalyst information

| | Fresh catalyst | | | Spent catalyst | | |
|--------------------------|-------------------------|----------------|--|-------------------------|----------------|--|
| | Mean particle size (nm) | Dispersion (%) | Fe species | Mean particle size (nm) | Dispersion (%) | Fe species |
| TEM | 3.6 - 4.6 | 26 - 37 | - | 4.4 | 24 | - |
| Tomography | 3.5 | 38 | - | - | - | - |
| Ex-situ XRD | - | - | α -Fe | - | - | - |
| In-situ XRD | - | - | - | - | - | - |
| Ex-situ Mössbauer | - | - | α -Fe, Fe ³⁺ , Fe ²⁺ | - | - | α -Fe, Fe ³⁺ , Fe ²⁺ , Fe ₅ C ₂ |
| In-situ Mössbauer | - | - | α -Fe, Fe ³⁺ , Fe ²⁺ | - | - | α -Fe, Fe ³⁺ , Fe ²⁺ |
| In-situ Xanes | - | - | FeO, Fe ₂ O ₃ , Fe ₃ O ₄ | - | - | FeO, Fe ₂ O ₃ , Fe ₃ O ₄ |

For ex-situ mössbauer: iron species in bold are in majority in the sample, iron species not in bold are in minority in the sample.

III. Characterization of a Fe/hollow-silicalite-1 catalyst

The synthesis procedure by dissolution-recrystallization explained in **Chapter 2 - Experimental procedure - I.3. Preparation of Fe@hollow-silicalite-1**, used to develop the well-controlled iron catalyst called Fe@hollow-silicalite-1 catalyst is not 100 % reproducible. Actually, Fe/hollow-silicalite-1 catalyst (Fe supported on hollow-silicalite-1) was obtained when several synthesis for Fe@hollow-silicalite-1 failed (**Figure 68**). Several parameters playing a role during the overall synthesis process most likely still escape from our understanding and will require further investigations.

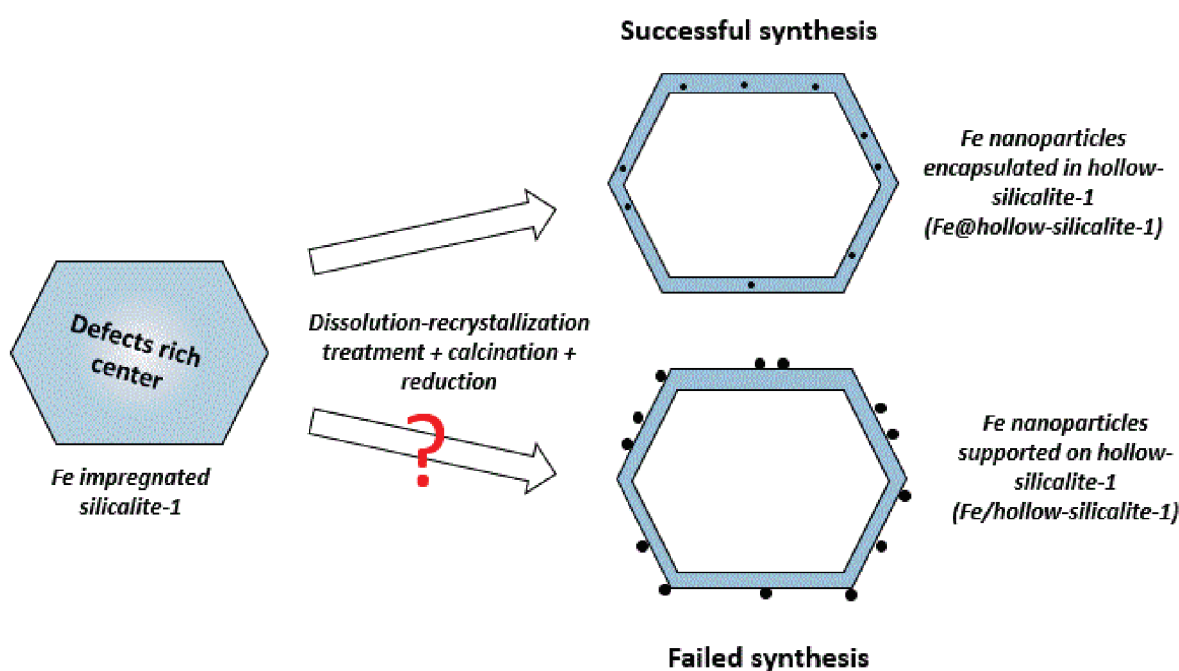


Figure 68 | Schematics of the failed synthesis process for the of Fe/hollow-silicalite-1 synthesis

Therefore, it was interesting to study and compare the two catalysts as they were relatively similar. These catalysts will be first characterized by various techniques such as transmission electron microscopy, X-ray diffraction and Mössbauer spectroscopy to have an overall understanding of the catalyst's main characteristics. The first part will deal with the fresh catalyst, the second part will focus on the spent catalyst.

III.1. Study of the Fe/hollow-silicalite-1 catalyst before FTS

III.1.1. Transmission electron microscopy (TEM)

The Fe/hollow-silicalite-1 catalyst transmission electron microscopy (TEM) images were taken with the Jeol 2010 LaB6 microscope. The catalysts were reduced at 750 °C with H₂ to form the nanoparticles. After reduction, the catalyst was brought back to air, therefore the catalyst most likely re-oxidized partially in air. The images and particles size distribution are shown in **Figure 69**.

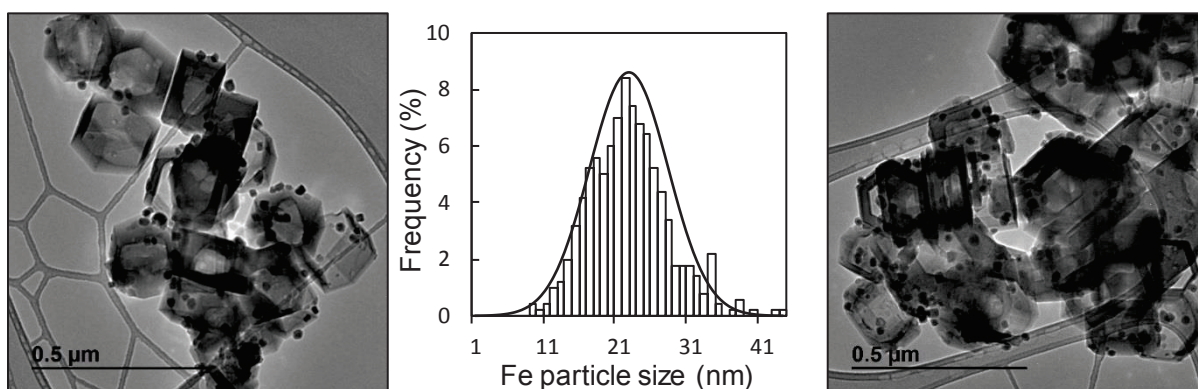


Figure 69 | TEM images and particle size distribution of Fe/hollow-silicalite-1.

Particles are mainly localized outside the hollow-silicalite-1 instead of inside as for the Fe@hollow-silicalite-1. The particle size distribution is well-defined even though wider than for the Fe@hollow-silicalite-1 catalyst. The particle distribution ranges from around 9 nm to 45 nm. The average particle size obtained is around 21.7 nm. In terms of dispersion, the Van Hardeveld and Hartog model gives 5.2%. Finally, the Fe loading in the sample was of 4.2 %wt Fe.

III.1.2. Powder X-ray diffraction (XRD)

The XRD shown in **Figure 70** is an example of a Fe/hollow-silicalite-1 catalyst after reduction under H₂ at 750 °C. After reduction, the catalyst was brought back to air, therefore the catalyst most likely re-oxidized partially in air.

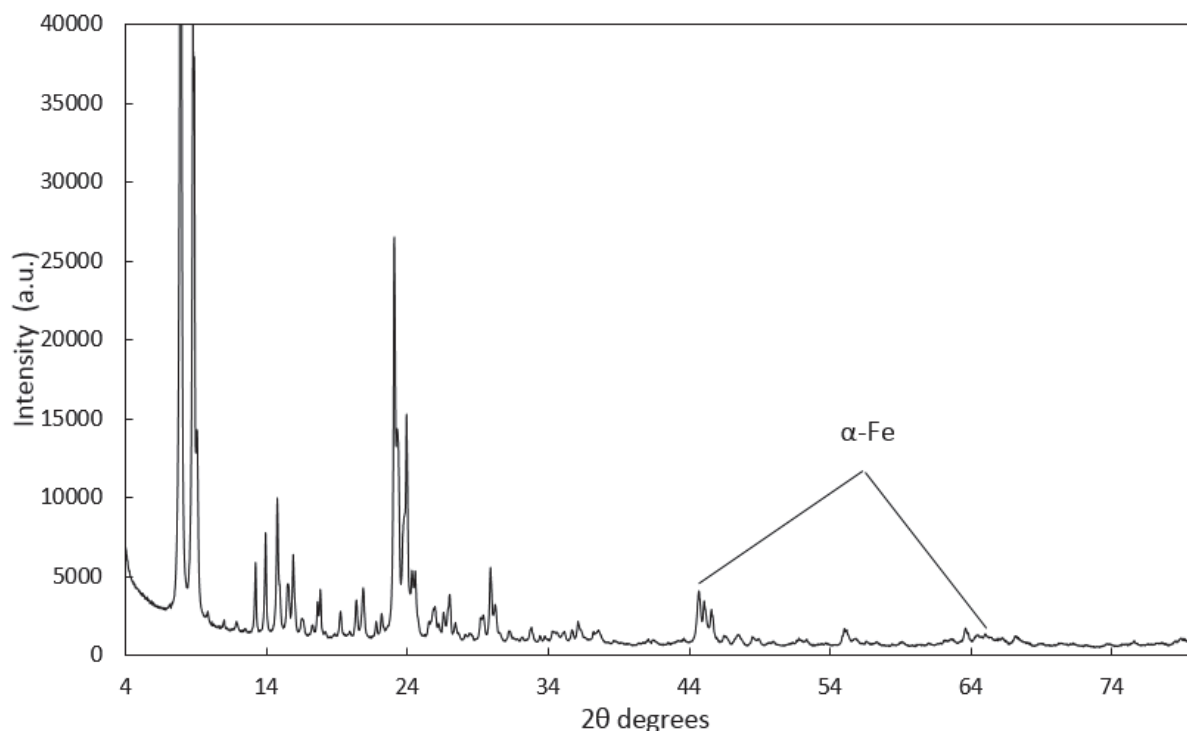


Figure 70 | X-ray diffraction spectrum of parent zeolite silicalite-1 (black line) and Fe@hollow-silicalite-1 (green line).

As the loading of iron is two time more important than in the Fe@hollow-silicalite-1 catalyst, the α -Fe peak can be easily observed this time. XRD shows a narrow peak ($2\theta = 45^\circ$) corresponding to the reduced Fe into metallic α -Fe. Oxide and/or carbides are hardly detectable, if any, as the amount of iron is quite low. Another really small peak corresponding to α -Fe can be observed around $2\theta = 65^\circ$. All the others peaks correspond to the silicalite-1 pattern.

III.1.3. Iron phases determination by ^{57}Fe Mössbauer spectroscopy

Mössbauer spectroscopy was applied at room temperature to gain insight of the iron species formed after reduction under H_2 at 750°C . After reduction, the catalyst was brought back to air, therefore the catalyst most likely re-oxidized partially in air. This technique permits to complete the observation made with XRD spectroscopy and to acquire a complete knowledge of the fresh catalyst composition before the Fischer-Tropsch synthesis. Mössbauer spectroscopy has been carried out on the Fe/hollow-silicalite-1 catalyst. The Mössbauer

spectrum is displayed on **Figure 71** and the hyperfine interaction parameter are summarized in **Table 23**.

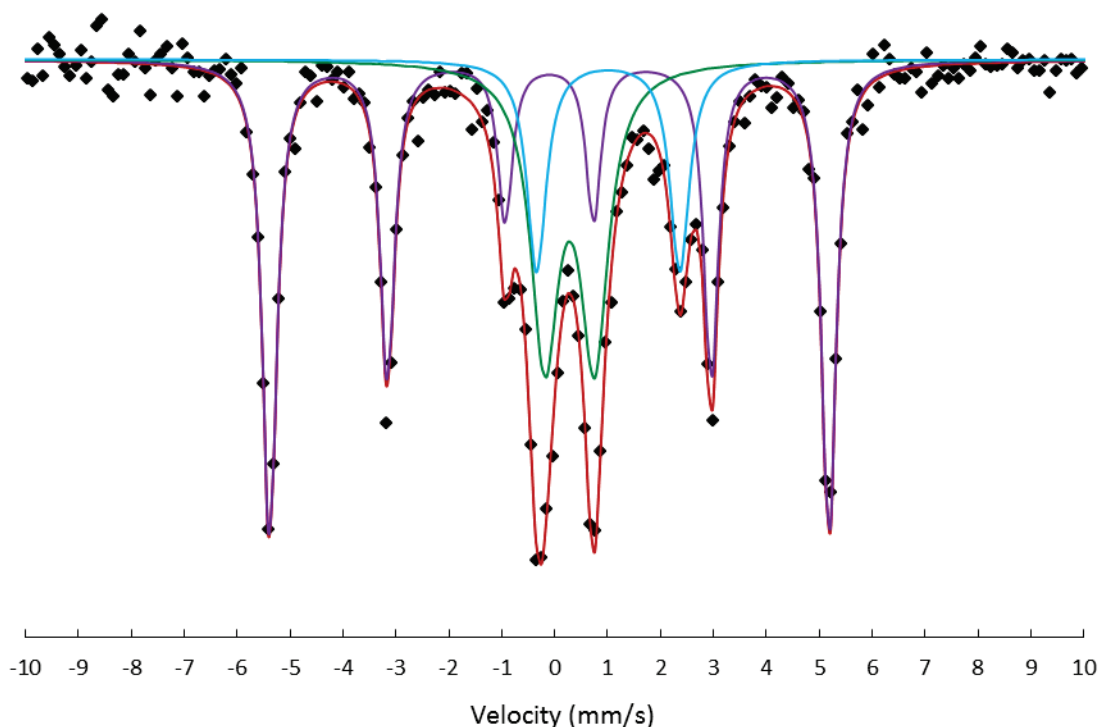


Figure 71 | ^{57}Fe Mössbauer spectrum of the Fe/hollow-silicalite-1: Experimental spectrum (black dot), experimental spectrum fit (red line), $\alpha\text{-Fe}$ (purple line), iron oxide Fe^{3+} (green line) and Fe^{2+} (blue line).

Three components can be identified on the fresh catalyst spectrum after reduction under H_2 at $750\text{ }^\circ\text{C}$: a magnetic hyperfine sextet with narrow lines and a hyperfine field of 32.7 T (relative intensity 53 %), a quadrupolar hyperfine doublet with a quadrupolar splitting $QS = 0.94\text{ mm}\cdot\text{s}^{-1}$ (relative intensity 53 %) and a second quadrupolar hyperfine doublet with a quadrupolar splitting $QS = 2.69\text{ mm}\cdot\text{s}^{-1}$ (relative intensity 16 %).

The two doublets with an isomer shift of $IS = 0.37\text{ mm}\cdot\text{s}^{-1}$ and $IS = 1.10\text{ mm}\cdot\text{s}^{-1}$ can be assigned respectively to Fe^{3+} and Fe^{2+} compounds [122, 123]. The sextet is assigned to relatively large metallic iron particles ($\alpha\text{-Fe}$) [120, 119, 121].

Table 23 | The Mössbauer fitted parameters for the fresh Fe/hollow-silicalite-1

| Sample | Splitting | IS (mm.s ⁻¹) | QS (mm.s ⁻¹) | Hyperfine field (T) | Species | Relative intensity (%) |
|------------------------|-----------|-----------------------------|-----------------------------|------------------------|------------------|---------------------------|
| Fe/hollow-silicalite-1 | Doublet | 0.37 | 0.96 | - | Fe ³⁺ | 31 |
| | Doublet | 1.10 | 2.69 | - | Fe ²⁺ | 16 |
| | Sextet | 0.00 | 0.00 | 32.7 | α-Fe | 53 |

In comparison with the Fe@silicalite-1 catalyst described in part II, the Fe/hollow-silicalite-1 does not show any singlet with an isomeric shift of 0.00 mm.s⁻¹ (corresponding to small metallic particles).

Fresh Fe@hollow-silicalite-1 and Fe/hollow-silicalite-1 catalysts are very similar in terms of iron phase composition. They are mainly composed of metallic iron and oxides (Fe²⁺ and Fe³⁺ species). The main difference between the two fresh catalysts is coming from their average particle size diameter, respectively 3.5 nm and 21.7 nm for Fe@hollow-silicalite-1 and Fe/hollow-silicalite-1. The proportion of α-Fe for the Fe/hollow-silicalite-1 was two times more important than in the Fe@hollow-silicalite-1 (**Table 24**). Alternatively, the relative amount of oxides species (Fe³⁺ and Fe²⁺) is lower.

Table 24 | The iron phases with their relative intensity determined by Mössbauer spectroscopy for the fresh Fe@hollow-silicalite-1 (left) and the fresh Fe/hollow-silicalite-1 (right)

| Sample | Species | Relative intensity (%) | Sample | Species | Relative intensity (%) |
|------------------------|------------------|------------------------------|------------------------|------------------|------------------------------|
| Fe@hollow-silicalite-1 | Fe ³⁺ | 62 | Fe/hollow-silicalite-1 | Fe ³⁺ | 31 |
| | Fe ²⁺ | 10 | | Fe ²⁺ | 16 |
| | α-Fe | 23 | | α-Fe | 53 |
| | Fe ⁰ | 5 | | Fe ⁰ | 0 |

This might be explained by the fact that the particles of the Fe/hollow-silicalite-1 are quite large compared to the one of the Fe@hollow-silicalite-1 material. When looking at TEM images (**Figure 72**), one can observe that large particles are composed of a core and a small layer. The core of the particles is most likely composed of metallic iron, whereas the small

layer all around the metallic core is mainly composed of oxides (For the particle in **Figure 72**, the size of the core is ~ 15 nm and the layer ~ 4.5 nm). The layer of iron oxide can be observed on relatively large iron particles in Fe@hollow-silicalite-1 sample. The oxide layer was most likely formed when the sample was brought back into air after reduction under H_2 at $750^\circ C$. It is recognized that small nanoparticles (< 5 nm) are quickly oxidized when being in contact with air.

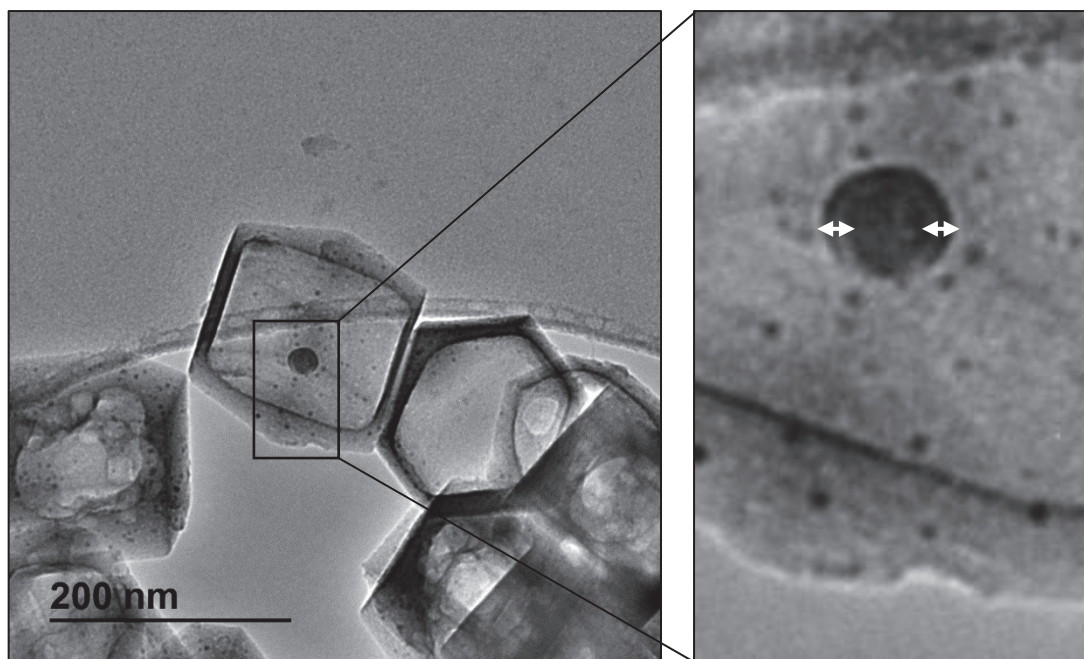


Figure 72 | Core-shell nanoparticles in a Fe@hollow-silicalite-1 catalyst

However, the core of large particles is being protected by the oxide layer formed by contact with air. Therefore, the metallic core being protected by the oxide layer, it is not surprising, that the Fe/hollow-silicalite-1 catalyst has more metallic iron in proportion, as its particles are way bigger than the one from the Fe@hollow-silicalite-1. Also, it is most likely to be the iron oxide that participates in the FTS reaction instead of the metallic iron. Furthermore, Fe^{2+} and Fe^{3+} species were observed in both catalysts. These two species can be found in several oxide types such as Fe_3O_4 , Fe_2O_3 and FeO . It is probable that the two catalysts are a mixture of several oxides, as in H_2 atmosphere iron oxide is generally reduced to Fe_3O_4 , FeO and then to metallic Fe [44, 45, 46].

III.2. Study of the Fe/hollow-silicalite-1 catalyst after FTS

III.2.1. Transmission electron microscopy (TEM)

The spent Fe/hollow-silicalite-1 catalyst transmission electron microscopy (TEM) images were taken with the Jeol 2010 LaB6 microscope. After FTS testing, the spent catalyst was recovered from the reactor. Therefore, the spent catalyst was in contact with air, meaning that the catalyst most likely re-oxidized partially with the oxygen. The images and particles size distribution are shown in **Figure 73**.

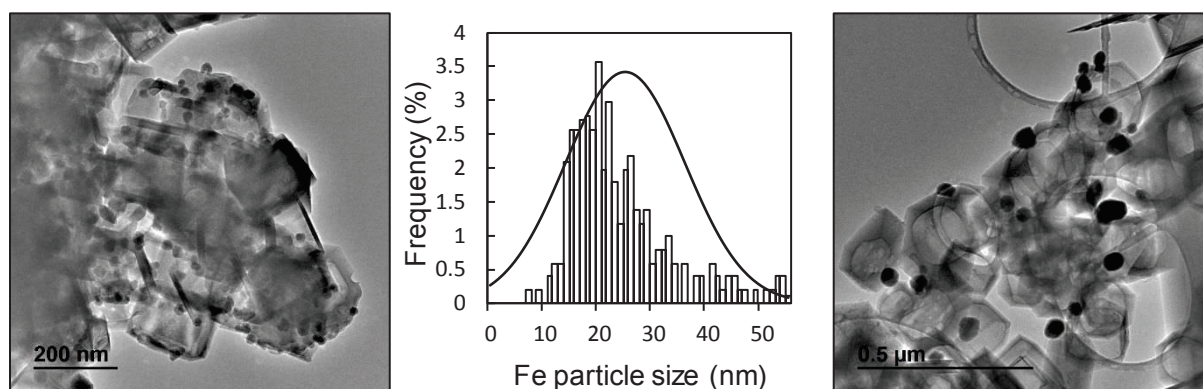


Figure 73 | TEM images and particle size distribution of the spent Fe/hollow-silicalite-1.

Again, particles are mainly localized outside the hollow-silicalite-1. The particle size distribution is wider than before the Fischer-Tropsch test. The particle distribution ranges from around 7 nm to 97 nm. The average particle size obtained is around 27.5 nm. In terms of dispersion, the Van Hardeveld and Hartog model gives 4.6 %. Some sintering occurred during the FTS reaction, as larger particles were observed. Therefore the Fe/hollow-silicalite-1 catalyst seems to be more impacted by sintering effect than the Fe@hollow-silicalite-1 catalyst that has particles inside the silicalite-1 walls.

III.2.2. Powder X-ray diffraction (XRD)

The XRD shown in **Figure 74** is an example of a Fe/hollow-silicalite-1 catalyst after the Fischer-Tropsch synthesis, with direct comparison with the fresh catalyst described in the previous part.

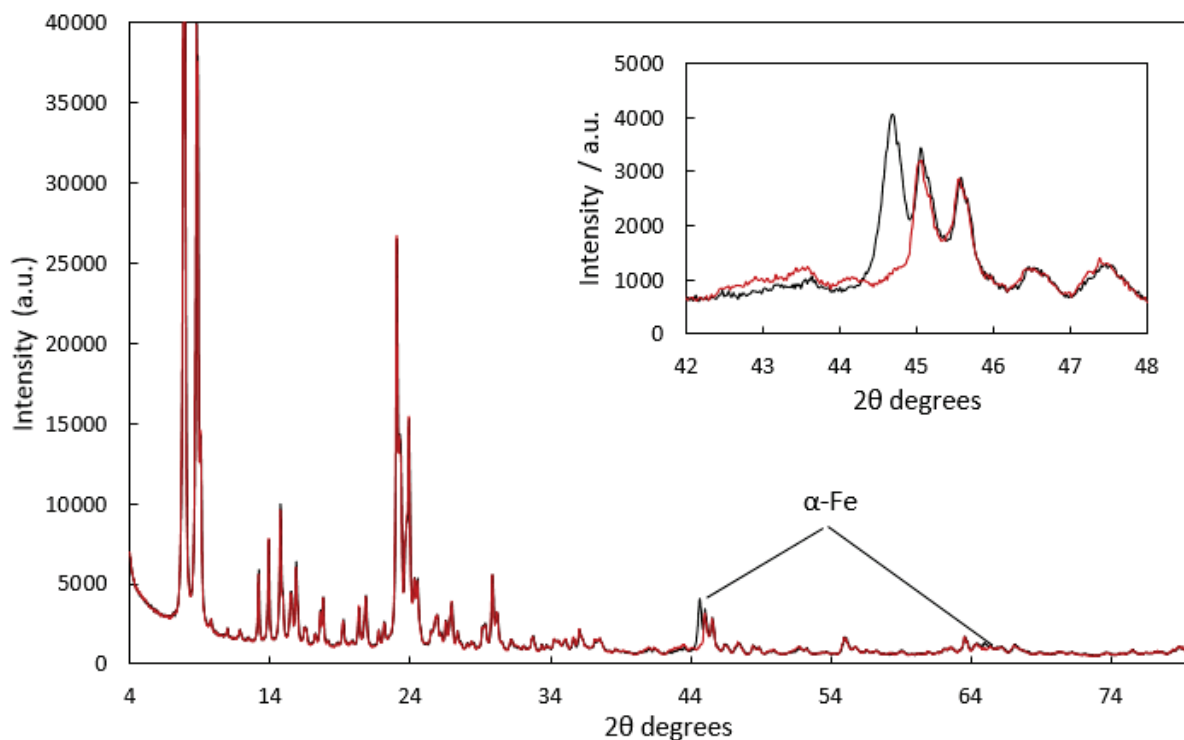


Figure 74 | X-ray diffraction spectrum of the spent Fe/hollow-silicalite-1 catalyst (red line) and fresh Fe/hollow-silicalite-1 (black line).

When looking only to the spent catalyst diffractogram (red line), no iron phase can be identified. The usual silicalite-1 pattern is present, but no other phase can be observed. By comparing the fresh and spent catalyst diffractograms, the metallic α -Fe peaks ($2\theta = 45^\circ$ and $2\theta = 65^\circ$) completely disappeared from the diffractogram. It can be assumed that the metallic iron phases has transformed during the Fischer-Tropsch synthesis. No other information can be gathered from these diffractograms.

III.2.3. Iron phases determination by ^{57}Fe Mössbauer spectroscopy

Mössbauer spectroscopy was applied (at room temperature) to gain insight of the iron species. After FTS testing, the spent catalyst was recovered from the reactor. Therefore, the spent catalyst was in contact with air, meaning that the catalyst most likely re-oxidized partially with the oxygen. The catalyst Mössbauer spectrum was taken after 100 hours on stream at 280 °C. Mössbauer spectroscopy has been carried out on the Fe/hollow-silicalite-1

catalyst. The Mössbauer spectrum is displayed on **Figure 75** and the hyperfine interaction parameter are summarized in **Table 25**.

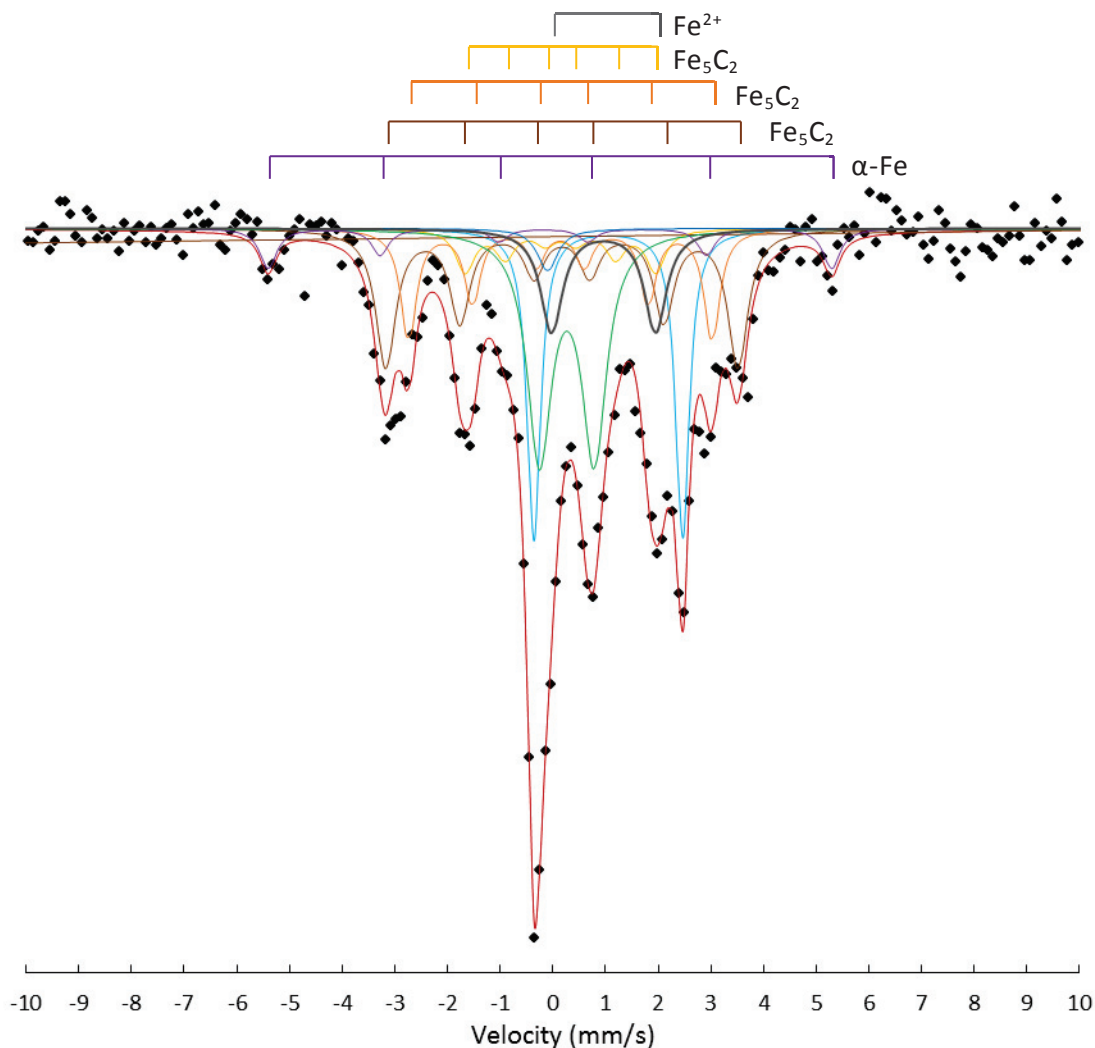


Figure 75 | ^{57}Fe Mössbauer spectrum of the Fe/hollow-silicalite-1 catalyst after FTS: Experimental spectrum (black dot), experimental spectrum fit (red line), α -Fe in large particles (purple line), metallic Fe^0 (blue line), Fe^{3+} (green line), Fe^{2+} (grey and blue line) and Fe_5C_2 carbides (brown, orange and yellow line).

Eight components can be distinguished for the spent catalyst spectrum: a magnetic hyperfine sextet with narrow lines and a hyperfine field of 33.0 T (relative intensity 6 %), three quadrupolar hyperfine doublets with a quadrupolar splitting of $QS = 1.04 \text{ mm}\cdot\text{s}^{-1}$, $QS = 1.13 \text{ mm}\cdot\text{s}^{-1}$ and $QS = 1.96 \text{ mm}\cdot\text{s}^{-1}$ (with a relative intensity respectively of 23 %, 17 % and 9 %), three small sextets with a magnetic field of 11.1, 17.8 and 20.7 T (with a relative intensity respectively of 7 %, 14 % and 23 %) and a hyperfine singlet (relative intensity 1 %).

Table 25 | The Mössbauer fitted parameters for the spent Fe/hollow-silicalite-1 catalyst

| Sample | Splitting | IS (mm.s ⁻¹) | QS (mm.s ⁻¹) | Hyperfine field (T) | Species | Relative intensity (%) |
|----------------------------|-----------|-----------------------------|-----------------------------|------------------------|--------------------------------|---------------------------|
| Fe/hollow- silicalite-1 | Singlet | 0.00 | - | - | α -Fe | 1 |
| | Sextet | -0.01 | - | 33.0 | α -Fe | 6 |
| | Doublet | 0.35 | 1.04 | - | Fe ³⁺ | 23 |
| | Doublet | 1.13 | 2.81 | - | Fe ²⁺ | 17 |
| | Doublet | 1.06 | 1.96 | - | Fe ²⁺ | 9 |
| | Sextet | 0.26 | - | 20.7 | Fe ₅ C ₂ | 23 |
| | Sextet | 0.24 | - | 17.8 | Fe ₅ C ₂ | 14 |
| | Sextet | 0.25 | - | 11.1 | Fe ₅ C ₂ | 7 |

The three doublets with an isomer shift of QS = 0.35 mm.s⁻¹, δ = 1.13 mm.s⁻¹ and QS = 1.06 mm.s⁻¹ can be assigned respectively to Fe³⁺ and the other two to Fe²⁺ compounds [122, 123]. The singlet is assigned to the small superparamagnetic metallic iron nano particles (α -Fe) [119]. The sextet is assigned to larger metallic iron particles (α -Fe) [120, 119, 121]. The remaining sextets with an isomeric shift of 0.26 mm.s⁻¹, 0.24 mm.s⁻¹ and 0.25 mm.s⁻¹ are attributed to iron carbides and more particularly to Hägg carbides (Fe₅C₂) [70, 118]. It can be noticed that between the fresh and spent catalyst, the relative proportion of Fe³⁺ and Fe²⁺ species remains similar (~50 %). However, the relative amounts of metallic iron after Fischer-Tropsch are quite remarkable. The amounts decrease from 53 % to less than 7 %. Also, a large amount of carbides can be identified (~44 %). When comparing the Fe/hollow-silicalite-1 and the Fe@hollow-silicalite-1 catalyst, it can be noticed that the two catalysts are quite similar in terms of iron phases. However, the relative intensity for those phases are different. In both cases the amounts of iron oxides (Fe³⁺ and Fe²⁺ species) did not decrease much during Fischer-Tropsch. These observations do not mean that oxides did not transform at all during FTS. In all cases, the significant observation is the diminution of the α -Fe sextet signal, from 23 % to 8 % for Fe@hollow-silicalite-1 and from 53 % to 6 % for Fe/hollow-silicalite-1. Also the formation of iron carbides phases is significant too, 10 % for Fe@hollow-silicalite-1 and from 44 % for Fe/hollow-silicalite-1. It is quite difficult to rightfully assume that the increasing in carbides correspond to the decreasing in metallic iron species. In literature [11, 120, 121], it is well known that iron carbides are prepared via carburization in CO medium of metallic iron. However, de Smit et al. [126] confirmed by in-situ XRD (during pretreatment steps and Fischer-

Tropsch synthesis) that α -Fe₂O₃ transformed into Fe₃O₄ and FeO and then in carbides without intermediate metallic iron species formation. Therefore, it is difficult to affirm that carbides formed in our case comes from metallic iron transformation. Even though iron oxides proportion remained similar before and after FTS. Understanding the behavior of iron phases before and after Fischer-Tropsch synthesis is really complex and difficult to apprehend fully.

Conclusion

The Fe/hollow-silicalite-1, even though issued from the failed synthesis for the Fe@hollow-silicalite-1 catalyst, has generated valuable information. It has a quite narrow iron particle distribution (centered on 21.7 nm) with a rather low dispersion (5.2 %). The iron phases contained in the sample are very similar to the Fe@hollow-silicalite-1, which are metallic iron and iron oxides. However, the proportion differs. The Fe/hollow-silicalite-1 catalyst has much larger metallic iron and no small metallic iron particles were observed with Mössbauer, which is logical as the particles are bigger in the Fe/hollow-silicalite-1 material.

This catalyst proves to be less stable and more sensitive to sintering than the Fe@hollow-silicalite-1 catalyst during the Fischer-Tropsch synthesis. This is most likely due to the particles being unprotected outside the zeolite walls. The iron phases obtained after the Fischer-Tropsch reaction are similar to the Fe@hollow-silicalite-1 catalyst. However the amount of iron carbides is significant (45 % in proportion) in the case of the Fe/hollow-silicalite-1. **Table 26** summarizes the main information regarding the Fe/hollow-silicalite-1 catalyst.

Table 26 | Fe/hollow-silicalite-1 catalyst information

| | Fresh catalyst | | | Spent catalyst | | |
|--------------------------|--------------------|----------------|---|-------------------------|----------------|--|
| | Particle size (nm) | Dispersion (%) | Fe species | Mean particle size (nm) | Dispersion (%) | Fe species |
| TEM | 9 - 45 | 5.2 | - | 7 - 97 | 4.6 | - |
| Ex-situ XRD | - | - | α -Fe | - | - | - |
| Ex-situ Mössbauer | - | - | α -Fe, Fe ³⁺ , Fe ²⁺ | - | - | α -Fe, Fe ³⁺ , Fe ²⁺ , Fe ₅ C ₂ |

For ex-situ mössbauer: iron species in bold are in majority in the sample, iron species not in bold are in minority in the sample.

IV. Characterization of a Fe/SiO₂ catalyst

The purpose of this part is to synthesize an iron catalyst with an iron loading similar to the Fe@hollow-silicalite-1 catalyst (~2.5 %wt Fe). A silica with a specific surface area of 750 m²/g is impregnated with an aqueous solution of the metal salt iron (III) nitrate nonahydrate (Fe(NO₃)₃·9H₂O). After calcination and reduction under H₂, a catalyst with iron nanoparticles supported on silica, called Fe/SiO₂ is obtained. It is interesting to study and compare this catalyst with the Fe/hollow-silicalite-1 catalyst as they are relatively similar. This catalyst will be first characterized by various techniques such as transmission electron microscopy, X-ray diffraction and Mössbauer spectroscopy to have an overall understanding of the fresh catalyst. The second part will focus on the spent catalyst.

IV.1. Study of the Fe/SiO₂ catalyst before FTS

IV.1.1. Transmission electron microscopy (TEM)

The Fe/SiO₂ catalyst transmission electron microscopy (TEM) images were taken with the Jeol 2010 LaB6 microscope. The catalysts was reduced at 750 °C with H₂ to form the nanoparticles. After reduction, the catalyst was brought back to air, therefore the catalyst most likely re-oxidized partially in air. The images and particles size distribution are shown in **Figure 76**.

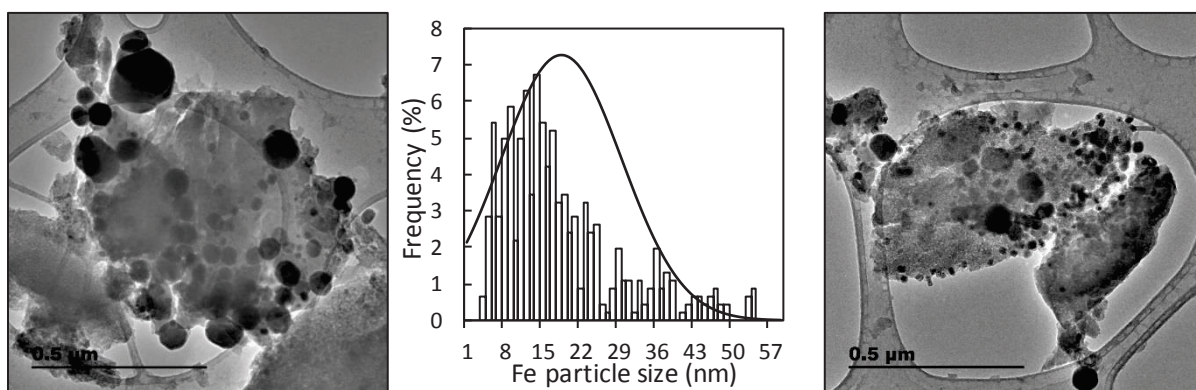


Figure 76 | TEM images and particle size distribution of Fe/SiO₂.

Particles are localized on the silica. The particle size distribution is wide and not well-defined. The particle distribution ranges from around 5 nm to 55 nm. The average particle size

obtained is around 16.7 nm. In terms of dispersion, the Van Hardeveld and Hartog model gives 4.7 %. Finally the Fe loading in the sample was of 2.3 %wt Fe.

IV.1.2. Powder X-ray diffraction (XRD)

The XRD shown in **Figure 77** displays three Fe/SiO₂ catalyst with different loadings (2.3 %wt, 5.8 %wt and 10.1 %wt) after reduction under H₂ at 750°C.

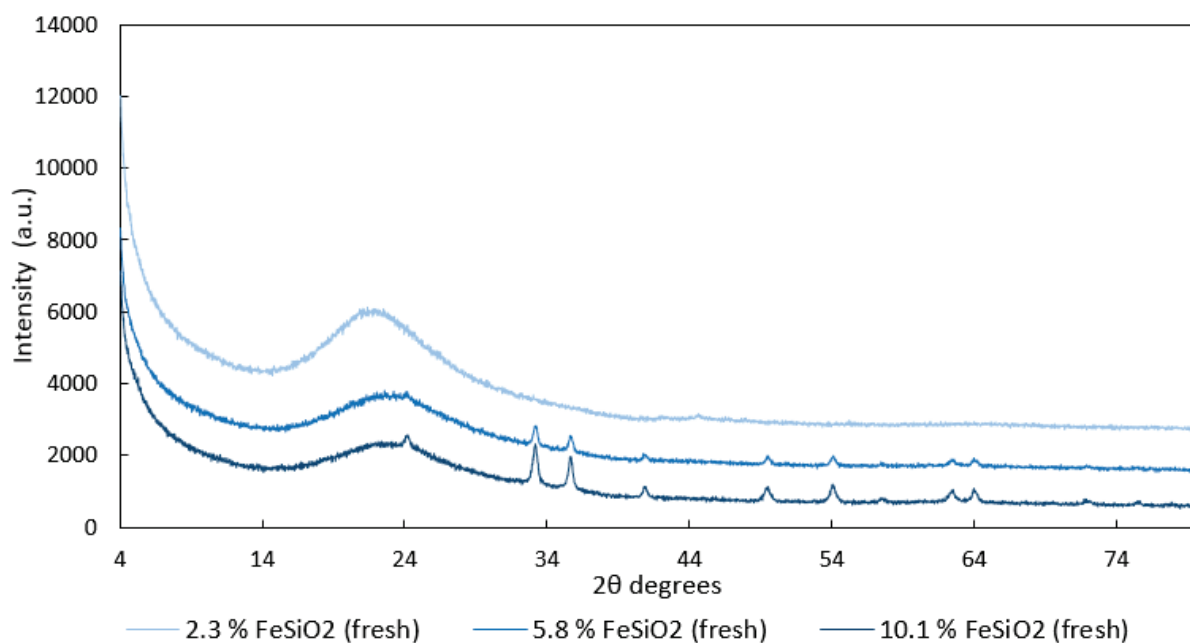


Figure 77 | X-ray diffraction spectrum of Fe/SiO₂ at different loading.

As the 2.3 %wt Fe/SiO₂ X-ray diffractogram did not present any peaks, the loading of Fe was increased to better see the iron phases patterns. The diffractions peaks shown for the sample with a loading of 10.1%wt corresponds to the hematite (Fe₂O₃) diffraction pattern. Therefore, it can be assumed that the sample with the lowest Fe loading, is composed of the exact same phase as its counterpart with higher Fe loading.

IV.1.3. Iron phases determination by ^{57}Fe Mössbauer spectroscopy

Mössbauer spectroscopy was applied (at room temperature) to gain insight of the iron species formed after reduction under H_2 at $750\text{ }^\circ\text{C}$. After reduction, the catalyst was brought back to air, therefore the catalyst most likely re-oxidized partially in air. Mössbauer spectroscopy has been carried out on the fresh Fe/SiO_2 catalyst. The Mössbauer spectrum is displayed on **Figure 78** and the hyperfine interaction parameter are summarized in **Table 27**.

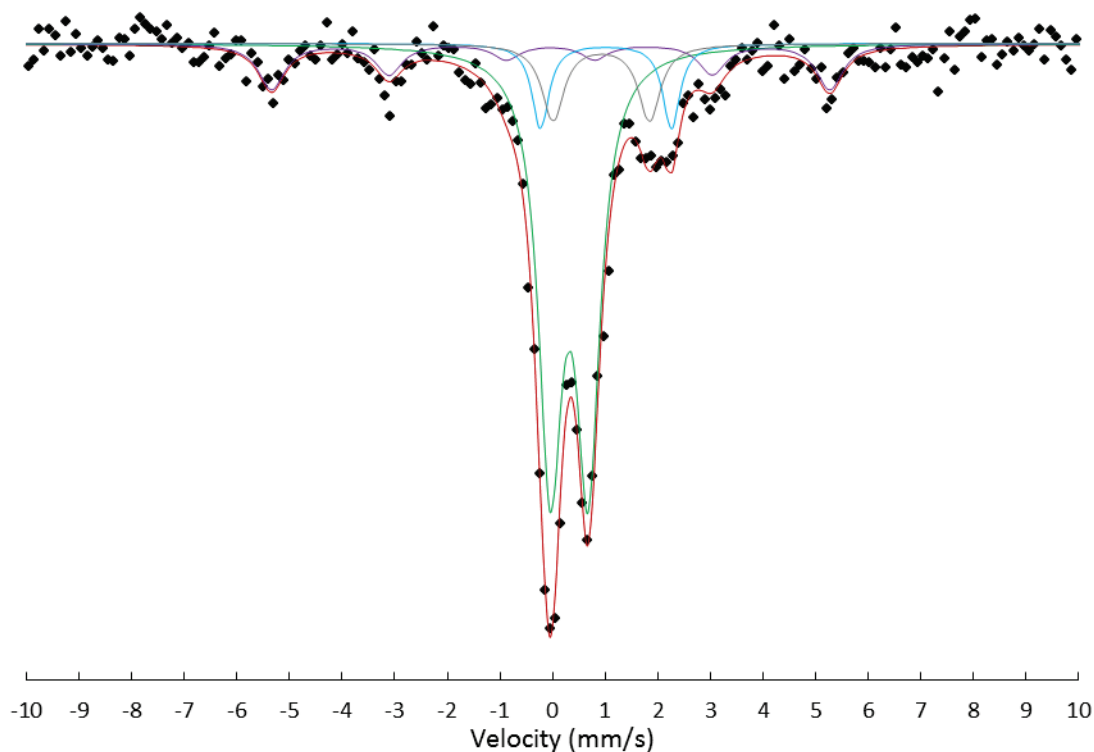


Figure 78 | ^{57}Fe Mössbauer spectrum of the Fe/SiO_2 : Experimental spectrum (black dot), experimental spectrum fit (red line), $\alpha\text{-Fe}$ (purple line), iron oxide Fe^{3+} (green line) and Fe^{2+} (grey line and blue line).

Four components can be identified on the fresh catalyst spectrum after reduction under H_2 at $750\text{ }^\circ\text{C}$: a magnetic hyperfine sextet with narrow lines and a hyperfine field of 32.8 T (relative intensity 16%), a quadrupolar hyperfine doublet with a quadrupolar splitting $QS = 0.72\text{ mm}\cdot\text{s}^{-1}$ (relative intensity 64%) and two quadrupolar hyperfine doublets with a quadrupolar splitting of $QS = 2.48\text{ mm}\cdot\text{s}^{-1}$ and $QS = 1.83\text{ mm}\cdot\text{s}^{-1}$ (relative intensity respectively 9% and 11%).

The two doublets with an isomer shift of $IS = 1.10\text{ mm}\cdot\text{s}^{-1}$ and $IS = 1.02\text{ mm}\cdot\text{s}^{-1}$ can be assigned to Fe^{2+} compounds [122, 123]. Fe^{3+} is attributed to the signal with an isomeric shift of $IS = 0.40\text{ mm}\cdot\text{s}^{-1}$. The sextet is assigned to relatively large metallic iron particles ($\alpha\text{-Fe}$) [120, 119, 121].

Table 27 | The Mössbauer fitted parameters for the fresh Fe/SiO₂

| Sample | Splitting | IS (mm.s ⁻¹) | QS (mm.s ⁻¹) | Hyperfine field (T) | Species | Relative intensity (%) |
|---------------------|-----------|-----------------------------|-----------------------------|------------------------|------------------|---------------------------|
| Fe/SiO ₂ | Doublet | 0.40 | 0.72 | - | Fe ³⁺ | 64 |
| | Doublet | 1.10 | 2.48 | - | Fe ²⁺ | 9 |
| | Doublet | 1.02 | 1.83 | - | Fe ²⁺ | 11 |
| | Sextet | 0.05 | 0.00 | 32.8 | α-Fe | 16 |

Again, the Fe/SiO₂ Mössbauer spectrum is not very different from the Fe/hollow-silicalite-1 and Fe@hollow-silicalite-1 catalyst. In terms of iron phases, the three catalysts are really close. They are mainly composed of iron oxides and metallic iron, but their proportions differ a little.

IV.2. Study of the Fe/SiO₂ catalyst post FTS

IV.2.1. Transmission electron microscopy (TEM)

The spent Fe/SiO₂ catalyst transmission electron microscopy (TEM) images were taken with the Jeol 2010 LaB6 microscope. After FTS testing, the spent catalyst was recovered from the reactor. Therefore, the spent catalyst was in contact with air, meaning that the catalyst most likely re-oxidized partially with the oxygen. The images and particles size distribution are shown in **Figure 79**.

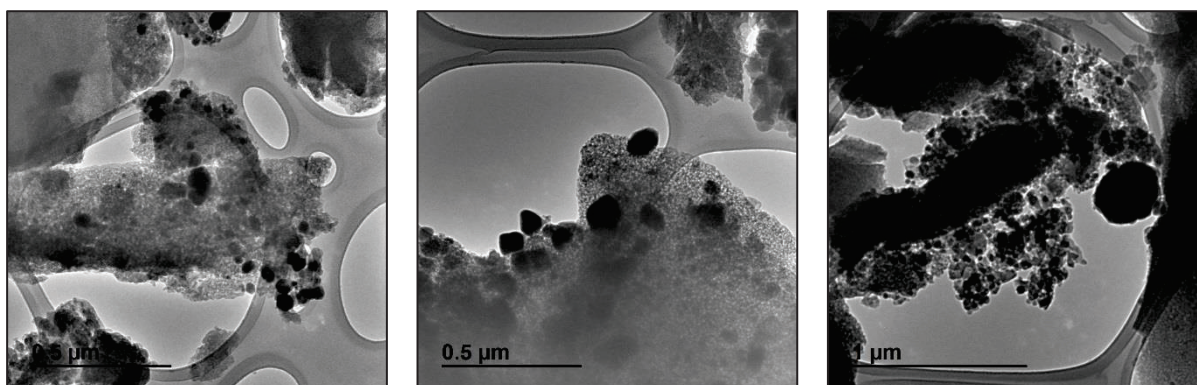


Figure 79 | TEM images of the spent Fe/SiO₂ after 100 hours on stream.

It is rather difficult to give an accurate estimate of the particles size distribution for this sample. The fresh catalyst already had a wide distribution of iron particles. Therefore, the particles size distribution for the spent catalyst might be really similar and no real modification before-after FTS might be seen. The fresh and spent catalysts are indeed similar.

IV.1.3. Powder X-ray diffraction (XRD)

The XRD shown in **Figure 80** displays three fresh Fe/SiO₂ catalyst with different loadings (2.3 %wt, 5.8 %wt and 10.1 %wt) after reduction under H₂ at 750 °C and the spent catalyst with a loading of 2.3 %wt.

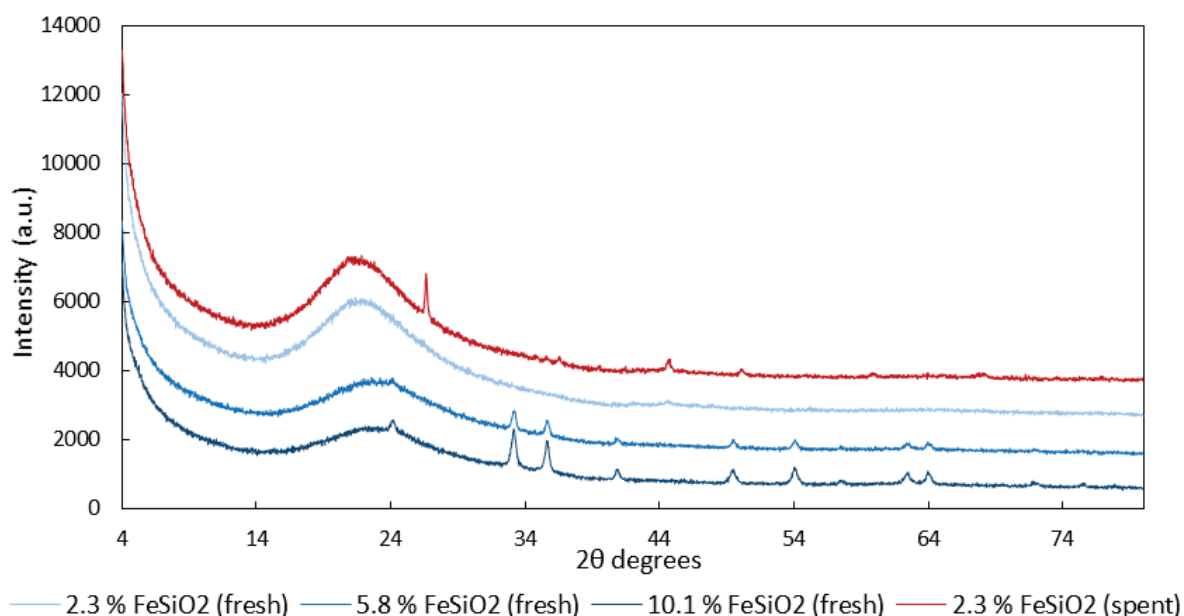


Figure 80 | X-ray diffraction spectrum of Fe/SiO₂ at different loading.

As the 2.3 %wt Fe/SiO₂ has a really low Fe loading, the iron phases peaks are hardly visible on the diffractogram. Still, a few peaks are observable. Those peaks have a different θ than the ones observed for the fresh sample with higher loading. Therefore the catalyst probably transformed during the Fischer-Tropsch synthesis, but no phase can be determined accurately. XRD is not well-adapted for the iron phases characterization on this low loading sample.

IV.2.4. Iron phases determination by ^{57}Fe Mössbauer spectroscopy

Mössbauer spectroscopy was applied (at room temperature) to gain insight of the iron species. Mössbauer spectroscopy has been carried out on the spent Fe/SiO₂ catalyst. After FTS testing, the spent catalyst was recovered from the reactor. Therefore, the spent catalyst was in contact with air, meaning that the catalyst most likely re-oxidized partially with the oxygen. The catalyst Mössbauer spectrum was taken after 100 hours on stream at 280 °C. The Mössbauer spectrum is displayed on **Figure 81** and the hyperfine interaction parameter are summarized in **Table 28**.

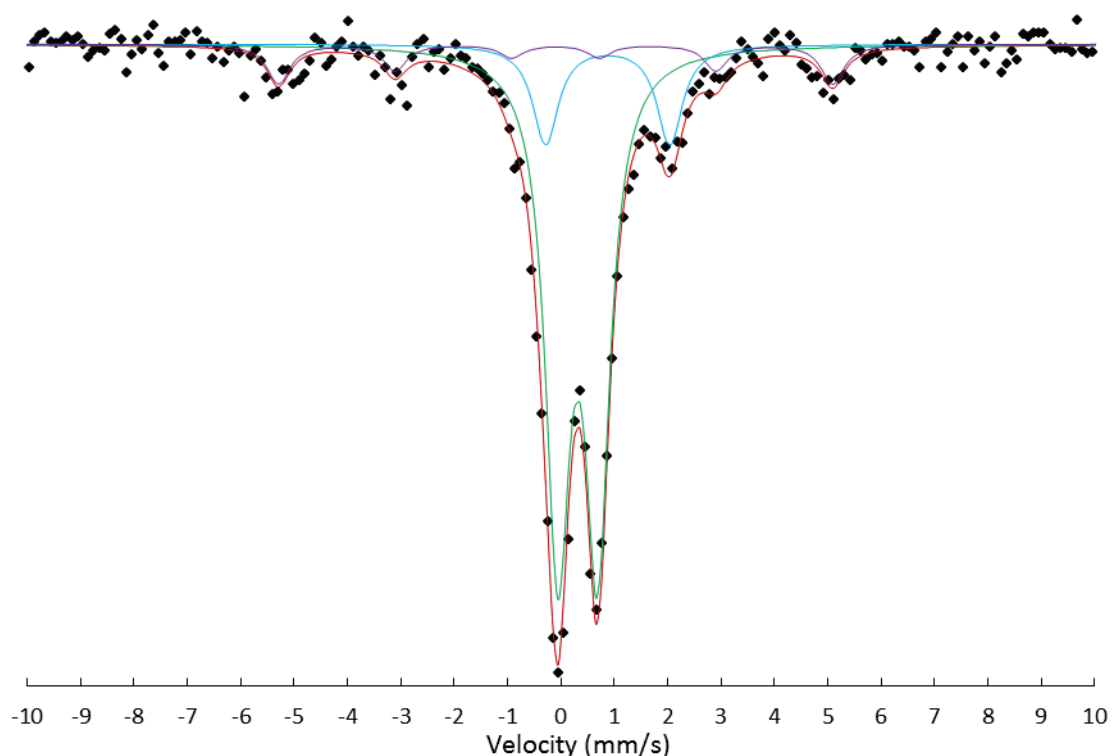


Figure 81 | ^{57}Fe Mössbauer spectrum of the spent Fe/SiO₂: Experimental spectrum (black dot), experimental spectrum fit (red line), α -Fe (purple line), iron oxide Fe³⁺ (green line) and Fe²⁺ (blue line).

Three components can be identified on the spent catalyst spectrum: a magnetic hyperfine sextet with narrow lines and a hyperfine field of 32.1 T (relative intensity 11 %), a quadrupolar hyperfine doublet with a quadrupolar splitting $QS = 0.74 \text{ mm}\cdot\text{s}^{-1}$ (relative intensity 74 %) and a quadrupolar hyperfine doublet with a quadrupolar splitting of $QS = 2.32 \text{ mm}\cdot\text{s}^{-1}$ (relative intensity 15 %).

The doublet with an isomer shift of $IS = 0.97 \text{ mm.s}^{-1}$ can be assigned to Fe^{2+} compounds [122, 123]. Fe^{3+} is attributed to the signal with an isomeric shift of $IS = 0.40 \text{ mm.s}^{-1}$. The sextet is assigned to relatively large metallic iron particles ($\alpha\text{-Fe}$) [120, 119, 121].

Table 28 | The Mössbauer fitted parameters for the spent Fe/SiO₂

| Sample | Splitting | IS (mm.s ⁻¹) | QS (mm.s ⁻¹) | Hyperfine field (T) | Species | Relative intensity (%) |
|---------------------|-----------|-----------------------------|-----------------------------|------------------------|--------------------|---------------------------|
| Fe/SiO ₂ | Doublet | 0.40 | 0.74 | - | Fe ³⁺ | 74 |
| | Doublet | 0.97 | 2.32 | - | Fe ²⁺ | 15 |
| | Sextet | 0.00 | 0.00 | 32.1 | $\alpha\text{-Fe}$ | 11 |

The fresh and spent Fe/SiO₂ catalysts do not show any significant difference. Both have the same iron phases (oxides and metallic) with nearly the same contribution. No carbide phase are observed. Therefore, it is questionable here if the catalyst really transformed during the Fischer-Tropsch reaction.

Conclusion

Fe/SiO₂ catalyst has a wide iron particle size distribution (centered on 16.7 nm) with a rather low dispersion (4.7 %). The sintering effect and/or particle size distribution of the spent Fe/SiO₂ catalyst prove to be difficult to estimate accurately by TEM, as the catalyst looks exactly the same before and after the Fischer-Tropsch synthesis. However XRD analysis reveals an evolution in the iron phases between the fresh and spent catalysts. Besides, Mössbauer spectroscopy shows that the fresh and spent Fe/SiO₂ catalysts present very similar phases to the Fe/hollow-silicalite-1 and Fe@hollow-silicalite1 catalysts, these are metallic iron and iron oxides. Only the proportion differs. Finally, the iron phase proportion of the fresh and spent catalysts, determined by Mössbauer, prove to be very similar, therefore it is difficult to evaluate the iron phase evolution. **Table 29** summarizes the essential information regarding the Fe/SiO₂ catalyst.

Table 29 | Fe/hollow-silicalite-1 catalyst information

| | Fresh catalyst | | | Spent catalyst | | |
|--------------------------|--------------------|----------------|---|-------------------------|----------------|---|
| | Particle size (nm) | Dispersion (%) | Fe species | Mean particle size (nm) | Dispersion (%) | Fe species |
| TEM | 5 - 55 | 4.7 | - | - | - | - |
| Ex-situ XRD | - | - | α -Fe ₂ O ₃ | - | - | - |
| Ex-situ Mössbauer | - | - | α -Fe, Fe³⁺ , Fe²⁺ | - | - | α -Fe, Fe³⁺ , Fe²⁺ |

For ex-situ mössbauer: iron species in bold are in majority in the sample, iron species not in bold are in minority in the sample.

V. Characterization of a nano-structured α -Fe₂O₃ catalyst

A well-controlled bulk-type iron-based catalyst was synthesized for better comparison with the commercial and Fe@hollow-silicalite-1 catalyst. Again this catalyst will be first characterized by various techniques such as transmission electron microscopy, X-ray diffraction and Mössbauer spectroscopy to get an overall understanding of its characteristics. The second part will focus on the evolution of the iron phases during the Fischer-Tropsch synthesis by in-situ XRD and XANES. The last part will concentrate on the spent catalyst characterization.

V.1. Preparation of nano-structured α -Fe₂O₃ catalyst

V.1.1. Preparation of SBA-15 support

Mesoporous silica SBA-15 was synthesized following the recipe from Kerdi et al. [127] adapted from the one reported by Zhao et al. [128]. Briefly a mixture containing 27.75 ml hydrochloric acid (Aldrich, 37 %wt in water), 6 g triblock copolymer (Pluronic® P123) and 192 ml distilled water is stirred for 45 min at room temperature. Then 13.65 ml tetraethyl orthosilicate (TEOS, Aldrich, 98%) is added to this mixture and mixed for 20 hours at 40 °C. The gel mixture obtained is then aged in an autoclave at 130 °C for 24 h. The aging period is required to create internal networks between mesopores to get a pseudo 3D array of pores. The silica SBA-15 is retrieved, washed and dried at 80 - 90 °C. Finally, the silica is calcined in air at 550 °C for 12 h to remove template and surfactant molecules.

V.1.2. Preparation of nanostructured α -Fe₂O₃

The nano-structured α -Fe₂O₃ is prepared following the recipe of Lupo et al. [129] adapted from the one reported by Jiao et al. [130]. Briefly 1.5 g Fe(NO₃)₃.9H₂O (Aldrich, 98% ACS reagent) salt are dissolved in 20 mL ethanol (Sigma-Aldrich, 96% ACS reagent). 1 g SBA-15 silica is added to the Fe in ethanol mixture and stirred at room temperature until complete evaporation of the solvent. At the end a dry powder is obtained (Fe@SBA-15). The brownish powder is calcined in air at 600 °C for 6 h. Finally the calcined powder is treated with a 2 M solution of sodium hydroxide (NaOH, Aldrich) to remove the SBA-15 silica template. The treated powder is

washed several times with distilled water until reaching pH = 7. At the end of the process, a nano-structured $\alpha\text{-Fe}_2\text{O}_3$ material is recovered. The catalyst was also reduced under H_2 for 6 h. Elemental analysis shows that mainly iron oxide is present in the sample, less than 1 %wt silica remains in the sample.

V.2. Study of the nano-structured $\alpha\text{-Fe}_2\text{O}_3$ catalyst before FTS

V.2.1. Transmission electron microscopy (TEM)

TEM images taken with the Jeol 2010 LaB6 microscope of the nano-structured $\alpha\text{-Fe}_2\text{O}_3$ catalyst are shown in **Figure 82**. Nano-filament of iron oxides can be observed with the TEM images and the particle size diameter can be determined. The particle diameter is between 8 to 12 nm. However, with the connections between particles, large well-ordered aggregates are generated.

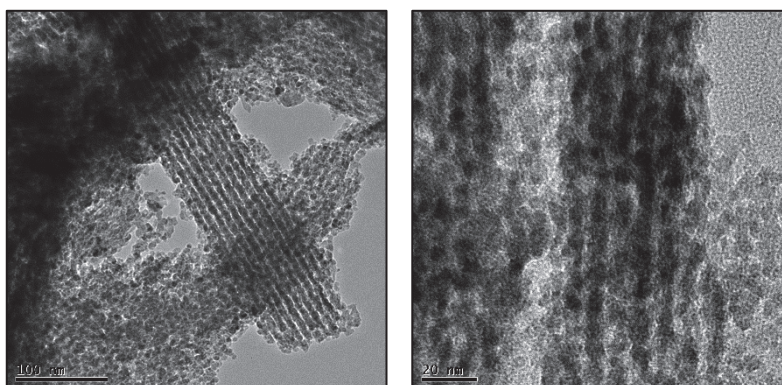


Figure 82 | TEM images of the nano-structured $\alpha\text{-Fe}_2\text{O}_3$ catalyst

A dispersion can be calculated with the particle diameter value obtained with TEM. However the dispersion value might not be accurate as we do not really have well defined particles but instead a continuous arrangement of particles connected with each other's. The dispersion is calculated with the handbook model described in **Chapter 2 - Experimental procedure - II.4.4. Study of nano-particles with TEM**. The dispersion is between 9.7 and 14.5 %.

V.2.2. Powder X-ray diffraction (XRD)

X-ray diffraction (XRD) patterns of the solid were recorded on a Bruker (Siemens) D5005 diffractometer using $\text{CuK}\alpha$ radiation. Diffraction patterns were collected at low angle between 0.45° and 3.45° and at high angle between 4 and 80° (2θ) respectively with steps of 0.01° and 1 s per step and with steps of 0.02° and 1 s per step. The X-ray diffraction pattern of the SBA-15 support, Fe@SBA-15 and the non-reduced and reduced nano-structured $\alpha\text{-Fe}_2\text{O}_3$ catalyst are displayed on **Figure 83**.

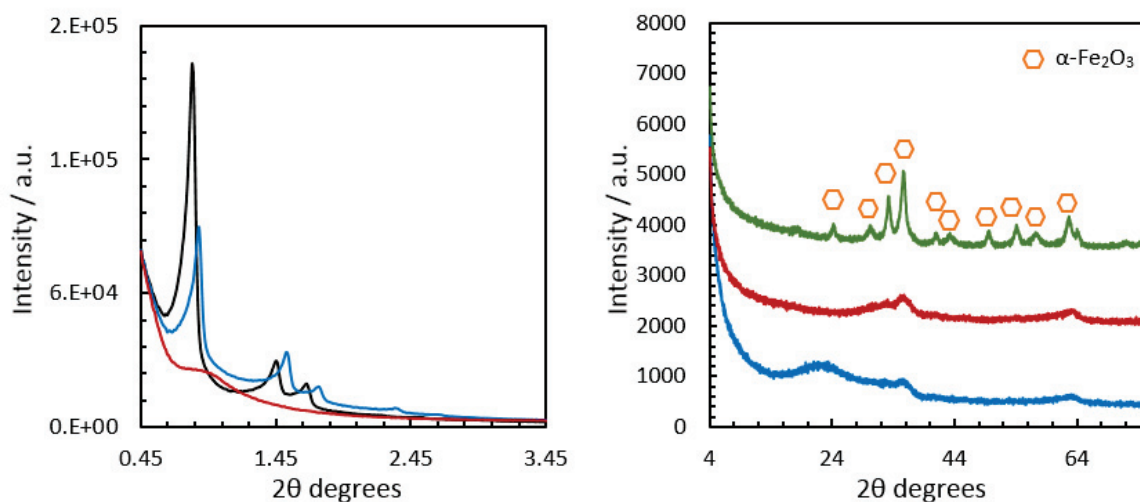


Figure 83 | X-ray diffraction spectrum at low angle (left) and at high angle (right): SBA-15 support (black spectrum), Fe@SBA-15 (blue spectrum), nano-structured $\alpha\text{-Fe}_2\text{O}_3$ (red spectrum) and nano-structured $\alpha\text{-Fe}_2\text{O}_3$ after reduction under H_2 (green spectrum).

We can clearly see the disappearance of the SBA-15 (black spectrum) after the basic treatment on the nano-structured $\alpha\text{-Fe}_2\text{O}_3$ catalyst (red line). We also observe that the catalyst obtained is mostly amorphous (before the reduction under H_2), therefore no phase can be attributed and no calculation of the crystallites size by Debye-Scherrer equation is possible. The catalyst was reduced under H_2 for 6 h and analyzed afterward with XRD, this time, the catalyst was crystallized, and the different peaks were attributed to hematite ($\alpha\text{-Fe}_2\text{O}_3$). The Debye-Scherrer equation could be used to determine the crystallites size and the dispersion. The average crystallites size was about 11.3 nm and the dispersion, calculated with the handbook model, was 10.3 %. These results are in agreement with the dispersion calculated with TEM images (between 9.7 and 14.5).

V.2.3. Iron phases determination by ^{57}Fe Mössbauer spectroscopy

Mössbauer spectroscopy was applied (at room temperature) to gain insight of the iron species present in the reduced nano-structured $\alpha\text{-Fe}_2\text{O}_3$ catalyst. The Mössbauer spectrum is given in **Figure 84** and the Mössbauer parameters (Isomeric shift (IS, $\text{mm}\cdot\text{s}^{-1}$), quadrupolar splitting (QS, $\text{mm}\cdot\text{s}^{-1}$), hyperfine field (T) and Relative intensity (%)) are given in **Table 30**.

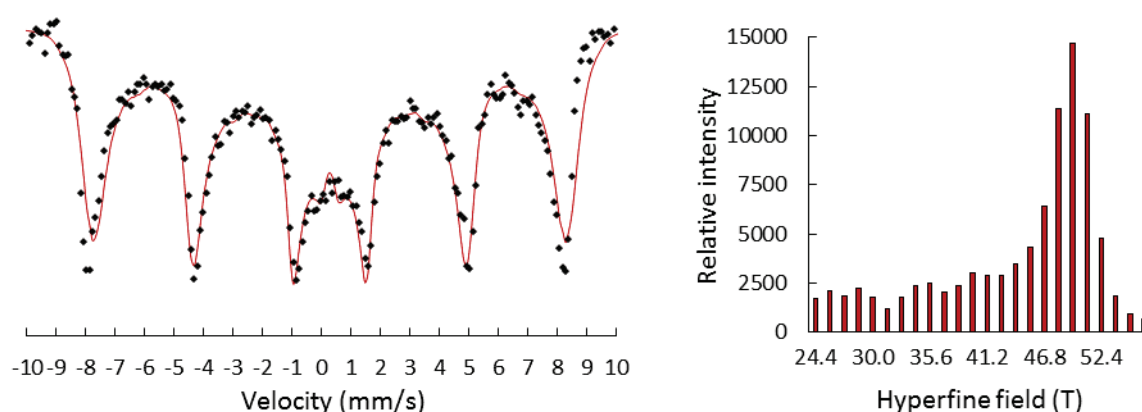


Figure 84 | ^{57}Fe Mössbauer spectrum of the reduced nano-structured $\alpha\text{-Fe}_2\text{O}_3$ catalyst (left): Experimental spectrum (black dot) and $\alpha\text{-Fe}_2\text{O}_3$ fit (red line). Hyperfine field (T) histogram for the magnetic sextet (right).

Table 30 | Mössbauer parameters of the reduced nano-structured $\alpha\text{-Fe}_2\text{O}_3$ catalyst

| Species | $\alpha\text{-Fe}_2\text{O}_3$ |
|--------------------------------------|--------------------------------|
| IS ($\text{mm}\cdot\text{s}^{-1}$) | 0.37 |
| QS ($\text{mm}\cdot\text{s}^{-1}$) | 0.00 |
| Hyperfine field (T) | 49.6 |
| Relative intensity (%) | 100 |

The Mössbauer spectrum is characterized by a wide sextet with a large hyperfine field distribution centered on 49.6 T (bottom-right). This observation is in agreement with Lupu et al. and Jiao et al. characterization of this material [129, 130]. Therefore we can conclude here that this catalyst is actually composed of only one phase, $\alpha\text{-Fe}_2\text{O}_3$.

V.3. Study of the nano-structured α -Fe₂O₃ catalyst during FTS

The *in-situ* measurements were carried out at the European Synchrotron Radiation Facility (ESRF) in Grenoble France, more precisely at the Swiss-Norwegian beam lines BM01. The aim of the experiments was to understand the evolution of the iron phases during FTS using two types of characterization, a surface (XRD) technique and a bulk (XAS) technique. The reduced nano-structured α -Fe₂O₃ catalyst was tested under FTS conditions (H₂:CO = 2:1, 18 bars) at different temperatures (230 °C, 250 °C and 280 °C, 6 h each).

V.3.1. Iron phases determination by *in-situ* XRD

Figure 85 below displays the evolution of the XRD spectrum of the nano-structured α -Fe₂O₃ catalyst in time.

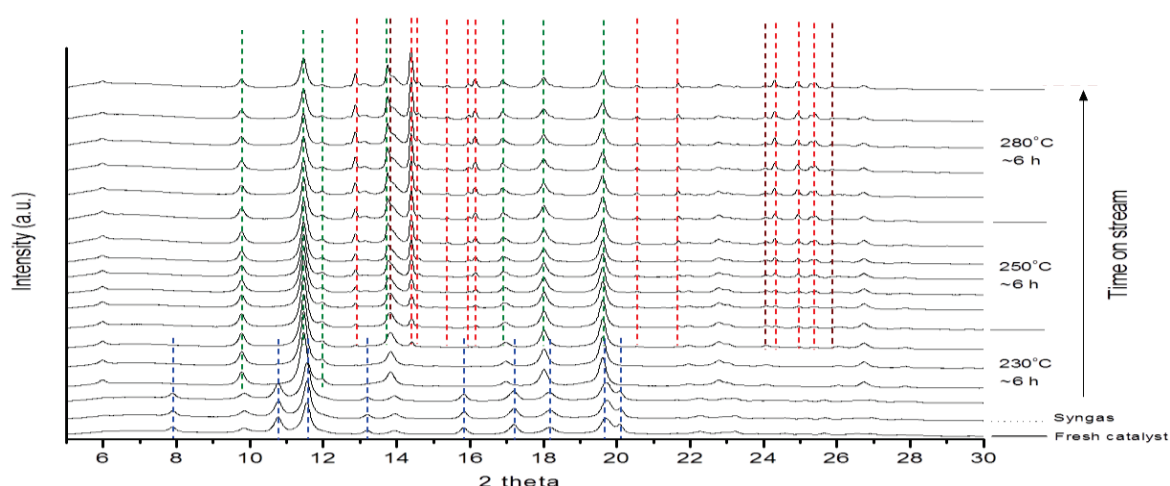


Figure 85 | Evolution of the iron phases with time and at different temperature (°C) by *in-situ* XRD. Fe₃O₄ species (green dashed line), Fe₂O₃ (blue dashed line), Fe₅C₂ (brown dashed line) and Fe₇C₃ (red dashed line).

The crystalline phase evolution suggested the transformation into α -Fe₂O₃ to Fe₃O₄ with formation of Hägg carbide (Fe₅C₂) and another carbide phase corresponding to Fe₇C₃, known as Eckstrom and Adcock carbide, also reported as an active iron carbide phase [11]. This carbide phase appeared at higher temperatures (250 °C and 280 °C) and the main diffraction peak ($2\theta \sim 14.4^\circ$) became narrow and more intense with time on stream, suggesting some sintering of this carbide phase nanoparticles.

V.3.2. Iron phases evolution by *in-situ* XANES

Figure 86 below displays the *in-situ* XANES data-set evolution and the linear combination fitting results. Changes in the pre-edge and white line (main absorption shoulder) during the FTS can be observed. The first scans showed a typical pre-edge characteristic of 1s - 3d electronic transitions in iron oxides compounds, however with increasing temperature, the pre-edge became more metallic and/or carbidic iron. In addition, the intensity of the white line decreased with increasing temperature, which may suggest a progressive reduction of the iron oxide phases. The linear combination fitting at 230 °C indicated the following progressive transformations: $\text{Fe}_2\text{O}_3 \rightarrow \text{Fe}_3\text{O}_4 \rightarrow \text{FeO} \rightarrow \text{Fe}_5\text{C}_2$. Nevertheless the fitting decreases in accuracy at higher temperatures (250 °C and 280 °C) where the Fe_7C_3 carbide phase starts to appear.

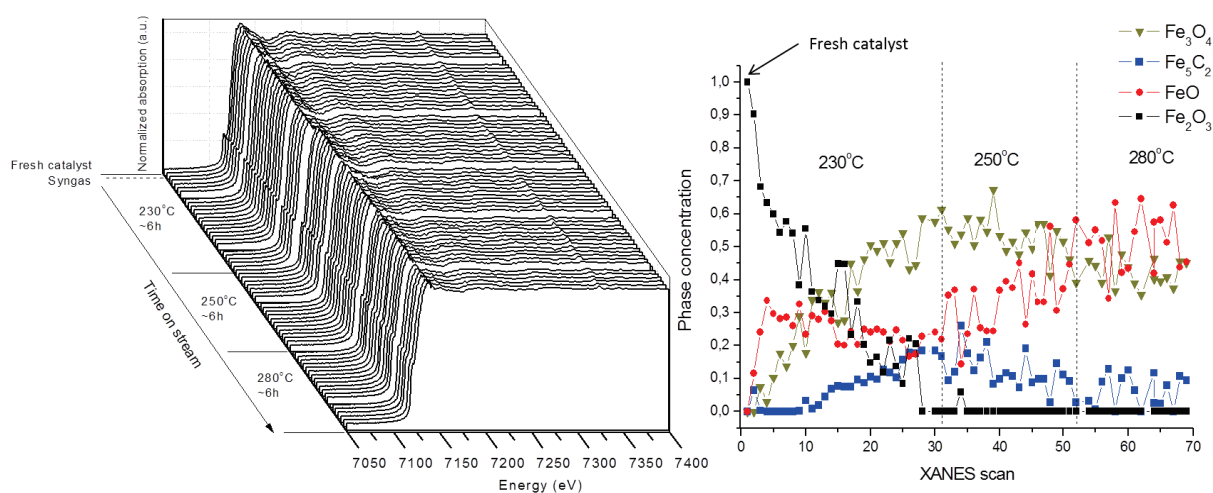


Figure 86 | *In-situ* Xanes evolution (left) and linear combination fitting of iron phases in time (right).

It is well known that the iron carbide phases are made *in-situ* because they can be easily oxidized by oxygen [11]. Consequently the preparation of this carbide as reference is critical here to obtain a better linear combination fitting for future works. Therefore the linear combination fitting does not take into account the Fe_7C_3 carbide. Also there is probably a progressive transformation of carbide phases from Fe_5C_2 to Fe_7C_3 at 250 °C. Both XRD and XANES seem to be in agreement on the evolution of iron phases during FTS.

V.4. Study of the nano-structured α -Fe₂O₃ catalyst after FTS

V.4.1. Transmission electron microscopy after FTS

TEM images taken with the Jeol 2010 LaB6 microscope of the spent nano-structured α -Fe₂O₃ catalyst are shown in **Figure 87**.

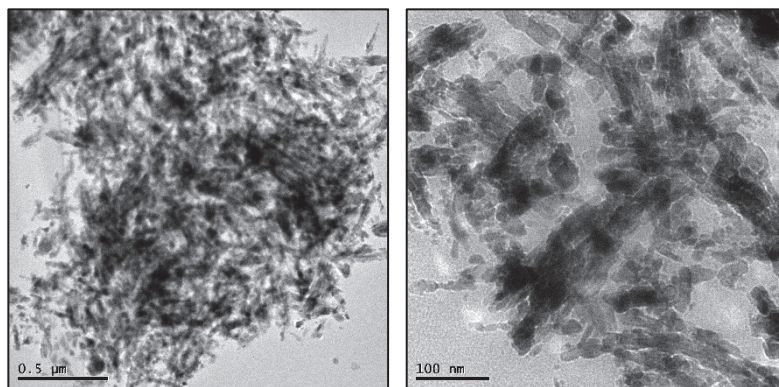


Figure 87 | TEM images of the nano-structured α -Fe₂O₃ catalyst after FTS

The nano-structured α -Fe₂O₃ is shattered. The catalyst structure is completely destroyed after the Fischer-Tropsch synthesis reaction. Therefore we can expect a huge loss in dispersion. Furthermore TEM images do not permit to determine an average particle size.

V.4.2. Determination of iron phases after FTS by *ex-situ* XRD

The X-ray diffraction pattern of the spent nano-structured α -Fe₂O₃ catalyst is displayed on **Figure 88**. After FTS testing, the spent catalyst was recovered from the reactor. Therefore, the spent catalyst was in contact with air, meaning that the catalyst most likely re-oxidized partially with the oxygen.

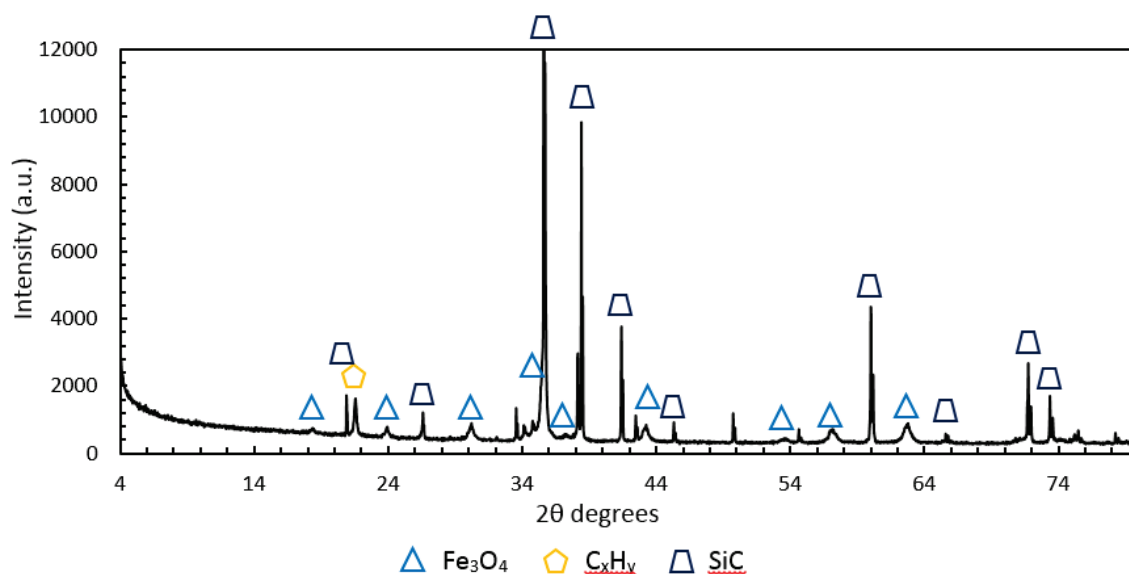


Figure 88 | X-ray diffraction spectrum of the spent nano-structured α - Fe_2O_3 catalyst.

The iron phases determined after Fischer-Tropsch with XRD is mainly magnetite (Fe_3O_4) which is in agreement with the in-situ XRD experiment. However, no other phase such as carbides or FeO can be observed here. Moreover, some SiC is present in the spectrum. SiC was used to maintain the sample in the middle of the reactor, therefore while retrieving the catalyst some of it was taken with the sample. Waxes can be observed in the sample (C_xH_y) [131]. The iron catalyst being crystallized, using the Debye-Scherrer equation to determine the particles size is possible (**Chapter 2 - Experimental procedure - II.1. Powder X-ray Diffraction (XRD)**). Following the Debye-Scherrer equation we could determine the average particle size based on the Fe_3O_4 peaks, an average value of 130.9 nm is obtained and using the handbook dispersion equation (**Chapter 2 - Experimental procedure - II.4.4. Study of nano-particles with TEM**) a dispersion of around 0.89 % is estimated.

V.4.3. Iron phases determination by ^{57}Fe Mössbauer spectroscopy

Mössbauer spectroscopy was applied at room temperature to gain insight of the iron species present in the nano-structured α - Fe_2O_3 catalyst after FTS. After FTS testing, the spent catalyst was recovered from the reactor. Therefore, the spent catalyst was in contact with air, meaning that the catalyst most likely re-oxidized partially with the oxygen. The catalyst Mössbauer spectrum was taken after 100 hours on stream at 280 °C. The Mössbauer spectrum is given in

Figure 89 and the Mössbauer parameters (Isomeric shift (IS, $\text{mm}\cdot\text{s}^{-1}$), quadrupolar splitting (QS, $\text{mm}\cdot\text{s}^{-1}$), hyperfine field (T) and Relative intensity (%)) are given in **Table 31**.

Seven components can be identified for the spent nano-structured $\alpha\text{-Fe}_2\text{O}_3$ catalyst. The Mössbauer spectrum is characterized by two well-defined magnetic sextets characterized by two magnetic field of 48.3 T and 45.0 T. (with a relative intensity respectively 26 % and 50 %), a quadrupolar hyperfine doublet with a quadrupolar splitting of $1.10 \text{ mm}\cdot\text{s}^{-1}$ (relative intensity 2 %), another sextet with a magnetic field of 49.2 T (relative intensity 10 %), and three well-defined sextets with a magnetic field of 10.1, 22.3 and 22.3 T (with a relative intensity of 2 %, 4 % and 5 %, respectively).

The two well-defined sextets are attributed to magnetite (Fe_3O_4) in relatively large particles [44]. The doublet with an isomeric shift of $0.21 \text{ mm}\cdot\text{s}^{-1}$ is attributed to ferric ion (Fe^{3+}) but it is not possible to make definitive assignments as to the exact nature of the species [44, 119], to do that we would need to do Mössbauer analysis at much lower temperature. The sextet with an isomeric shift of $0.34 \text{ mm}\cdot\text{s}^{-1}$ can be attributed to Fe_2O_3 oxide species. The remaining sextets with an isomeric shifts of $0.23 \text{ mm}\cdot\text{s}^{-1}$, $0.24 \text{ mm}\cdot\text{s}^{-1}$ and $0.28 \text{ mm}\cdot\text{s}^{-1}$ are attributed to iron carbides and more particularly to Hägg carbides (Fe_5C_2) [70, 118].

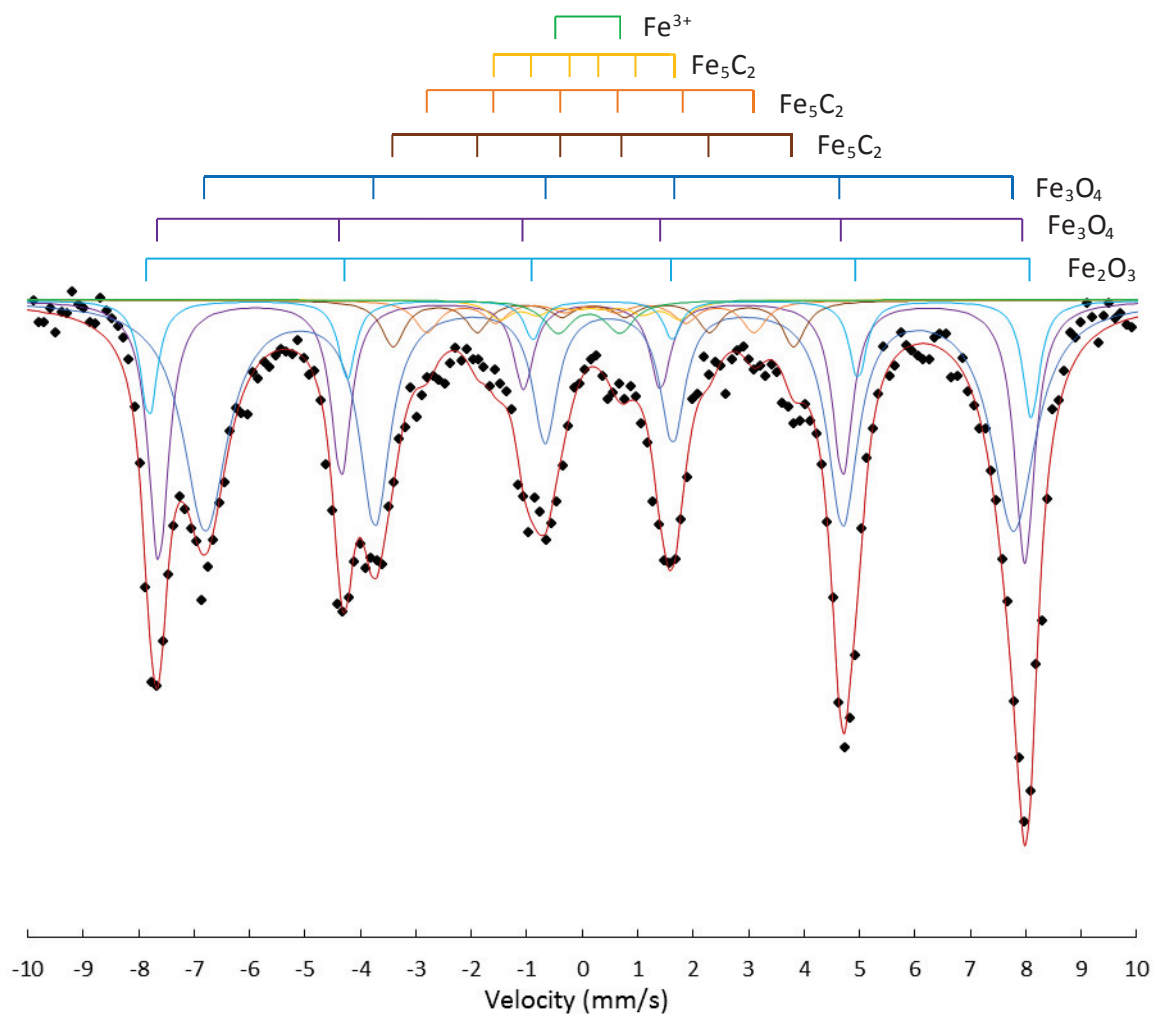


Figure 89 | ^{57}Fe Mössbauer spectrum of the nano-structured $\alpha\text{-Fe}_2\text{O}_3$ catalyst after FTS: Experimental spectrum (black dot), experimental spectrum fit (red line), Fe_3O_4 in large particles (blue line and purple line), Fe^{3+} (green line), Fe_2O_3 (blue line) and Fe_5C_2 carbides (brown, orange and yellow line).

Table 31 | The Mössbauer fitted parameters for the spent nano-structured $\alpha\text{-Fe}_2\text{O}_3$ catalyst

| Sample | Splitting | IS ($\text{mm}\cdot\text{s}^{-1}$) | QS ($\text{mm}\cdot\text{s}^{-1}$) | Hyperfine field (T) | Species | Relative intensity (%) |
|---|-----------|---|---|------------------------|-------------------------|---------------------------|
| Spent nano-structured $\alpha\text{-Fe}_2\text{O}_3$ catalyst | Sextet | 0.26 | 0.00 | 48.3 | Fe_3O_4 | 26 |
| | Sextet | 0.57 | 0.00 | 45.0 | Fe_3O_4 | 50 |
| | Doublet | 0.21 | 1.10 | - | Fe^{3+} | 2 |
| | Sextet | 0.34 | -0.22 | 49.2 | Fe_2O_3 | 10 |
| | Sextet | 0.28 | - | 22.3 | Fe_5C_2 | 5 |
| | Sextet | 0.23 | - | 10.1 | Fe_5C_2 | 2 |
| | Sextet | 0.24 | - | 22.3 | Fe_5C_2 | 4 |

In comparison with the fresh catalyst where only one iron phase was present, the α -Fe₂O₃ oxide, the spent catalyst shows various iron phases (oxides and carbides) revealing the huge difficulty to understand the behavior of iron during Fischer-Tropsch synthesis. The Mössbauer analysis is in agreement with the *in-situ* Xanes analysis. The same phases are observed in both cases (Fe₃O₄, Fe₅C₂). However the duration of the FTS test (time on stream) was different between the two cases, which may explain the small differences (no FeO for the Mössbauer analysis and no more α -Fe₂O₃ oxide for *in-situ* Xanes).

In-situ XRD shows the presence of Eckstrom and Adcock carbide Fe₇C₃. However, this phase was not incorporated in the Mössbauer spectrum of the spent catalyst (**Figure 89**). Therefore, another fit of the experimental spectrum was done, to add this particular phase, and see if the interpretation would change. The Mössbauer spectrum is given in **Figure 90** and the Mössbauer parameters (Isomeric shift (IS, mm.s⁻¹), quadrupolar splitting (QS, mm.s⁻¹), hyperfine field (T) and Relative intensity (%)) are given in **Table 32**.

Again, the two well-defined sextets are attributed to magnetite (Fe₃O₄) in relatively large particles [44]. The sextet with an isomeric shift of 0.34 mm.s⁻¹ can be attributed to Fe₂O₃ oxide species. The remaining sextets with an isomeric shift of 0.30 mm.s⁻¹, 0.25 mm.s⁻¹, 0.24 mm.s⁻¹ and 0.14 mm.s⁻¹ can be attributed to iron carbides (Fe₅C₂, Fe₃C) [70, 118] but, in this case, with Fe₇C₃ carbides [132]. However, as the three carbides have nearly the same Mössbauer parameters, it is difficult to distinguish accurately between them.

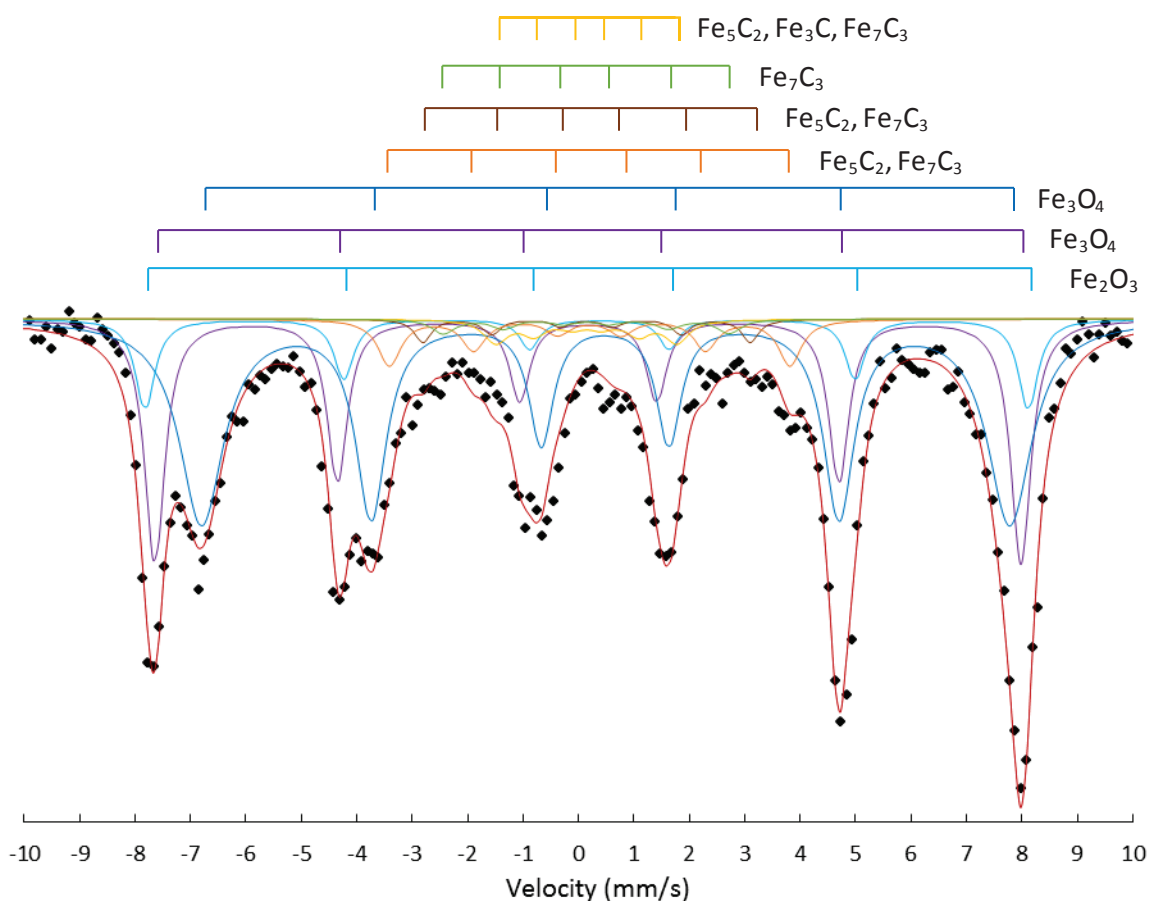


Figure 90 | ^{57}Fe Mössbauer spectrum of the nano-structured $\alpha\text{-Fe}_2\text{O}_3$ catalyst after FTS: Experimental spectrum (black dot), experimental spectrum fit (red line), Fe_3O_4 in large particles (blue line and purple line), Fe^{3+} (blue line) and Fe_5C_2 , Fe_3C and Fe_7C_3 carbides (brown, orange, yellow line and green line).

Table 32 | The Mössbauer fitted parameters for the spent nano-structured $\alpha\text{-Fe}_2\text{O}_3$ catalyst

| Sample | Splitting | IS ($\text{mm}\cdot\text{s}^{-1}$) | QS ($\text{mm}\cdot\text{s}^{-1}$) | Hyperfine field (T) | Species | Relative intensity (%) |
|---|-----------|---|---|------------------------|--|---------------------------|
| Spent nano- structured $\alpha\text{-Fe}_2\text{O}_3$ catalyst | Sextet | 0.27 | 0.00 | 48.3 | Fe_3O_4 | 27 |
| | Sextet | 0.57 | 0.00 | 45.0 | Fe_3O_4 | 50 |
| | Sextet | 0.35 | -0.23 | 49.2 | Fe_2O_3 | 10 |
| | Sextet | 0.30 | - | 22.3 | Fe_3C , Fe_5C_2 , Fe_7C_3 | 6 |
| | Sextet | 0.25 | - | 18.2 | Fe_5C_2 , Fe_7C_3 | 2 |
| | Sextet | 0.24 | - | 15.9 | Fe_7C_3 | 2 |
| | Sextet | 0.14 | - | 10.0 | Fe_5C_2 , Fe_7C_3 | 3 |

The interpretation does not change at all by adding the Fe_7C_3 carbide phase.

Conclusion

The synthesis procedure for the nano-structured α -Fe₂O₃ catalyst is simple and well reproducible. The iron particles are well-ordered and defined. The particle diameter varies between 8 to 12 nm with an iron dispersion of 9.7 to 14.5 %. After Fischer-Tropsch reaction the well-ordered structure is completely shattered and the dispersion drops to < 1 %. XRD, Mössbauer and XANES shows that the fresh catalyst is composed of α -Fe₂O₃. After testing, other types of oxides (Fe₃O₄, Fe₂O₃ and FeO) and carbides (Fe₅C₂ and Fe₇C₃) are observed. The catalyst proves to be really complex in terms of iron phases and looks very similar to the commercial catalyst. **Table 33** summarizes the essential information regarding the nano-structured α -Fe₂O₃ filament catalyst.

Table 33 | Nano-structured α -Fe₂O₃ catalyst information

| | Fresh catalyst | | | Spent catalyst | | |
|--------------------------|-------------------------|----------------|--|-------------------------|----------------|---|
| | Mean particle size (nm) | Dispersion (%) | Fe Species | Mean particle size (nm) | Dispersion (%) | Fe Species |
| TEM | 8 - 12 | 9.7 - 14.5 | - | - | - | - |
| Ex-situ XRD | 11.3 | 10.3 | α -Fe ₂ O ₃ | 130.9 | 0.89 | Fe ₃ O ₄ |
| Ex-situ Mössbauer | - | - | α-Fe₂O₃ | - | - | Fe₃O₄ , Fe ₂ O ₃ , Fe ₅ C ₂ , Fe ³⁺ , (Fe ₇ C ₃) |
| In-situ XRD | - | - | α -Fe ₂ O ₃ | - | - | Fe ₃ O ₄ , Fe ₅ C ₂ , Fe ₇ C ₃ |
| In-situ Xanes | - | - | α -Fe ₂ O ₃ | - | - | Fe ₃ O ₄ , Fe ₂ O ₃ , Fe ₅ C ₂ , FeO |

For ex-situ mössbauer: iron species in bold are in majority in the sample, iron species not in bold are in minority in the sample.

Conclusion

The objectives of this chapter was to characterize the well-controlled iron-nanoparticles encapsulated catalyst to facilitate the establishment of a structure-activity relationship. Herein, transmission electron microscopy (TEM), *ex-situ* and *in-situ* X-ray diffraction (XRD), *ex-situ* and *in-situ* Mössbauer spectroscopy and X-ray absorption near-edge structure spectroscopy (XANES) were the key techniques used in this study. These characterizations have enable the determination of the evolution of the iron phases during the Fischer-Tropsch synthesis and the full characterization of the fresh and spent catalysts in terms of iron phases. Also, the particle size distribution and dispersion of iron particles have been estimated for a better understanding of the catalyst performances during the Fischer-Tropsch synthesis.

The analytical techniques used here can be divided into two categories: the first one to get information on structure and particle size, the other one to have information on the iron phases. TEM and TEM-tomography were mainly used for the determination of the particle size distribution, precise localization of the particles in the sample, and calculation of the dispersion. XRD, Mössbauer spectroscopy and XANES were used for characterizing the state of the catalyst before, during and after the Fischer-Tropsch synthesis.

The studied iron-based catalysts can also be divided into two categories: on one hand there are the bulk-type iron catalysts, such as the commercial and the nano-structured $\alpha\text{-Fe}_2\text{O}_3$ catalysts, and on the other hand, there are the Fe supported on silica-type catalyst, with the Fe@hollow-silicalite-1, Fe/hollow-silicalite-1 and Fe/SiO₂ catalysts.

For the first category, the bulk-type, it was difficult to get an accurate and/or precise information on the particle size distribution and then a proper calculation of the dispersion. The fresh catalysts, both the commercial and the nano-structured $\alpha\text{-Fe}_2\text{O}_3$ ones, were mainly composed of hematite ($\alpha\text{-Fe}_2\text{O}_3$), which makes the fresh catalyst easy to understand. However, the large amount of iron phases present after the Fischer-Tropsch reaction (carbides, oxides) enhanced the difficulty to understand the behavior of the catalyst and/or of each iron phases, during the Fischer-Tropsch synthesis. Finally, the bulk-type catalyst proved to be more impacted by sintering effect during FTS.

The second category, the Fe supported on silica, was easier to characterize in terms of particle size and dispersion. The Fe@hollow-silicalite-1 catalyst has a really narrow particle size distribution and particles located inside the zeolite walls. This catalyst proved to be particularly stable during the Fischer-Tropsch synthesis, as its particles did not sinter much compared to all the other iron-based catalyst studied. In terms of iron phases, the three iron catalysts (Fe@hollow-silicalite-1, Fe/hollow-silicalite-1 and Fe/SiO₂) have the same iron phases (oxides and metallic iron) before and after the Fischer-Tropsch synthesis. However the different phases contributions were not identical. Generally, iron carbides tend to be formed during the FTS, whereas the metallic iron tends to decrease in quantity. In the case of Fe/SiO₂ however, the iron phases remained nearly similar in proportion before and after the FTS. Consequently, it is questionable whether the catalyst really transformed during the Fischer-Tropsch reaction.

A summary table of the main characteristics and features of all the studied catalysts are shown in **Table 34** (for fresh catalysts) and **Table 35** (for spent catalysts) below.

The relation between the structure and characteristics of these catalysts with their Fischer-Tropsch performances (activity, selectivity) will be fully described and discussed in **Chapter 5 - Study of the Fe@hollow-silicalite-1 catalyst: Determination of the relationship between structural features and catalytic performances.**

Table 34 | Summary of the size, dispersion, Fe loading and iron species of the fresh iron catalysts

| Catalysts: | Fe@hollow-silicalite-1 | Fe/hollow-silicalite-1 | Fe/SiO ₂ | Commercial catalyst | Nano-structured α -Fe ₂ O ₃ |
|-----------------------------------|--|---|---|--|--|
| Catalyst info: | | | | | |
| Fe loading (%wt) | 2.5 | 4.2 | 2.3 | Bulk ¹ | Bulk ² |
| Particle size distribution (nm) | 3.6 - 4.6 | 9 - 45 | 5 - 55 | - | 8 - 12 ³ |
| Dispersion (%) | 29 | 5.2 | 4.7 | - | 9.7 - 14.5 |
| Iron phases by techniques: | | | | | |
| <i>Ex-situ</i> XRD | α -Fe | α -Fe | α -Fe ₂ O ₃ | - | α -Fe ₂ O ₃ |
| <i>In-situ</i> XRD | - | - | - | - | α -Fe ₂ O ₃ |
| <i>Ex-situ</i> Mössbauer | α -Fe, Fe ³⁺ , Fe ²⁺ | α -Fe, Fe ³⁺ , Fe ²⁺ | α -Fe, Fe ³⁺ , Fe ²⁺ | α -Fe ₂ O ₃ | α -Fe ₂ O ₃ |
| <i>In-situ</i> Mössbauer | | - | - | - | - |
| <i>In-situ</i> Xanes | FeO, Fe ₂ O ₃ , Fe ₃ O ₄ | - | - | - | α -Fe ₂ O ₃ |

¹ 78.4 %wt Fe₂O₃ for the commercial catalyst. ² The nano-structured α -Fe₂O₃ catalyst is mainly composed of iron oxide.

³ The nano-structured α -Fe₂O₃ does not really have well defined particles but continuous arrangement of particles connected with each other's so the particle size may not be accurate. For ex-situ mössbauer: iron species in bold are in majority in the sample, iron species not in bold are in minority in the sample.

Table 35 | Summary of the size, dispersion, Fe loading and iron phases of the spent iron catalysts (TOS = 100h)

| Catalysts: | Fe@hollow-Silicalite-1 | Fe/hollow-silicalite-1 | Fe/SiO ₂ | Commercial catalyst | Nano-structured α -Fe ₂ O ₃ |
|-----------------------------------|--|--|---|--|---|
| Catalyst info: | | | | | |
| Fe loading (%wt) | 2.5 | 4.2 | 2.3 | Bulk ¹ | Bulk ² |
| Particle size distribution (nm) | 2 - 8 | 7 - 97 | - | 24.6 ³ | 130.9 ³ |
| Dispersion (%) | 19 | 4.6 | - | 4.7 ³ | 0.87 ³ |
| Iron phases by techniques: | | | | | |
| <i>Ex-situ</i> XRD | - | - | - | Fe ₃ O ₄ , Fe ₅ C ₂ , FeO | Fe ₃ O ₄ |
| <i>In-situ</i> XRD | - | - | - | - | Fe ₃ O ₄ , Fe ₅ C ₂ , Fe ₇ C ₃ |
| <i>Ex-situ</i> Mössbauer | α -Fe, Fe ³⁺ , Fe ²⁺ , Fe ₅ C ₂ | α -Fe, Fe ³⁺ , Fe ²⁺ , Fe ₅ C ₂ | α -Fe, Fe ³⁺ , Fe ²⁺ | Fe ₃ O ₄ , Fe ₂ O ₃ , Fe ₅ C ₂ , Fe ³⁺ , Fe ²⁺ | Fe₃O₄ , Fe ₂ O ₃ , Fe ₅ C ₂ , Fe ³⁺ |
| <i>In-situ</i> Mössbauer | | - | - | - | - |
| <i>In-situ</i> Xanes | FeO, Fe ₂ O ₃ , Fe ₃ O ₄ | - | - | - | Fe ₃ O ₄ , Fe ₂ O ₃ , Fe ₅ C ₂ , FeO |

¹ 78.4 %wt Fe₂O₃ for the commercial catalyst. ² The nano-structured α -Fe₂O₃ catalyst is mainly composed of iron oxide. ³ The average size and dispersion were calculated with Debye-Scherrer equation, these values may not be totally accurate. For *ex-situ* Mössbauer: iron species in bold are in majority in the sample, iron species not in bold are in minority in the sample.

Chapter 4 - Study of the Fischer-Tropsch synthesis on iron-based catalysts

Chapter 4 - Study of the Fischer-Tropsch synthesis on iron-based catalysts. 145

| | |
|---|------------|
| Introduction | 146 |
| I. Catalytic testing on the iron co-precipitated commercial catalyst..... | 147 |
| I.1. Fischer-Tropsch synthesis catalytic study..... | 147 |
| I.1.1. Validation of rig test..... | 147 |
| I.1.2. Fischer-Tropsch synthesis study at a CO conversion of 20 %..... | 149 |
| I.1.3. Conclusion..... | 151 |
| I.2. Water-gas-shift testing of the commercial catalyst..... | 151 |
| II. Catalytic testing on the Fe@hollow-silicalite-1 catalyst..... | 153 |
| II.1. Fischer-Tropsch synthesis catalytic study | 153 |
| a. Effect of temperature on Fe@hollow-silicalite-1 during FTS..... | 153 |
| b. Effect of GHSV on Fe@hollow-silicalite-1 during FTS..... | 155 |
| c. Effect of Promoters on Fe@hollow-silicalite-1 during FTS..... | 157 |
| d. Conclusion..... | 158 |
| II.2. Fischer-Tropsch synthesis catalytic study: stoichiometry conditions $H_2:CO:CO_2 = 2:0.8:0.2$ | 159 |
| II.3. Water-gas-shift catalytic testing of Fe@hollow-silicalite-1 material | 161 |
| III. Fischer-Tropsch catalytic testing on the other iron-based catalysts..... | 162 |
| Conclusion | 164 |

Introduction

This chapter deals with the catalytic performances of all the well-characterized catalysts described in details in the previous chapter (**Chapter 3 - Characterization of iron-based catalysts**). Catalysts were tested under Fischer-Tropsch synthesis conditions to evaluate their activity, selectivity and stability performances. More importantly, these Fischer-Tropsch tests aimed to unveil and understand the possible relationships between the structural and characteristic features of the different iron catalysts and their catalytic performances.

First of all, the Fischer-Tropsch testing rig was tuned and validated by using a Fe commercial catalyst given by our project partner Johnson Matthey. Our partner provides us with the testing conditions parameters used for Fischer-Tropsch synthesis and the catalyst performances results obtained on their own rig. The aim of this validation was to compare the activity and selectivities data of the commercial catalyst obtained on our rig with the data obtained by Johnson Matthey on their own rig. This comparison work should help to determine if there were deviations between our rig and the one from our partner.

Secondly, each catalyst studied in this study would be tested under Fischer-Tropsch synthesis conditions. However, as each of them are drastically different in terms of structure and features, especially between the bulk-type catalyst and the supported/encapsulated ones, comparison between them proves to be challenging. For an easier and more accurate comparison, all catalysts would be tested at the same pressure, temperature and H₂/CO ratio conditions. However the loading of catalyst and therefore the GHSV will be adapted, so that the CO conversion could be maintained around 20 % \pm 5 %. In that way, catalysts would be compared at quasi iso-conversion and iso-temperature. 20 % conversion allows to have decent activities and selectivities for the various catalysts.

In some cases, the water-gas-shift activity would be investigated to better understand the behavior of CO₂ onto the FTS reaction and the catalysts performances.

The interpretation and discussion of the relationship between the structural and characteristic features of iron catalysts and the catalytic performances will be discussed in more details in **Chapter 5**. This chapter mainly focuses on the catalytic tests without relating directly to the characterization part.

I. Catalytic testing on the iron co-precipitated commercial catalyst

The commercial iron catalyst provided by our partner Johnson Matthey (JM) was tested in Fischer-Tropsch conditions. This co-precipitated catalyst contains 78.4 % Fe₂O₃, 3.4 % CuO, 2.6 % K₂O, 0.04 % Na₂O and 15 % SiO₂. The Fischer-Tropsch synthesis results were compared with those obtained at Johnson Matthey.

I.1. Fischer-Tropsch synthesis catalytic study

I.1.1. Validation of rig test

Validation tests were carried out on a Fe commercial catalyst delivered by our partner Johnson Matthey. This commercial catalyst is a typical iron-based catalyst used in the industry, its Fischer-Tropsch performances are well-known by JM. Our partner provided us with the catalyst, the testing conditions parameters and their recorded performances data. Therefore, to validate and tune our rig properly, the commercial catalyst was tested in the conditions provided, such as we could compare the performances obtained with our testing facility with the data obtained from JM. The aim was to validate the activity and selectivity measurements of the catalyst and to determine if there was any deviation between the two sets of equipment.

For that, 3 g of the commercial catalyst were loaded into a down-flow fixed bed stainless-steel reactor. Due to the low density of the sample, and for ease of post reaction characterization, no diluent was used. The sample was first pre-treated in H₂ at 210 °C for 7 h. After the pre-treatment process, the syngas mixture was passed through the samples. The Fischer-Tropsch reaction was carried out at 20 bar pressure with a syngas mixture H₂:CO with a ratio of 2:1 and a GHSV of 0.6 L.g_{cat}⁻¹.h⁻¹. N₂ was added in the feed as internal standard. The temperature of operation was ramped up to 230 °C, 250 °C and 280 °C during the test to investigate the conversion and selectivity behavior of the catalyst. The catalyst was studied over a period of 100 h (**Figure 91**).

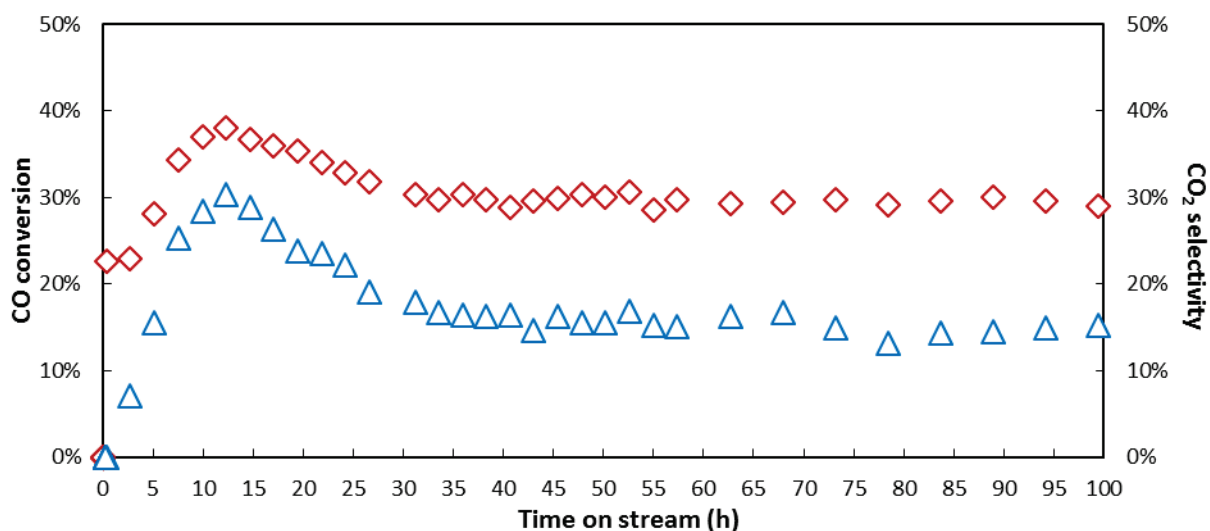


Figure 91 | Stability with time of the JM commercial catalyst at 230 °C. CO conversion in time (◊) and CO₂ selectivity in time (Δ).

Firstly, the catalyst passes through a period of activation for 24 h, where CO conversion increase. Then the CO conversion and CO₂ selectivity tend to stabilized. No important deactivation can be recorded during the first 100 hours on stream. The deactivation characteristics are not measurable over the time period and temperatures studied here. The conversion and selectivities are reported in **Table 36**. For comparison, the data results provided by Johnson Matthey are also reported in **Table 36**.

Table 36 | FTS data of the validation test on the JM commercial catalyst.

| | T (°C) | Conversion (%) | Selectivity (%) | | | |
|-----------------|--------|----------------|-----------------|--------------------------------|-----------------|------------------|
| | | CO | CH ₄ | C ₂ -C ₄ | CO ₂ | C ₅ + |
| CNRS rig | 230 | 29.0 | 2.4 | 6.0 | 14.5 | 77.1 |
| | 250 | 43.9 | 2.3 | 6.2 | 19.5 | 72.0 |
| | 280 | 68.4 | 2.8 | 6.5 | 32.2 | 58.5 |
| JM rig | 230 | 20.5 | 1.9 | 5.4 | 14.1 | 78.6 |
| | 250 | 37.1 | 2.0 | 5.8 | 18.9 | 73.2 |
| | 280 | 62.1 | 2.8 | 6.9 | 29.8 | 60.5 |

Light hydrocarbons selectivity (CH₄ and C₂-C₄ fractions) is rather low compared to other state of the art catalyst which are typically > 10 % for CH₄ and > 15 % for C₂-C₄ fractions (**Chapter 1**

– State of the art – a review a. Products selectivity of Fe-based catalyst during FTS). The CO₂ fraction (32.2 %) at 280 °C is similar to other standard iron catalysts typically ranging from 7.4 % to 44.8 % for temperatures between 250 °C and 300 °C (however it is difficult to really compare catalysts from the literature as each of them is tested under diverse conditions and at different CO conversion levels). The low selectivities in methane and light hydrocarbons as well as the fairly amount of CO₂ results in high selectivity of the desired products, here the C₅₊ hydrocarbon fraction (> 55 %). The C₅₊ selectivity is calculated by $1 - (\%CH_4 + \%C_2-C_4 + \%CO_2)$. A small discrepancy can be observed between our results and those of JM concerning the CO conversion, most likely due to GC chromatography peak integration. However, selectivities are in good agreement between the two rigs. The JM commercial catalyst is particularly water-gas-shift active, as the selectivity of CO₂ indicates. This high CO₂ selectivity is detrimental to the C₅₊ selectivity.

In conclusion, selectivity and activity catalytic measurements on the commercial catalyst are in good agreement with the data performances provided by JM within experimental error.

I.1.2. Fischer-Tropsch synthesis study at a CO conversion of 20 %

Comparing catalysts accurately is difficult as they have different structures and properties. Therefore, for this work, we decided to focus our study for a CO conversion around 20 % at 250 °C (a CO conversion between 15 to 24 % will be tolerated). As explained in the characterization chapter, the iron catalysts are quite different in terms of structure, morphology, particle size and dispersion. For this reason, the mass of catalyst and/or GHSV is adjusted for each catalyst to maintain a 20 % CO conversion at 250 °C. All other conditions such as pressure (P, bar), temperature (T, °C) and H₂/CO ratio of 2:1 will not change (if particular or additional conditions are used, they will be specified in the text). The catalysts comparison will therefore be done at quasi-iso-conversion and iso-temperature.

The following conditions are used all along this chapter: The Fischer-Tropsch reaction is carried out at 20 bar pressure with a syngas mixture H₂:CO in a 2:1 ratio. The operating temperature is ramped up to 250 °C, 260 °C, 270 °C and 280 °C during the test to investigate the conversion and selectivity performances of the catalyst. The catalyst is studied over a standard period of 100 h.

- On Johnson Matthey FTS rig, the Fischer-Tropsch reaction was carried out at a GHSV of $1.57 \text{ L}_{\text{syngas}} \cdot \text{g}_{\text{cat}}^{-1} \cdot \text{h}^{-1}$ from 250 to 270 °C and at a GHSV of $1.32 \text{ L}_{\text{syngas}} \cdot \text{g}_{\text{cat}}^{-1} \cdot \text{h}^{-1}$ for 280 °C. The conversion and selectivities are reported in **Table 37**.

Table 37 | Fischer-Tropsch synthesis results on the commercial catalyst (JM).

| | Conversion (%) | Selectivity (%) | | | |
|--------|----------------|-----------------|--------------------------------|-----------------|------------------|
| T (°C) | CO | CH ₄ | C ₂ -C ₄ | CO ₂ | C ₅ + |
| 250 | 16.3 | 2.8 | 6.9 | 15.7 | 74.6 |
| 260 | 22.5 | 3.1 | 7.8 | 17.9 | 71.2 |
| 270 | 27.8 | 3.5 | 8.1 | 20.2 | 68.2 |
| 280 | 35.5 | 4.7 | 10.4 | 25.8 | 59.1 |

The CO conversion at 250 °C for both rigs remained in the accepted range of comparison (15 to 24 %). The CH₄ and C₂-C₄ selectivities are also in the same range as for the test carried out on our own rig. The activation energy of the commercial catalyst was provided by Johnson Matthey, $E_a = 50 \text{ kJ} \cdot \text{mol}^{-1}$. The apparent activation energy for the kinetic constant is low in comparison to most activation energies for Fischer-Tropsch reaction rates which are typically between 70 and 105 $\text{kJ} \cdot \text{mol}^{-1}$ [133, 134].

- On Johnson Matthey FTS rig, the JM commercial catalyst is tested again to maintain a 20% CO conversion at 250 °C for better comparison letter on. 3 g of the commercial catalyst is tested for a GHSV of $1.28 \text{ L}_{\text{syngas}} \cdot \text{g}_{\text{cat}}^{-1} \cdot \text{h}^{-1}$. The conversion and selectivities are reported in **Table 38**.

Table 38 | Fischer-Tropsch synthesis results on the commercial catalyst at GHSV = $1.28 \text{ L} \cdot \text{g}_{\text{cat}}^{-1} \cdot \text{h}^{-1}$

| | Conversion (%) | Selectivity (%) | | | |
|--------|----------------|-----------------|--------------------------------|-----------------|------------------|
| T (°C) | CO | CH ₄ | C ₂ -C ₄ | CO ₂ | C ₅ + |
| 250 | 23.2 | 2.25 | 5.18 | 14.38 | 78.19 |

Under the above conditions, the CO conversion was maintained around 20 % by adjusting the GHSV (**Figure 92**). The CH₄ and C₂-C₄ selectivities remained low compared to the ones from the ones derived from literature (typically > 10 % for CH₄ and > 15 % for C₂-C₄ fractions). The

CO₂ selectivity is in the same order of magnitude than the previous conditions used for the rig validation test.

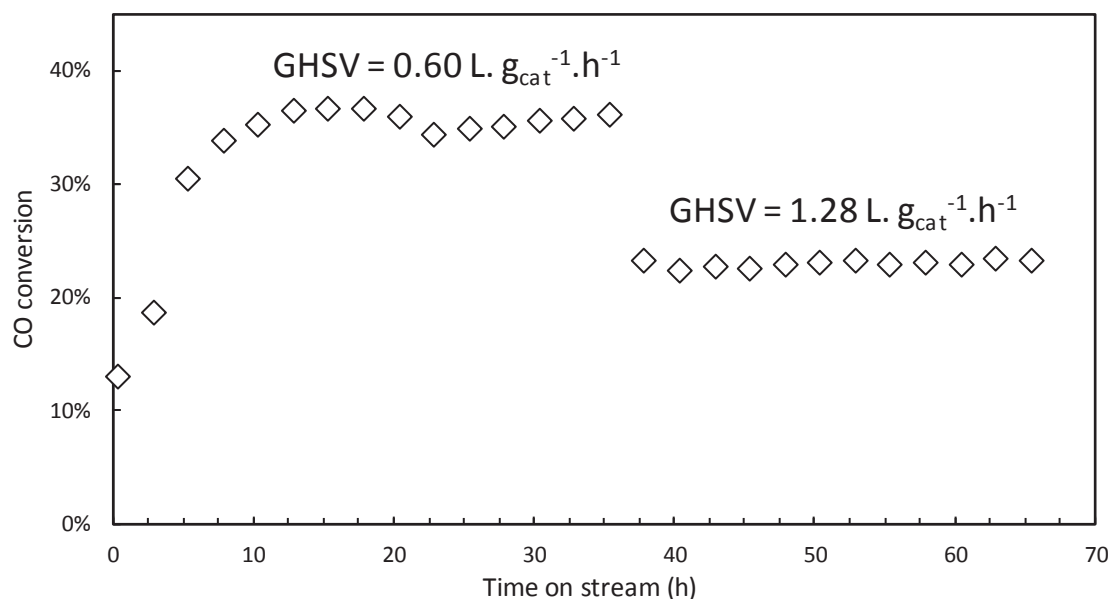


Figure 92 | Stability with time of the JM commercial catalyst at 250 °C. The GHSV is adjusted to maintain a 20 % CO conversion.

I.1.3. Conclusion

The commercial catalyst is a typical co-precipitated iron catalyst for Fischer-Tropsch synthesis. The catalyst proved to have a good overall selectivity to C₅₊ hydrocarbons, with deactivation characteristics that are not measurable over the time period and temperatures studied. The selectivity to CO₂ via the well reported Water-Gas-Shift reaction has the biggest detrimental impact on the C₅₊ hydrocarbons fraction. To fully assess the WGS activity, WGS testing will be carried out.

I.2. Water-gas-shift testing of the commercial catalyst

Water-gas-shift tests were conducted on the commercial catalyst to evaluate its capacity to produce CO₂.

(Equation 46) Water-gas-shift: $\text{CO} + \text{H}_2\text{O} \rightleftharpoons \text{H}_2 + \text{CO}_2$ $\Delta H_{298\text{K}} = -41.1 \text{ kJ.mol}^{-1}$

100 mg of the commercial catalyst was placed in a 4 mm ID fixed-bed continuous-flow quartz reactor.

The catalyst was studied at 2.2 bar with a mixture of H₂O/CO with a ratio of 1:2. N₂ was added in the feed as internal standard. Water was added to the feed via a water saturator. The flow of CO passes through the saturator and takes the water to the reactor. The effect of temperature was studied on the iron catalyst. The operating temperature of operation was ramped up to 250 °C, 260 °C, 270 °C and 280 °C. Each temperature was maintained for 45 min. After the 280 °C plate, the temperature was brought back to 250 °C to evaluate the impact of water on the catalyst. The CO conversion and the evolution of CO₂ and H₂ formation are represented in **Figure 93**.

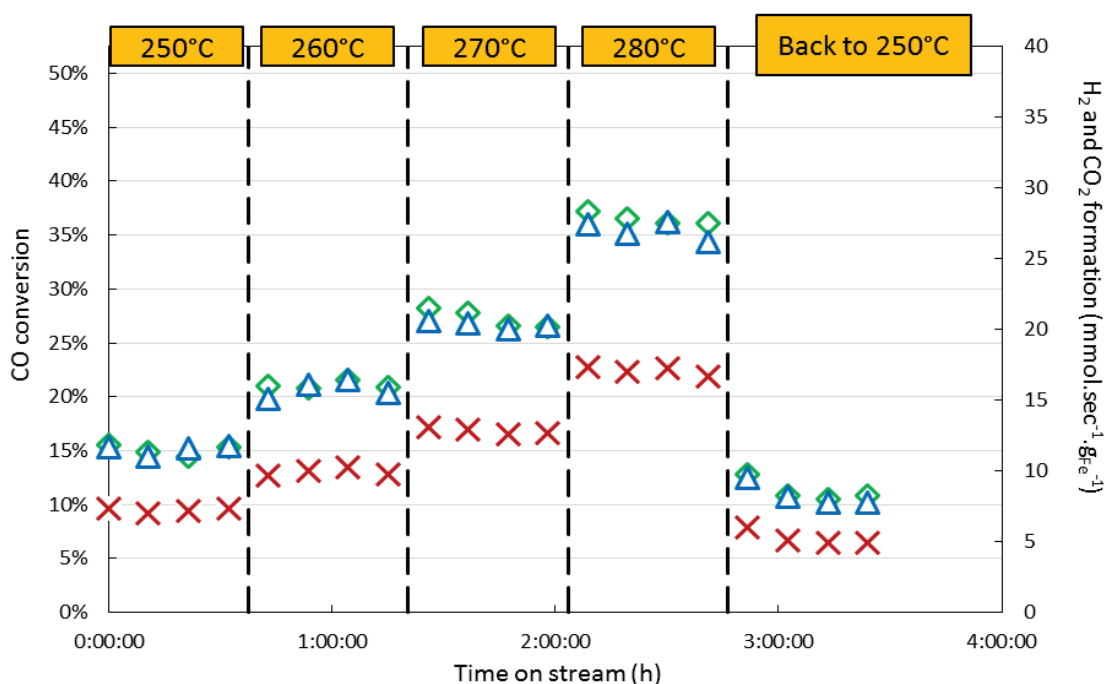


Figure 93 | Evolution of the CO conversion (X), CO₂ formation (Δ) and H₂ formation (◇) with time for the commercial catalyst.

An impact of the temperature on the water-gas-shift activity can be observed. Increasing the temperature increases the CO conversion. Also, the formation of H₂ and CO₂ can be observed. The ratio of H₂ and CO₂ formed is precisely of 1, which is perfectly logical as 1 molecule of CO consumed gives exactly 1 molecule of H₂ and 1 molecule of CO₂. Therefore the commercial catalyst is clearly a water-gas-shift active catalyst.

A diminution of the CO conversion can be noticed when comparing the conversion at 250 °C and post 250 °C. The conversion has decreased by nearly 40 %. Therefore it can be assumed that water is responsible for the catalyst deactivation.

II. Catalytic testing on the Fe@hollow-silicalite-1 catalyst

II.1. Fischer-Tropsch synthesis catalytic study

The well-controlled iron-based catalyst developed in this study denoted Fe@hollow-silicalite-1 was studied in the Fischer-Tropsch conditions detailed above.

a. Effect of temperature on Fe@hollow-silicalite-1 during FTS

The operating temperature was varied during the test to investigate the conversion and selectivity behavior of the catalyst.

▪ At low catalyst loading

To start, a preliminary test was carried out. 440 mg of a 3.4%wtFe@hollow-silicalite-1 catalyst were loaded in the center of the reactor. The experimental data are reported in **Table 39**.

Table 39 | Fischer-Tropsch synthesis data on 3.4%wt Fe@hollow-silicalite-1 at GHSV = 2.2 L.g_{cat}⁻¹.h⁻¹

| T (°C) | Conversion (%) | Selectivity (%) | | | |
|--------|----------------|-----------------|--------------------------------|-----------------|-----------------|
| | CO | CH ₄ | C ₂ -C ₄ | CO ₂ | C ₅₊ |
| 230 | 4.6 | 1.5 | 1.9 | - | 96.6 |
| 250 | 5.5 | 3.5 | 4.9 | - | 91.6 |
| 280 | 7.6 | 11.7 | 15.5 | - | 72.8 |

The Fe@hollow-silicalite-1 catalyst displays a low CO conversion (< 10 %). However in terms of selectivity the catalyst produces really low amounts of CH₄ (< 4 %) and light hydrocarbons (< 5 %) at low temperatures (230 °C - 250 °C). Furthermore no CO₂ is produced by the catalyst. In the end, the desired hydrocarbons fraction (C₅₊) is very high (> 90 %). Those preliminary results are interesting since the catalyst does not produce any CO₂ in contrast to all other known Fe-catalysts [61, 64, 65, 66]. This encapsulated iron-based catalyst does not show activity for the water-gas-shift reaction during Fischer-Tropsch synthesis at low temperature. However, due to the low CO conversions of this catalyst during the FTS we have to remain cautious and critical about the interpretation. Therefore, even though this first test looked motivating, tests at a higher catalyst loading in the reactor would be necessary before making any assumption.

- **At high catalyst loading**

Several tests were conducted at a higher catalyst loading: 1.85 g (~4 times more catalyst than in preliminary test, the highest loading allowed in our setup following the low density of this catalyst). Hence a 2.5%wtFe@hollow-silicalite-1 catalyst is tested. The catalyst is tested for a duration of minimum 100 h for each temperature. The experimental data are reported in **Table 40**.

Table 40 | Fischer-Tropsch synthesis data on 2.5%wtFe@hollow-silicalite-1 at GHSV= 0.53 L.g_{cat}⁻¹.h⁻¹

| T (°C) | Conversion (%) | Selectivity (%) | | | |
|--------|----------------|-----------------|--------------------------------|-----------------|------------------|
| | CO | CH ₄ | C ₂ -C ₄ | CO ₂ | C ₅ + |
| 250 | 19.9 | 15.1 | 22.7 | - | 62.2 |
| 260 | 25.9 | 17.2 | 24.8 | - | 58.0 |
| 270 | 35.1 | 22.4 | 29.2 | 10.0 | 38.4 |
| 280 | 41.4 | 24.9 | 32.1 | 15.4 | 27.6 |

This time the Fe@hollow-silicalite-1 catalyst displays a CO conversion at 250 °C within the range specified (between 15 - 24 %). The conversion is 4 times more important than in the preliminary test. On the other hand the selectivity in CH₄ and C₂-C₄ are quite high compared to JM commercial (between 2 % and 5 % for CH₄ and 6 % to 10 % for C₂-C₄). An increase in temperature tends to increase selectivities in light hydrocarbons and lowering the C₅+ fraction. Again no CO₂ was produced at 250 °C and 260 °C. However, when increasing temperature, the CO₂ starts being produced and reaches 10 - 15 % of selectivity. From these data one can conclude that the catalyst has a water-gas-shift apparent inactivity at low temperature (< 260 °C) and is WGS active at higher temperature (> 260 °C). The Fe@hollow-silicalite-1 catalyst has been tested for 150 h at each temperature and no deactivation was seen during this laps of time (**Figure 94**). The catalyst looks stable with time and resistant to deactivation. The olefin to paraffin ratio are indicated in **Appendix 2**.

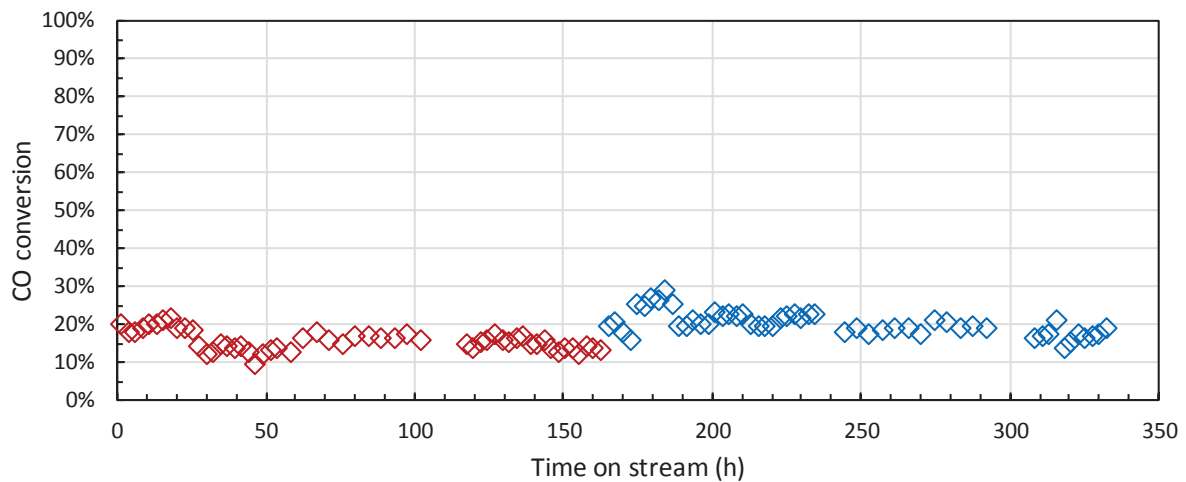


Figure 94 | Stability with time of the Fe@hollow-silicalite-1 catalyst at 250 °C (◊) and 260 °C (◊).

b. Effect of GHSV on Fe@hollow-silicalite-1 during FTS

This time, the gas hourly space velocity (GHSV, $L.g_{cat}^{-1}.h^{-1}$, syngas only) is varied on 1.85 g of a 2.5%wt.Fe@hollow-silicalite-1 catalyst to understand the impact on the Fischer-Tropsch performances (conversion and selectivity). The influence of GHSV on the CO conversion is shown in **Figure 95**. The apparent activation energy (E_a) can be calculated afterwards.

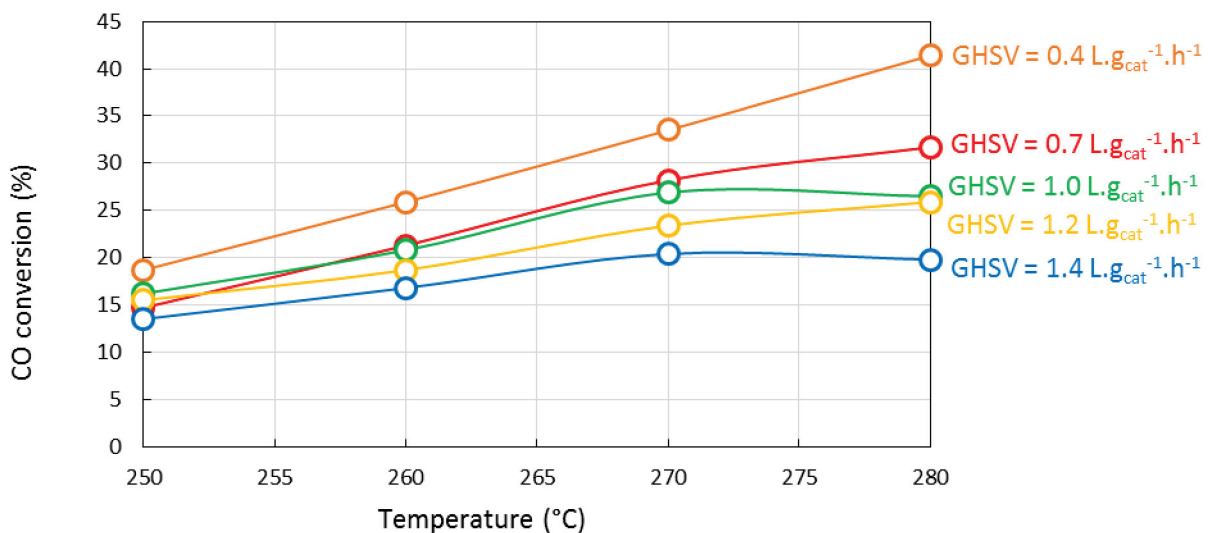


Figure 95 | Influence of GSHV and temperature on CO conversion.

This diagram demonstrates that, as expected, increasing temperature helps to increase the CO conversion. Also as the GHSV increases, the CO conversion decrease. The influence of GHSV has also been observed on selectivity. CH_4 and CO_2 selectivity evolution with GHSV are displayed on **Figure 96**.

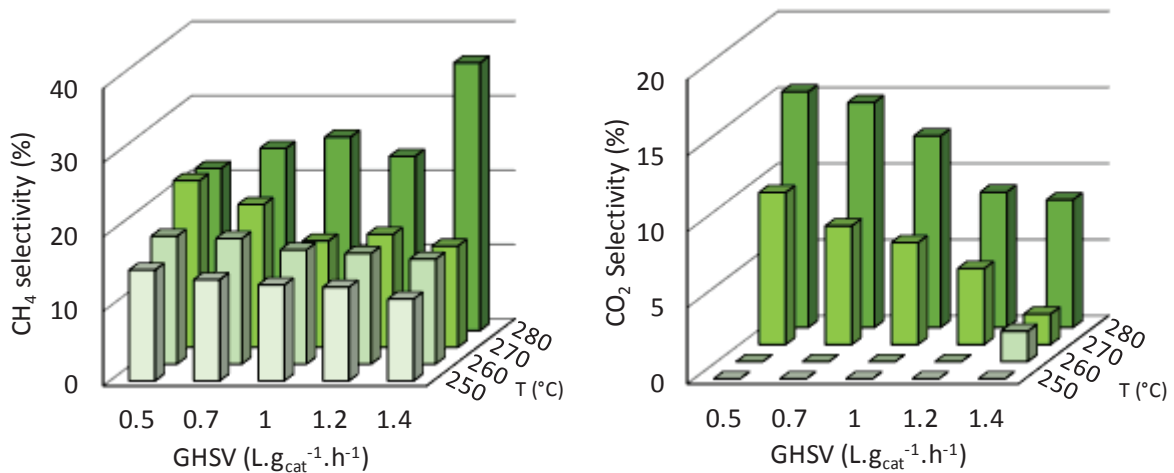


Figure 96 | Influence of GSHV and temperature on CH₄ (left) and CO₂ (right) selectivity

When the GHSV increases, the selectivity in products (CH₄ and C₂-C₄) decreases, especially at temperatures below 270 °C. At 280 °C, the CH₄ selectivity seems to have the opposite behavior. CO₂ is not visible at low temperature which is in agreement with the observation made so far. At higher temperature (270 °C and 280 °C) the CO₂ selectivity tends to decrease when the GHSV increases. The energy of activation (E_a, kJ.mol⁻¹) was determined for each GHSV. Here we make the hypothesis that the rate of reaction (r) evolved linearly with the conversion, furthermore as FTS has an order in CO near 0, we can make the hypothesis that we can calculate the reaction rate and therefore determined an apparent activation energy. The values of the energy of activation are indicated in **Figure 97**.

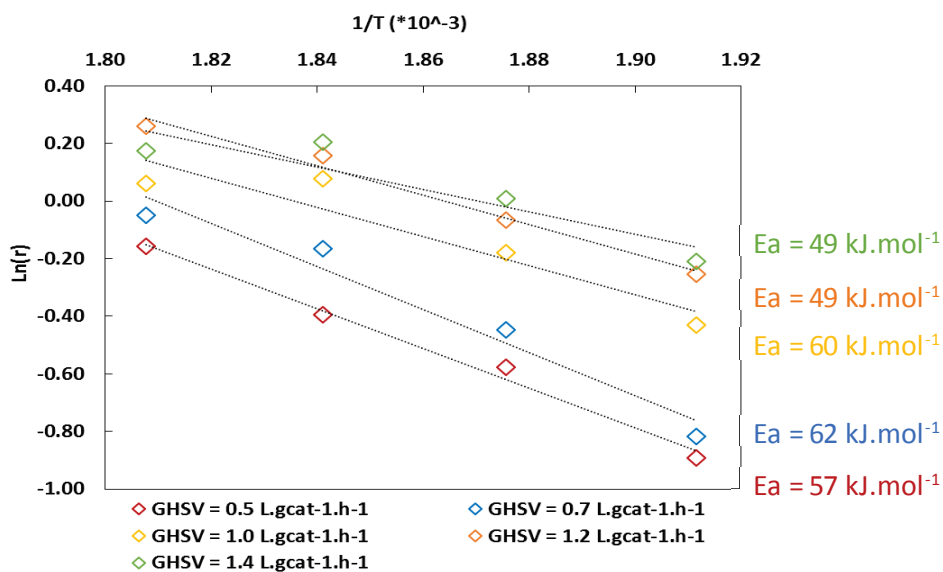


Figure 97 | Energy of activation at different GSHV.

The apparent activation energy for the kinetic constant is low in comparison to most activation energies for Fischer-Tropsch reaction rates which are typically between 70 and 105 kJ.mol⁻¹ [133, 134]. Nevertheless, the activation energy of the Fe@hollow-silicalite-1 is in the same range than the one reported for the JM commercial catalyst (50 kJ.mol⁻¹).

c. Effect of Promoters on Fe@hollow-silicalite-1 during FTS

The effect of promoters (Cu, K) was studied on the iron catalyst. Several tests were carried out at a catalyst loading of 2.0 g of a 2.8%wtFe0.08%wtCu0.03%wtK@hollow-silicalite-1 catalyst. The experimental data are reported in **Table 41**, the unpromoted Fe@hollow-silicalite-1 FTS results obtained previously are also reported here for a better comparison. The catalyst was tested for a duration of minimum 100 h for each temperature.

Table 41 | Fischer-Tropsch synthesis data on 2.8%wtFeCuK@hollow-silicalite-1 at GHSV=0.45 L.g_{cat}⁻¹.h⁻¹

| | | FeCuK@hollow-silicalite-1 | | Fe@hollow-silicalite-1 | |
|-----------------|--------------------------------|---------------------------|--------|------------------------|--------|
| | | 250 °C | 280 °C | 250 °C | 280 °C |
| Conversion (%) | CO | 20.0 | 40.8 | 19.9 | 41.4 |
| | CH ₄ | 7.3 | 18.4 | 15.1 | 24.9 |
| Selectivity (%) | C ₂ -C ₄ | 13.6 | 34.0 | 22.7 | 32.1 |
| | CO ₂ | - | 9.2 | - | 15.4 |
| | C ₅₊ | 79.2 | 38.4 | 62.2 | 27.6 |

The selectivities can be compared since they have been obtained at iso-temperature, iso-GHSV and iso-conversions. We can clearly see that the promoters have a significant effect on the selectivity of the catalyst. Indeed at 250 °C, a decrease in light hydrocarbons fraction (CH₄ and C₂-C₄) can be seen (from 15.1 % to 7.3 % for CH₄ and 22.7 % to 13.6 % for C₂-C₄ fractions) and therefore an increase in the C₅₊ fraction. The decrease in selectivity for light hydrocarbons when adding promoters to the catalyst has been reported in the literature [43, 45, 46, 49, 51, 56]. Promoter such as K was reported to influence the catalytic performances of iron-based FTS catalyst. K is the most widely studied promoter and is known to decrease or suppress the methane formation, improve the olefin selectivity and shift selectivity to higher hydrocarbons chain. Also it improves the dissociative adsorption of CO, strengthens the Fe-C bonds, and

facilitates carbon deposition and catalysts deactivation [43, 45, 46, 49, 51, 56]. While the role of Cu in facilitating catalyst reduction has been widely accepted, its influence on the FTS product distribution has not been well addressed. Some found that Cu has no effect on selectivity whereas others found that selectivity is improved or suppressed [43, 52, 54, 55]. Therefore, the performances modifications when adding K and Cu promoters are in agreement with the literature.

The CO₂ is not produced by the promoted catalyst. At 280 °C, the CO₂ production of the promoted catalyst is ~2 times lower than the CO₂ production from the unpromoted catalyst.

The selectivities of the promoted iron-based encapsulated catalyst is coming closer to the selectivities values of the commercial catalyst (in terms of CH₄ and C₂-C₄). Still more work needs to be done on the addition of promoters to the catalyst. The promoters loading needs to be investigated further to find the best iron-to-promoters ratio. Hence, getting better and competitive selectivities like the commercial catalyst.

The apparent activation energy (E_a) for the promoted catalyst is ~45 kJ.mol⁻¹.

d. Conclusion

There is no apparent CO₂ production for the promoted and unpromoted Fe@hollow-silicalite-1 catalyst at 250 °C. Contrarily, to all other known iron-based catalysts, this Fe@hollow-silicalite-1 catalyst does not show apparent activity for the water-gas-shift (WGS) reaction during Fischer-Tropsch synthesis at low temperature. It shows a high C₅₊ selectivity but CH₄ and C₂ - C₄ selectivities are much higher than the commercial catalyst. The catalyst remained stable with time and no deactivation was observed after a few weeks of testing. It would be interesting to investigate further the WGS reaction on this catalyst. Also adding a small amount of CO₂ in the feed might help to understand the particular behavior of this catalyst.

II.2. Fischer-Tropsch synthesis catalytic study: stoichiometry conditions

H₂:CO:CO₂ = 2:0.8:0.2

Two WGS tests are carried out on the unpromoted 2.5wtFe@hollow-silicalite-1 and the promoted 2.8wtFe0.08wtCu0.03wtK@hollow-silicalite-1. The Fischer-Tropsch reaction is carried out at 20 bar pressure with a H₂:CO:CO₂ ratio of 2:0.8:0.2 with a GHSV of 1.0 L.g_{cat}⁻¹.h⁻¹ syngas (H₂, CO, CO₂) and 0.9 L.g_{cat}⁻¹.h⁻¹ syngas (H₂, CO, CO₂), respectively for the unpromoted and promoted iron catalyst. The CO conversion and selectivities are showed in **Table 42** below. The selectivities can be compared because they have been obtained at iso-temperature, (quasi) iso-GHSV and (quasi) iso-conversions.

In terms of conversion and selectivities, observations and conclusions made earlier on the previous tests are still valid. This time, the CO₂ behavior is of interest. In **Table 42** one can observed negative value of the conversion in CO₂, the “negative conversion” means that the CO₂ is not converted. A negative CO₂ selectivity means that the CO₂ is being converted.

Table 42 | Fischer-Tropsch synthesis data on Fe@ and FeCuK@hollow-silicalite-1

| | | Fe@hollow-silicalite-1 | | | | FeCuK@hollow-silicalite-1 | | | |
|-----------------|--------------------------------|------------------------|-------|-------|-------|---------------------------|-------|-------|-------|
| | | 250°C | 260°C | 270°C | 280°C | 250 °C | 260°C | 270°C | 280°C |
| Conversion (%) | CO | 23.5 | 29.1 | 37.2 | 43.7 | 18.8 | 23.0 | 28.0 | 33.3 |
| | CO ₂ (±1.7%) | 6.2 | 4.5 | -0.4 | -7.0 | 1.2 | -1.2 | -2.6 | -3.6 |
| Selectivity (%) | CH ₄ | 11.8 | 13.9 | 18.3 | 21.7 | 8.9 | 12.9 | 16.7 | 18.0 |
| | C ₂ -C ₄ | 14.8 | 16.7 | 20.6 | 25.6 | 14.6 | 21.2 | 25.7 | 26.9 |
| | CO ₂ | -6.5 | -3.2 | 0.3 | 4.0 | -0.6 | 1.4 | 2.4 | 2.4 |
| | C ₅ + | 73.4 | 69.4 | 60.8 | 52.7 | 76.5 | 65.9 | 57.6 | 55.0 |

Indeed in **Table 42** we can clearly see that CO₂ coming from the feed is slightly converted ~6 % at 250 °C for the unpromoted catalyst. Because CO₂ is converted, the CO₂ selectivity has a negative value, as less CO₂ can be observed at the outlet than at the inlet. For the promoted one the CO₂ conversion is less apparent. Even more interesting, the CO₂ ceases to be converted and is produced after reaching 270 °C. Again this behavior is less obvious for the

promoted catalyst. These observations mean that, at low temperature, in presence of CO₂, the reverse water-gas-shift seems to be happening whereas when increasing the temperature the reverse phenomena is visible, the water-gas-shift reaction. **Figure 98** displays the evolution of the CO₂ conversion with temperature.

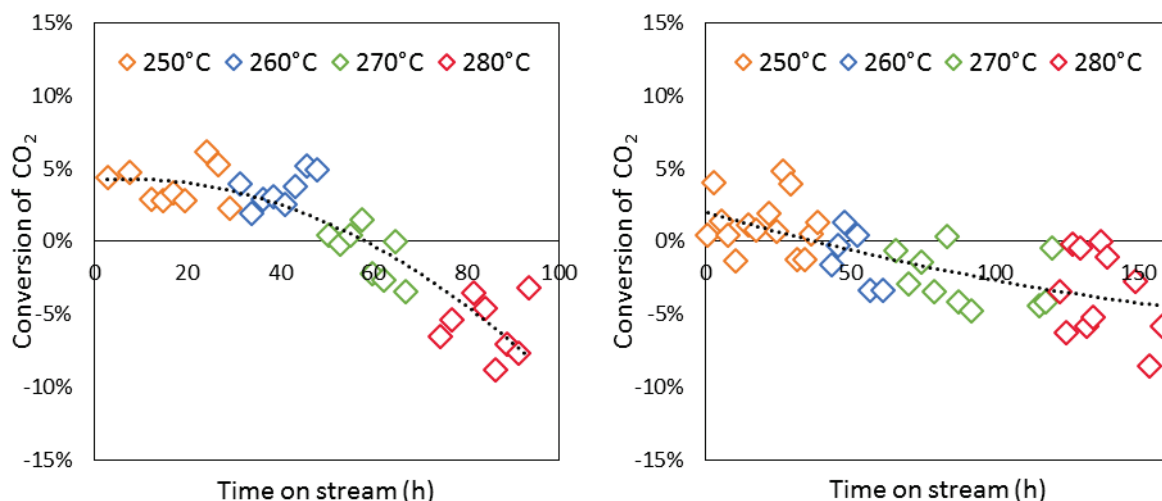


Figure 98 | Evolution of the CO₂ conversion with temperature and time on stream for Fe@hollow-silicalite-1 (left) and FeCuK@hollow-silicalite-1 (right)

The promoted catalyst shows approximately the same CH₄ and C₂ - C₄ selectivities with and without CO₂ in the feed. Whereas for the unpromoted catalyst, the CH₄ and C₂ - C₄ selectivities are lower while adding CO₂ in the feed (15.1 % without CO₂ in the feed and 11.8 with CO₂ in the feed for CH₄ selectivity, 22.7 % without CO₂ in the feed and 14.8 with CO₂ in the feed for C₂ - C₄ selectivity). The catalyst remained stable with time and no deactivation is observed after a few weeks of testing. The major interest here is the absence of CO₂ produced during the Fischer-Tropsch reaction at low temperature. Furthermore, when adding little CO₂ in the feed, one can see that CO₂ is consumed at low temperature, probably meaning that reverse-WGS is happening. By increasing temperature, the WGS reaction is finally happening. These results and the interpretation of this phenomena will be discussed in more details in **Chapter 5 - Study of the Fe@hollow-silicalite-1 catalyst: Determination of the relationship between structural features and catalytic performances.**

II.3. Water-gas-shift catalytic testing of Fe@hollow-silicalite-1 material

We saw earlier that the Fe@hollow-silicalite-1 catalyst does not produce any CO₂ at low temperature during Fischer-Tropsch synthesis. Therefore water-gas-shift tests were conducted on the Fe@hollow-silicalite-1 catalyst to evaluate its capacity to produce CO₂.

(Equation 47) Water-gas-shift: $\text{CO} + \text{H}_2\text{O} \rightleftharpoons \text{H}_2 + \text{CO}_2$ $\Delta H_{298\text{K}} = -41.1 \text{ kJ}\cdot\text{mol}^{-1}$

For that, 250 mg of the catalyst were placed in a 4 mm ID fixed-bed continuous-flow quartz reactor. The catalyst was studied at 2.2 bar with a mixture of H₂O/CO with a ratio of 1:2. N₂ was added in the feed as internal standard. Water was added to the feed via a water saturator. The flow of CO passes through the saturator and take the water to the reactor. The effect of temperature was studied on the iron catalyst. The operating temperature was ramped up to 250 °C, 260 °C, 270 °C and 280 °C. Each temperature was maintained for 45 min. After the 280 °C plate, the temperature was brought back to 250 °C to evaluate the impact of water on the catalyst. The CO conversion and the evolution of CO₂ and H₂ formation are represented in Figure 99.

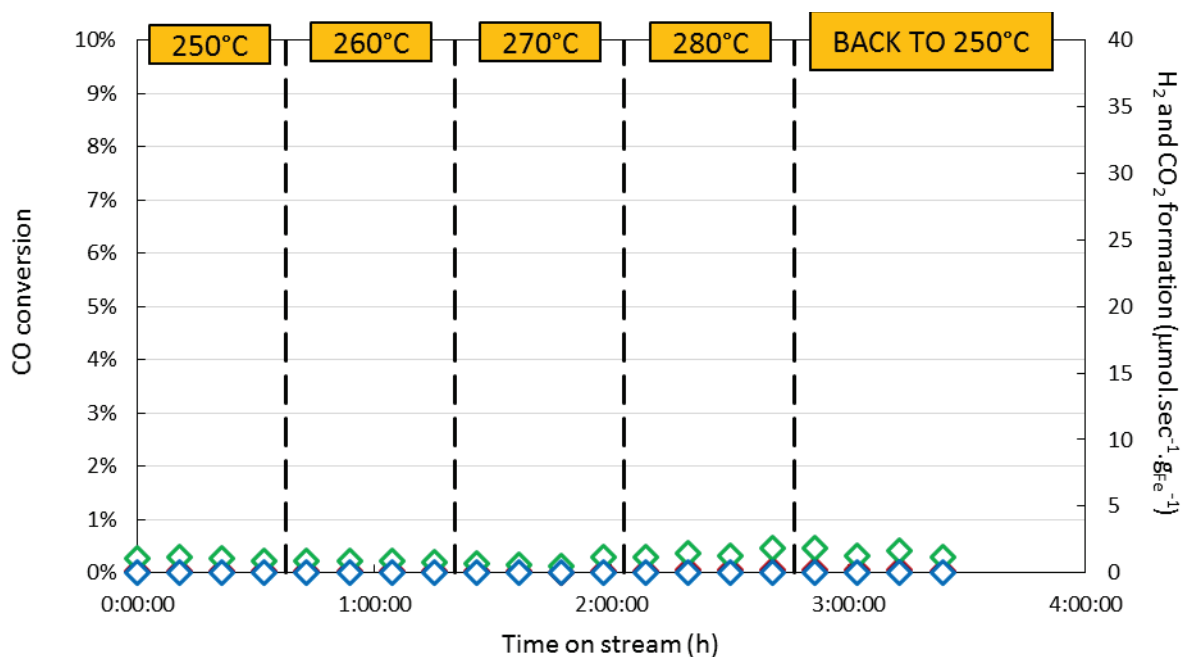


Figure 99 | Evolution of the CO conversion (◇), CO₂ formation (◇) and H₂ formation (◇) with time for the Fe@hollow-silicalite-1 catalyst.

No CO conversion was observed. Therefore no CO₂ or H₂ were produced during this test. This result might be explained either by the fact that we do not have water-gas-shift happening on this catalyst or that the really low loading of iron inside the sample does not permit to observe any activity under the current operating conditions.

The total iron surface area of this sample (250 mg of catalyst) was calculated using the dispersion calculated previously a value of 1.4 m².g⁻¹ is obtained. When comparing this value to the one of the commercial catalyst (1.3 m².g⁻¹), we can see that both are really close. Therefore the same amount of iron surface area is present in both sample. So it can be assumed that, not seeing any water-gas-shift activity for the Fe@hollow-silicalite-1 catalyst, might not be due to the amount of iron present in the sample.

III. Fischer-Tropsch catalytic testing on the other iron-based catalysts

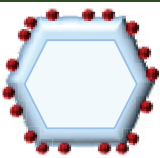


In this part last part, the three other iron-based catalysts studied in **Chapter 3 - Characterization of iron-based catalysts** are tested. A 4.2%wtFe/hollow-silicalite-1 catalyst (GHSV = 0.7 L.g_{cat}⁻¹.h⁻¹), 2.3%wtFe/SiO₂ catalyst (GHSV = 0.3 L.g_{cat}⁻¹.h⁻¹) and the bulk-type nano-structured α-Fe₂O₃ material (GHSV = 2.25 L.g_{cat}⁻¹.h⁻¹) are studied by Fischer-Tropsch synthesis. The conditions of testing are reported at the beginning of this chapter. The catalysts are tested for a duration of minimum 50 h for each temperature. The experimental data of the three catalysts are reported in **Table 43**.

The Fe/hollow-silicalite-1 is very close in terms of structure than the Fe@hollow-silicalite-1 catalyst. The main difference being that its particles are not encapsulated in the zeolite but are mainly localized onto the external surface of the zeolite crystals. The major interest of this catalyst is its quasi non-existence of CO₂ production (1.2 %) which is really similar to the Fe@hollow-silicalite-1 (no production in this case).

The Fe/SiO₂ catalyst shows very poor activity. The methane and C₂-C₄ hydrocarbons fractions selectivities are pretty low (< 2 % for CH₄ and <2 % for C₂-C₄ at 250 °C). The same goes for the CO₂ which is not visible on the chromatogram. The low CO₂ selectivity probably comes from

the low activity of this catalyst, most likely due to no or low water production and poor WGS activity. The Fe/SiO₂ catalyst mass used for this test is two times higher than in the FTS test for the Fe@hollow-silicalite-1 catalyst. The loading in iron is almost identical (2.4 %wt for Fe@hollow-silicalite-1 and 2.3 %wt for Fe/SiO₂). However the big difference is in the dispersion of the iron particle, which is 6 times less than for the Fe@hollow-silicalite-1 catalyst (4.7 % for Fe/SiO₂ and 29 % for Fe@hollow-silicalite-1). In conclusion, the Fe/SiO₂ is most likely not active. Unfortunately, the size of our reactor, did not allow to increase the mass of this catalyst to reach higher conversion levels.

Table 43 | Fischer-Tropsch synthesis data on the three other iron-based catalysts

| T (°C) | Conversion (%) | Selectivity (%) | | | | Catalyst |
|--------|----------------|-----------------|--------------------------------|-----------------|------------------|--|
| | CO | CH ₄ | C ₂ -C ₄ | CO ₂ | C ₅ + | |
| 250 | 28.4 | 18.0 | 34.5 | 1.2 | 46.3 |  Fe/hollow-silicalite-1 |
| 280 | 49.2 | 21.9 | 24.1 | 22.5 | 31.5 | |
| 250 | 7.0 | 1.2 | 1.8 | - | 97.0 |  Fe/SiO ₂ |
| 280 | 9.0 | 4.3 | 6.4 | - | 89.4 | |
| 230 | 19.0 | 1.9 | 7.3 | 23.5 | 67.3 |  Nanostructured α-Fe ₂ O ₃ catalyst |
| 250 | 33.4 | 2.8 | 8.6 | 22.2 | 66.3 | |
| 280 | 69.7 | 5.0 | 14.3 | 31.0 | 49.6 | |

The nano-structure α-Fe₂O₃ catalyst proved to be relatively active with good selectivities. Even though the CO conversion value are not strictly the same than the one of the commercial catalyst (33.4 % conversion for the nano-structure α-Fe₂O₃ and 23.7 % conversion for JM commercial catalyst), selectivities in light hydrocarbons and CH₄ are of the same order of magnitude (~2 - 4 % for CH₄ and ~7 - 10 % for C₂-C₄ at 250 °C). The main issue with this catalyst is its CO₂ selectivity (> 20 %).

Conclusion

The objectives of this chapter was to evaluate the Fischer-Tropsch catalytic performances (mainly activity, selectivity and stability) of well-controlled iron-based catalysts. The most important factor for the Fischer-Tropsch catalyst is the selectivity in hydrocarbons, notably the capacity to favor long chain hydrocarbons (C_{5+}). On the contrary, a low selectivity in CH_4 and light hydrocarbons is desired. For iron-based catalysts in particular, the CO_2 selectivity is one of the most essential data that needs to be evaluate.

The studied iron-based catalysts can be divided into two categories: iron-based catalysts producing high amount of CO_2 ($> 15\%$, commercial and the nano-structured $\alpha-Fe_2O_3$ catalyst) and iron-based catalysts producing no or very little CO_2 ($< 1\%$, Fe@hollow-silicalite-1, Fe/hollow-silicalite-1 and Fe/SiO₂ catalysts).

The first category, represented by the bulk-type catalysts, has a really high iron loading and is mainly composed of iron oxides. Both the commercial and the nano-structured catalysts are active and have a really good selectivity in light hydrocarbons (CH_4 and C_2-C_4). However, their selectivity in the undesired CO_2 product is really high ($> 15\%$). In terms of stability, the catalysts were not tested long enough to see any important deactivation. Through water-gas-shift testing, the commercial catalyst proved to be a really good WGS catalyst.

The second category, represented by the Fe supported on silica, has really low iron loading. However, they appeared to be active in Fischer-Tropsch conditions, probably due to their shape and high iron particle dispersion. All catalysts in this category seem to have a higher light hydrocarbons (CH_4 and C_2-C_4) selectivity than the bulk-type catalyst. Except for the Fe/SiO₂ catalyst believed to be low in activity. Both Fe@hollow-silicalite-1 and Fe/hollow-silicalite-1 despite having high CO conversion (respectively 20 % and 28 %) do not produce any or very few CO_2 . Even more interesting, the Fe@hollow-silicalite-1 catalysts consumed CO_2 when adding some in the feed, meaning that reverse water-gas-shift (R-WGS) is occurring. This phenomena will be discussed in more details in **Chapter 5 - Study of the Fe@hollow-silicalite-1 catalyst: Determination of the relationship between structural features and catalytic performances.**

A summary table of the different tests conducted on all catalysts is shown in **Table 44** below. The relation between the structure and characteristics of these catalysts with their Fischer-Tropsch performances (activity, selectivity) will be fully described and discussed in **chapter 5.**

Table 44 | Summary of the Fischer-Tropsch synthesis data on the iron-based catalyst studied (at 250 °C)

| Catalysts: | Fe@hollow-Silicalite-1 | FeCuK@hollow-silicalite-1 | Fe/hollow-silicalite-1 | Fe/SiO ₂ | Commercial catalyst | Nano-structured α -Fe ₂ O ₃ |
|---|------------------------|---------------------------|------------------------|---------------------|---------------------|--|
| Catalyst info: | | | | | | |
| Fe loading (wt%) | 2.5 | 2.8 | 4.2 | 2.3 | Bulk* | Bulk** |
| Dispersion (%) | 29 | 27 | 5.2 | 4.7 | ~4.7*** | 9.7 - 14.5 |
| Conditions of operations: | | | | | | |
| Temperature (°C) | 250 | 250 | 250 | 250 | 250 | 250 |
| Conversion: | | | | | | |
| GHSV (L.g _{cat} ⁻¹ .h ⁻¹ , syngas) | 0.53 | 0.45 | 0.70 | 0.30 | 1.28 | 2.25 |
| CO (%) | 19.9 | 20.0 | 28.4 | 7.0 | 23.2 | 33.4 |
| Selectivity: | | | | | | |
| CH ₄ (%) | 15.1 | 7.3 | 18.0 | 1.2 | 2.25 | 2.8 |
| C ₂ - C ₄ (%) | 22.7 | 13.6 | 34.5 | 1.8 | 5.2 | 8.6 |
| CO ₂ (%) | - | - | 1.2 | - | 14.4 | 22.2 |
| C ₅₊ (%) | 62.2 | 79.2 | 46.3 | 97.0 | 78.2 | 66.3 |

* 78.4 % Fe₂O₃ for the commercial catalyst. **The nano-structured α -Fe₂O₃ catalyst is mainly composed of iron oxide.

***This value of dispersion was calculated from the spent catalyst (**Chapter 3**).

Chapter 5 - Study of the Fe@hollow-silicalite-1 catalyst: Determination of the relationship between structural features and catalytic performances

Chapter 5 - Study of the Fe@hollow-silicalite-1 catalyst: Determination of the relationship between structural features and catalytic performances 167

| | |
|--|------------|
| Introduction | 168 |
| I. Study of the stability of iron-based catalysts | 168 |
| II. Study of the activity and selectivity of the iron-based catalysts..... | 175 |
| II.1. Activity, dispersion and structure sensitivity of iron catalyst..... | 175 |
| II.2. Study of the effects of the iron phases on the activity | 180 |
| II.3. Study of the effects of iron phases on the CO ₂ selectivity | 183 |
| III. Effect of the hydrophobicity of silicalite-1 on the selectivity and especially on CO₂.185 | |
| III.1. Hydrophobicity of silicalite-1..... | 185 |
| III.2. Hydrocarbons adsorption properties of silicalite-1..... | 189 |
| III.3. Relation between silicalite-1 hydrophobicity and FTS performances | 191 |
| III.3.1. Behavior of the catalyst at the nano-scale..... | 191 |
| III.3.2. Behavior of the catalyst at the reactor scale..... | 195 |
| IV. Study of the CO₂ transformation mechanism using labelled ¹³CO₂, MS and GC-MS analysis..... | 198 |
| IV.1. Testing conditions and analytical apparatus | 198 |
| IV.2. ¹³ C analysis by mass spectrometer | 199 |

Introduction

This chapter focuses on the study of the possible relationships between the structural features of the Fe@hollow-silicalite-1 catalyst and its catalytic performances. Fe@hollow-silicalite-1 catalyst proved to be particularly interesting as it does not produce any CO₂ at low temperature. Even more motivating, the catalysts consumed CO₂ when adding some in the feed, meaning that reverse water-gas-shift (R-WGS) is occurring. Would the non CO₂ production be due to the iron phases that composed the material or is it due to the “encapsulation” of the nano-particles inside the zeolite? This chapter aims at answering these questions. For that, the comparison with the other iron-based catalysts studied along with literature examples will provide additional information to support our arguments and point of view. In a first part, this chapter will deal with understanding and discussing the stability aspect of the Fe@hollow-silicalite-1 and with comparing it with the other iron-based catalysts. A second part will mainly focus on the understanding of the activity, in other word, the influence of the particle size and the different iron phases will be discussed. Finally, we will discuss our hypothesis that the high hydrophobicity of the silicalite-1 is at the origin of the non WGS reactivity. The last part deals with the characterization of adsorption properties as supporting evidence to our hypothesis.

I. Study of the stability of iron-based catalysts

One of the main challenges for Fischer-Tropsch catalysts is to overcome their fast deactivation, in other word increasing their stability with time on stream (TOS). As explained in **Chapter 1 - State of the art - A review - II.2. Iron-based FTS catalysts**, compared to cobalt-based catalysts, iron-based catalysts are known to deactivate rather quickly [11]. Therefore, from an industrial point of view, the cost for replacement and/or regeneration of a catalyst is relatively high and is not something desired. Consequently, more stable iron-based catalysts are required.

For a period of 100 h on stream, the Fe@hollow-silicalite-1 catalyst proved to be stable and sintering resistant. Indeed, when looking at the CO conversion with time (**Figure 100**), the conversion remains stable ($\sim 17\% \pm 5\%$) for a period of more than 100 hours at 250 °C.

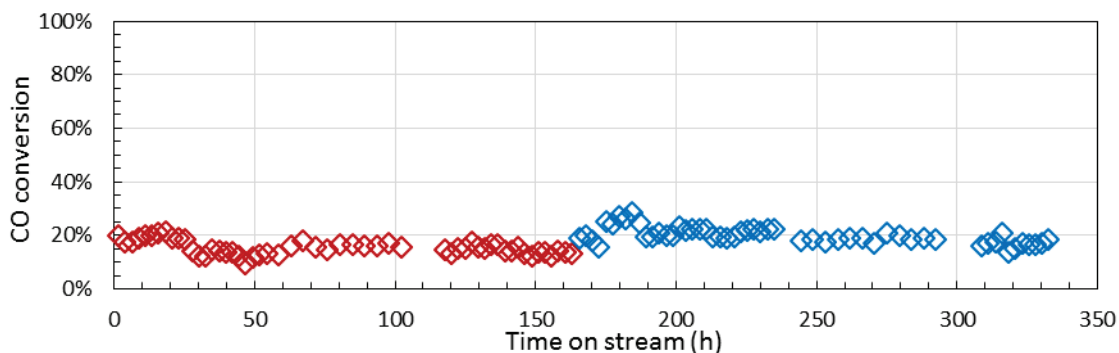


Figure 100 | Stability with time of the Fe@hollow-silicalite-1 catalyst at 250 °C (◊) and 260 °C (◊).

When increasing the temperature to 260 °C, the CO conversion remains stable for more than 100 hours. This suggests that the catalyst does not deactivate during this period of time. On TEM images, the particles size distribution can be calculated, and by applying the Van Hardeveld and Hartog model, the dispersion can be determined. When looking at the evolution of the particles size distribution with time (**Figure 101**), one can say that the particles are relatively stable and that no significant sintering is observed. Indeed, the average particle size evolved from 3.5 nm to 4.4 nm after 100 h on stream. The dispersion goes from 29 % to 24 %.

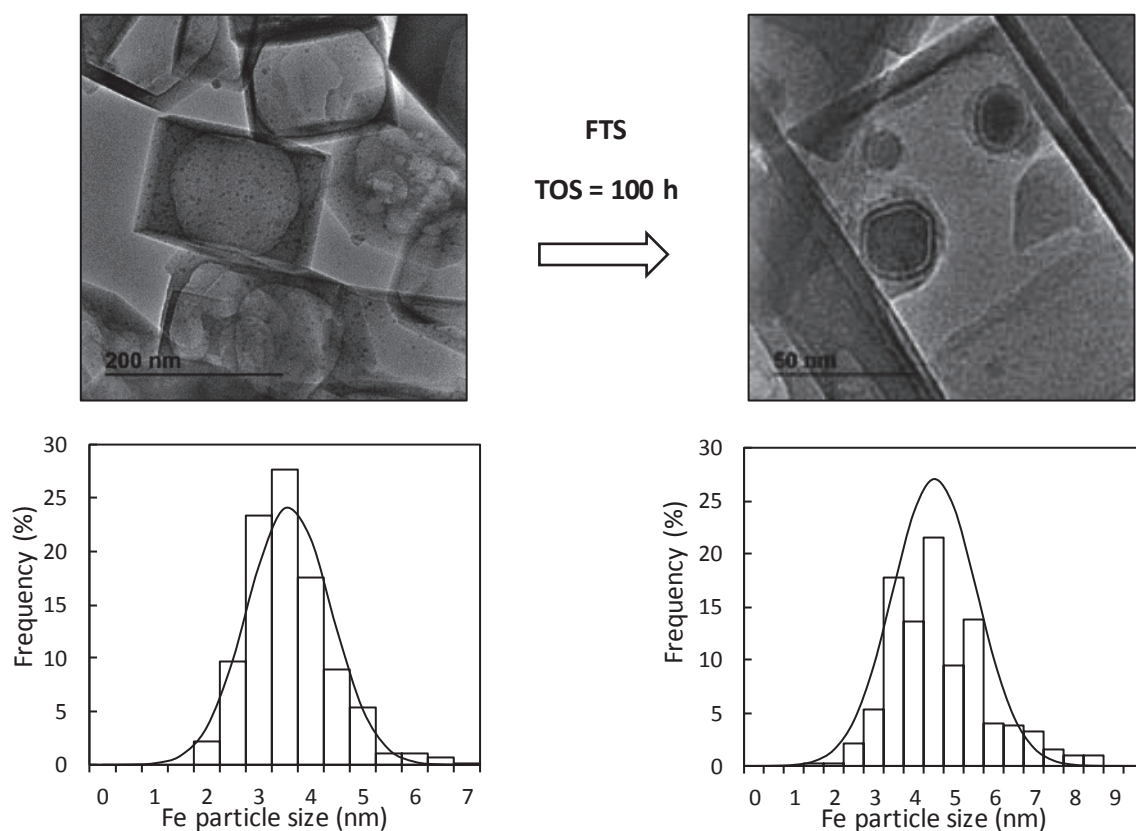


Figure 101 | Evolution of the iron nanoparticle distribution for the Fe@hollow-silicalite-1 catalyst before (left) and after (right) Fischer-Tropsch reaction after 100 h.

For a better understanding of the reason why the Fe@hollow-silicalite-1 is stable and sintering resistant, the other iron-based catalysts stability with time will be discussed.

Fe/hollow-silicalite-1 catalyst is the supported version or non-encapsulated iron nanoparticles version of the Fe@hollow-silicalite-1. Therefore, its study will provide valuable information when comparing its stability with the one of the Fe@hollow-silicalite-1 catalyst. For a period of 100 h on stream, the Fe/hollow-silicalite-1 catalyst remains stable. The CO conversion remains stable ($\sim 27\% \pm 3\%$) during a 100 h under Fischer-Tropsch reaction conditions (**Figure 102**).

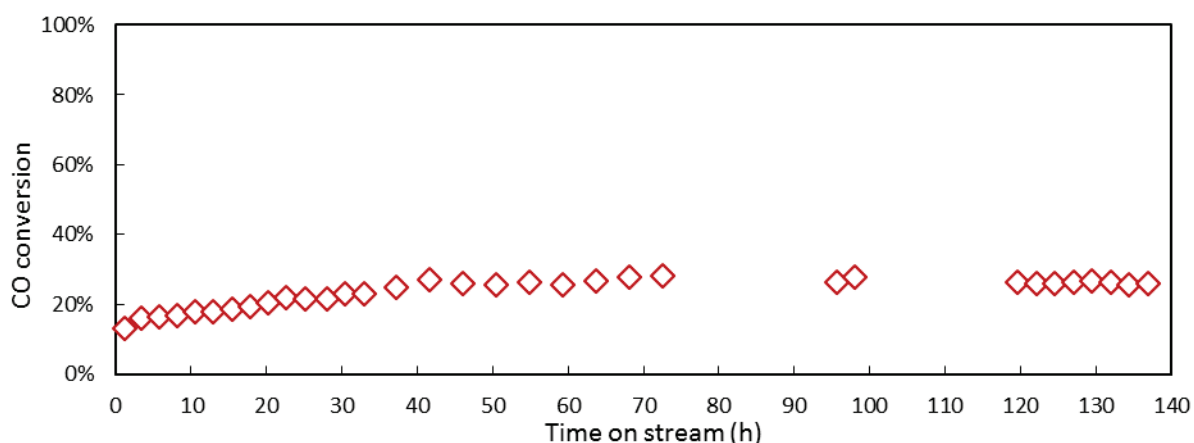


Figure 102 | Stability with time of the Fe/hollow-silicalite-1 catalyst at 250 °C (◊).

TEM images was used again for the particles size distribution and dispersion determination.

When looking at the evolution of the particles size distribution with time (**Figure 103**), the distribution is shifted toward the higher values. Indeed, the average particle size evolved from 21.7 nm to 27.5 nm after 100 hours on stream. The dispersion goes from 5.2 % to 4.6 %. Even though the difference is not large, it is significant.

The iron supported on silica, Fe/SiO₂, is poorly active. No deactivation could be therefore observed in this case. The low activity probably comes from the really low iron loading (2.3%) and the really low dispersion (4.4 %) of the iron particles on the fresh catalyst. No much can be said on this catalyst regarding its deactivation, stability and evolution with time.

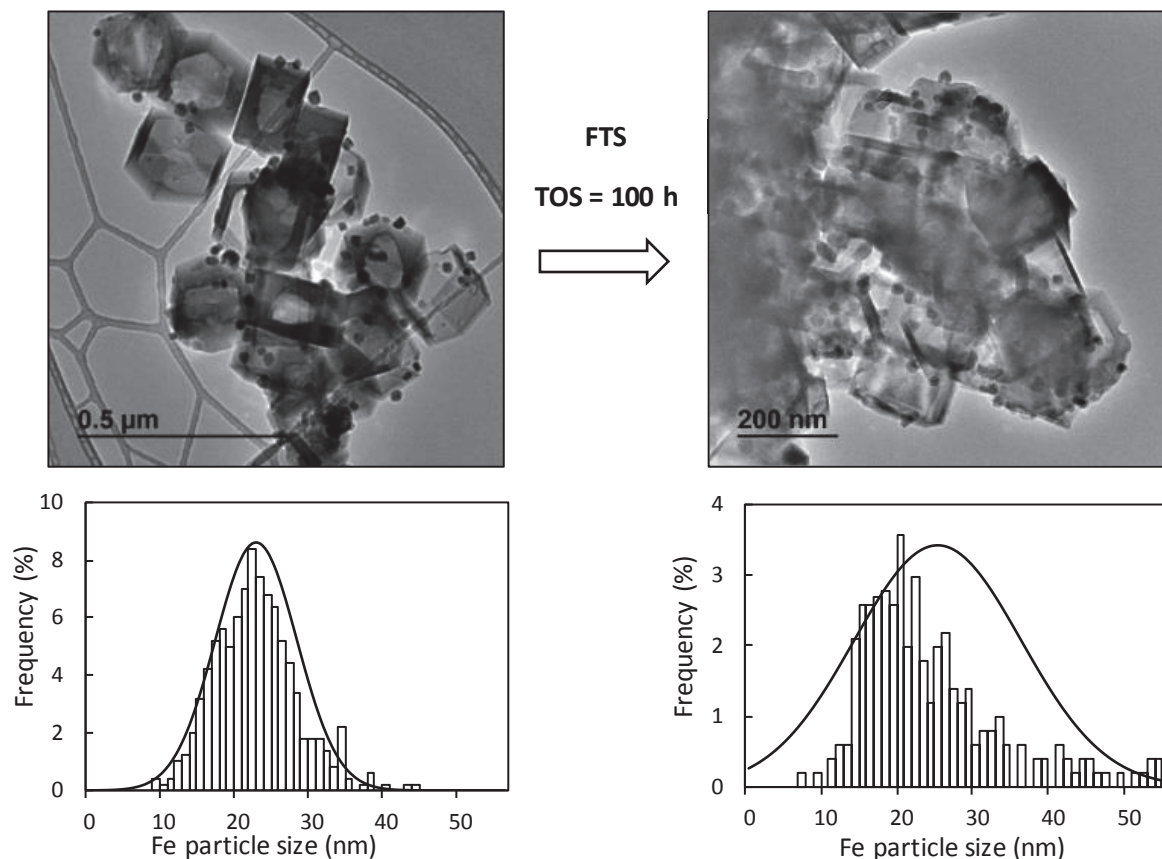


Figure 103 | Evolution of the iron nanoparticle distribution for the Fe/hollow-silicalite-1 catalyst before (left) and after (right) Fischer-Tropsch reaction after 100 h.

The two remaining catalysts, the bulk-types, are more affected by the TOS, especially the nano-structured α -Fe₂O₃ catalyst. The bulk-type catalyst as shown in **Chapter 3 - Characterization of iron-based catalysts** were proved to be largely altered during the Fischer-Tropsch reaction.

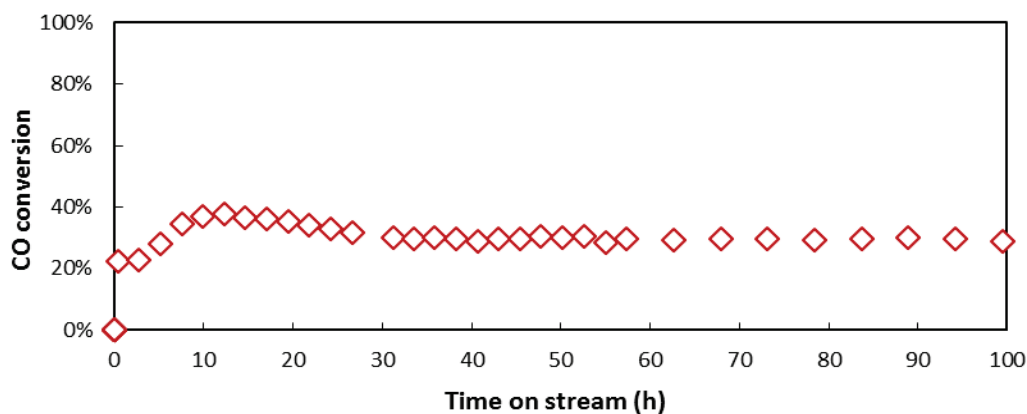


Figure 104 | Stability with time of the JM commercial catalyst at 230 °C (◊).

The JM commercial catalyst, after a period of activation of 24 hours, tends to stabilize and remains stable for a 100 hours (around 30 % \pm 2 % CO conversion, at 230 °C). No significant deactivation can be observed for this catalyst in a reasonable amount of time (**Figure 104**). This time, TEM images did not permit the calculation of the size distribution of the catalyst, as no well-defined particles can be observed. Also, due to its amorphous phase, the dispersion or iron particles size distribution could not be calculated by XRD (Debye-Scherrer). Only the spent crystalline catalyst could be evaluated in terms of dispersion (4.7 %) and average particles size (24.6 nm). With these information only, it is particularly difficult to conclude on the commercial catalyst stability with time.

For a better understanding of the bulk-type catalysts' behavior and transformation during Fischer-Tropsch synthesis, the nano-structured α -Fe₂O₃ catalyst looks more appropriate. For a period of 50 hours of stream at 230 °C, the CO conversion remains stable (\sim 19 % \pm 2 %) (**Figure 105**).

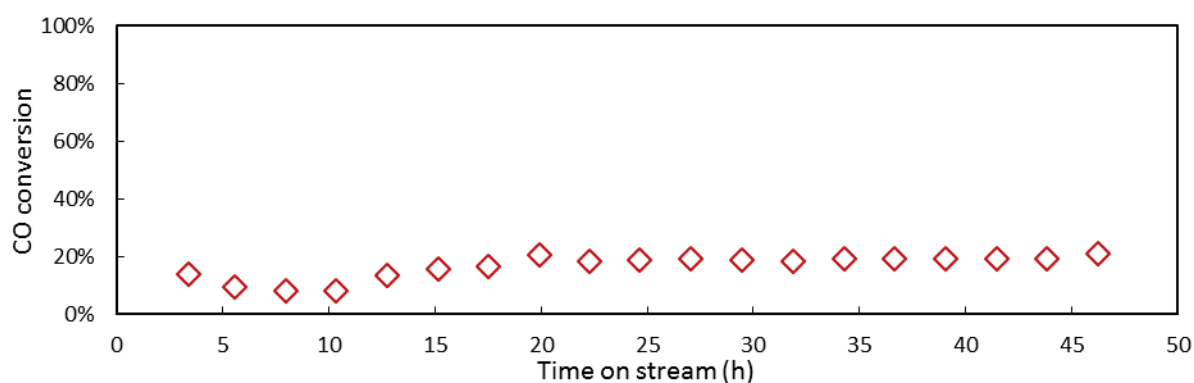


Figure 105 | Stability with time of the nano-structured α -Fe₂O₃ catalyst at 230 °C (◊).

No significant deactivation can be observed during this amount of time. On the other hand, major catalyst re-structuration can be observed with TEM images (**Figure 106**).

Indeed, the well-defined iron particles alignment totally shattered during the reaction. The well-defined particles evolves from 8 - 12 nm to an average of 131 nm. Also, the dispersion, changes from \sim 12 % to lower than 1 %. In conclusion, the catalyst activity remains constant while the dispersion decreases. This indicates that there is most likely generation of more active iron species with time.

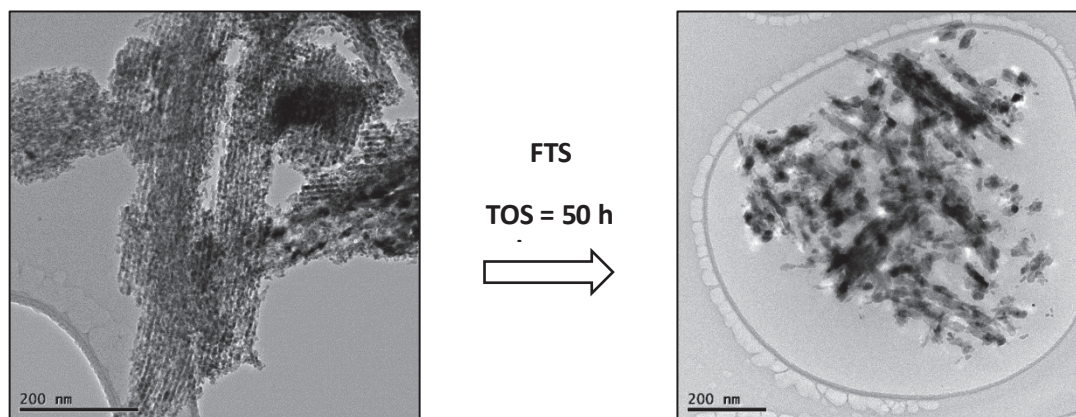
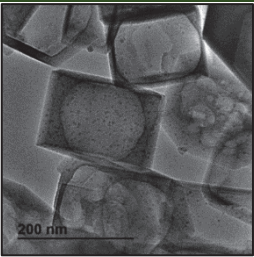
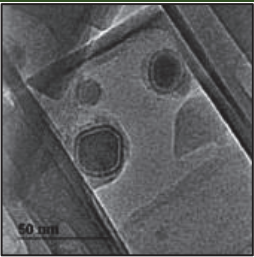
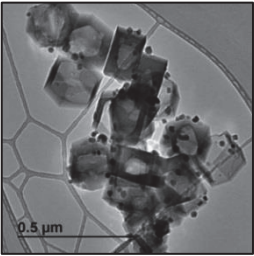
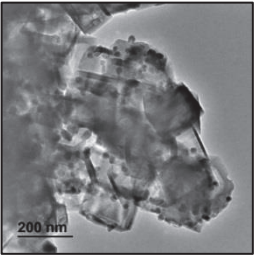
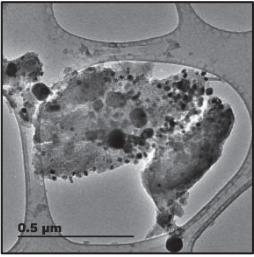
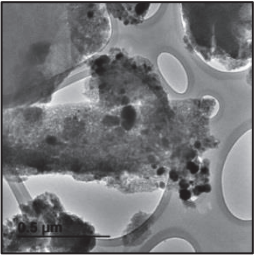
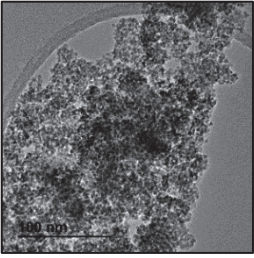
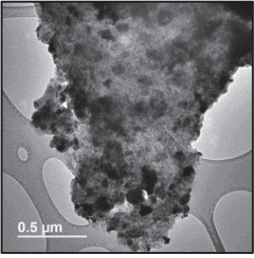
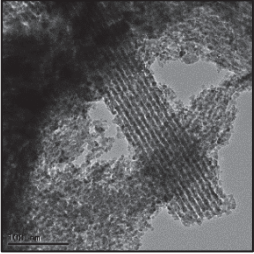
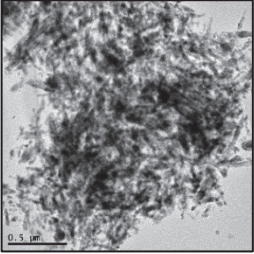


Figure 106 | TEM images of the nano-structured α - Fe_2O_3 catalyst before (left) and after (right) FTS.

Table 45 shows a summary of the evolution of the average particle size and dispersion of the five catalysts described beforehand.

For Fe@hollow-silicalite-1, the iron nanoparticles are localized inside the zeolite walls. Particles are probably in small cavities inside the silicalite-1 walls. As shown previously, the particles average size is 3.5 nm for the fresh and 4.4 nm for the spent catalyst, whereas the silicalite-1 pores size are known to be around 0.55 nm (5.5 Å). Therefore, the particles are trapped inside the defect of porous network. There are two possible mechanisms that can explain sintering, namely the particle migration and coalescence (PMC) and the Ostwald ripening (OR) (**Chapter 1 - State of the art - A review - c. Sintering and loss of catalytic surface area**). In the first case, PMC implicates particles mobility and diffusion on the catalyst surface, following by coalescence which leads to the particles growth when they come in close proximity with each other. However, this mechanism is unlikely to happen as the particles are trapped and cannot move in the pores of the silicalite-1 due to their size. Whereas, Ostwald ripening implicates migration and transport of ad-atoms and/or molecular species with larger particles growing at the expense of smaller particles due to surface free energy differences (large particles have a lower free energy than small particles). Therefore, OR could explain the small increase in particles size observed after reaction (3.5 nm to 4.4 nm in average). The encapsulation provides sintering resistance, but cannot explain the catalyst stability alone as the iron structure may change.

Table 45 | Evolution of the average particle size and the dispersion with TOS

| | At TOS = 0 h | | | At TOS = 100 h ^[a] | | |
|--|--|-------------------------------|---|--|-------------------------------|---|
| | Mean Particle size (nm) ^[b] | Dispersion (%) ^[c] | Structure | Mean particle size (nm) ^[b] | Dispersion (%) ^[c] | Structure |
| Fe@hollow-silicalite-1 | 3.5 | 29.0 |  | 4.4 | 24.0 |  |
| Fe/hollow-silicalite-1 | 21.7 | 5.2 |  | 27.5 | 4.6 |  |
| Fe/SiO₂ | 16.7 | 4.4 |  | - | - |  |
| Commercial catalyst | - | - |  | 24.6 ^[d] | 4.7 ^[e] |  |
| Nano-structured α-Fe₂O₃ bulk catalyst | 10 | 12.1 |  | 131 ^[d] | <1 ^[e] |  |

[a] 50 hours for the nano-structured α-Fe₂O₃ catalyst [b] Mean particles size calculated with TEM images, [c] Particles dispersion calculated with Van Hardeveld and Hartog model, [d] Mean particles size calculated with XRD (Debye-Scherrer), [e] Dispersion calculated with Handbook equation

II. Study of the activity and selectivity of the iron-based catalysts

As explained in **Chapter 1 - State of the art - A review** one of the main challenges in designing iron-based FTS catalysts lies in developing a more active catalyst. The Fischer-Tropsch studies on the Fe@hollow-silicalite-1 catalyst (**Chapter 4 – Part II.1.**) demonstrated that this material is active and is mainly forming light (CH_4 , $\text{C}_2\text{-C}_4$) and liquid hydrocarbons (C_{5+}). No CO_2 is observed in this particular case, despite iron-based catalysts being known to be active water-gas-shift catalysts. The Fe@hollow-silicalite-1 catalyst, even though having low iron loading ($\sim 2.5\%$), exhibits a high iron dispersion ($\sim 30\%$), which could explain the relatively good activity for such a small amount of iron. However, another aspect of iron-based catalysts can strongly impact the catalyst activity, its various iron phases content. Again, it is well-known that iron-based FTS catalysts in general are complex mixture of different iron phases formed during the synthesis. Through the different reaction steps of the Fischer-Tropsch synthesis (activation, deactivation...), metallic iron, iron oxides (hematite $\alpha\text{-Fe}_2\text{O}_3$, maghemite $\gamma\text{-Fe}_2\text{O}_3$, magnetite Fe_3O_4 , wüstite FeO ...) and iron carbides (cementite Fe_3C , Hägg's-carbides $\chi\text{-Fe}_5\text{C}_2$) may coexist^[11, 43]. Even though in literature carbides iron species are believed to be the active phases for FTS, the exact role of each phases in the activation and deactivation of iron-based catalyst materials is still highly disputed and remained controversial^[11].

The first part of this chapter focuses on the study of the relationships between site time yield (STY), dispersion and particles size. The second part will aim at linking the iron phases with the activity and selectivities of the iron-based catalysts.

II.1. Activity, dispersion and structure sensitivity of iron catalyst

In this part of this chapter, the activity of the different catalysts studied will be explained and compared by trying to understand the relationship between their dispersion-particles size and their activity. First of all, **Table 46** shows the activity of the different catalysts considered. For better comparison between all those very different catalysts, the activity per volume of catalyst and the site time yield (STY) are determined (**Chapter 2 - Experimental procedure - III.1.3. Catalytic data treatment and calculation**) for the calculation formula of activities and STY). All activities are calculated at steady state (after the CO conversion has been stabilized at a temperature of 250 °C).

Table 46 | Activities and TOFs of the different catalysts taken at steady state

| Catalysts | Average particle size (nm) | Average dispersion (%) | Activity per volume ($\mu\text{molCO}\cdot\text{cm}^{-3}\cdot\text{s}^{-1}$) | Activity ($\mu\text{molCO}\cdot\text{g}^{-1}\cdot\text{s}^{-1}$) | | | STY 10^{-3} (s^{-1}) |
|--|----------------------------|------------------------|--|--|-------------|-------------------|-----------------------------------|
| | | | | Per g of catalyst | Per g of Fe | Per g of Fe surf. | |
| Fe@hollow-silicalite-1 | 4.4 | 24 | 0.09 | 0.4 | 16.4 | 68.3 | 3.7 |
| FeCuK@hollow-silicalite-1 | | | 0.09 | 0.4 | 13.3 | 55.2 | 3.3 |
| Fe/hollow-silicalite-1 | 27.5 | 4.6 | 0.18 | 0.8 | 19.0 | 415.0 | 23.1 |
| Fe/SiO₂ | 16.7 | 4.4 | 0.07 | 0.07 | 3.1 | 67.1 | 3.9 |
| Commercial catalyst | 24.6 | ~ 4.7 | 1.1 | 1.2 | 2 | 44.1 | 2.5 |
| Nano-structured α-Fe₂O₃ | 130.9 | 0.9 | 2.6 | 3.1 | 5.1 | 569.6 | 28.1 |

In terms of activity per volume of catalyst, it is evident when looking at the table, that bulk type catalysts are much better than the supported catalysts, $\gg 1 \mu\text{molCO}\cdot\text{cm}^{-3}\cdot\text{s}^{-1}$ for bulk type catalyst and $\ll 1 \mu\text{molCO}\cdot\text{cm}^{-3}\cdot\text{s}^{-1}$ for nano-sized supported catalysts. From a structural point of view the commercial and nano-structured α -Fe₂O₃ catalysts are denser, therefore they require a smaller reactor than the Fe@hollow-silicalite-1 catalyst, which is 4 times less active. Indeed, the commercial catalyst has an apparent density of $0.86 \text{ g}\cdot\text{cm}^{-3}$ whereas the Fe@hollow-silicalite-1 has a $0.23 \text{ g}\cdot\text{cm}^{-3}$ density. The large cavity of the nano-boxes are responsible for the very low density. Breaking the boxes in small pieces could increase the powder density, but it cannot be achieved by grinding because of the small crystal sizes. We can observe that the activity per mass unit of iron is about 8 times larger than for the commercial catalysts, but the Fe loading is much smaller. Hence, another option for the enhancement of the volumetric and gravimetric activities would be to increase the iron loading of the Fe@hollow-silicalite-1 catalyst. Increasing the number of small particles per unit volume would certainly increase the activity of the catalyst. However this was proved to be hard to implement, as increasing the amount of iron in the impregnation solution, did not increase the loading in this kind of sample.

The best way to relate the activity of a catalyst to its active site, is the site time yield, better known as STY. The Fe/ hollow-silicalite-1 and nano-structured α -Fe₂O₃ have a much more

higher STY than the Fe@ hollow-silicalite-1 and commercial catalysts, respectively in the 10^{-2} s^{-1} for the first two and 10^{-3} s^{-1} for the others. What is noteworthy here is the STY of the Fe@hollow-silicalite-1 ($3.7 \cdot 10^{-3}$ s^{-1}) which is of the same order of magnitude than the commercial catalyst used in the industry whereas the Fe/hollow-silicalite-1 STY is 10 times higher than the one from the commercial catalyst. STY is a similar notion than TOF. TOF is widely used in the literature, few mention of STY can be found. The TOF is calculated by using the reaction rate whereas the STY used the conversion. Nevertheless we can generally admit that $STY \sim TOF$, or is generally in the same order of magnitude. When looking at literature, the average value of TOF for iron-based catalysts seems to be between 10^{-2} for large particles (> 7 nm) and 10^{-3} for smaller particles (< 7 nm) [59, 60, 125, 135, 136]. Therefore, the STY value calculated in this work are of the same order of magnitude than the TOF found in literature. Therefore in terms of active surface sites, our Fe@silicalite-1 catalyst is at the same level than the commercial catalyst.

Errors on STY calculation may originate from particle size measurements of iron in the catalyst. Therefore, we need to be critical on the way dispersion was calculated. In the case of iron-based supported catalysts (Fe@ hollow-silicalite-1, Fe/hollow-silicalite-1 and Fe/SiO₂), the particles size distribution is well-defined when observing the catalysts by TEM, therefore, the calculated dispersion is most likely accurate (Van Hardeveld and Hartog model). However, in the case of bulk-type catalysts, it was more difficult to have a precise dispersion calculation on the spent catalysts. For the commercial and nano-structured iron-based catalysts, TEM images couldn't be used to calculate the dispersion as no well-defined particles could be observed after several hours on stream. XRD was used to determine the average crystallite size, the dispersion was calculated (Handbook formula) assuming that all atoms of crystallites are accessible from the surface which is certainly not true. Indeed a particle could be made of several crystallites, therefore, the calculated dispersion is most likely overestimated. In that case, calculated STY could be underestimated and could hence be higher.

In conclusion so far, the nano-dispersed-type catalysts (encapsulated and supported ones) are actually more active than bulk-type catalysts per gram of iron which indicates that in principle supported catalysts could largely surpass bulk-type catalysts if iron high loading and high

dispersion could be achieved. Furthermore in terms of active surface sites, the encapsulated Fe@hollow-silicalite-1 catalyst as similar STY than the commercial catalyst.

Particles size is believed to have an impact on the activity of iron-based catalysts. Amongst the few, Mabaso et al. showed in their work [59] that small iron particles (< 7 - 9 nm) supported on carbon nanotubes were less active and had a higher methane selectivity compared to bigger particles. Recent studies by Park et al. showed an optimum Fe particle size of ~6 nm in the case of Fe supported on Al₂O₃ catalysts (**Figure 107**) [60].

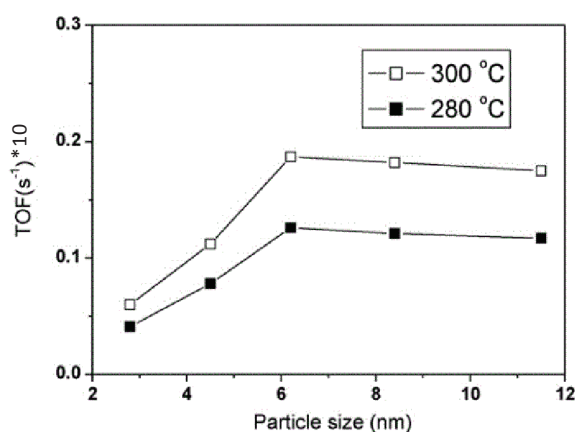


Figure 107 | The influence of iron particle size on the TOF (right) (280 °C and 300 °C, Space velocity = 3600 L.kg_{cat}⁻¹.h⁻¹, H₂:CO:Ar = 63.2:31.3:5.5, 10 bar) [60].

Figure 108 shows the STY (s⁻¹) as a function of the average particle size (nm) of the iron-based catalysts studied. In this figure, we can identify two groups: the nano-structured α-Fe₂O₃ catalyst and the Fe/hollow-silicalite-1 with a TOF in the 10⁻² order, and the Fe@hollow-silicalite-1, commercial catalyst and Fe/SiO₂ catalysts with a TOF in the 10⁻³ order.

The Fe@hollow-silicalite-1 catalyst has an average particle size of 3.5 nm and a STY in the order of 10⁻³.

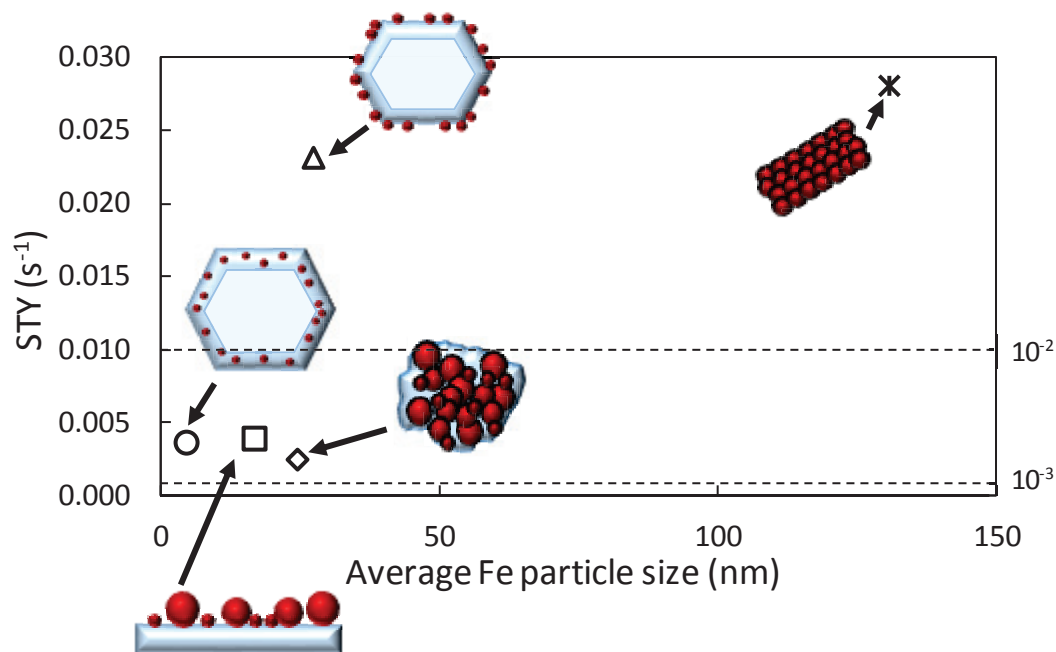


Figure 108 | TOF (s⁻¹) vs average particle size D (nm) for the iron-based catalysts of this study

Surprisingly, it can be noted that large particles (Fe/hollow-silicalite-1) have a significant higher STY than small particles (Fe@hollow-silicalite-1). The trend between STY and particles critical size is analogous to Park et al. (Figure 107) and Mabaso et al. observations on TOF. It would have been interesting to modify the average particle size on the Fe@hollow-silicalite-1 to verify if the same kind of graphic (Figure 107) could be obtained. However, due to loading limitation for this catalyst, we were not able to carry out this study with the developed synthesis procedures.

Diffusion limitation might possibly explain the difference in activity and STY for the Fe@hollow-silicalite-1 catalyst (with respect to Fe/hollow-silicalite-1), as particles are localized inside the zeolite support. In Chapter 4 - Study of the Fischer-Tropsch synthesis on iron-based catalysts, the energy of activation for the Fe@hollow-silicalite-1 catalyst was determined. The observed activation energy for the kinetic constant is between 48 to 62 kJ.mol⁻¹. These values are low in comparison to most reported activation energies in the literature, typically between 70 and 105 kJ.mol⁻¹ [133, 134]. Therefore, the low activation energy compared to the ones in literature may be due to diffusion limitation [134]. On the other hand, the bulk-type commercial catalyst activation energy was determined to be 50 kJ.mol⁻¹, which

is also much lower than reported activation energy in literature. Furthermore, the iron particles of the Fe/SiO₂ catalyst are not encapsulated compared to the Fe@hollow-silicalite-1. Additionally, the Fe/SiO₂ catalyst has a similar activity or STY than the Fe@hollow-silicalite-1 catalyst (respectively $3.9 \cdot 10^{-3} \text{ s}^{-1}$ and $3.7 \cdot 10^{-3} \text{ s}^{-1}$). Consequently, based on these information, it can be concluded that the Fe@hollow-silicalite-1 is not limited by diffusion.

Also, the structure sensitivity of iron-based particles could explain the activities and STY. However for particles larger than 6 nm in size the number of corners, terraces and edges are not varying significantly. Therefore, as STY for the Fe/hollow-silicalite-1 is similar to the nano-structured α -Fe₂O₃, STY do not depends on the number of corners, terraces and edges. In conclusion, the different activities and STY of the iron-based catalysts cannot be explained by diffusion limitation or size sensitivity of the structure (corners, terraces and edges). Therefore, the nature of the iron phases may potentially be the major topic to follow to explain these differences.

II.2. Study of the effects of the iron phases on the activity

- For catalysts with high STY (nano-structures α -Fe₂O₃ and Fe/hollow-silicalite-1 catalysts) (Table 47). Even though the STY is slightly higher in the case of the nano-structured α -Fe₂O₃ catalyst (+22%).

Table 47 | Activities of the high STY catalysts taken at steady state after 100 hours on stream

| | Average particles/crystallite size (nm) | Average dispersion (%) | Activity per volume ($\mu\text{molCO} \cdot \text{cm}^{-3} \cdot \text{s}^{-1}$) | Activity ($\mu\text{molCO} \cdot \text{g}^{-1} \cdot \text{s}^{-1}$) | | | STY $10^{-3} (\text{s}^{-1})$ |
|--|---|------------------------|--|--|-------------|-------------------|-------------------------------|
| | | | | Per g of catalyst | Per g of Fe | Per g of Fe surf. | |
| Nano-structured α-Fe₂O₃ | 130.9 | 0.9 | 2.6 | 3.1 | 5.1 | 569.6 | 28.1 |
| Fe/hollow-silicalite-1 | 27.5 | 4.6 | 0.18 | 0.8 | 19.0 | 415.0 | 23.1 |

⁵⁷Fe Mössbauer spectroscopy is the key technique to address the relationship between their nature of the phases and the activity. The two spent catalysts Mössbauer spectra are a mixture of iron phases (carbides, iron oxides and metallic iron) in different proportions (Table 48).

Table 48 | The iron phases with their relative intensity determined by Mössbauer spectroscopy for the spent nano-structured α -Fe₂O₃ and spent Fe/hollow-silicalite-1 catalysts

| Sample | Species | Relative intensity (%) | Sample | Species | Relative intensity (%) |
|------------------------|--------------------------------|------------------------|---|--------------------------------|------------------------|
| Fe/hollow-silicalite-1 | α -Fe | 7 | Spent nano-structured α -Fe ₂ O ₃ catalyst | Fe ₃ O ₄ | 76 |
| | Fe ³⁺ | 23 | | Fe ³⁺ | 2 |
| | Fe ²⁺ | 25 | | Fe ₂ O ₃ | 10 |
| | Fe ₅ C ₂ | 44 | | Fe ₅ C ₂ | 11 |

The majority of the iron is present under the form of oxides (Fe₃O₄, Fe₂O₃, Fe³⁺, Fe²⁺ species), more exactly 89 % and 48 % for the nano-structured α -Fe₂O₃ and the Fe/hollow-silicalite-1 catalysts respectively. In the particular case of the Fe/hollow-silicalite-1 catalyst, 7 % of metallic iron-containing can be detected. The remaining proportion is composed of carbides.

In conclusion, the nano-structured α -Fe₂O₃ catalyst and Fe/hollow-silicalite-1 are particularly active and exhibit a large mixture of iron phases, mainly oxides and carbides (with very few metallic iron (~7 %) in the case of the Fe/hollow-silicalite-1).

- For catalysts with low STY (commercial catalyst, Fe@hollow-silicalite-1 and Fe/SiO₂ catalysts) (Table 49).

Table 49 | Activities of the low STY catalysts taken at steady state

| | Average particle size (nm) | Average dispersion (%) | Activity per volume ($\mu\text{molCO}\cdot\text{cm}^{-3}\cdot\text{s}^{-1}$) | Activity ($\mu\text{molCO}\cdot\text{g}^{-1}\cdot\text{s}^{-1}$) | | | STY $10^{-3} (\text{s}^{-1})$ |
|---------------------------|----------------------------|------------------------|--|--|-------------|-------------------|-------------------------------|
| | | | | Per g of catalyst | Per g of Fe | Per g of Fe surf. | |
| Fe@hollow-silicalite-1 | 4.4 | 24 | 0.09 | 0.4 | 16.4 | 68.3 | 3.7 |
| FeCuK@hollow-silicalite-1 | | | 0.09 | 0.4 | 13.3 | 55.2 | 3.3 |
| Fe/SiO ₂ | 16.7 | 4.4 | 0.07 | 0.07 | 3.1 | 67.1 | 3.9 |
| Commercial catalyst | 24.6 | ~ 4.7 | 1.1 | 1.2 | 2 | 44.1 | 2.5 |

The three spent catalysts Mössbauer spectra present the same iron phases (**Table 50**).

Table 50 | The iron phases with their relative intensity determined by Mössbauer spectroscopy for the spent commercial catalyst, spent Fe@hollow-silicalite-1 (left) and the spent Fe/SiO₂ (right)

| Sample | Species | Relative intensity (%) | Sample | Species | Relative intensity (%) |
|------------------------|--------------------------------|------------------------|---------------------|--------------------------------|------------------------|
| Commercial catalyst | Fe ₃ O ₄ | 29 | Fe/SiO ₂ | Fe ³⁺ | 74 |
| | Fe ³⁺ | 29 | | Fe ²⁺ | 15 |
| | Fe ²⁺ | 14 | | α-Fe | 11 |
| | Fe ₅ C ₂ | 28 | | Fe ₅ C ₂ | 0 |
| Fe@hollow-silicalite-1 | Fe ³⁺ | 35 | | | |
| | Fe ²⁺ | 29 | | | |
| | α-Fe | 26 | | | |
| | Fe ₅ C ₂ | 10 | | | |

It can be first noticed that, again, the three catalysts present the same iron phases. The majority of the iron is present under the form of oxides (Fe₃O₄, Fe³⁺ and Fe²⁺ species), more precisely 72 %, 64 % and 89 % for the commercial catalyst, Fe@hollow-silicalite-1 and the Fe/SiO₂ catalysts respectively. A small amount of carbides can be observed in the case of the Fe@hollow-silicalite-1 and commercial catalyst (relative intensity 10 % and 28 % respectively). However no carbides can be observed in the case of the Fe/SiO₂, probably due to its low conversion and low heavy hydrocarbons formation. Also, metallic iron can be detected, 26 % and 11 % for Fe@hollow-silicalite-1 and Fe/SiO₂ catalysts respectively.

- So far, we noted that high STY and low STY catalysts contain mainly oxides, carbides and metallic iron. However, we saw in **Chapter 3 - Characterization of iron-based catalysts**, with TEM and Mössbauer spectroscopy, that reduced catalysts have a core-shell structure with most likely metallic iron as the core and oxides species as the shell. Therefore it is unlikely that metallic iron of the nano-dispersed type catalysts participate to the FTS reaction. Finally, it is difficult to assume or conclude that iron phases are responsible for

the difference in activity between the low STY and high STY catalysts. Here we looked at the phases of the particle, however it would be necessary to investigate more carefully the surface phases of the particle, as it is the place where the reactions occur. In Fe@hollow-silicalite-1 particles case, we cannot conclude at the exact nature of the iron phase at the surface. No surface analysis technique, such as XPS, could be used to determine the exact surface phases, as the particles are localized inside the zeolite.

II.3. Study of the effects of iron phases on the CO₂ selectivity

The Fe@hollow-silicalite-1 catalyst has interesting selectivity properties. Indeed in **Chapter 4 - Study of the Fischer-Tropsch synthesis on iron-based catalysts**, no CO₂ could be observed at 250 °C in the case of the iron nanoparticles encapsulated catalyst. Furthermore, the Fe/hollow-silicalite-1 also presents limited amount of CO₂ (~1 %) during Fischer-Tropsch reaction at 250 °C. These observations are quite surprising as iron-based catalyst are known to be particularly water-gas-shift (WGS) active. It is well known that magnetite (Fe₃O₄) catalyzes the water-gas-shift reaction [30]. Researchers consider that magnetite may be the phase responsible for the WGS activity of iron catalysts during FTS. However, magnetite is co-existing with other iron phases during FTS, thus it remains difficult to determine the exact impact of all phases on the CO₂ selectivity of the catalyst. In these two catalysts case (Fe@hollow-silicalite-1 and Fe/hollow-silicalite-1), Mössbauer spectroscopy of the spent catalysts reveals an important amount of oxides (64 % for Fe@hollow-silicalite-1 and 48 % for Fe/hollow-silicalite-1). Therefore, it should be expected to have a reasonable amount of CO₂ formed, even in small quantities. But no such results were observed.

Bulk-type catalysts have the same kind of oxides phases than supported catalysts, however, a huge amount of CO₂ was produced (> 15 %). Mössbauer analysis on the spent catalysts shows a large quantity of oxides (72 % for the commercial catalyst and 88 % for the nano-structured α -Fe₂O₃ catalyst).

Table 51 compared the Fe@hollow-silicalite-1, Fe/hollow-silicalite-1 and the nano-structured α -Fe₂O₃ catalysts in terms of catalytic performances. Both supported catalysts do not produce CO₂, however their STY is not of the same order of magnitude. Even though, the nano-

structured and the Fe/hollow-silicalite-1 catalysts have STY of the same order of magnitude, the first one produces a large quantity of CO₂ whereas the second produce very low amount of CO₂. Therefore, no obvious correlations can be made between activity of the catalyst and its CO₂ selectivity.

Table 51 | Catalytic performances of the Fe@hollow-silicalite-1, Fe/hollow-silicalite-1 and nano-structured α -Fe₂O₃ at 250 °C

| | Average particle size (nm) | Conversion (%) | Selectivity (%) | | | | STY (s ⁻¹) |
|--|----------------------------|----------------|-----------------|--------------------------------|------------------|-----------------|------------------------|
| | | CO | CH ₄ | C ₂ -C ₄ | C ₅ + | CO ₂ | |
| Fe@hollow-silicalite-1 | 4.4 | 19.9 | 15.1 | 22.7 | 62.2 | 0 | 10⁻³ |
| Fe/hollow-silicalite-1 | 27.5 | 28.4 | 18.0 | 34.5 | 46.3 | ~1 | 10⁻² |
| Nano-structured α-Fe₂O₃ | 130.9 | 33.4 | 2.8 | 8.6 | 66.3 | 22.2 | 10⁻² |

From all these observations, it can be concluded that the CO₂ selectivity is most likely not linked to the activity, the particle size or the iron phases.

The main difference between the two categories of catalysts (bulk and silica supported) is mainly the silica support and even more in the case of the Fe@hollow-silicalite-1 where the iron nanoparticles are encapsulated. Therefore a deeper look at the silicalite-1 properties and effect on the FTS reaction is needed.

III. Effect of the hydrophobicity of silicalite-1 on the selectivity and especially on CO₂.

The Fischer-Tropsch studies on the Fe@hollow-silicalite-1 catalyst (**Chapter 4 – Part II.1.**) demonstrated that this material had a particular behavior regarding CO₂ production. Indeed, the major interest of this catalyst was the lack of CO₂ produced during the Fischer-Tropsch reaction at low temperature. Furthermore when adding a little amount of CO₂ in the feed, one can see that CO₂ is consumed at low temperature probably meaning that reverse-WGS is happening. Furthermore, when increasing temperature, the WGS is finally happening. Therefore, the understanding of this phenomenon is of great interest, as CO₂ is one of the main reason explaining the low selectivity in hydrocarbons of iron-based catalysts. As explained earlier in this study, there are two main hypothesis to the apparent lack of WGS activity:

- The encapsulation of iron particles may prevent the formation of certain carbides or oxides phases which are known or thought to be WGS active. However, in the case of Fe/hollow-silicalite-1, we observe the same iron phases and a similar CO₂ selectivity. Therefore, this first hypothesis can most likely be ruled out.
- The low water content around the encapsulated iron nanoparticles inside the hydrophobic silicalite-1 may be limiting the WGS kinetic.

Hence we assume that the CO₂ low selectivity arises from the peculiar adsorption properties of the silicalite-1 zeolite.

III.1. Hydrophobicity of silicalite-1

For silicalite-1, the hydrophobicity is mainly attributed to Si-O-Si bonds that composed the framework [137, 138]. Several studies show that modification of the internal defect density, by composition variations or synthesis procedures, have a significant effect on water transport in zeolite and consequently have an impact on hydrophobicity [139, 140, 141, 142, 137, 143]. Defects can be found in the framework. Generally during the synthesis process, broken Si-O bonds react with water to form silanol species Si-O-H instead of continuous Si-O-Si network. ²⁹Si NMR is the perfect technique to quantify the number of defects present inside a zeolite by looking

at the silica centers that are known has Q_1 ($\text{SiO-Si}(\text{OH})_3$, -83 ppm), Q_2 ($(\text{SiO})_2\text{-Si}(\text{OH})_2$, -91 ppm), Q_3 ($(\text{SiO})_3\text{-Si}(\text{OH})_1$, -101 ppm) and Q_4 ($(\text{SiO})_4\text{-Si}$, -110 ppm) (**Figure 109**). These silanol defects (Si-OH) allow water adsorption in the zeolite. To improve the hydrophobicity of the silicalite-1 by lowering the density of internal defects, the crystals can be synthesized by using fluorine ions as mineralizing agent under neutral conditions as a substitute to traditional OH^- mineralizing agent under alkaline conditions [144, 145, 146].

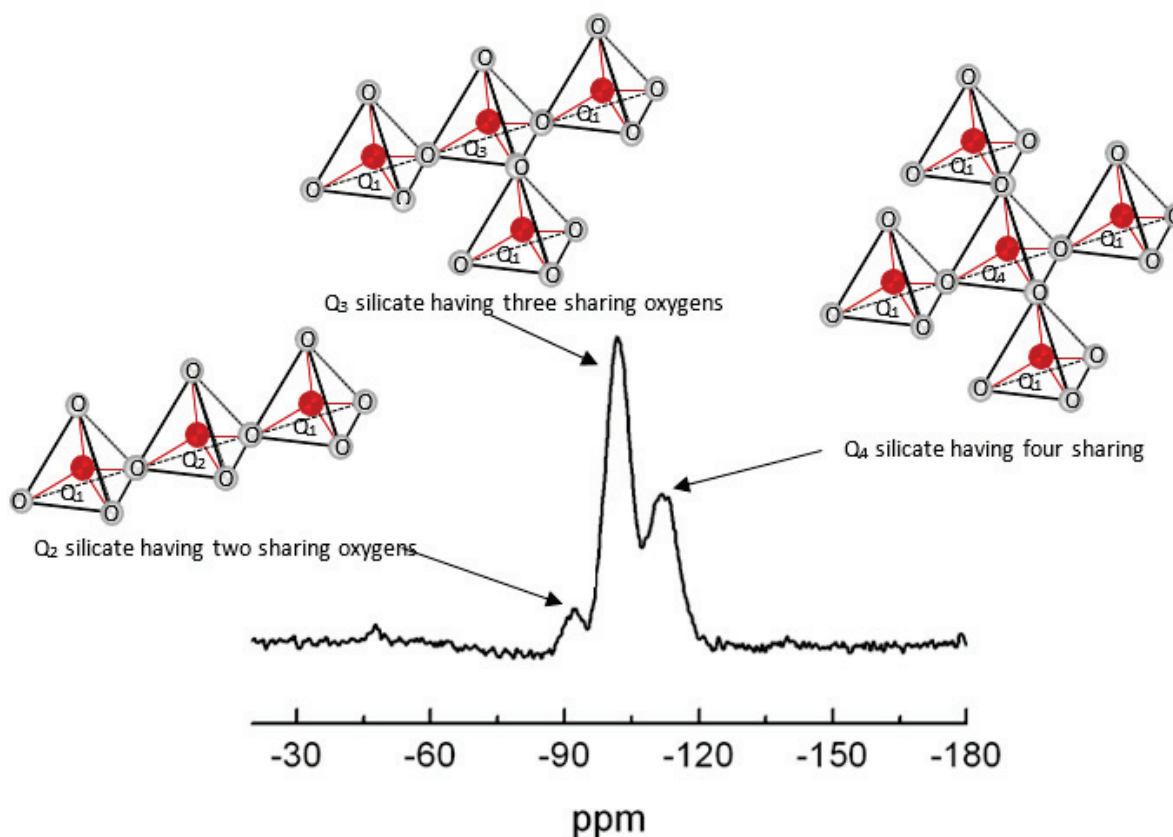


Figure 109 | ^{29}Si NMR spectrum of silica (SiO_2) [147].

In this study, nano-sized silicalite-1 mono-crystals inner part was dissolved and recrystallized in presence of TPAOH in hydrothermal conditions, to form the so-called hollow-silicalite-1 structure. Burel & Tuel [147] reported that the formation of the hollow structure significantly reduced the amount of silanol groups presented in the silicalite-1 zeolite (**Figure 110**).

Burel & Tuel [147] show that the ^{29}Si NMR peak at -102.5 ppm which initially represented more than a third of the total NMR spectrum (**Figure 110 - b**) drastically decreased (**Figure 110 - e**) with the formation of the hollow structure. They estimated that approximately 80 % of the

silanol population has disappeared with the formation of the hollow-structure (**Figure 110 - e**). Also, after calcination of the hollow-structure the -102.5 ppm signal almost completely disappeared, therefore the NMR spectrum contains mainly Q4 species at -111 ppm (**Figure 110 - f**). Therefore, one can argue that hollow-silicalite-1 is particularly defect free and so should be hydrophobic.

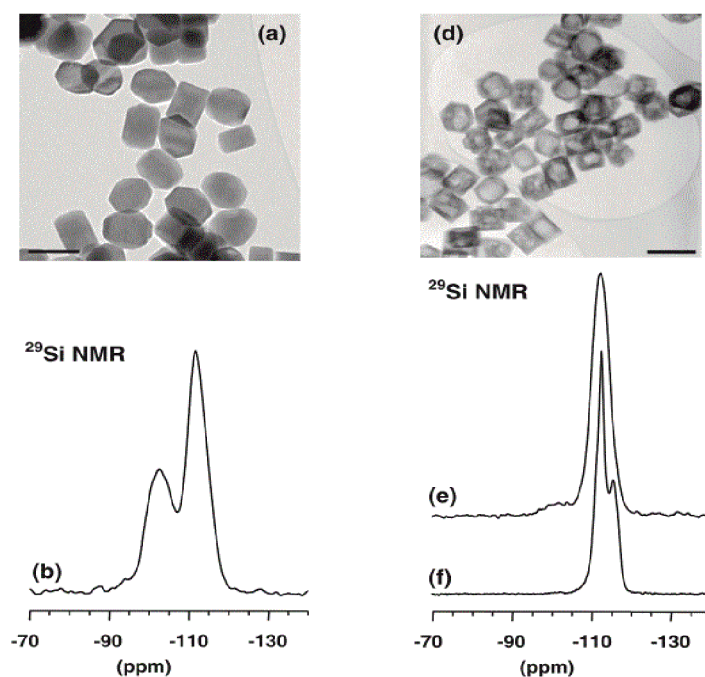


Figure 110 | TEM image of the parent silicalite-1 material (a) with its corresponding ^{29}Si NMR spectrum (b). TEM image of the hollow-silicalite-1 material (d) with its corresponding ^{29}Si NMR spectrum before calcination (e) and after calcination (f) [147].

Adsorption of water experiments have been carried out on various samples by using a Belsorp instrumental apparatus. This technique has been used to provide information regarding the hydrophobicity and/or hydrophilicity of various samples. **Figure 111** delivers information on the hydrophobicity of the hollow-silicalite-1 catalyst. When comparing the profile of hollow-silicalite-1 with the SiO_2 (specific surface area 750 m^2/g), we can clearly see that the hollow catalyst is more hydrophobic than the silica. Furthermore, the hollow-silicalite-1 catalyst does not absorb as much water as the state of the commercial catalyst. Henry constants provide a quantitative description of the surface hydrophobicity. For that, the slope of the curves is calculated, and gives the Henry constant. Hollow-silicalite-1 has a Henry constant of 0.029 $\mu\text{mol}\cdot\text{g}^{-1}\cdot\text{Pa}^{-1}$ whereas the silica has a Henry constant of 1.6 $\mu\text{mol}\cdot\text{g}^{-1}\cdot\text{Pa}^{-1}$. The commercial

catalyst has a Henry constant of $1.5 \mu\text{mol.g}^{-1}.\text{Pa}^{-1}$. The lower the Henry constant, the higher the surface hydrophobicity. Therefore, it is clear when looking at these constants, that the hollow-silicalite-1 is much more hydrophobic than the parent silicalite-1 and the commercial catalyst.

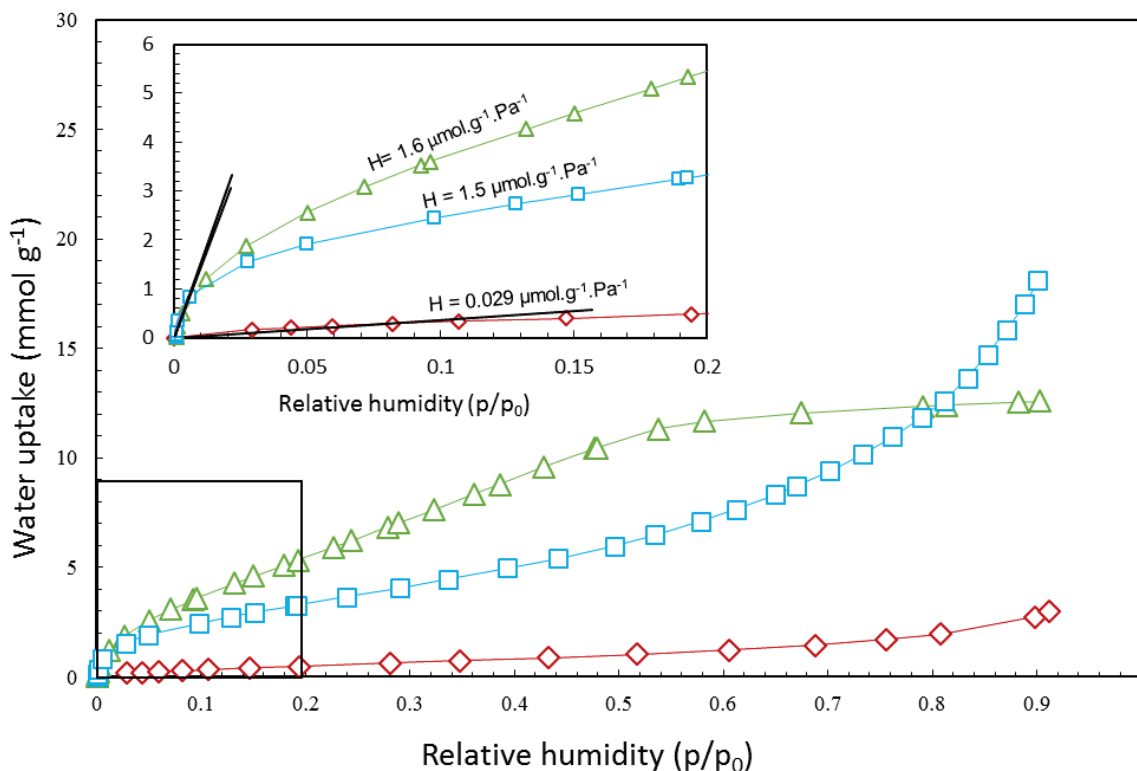


Figure 111 | Water adsorption isotherms for hollow-silicalite-1 (\diamond), silica (SiO_2 , Δ) and the commercial catalyst (\square).

Furthermore, our hollow-silicalite-1 catalyst matches well with the silicalite-1 (F) from Zhang et al. study (Figure 112) [137]. By increasing the Al content in the framework (decrease of the Si/Al ratio) the zeolite's hydrophilicity is enhanced and considerably increases the water adsorption. Also, the cations in the framework, compensating for the presence of aluminum charges to get a neutral zeolite, affect the water adsorption properties of the zeolite (Figure 112) [137].

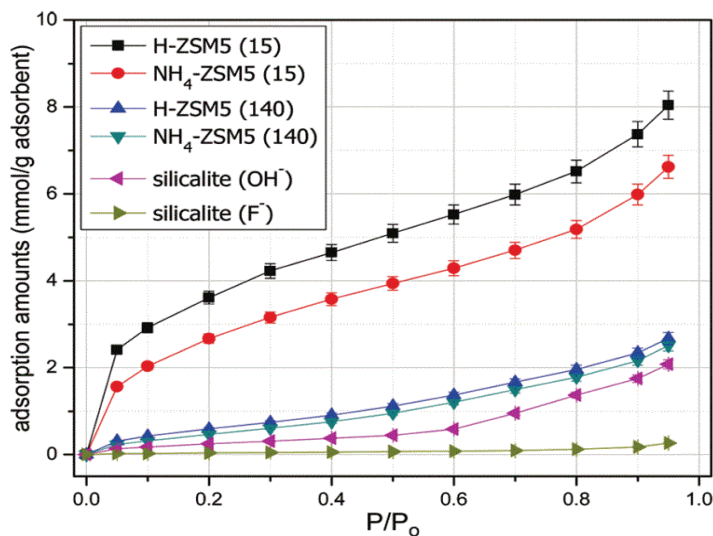


Figure 112 | Water adsorption isotherms for different MFI zeolite types at 35 °C [137].

III.2. Hydrocarbons adsorption properties of silicalite-1

Another interesting property of MFI-type zeolite is their ability to preferentially adsorb organics from water [137, 148, 149, 150]. Zhang et al. investigate in their study [137] the water and organic adsorption in MFI-type zeolite (silicalite-1 and ZSM-5). They show that while the water adsorption response depends significantly on the MFI-type zeolite and cations present in the framework (H^+ , NH_4^+), the ethanol adsorption response is relatively similar in each cases. The weak hydrophilic structural defects in silicalite-1 seem to have no apparent influence on ethanol adsorption even though their presence affects the water adsorption significantly (Figure 113).

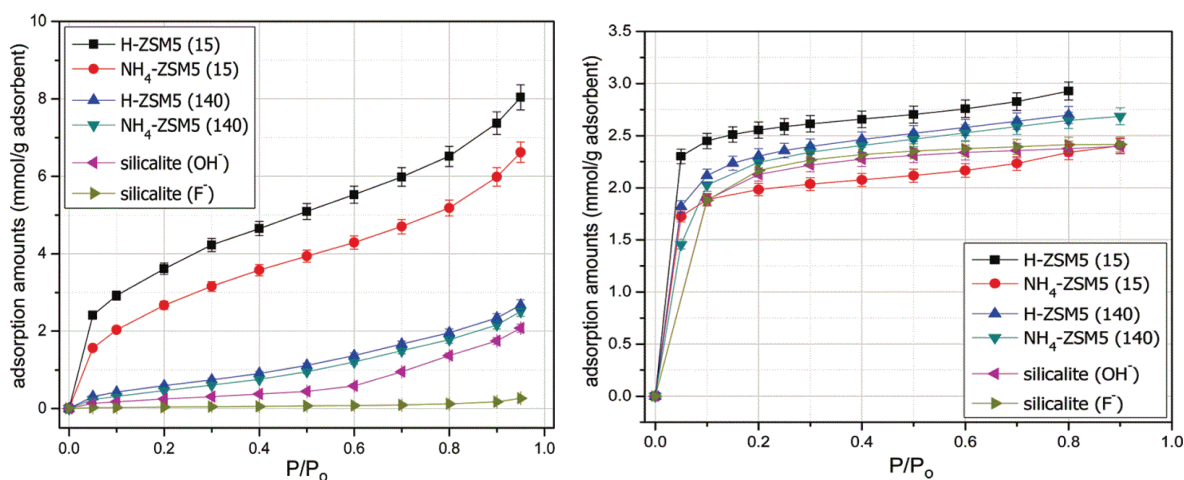


Figure 113 | Water adsorption isotherms (left) and ethanol adsorption isotherms (right) for different MFI zeolite type at 35 °C [137].

Other studies by Pascual et al. [151] simulated and predicted the adsorption of several linear and branched alkanes in silicalite-1 zeolite by Monte Carlo method (**Figure 114**). The water enthalpy of vaporization has been added to the figure. The experiments made by Pascual et al. [151] clearly demonstrated that silicalite-1 had a better affinity for hydrocarbons than for water molecules. The figure represents the adsorption heats of linear alkanes as a function of the molecule coverage. It can be noted that the silicalite-1 adsorbs preferentially high weighted hydrocarbons than small hydrocarbons and/or water. Pascual et al. [151] and Zhang et al. [137] proved that silicalite-1 preferentially adsorb hydrocarbons molecules than water.

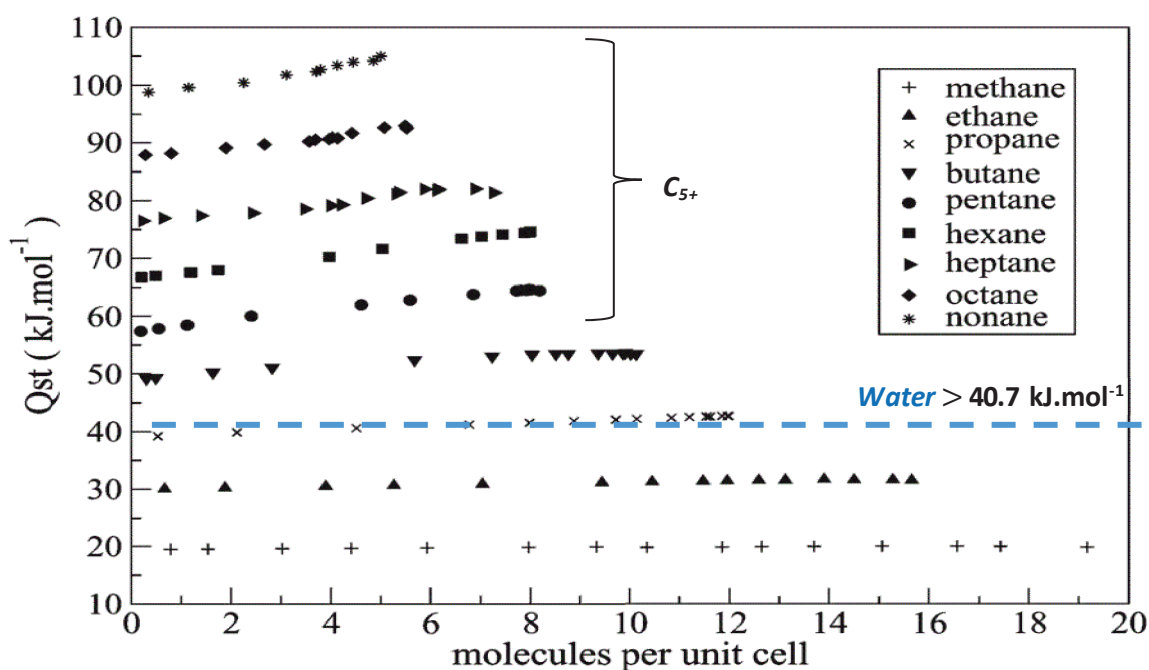


Figure 114 | Adsorption heats of linear alkanes in silicalite-1 at 300 - 308 K as a function of coverage [151].

III.3. Relation between silicalite-1 hydrophobicity and FTS performances

III.3.1. Behavior of the catalyst at the nano-scale

From a particle scale point of view, there could exist a competition between the water and the hydrocarbons produced during the Fischer-Tropsch synthesis. As the reaction goes on, water and hydrocarbons are produced at the iron particles, therefore we should observe a water-gas-shift activity. However, no such activity was seen during the test conducted on the Fe@hollow-silicalite-1 catalyst. As explained in the first part of this chapter, Pascual et al. [151] and Zhang et al. [137] proved that silicalite-1 preferentially adsorbs organic molecules than water. Therefore, a more hydrophobic silicalite-1 should enhance the affinity for organic molecules. Several studies proved that using hydrophobic zeolite support favored the activity of the reaction and increased the yield of organic production [152, 153, 154].

Corma et al. described in [152] two strategies to improve the catalytic activity of Ti-MCM-41 for the epoxidation of olefins. One of those involves the silylation of the surface of Ti-MCM-41 to render the material highly hydrophobic. Corma explained that controlling the hydrophobicity of the surface is a key step for optimizing catalyst especially for improving and/or worsening the adsorption of reactants and products. Indeed he explains that epoxide favorably adsorbs on hydroxylated surface or silanols therefore resulting in epoxide opening and diol formations (**Figure 112**).

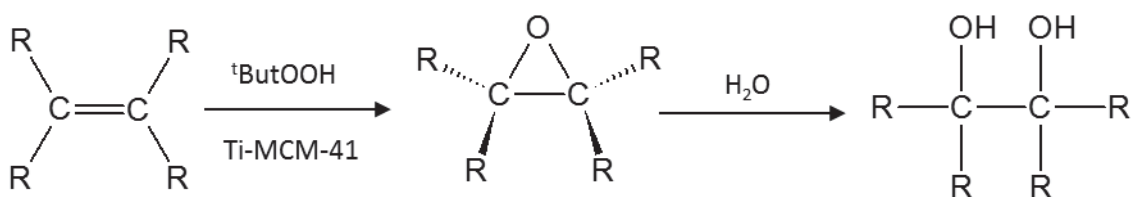


Figure 115 | Reaction of olefins into epoxides followed by the diols formation in presence of water

Corma demonstrated that a high level of silylation of the catalyst surface significantly improves the selectivity of epoxide (**Figure 116**) even though very little influence is seen on the catalyst conversion.

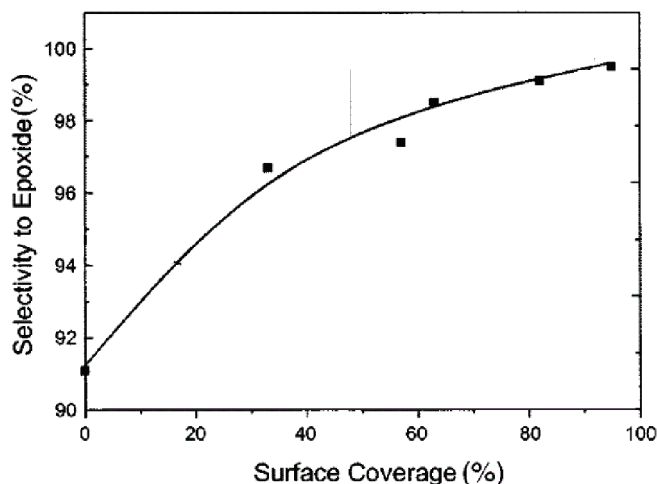


Figure 116 | Selectivity of epoxide for the silylated Ti-MCM-41 at different degrees of surface coverage.

Water present in the medium generally reacts with the epoxide to form the diols. However in the case of the highly hydrophobic Ti-MCM-41, water is prevented from reaching the catalytic sites and therefore forming the diols. In conclusion, Corma proves that selectivity for this reaction can be improved by increasing the catalyst surface hydrophobicity. This concept could be extended to other kind of catalysts.

By taking into account Corma et al. [152] strategies to improve the catalytic activity of Ti-MCM-41 for the epoxidation of olefins, it is possible to explain the CO₂ behavior observed on the Fe/hollow-silicalite-1 catalyst. Therefore, as the support, here the silicalite-1, was proven to be highly hydrophobic, the effect of this enhanced hydrophobicity might be in principle the same as in the case of the highly hydrophobic Ti-MCM-41 of Corma.

Another example, Shanks and MBaraka [153] worked on the design of multifunctionalized mesoporous silicas for the esterification of fatty acid with methanol. The idea here is to functionalize the mesoporous silica with hydrophobic organic groups either by post-synthesis grafting or by one-step co-condensation synthesis methods to render the silica more effective towards the esterification of fatty acid by preventing water from reaching the proximity of the active site. Previous work on esterification of fatty acid by MBaraka et al. [155], through the use of organic-inorganic hybrid mesoporous mono-functionalized silica with propylsulfonic acid and arenesulfonic acid groups, shows that the water released during the esterification

reaction was affecting the extent of the reaction. Furthermore they conclude that the effect of water on the reaction may have been aggravated by the hydrophilic environment inside the pores of the mono-functionalized organic-inorganic hybrid mesoporous silica. Following the conclusion of this study, Brent and Shanks [153] decided to functionalize the mesoporous silica with hydrophobic organic groups to create a reaction environment where water would be continuously removed or, at least, could not reach the adjacent environment of the acid catalytic sites (organosulfonic acid sites) and therefore would improve the esterification of fatty acid reaction performances (Figure 117).

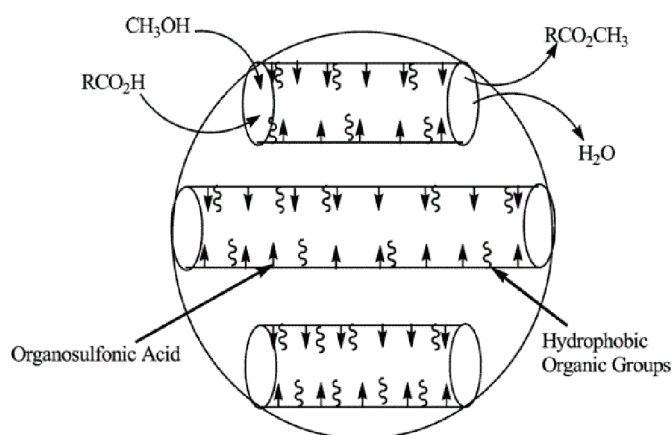


Figure 117 | Schematic of desired water exclusion process with a multi- functionalized mesoporous silica in the esterification of fatty acid with methanol [153].

They found out that the addition of such hydrophobic groups inside the pores of the silica improves the performance of the catalyst. Therefore a more hydrophobic environment tends to reduce the amount of water adsorbed into the mesoporous silica and thus improves the selectivity of the reaction. This work clearly proves the importance of using hydrophobic groups or having a hydrophobic environment in silica to improve heterogeneous catalysis in the case of oil and water forming reaction.

In our case, we can assume that water and hydrocarbons (oil) are produced at the iron particle active sites. Thus, due to the high affinity of oil with the hollow-silicalite-1 zeolite, the hydrocarbons diffuse slowly compared to water, which has no affinity at all. Therefore, after some time the environment near the iron particles is full of oily products. Water, being non-miscible with the oil medium will be expelled from the environment near the iron particles

(Figure 118). Consequently, water cannot react anymore with the iron particles, preventing the sintering and deactivation of the active phase. This may explain the lack of CO_2 at low temperature, the WGS cannot happen due to the non-presence of water around the iron particle. The concentration of water being particularly low around the particle, it makes sense that R-WGS could happened.

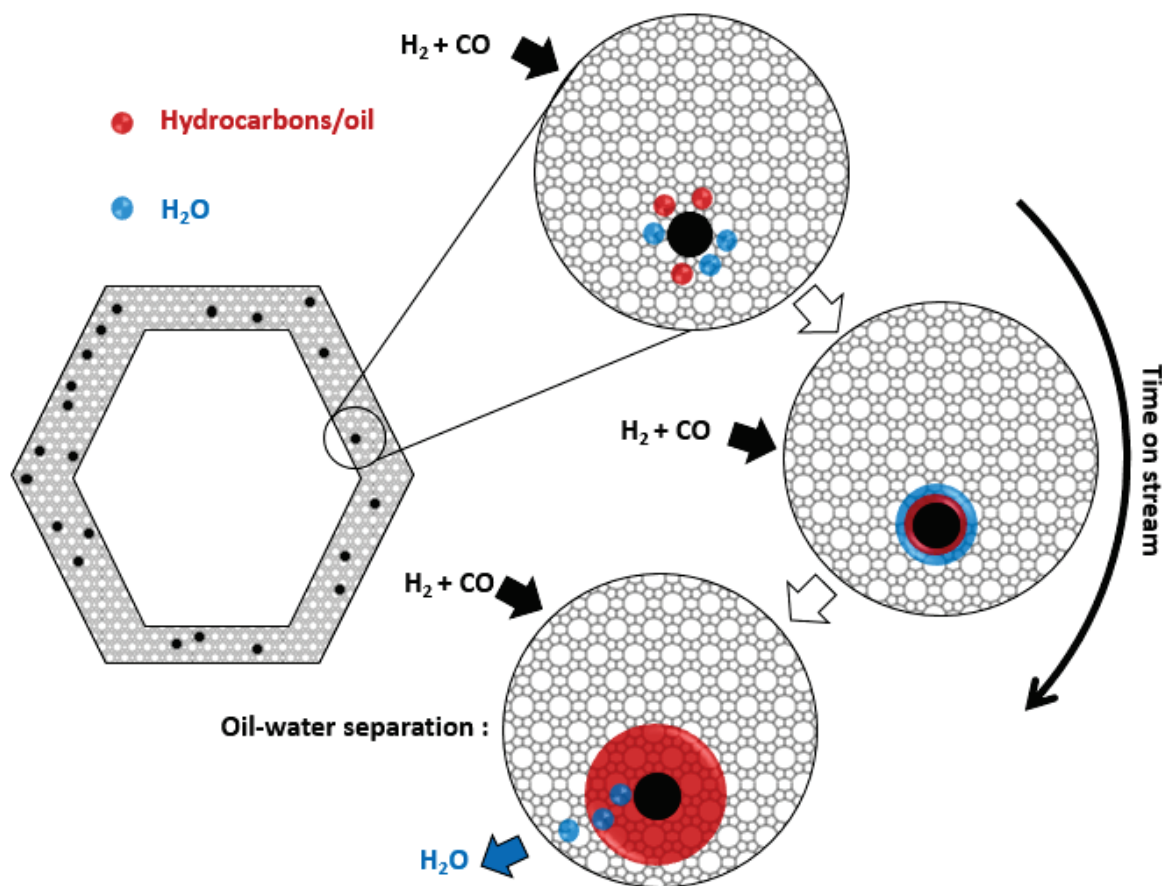


Figure 118 | Schematic of the behavior of water and oil in the Fe@hollow-silicalite-1 catalyst.

However, we saw that at higher temperature, the CO_2 ($> 280\text{ }^\circ\text{C}$) starts being produced. This may come from the fact that the high hydrocarbons fractions decrease with temperature. More methane and $\text{C}_2\text{-C}_4$ gaseous fraction is produced at higher temperature. Therefore, the environment near the iron particle is not anymore full of oily hydrocarbons. Therefore, the WGS can happen again. On that, the water/oil competition is less favorable at high temperature.

III.3.2. Behavior of the catalyst at the reactor scale

From a reactor scale point of view, the water produced from the FTS reaction on the active site (iron nanoparticles), goes down the reactor. While going down in the reactor the amount of water increases. Since the hollow-silicalite-1 crystals are hydrophobic, water does not re-enter into the zeolite, therefore water does not have the opportunity to get near the iron particles again. Therefore, a gradient of water is present down the tubular reactor. The hydrophobic protection prevent water from reaching the iron nanoparticles, therefore the water-gas-shift reaction can hardly happen in these conditions. As the water-gas-shift reaction needs water to form CO_2 , the low concentration of water close to the nanoparticles could explain the lack of CO_2 during the Fischer-Tropsch reaction on Fe@hollow-silicalite-1 at low temperature. **Figure 119** represents a schematic way of representing the water going through the reactor without reaching the nanoparticles inside the hydrophobic hollow-silicalite-1 catalyst.

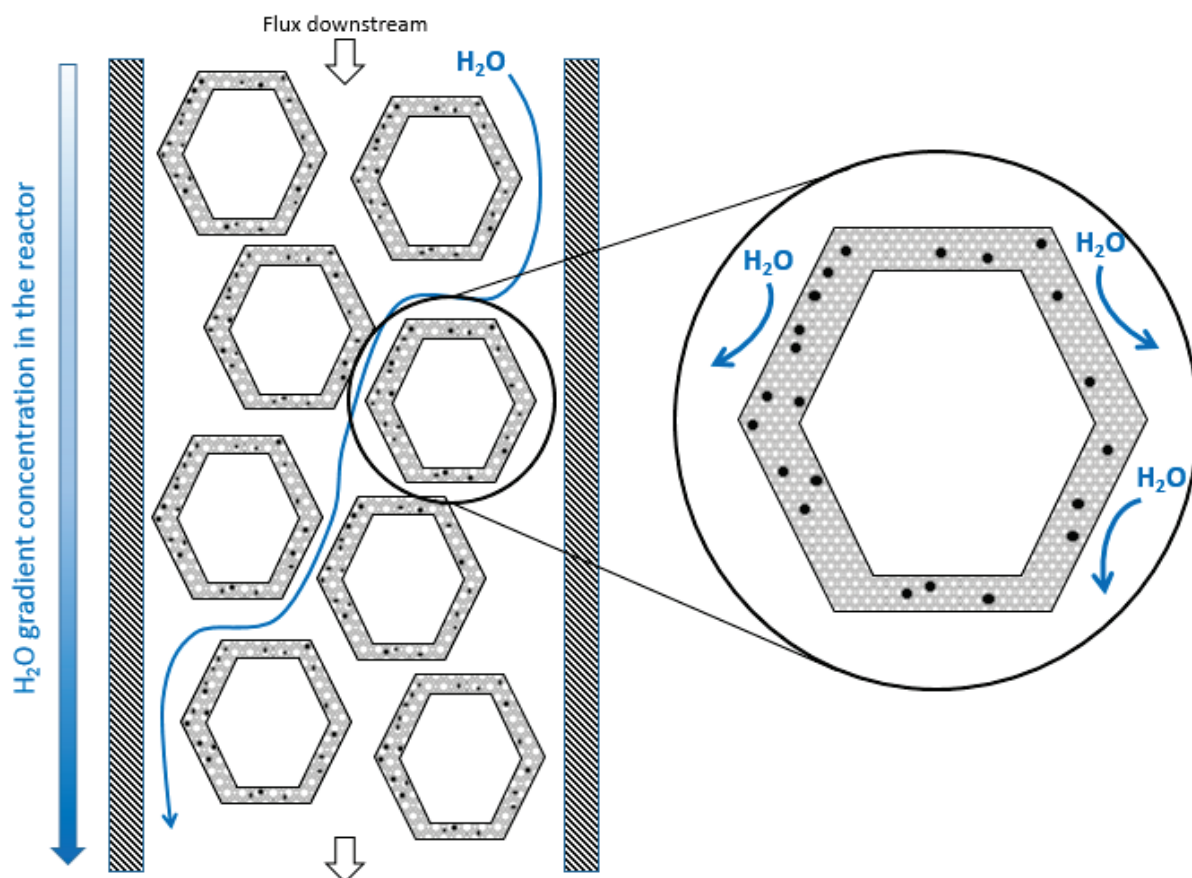


Figure 119 | Scheme of the reactor with the Fe@hollow-silicalite-1 catalyst. Water is stopped from entering the hollow-silicalite-1 due to its high degree of hydrophobicity.

The hollow-silicalite-1 material acts like a “membrane”. Molecules such as H₂, CO, CO₂ and hydrocarbons can go through the zeolite membrane, whereas water is stopped and prevented from going through. The use of a hydrophobic zeolite “membrane” to prevent or remove water is similar to the in-situ H₂O removal during Fischer-Tropsch synthesis concept proposed by Espinoza et al. [156, 157]. High water partial pressures can inhibit the reaction rate or can lead to accelerated catalyst deactivation, by phase transformation and sintering, therefore Espinoza et al. [156, 157] carried out experiments under simulated non-reactive Fischer-Tropsch conditions, using microporous zeolite membrane to enhance productivity in Fischer-Tropsch reactors. This concept applies a reactor such as slurry, packed bed or fluidized bed reactor, in which a suitably large membrane area is integrated, that way H₂O can be removed fast enough during the reaction. The membrane is swept with a sweep gas at low pressure to maintain a high driving force across the membrane. The membrane should be highly permeable towards H₂O and retain H₂, CO, CO₂ and hydrocarbons to avoid a costly recovery of the reactants or products from the sweep gas stream (**Figure 120**).

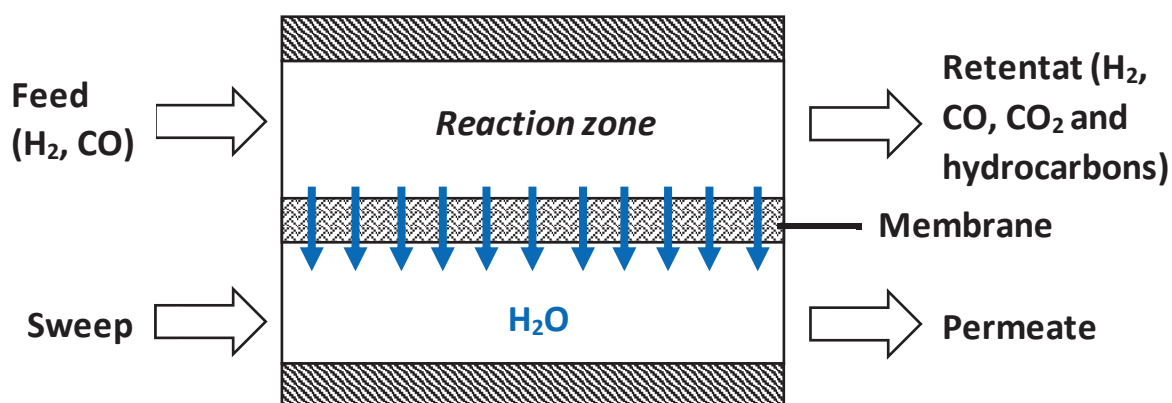


Figure 120 | Simplified scheme of the membrane-type reactor for in-situ H₂O removal.

Others studies by Unruh et al. [158, 159, 160] and Rohde et al. [136–138] proved the positive effect of in-situ H₂O removal by applying hydrophilic membranes to enhance the conversion of CO₂ over WGS shift-active Fe-based catalysts to long chain hydrocarbons. Conversion of CO₂ with H₂ to long chain hydrocarbons using WGS-active Fe catalysts was chosen as the H₂O removal is directly linked to an increase of CO₂ conversion by WGS equilibrium displacement. They demonstrated the feasibility of in-situ H₂O removal under reactive Fischer-Tropsch conditions in lab-scale packed bed reactors, using a tubular hydrophilic amorphous silica membrane and

a tubular hydrophilic supported polymer membrane. Using this type of concept has three major impact:

- (a) to reduce H₂O promoted catalyst deactivation
- (b) to boost the reactor productivity
- (c) to displace the water gas shift (WGS) equilibrium to enhance the conversion of CO₂ to hydrocarbons

Hence, this water removal concept is similar to the hollow-silicalite-1 concept of this study. Therefore, it is not typical to say that the zeolite acts like a membrane to remove water or at least prevent it from re-entering, to reach the iron nanoparticles. This could explain the fact that the WGS is not active at low temperature for this catalyst. The water being removed from the active site, the WGS hardly occurred. This would also explained the Reverse-WGS observed when adding some CO₂ in the feed. The WGS equilibrium being disturbed by the low water concentration. Water is also known as one of the main reason of catalyst deactivation and sintering, however we saw in **Chapter 3** that the Fe@hollow-silicalite-1 didn't sintered and remained stable in time. Therefore, this resistance could also come from the water being quasi non-present near the iron particles due to its removal from the active site area.

To conclude so far, at the reactor scale, the hydrophobicity of the hollow-silicalite-1 may prevent water from re-entering the zeolite to reach and deactivate the iron nanoparticles. Therefore preventing sintering of the nano-particles. Also, due to the low concentration of water around the particles the WGS reaction hardly occurred, therefore, CO₂ is not produced.

IV. Study of the CO₂ transformation mechanism using labelled ¹³CO₂, MS and GC-MS analysis.

It was shown all along this study, that the Fe@hollow-silicalite-1 catalyst did not present any CO₂ formation at low temperature (< 260 °C). A few reason to this phenomena were exposed in the previous part, notably the hydrophobic character of the silicalite-1 hollow-zeolite. Therefore, CO₂ is supposed to be converted into products. The last remaining questions are the following: does the R-WGS reaction really occurs? Or does the silicalite-1 “membrane” prevent both WGS and R-WGS? To answer these questions, labeled ¹³CO₂ was used to follow the products produced during the Fischer-Tropsch synthesis. For that a gas chromatogram coupled with a mass spectrometer were used to analyze the products.

IV.1. Testing conditions and analytical apparatus

Briefly, 1.30 g of 2.5%wtFe@hollow-silicalite-1 with a particle dispersion of 29 % were loaded into a down-flow fixed bed stainless-steel reactor. The Fischer-Tropsch reaction was carried out at 20 bar pressure with a H₂:CO:¹²CO₂ ratio of 2:0.8:0.2 with a GHSV of 1.3 L.g_{cat}⁻¹.h⁻¹ syngas (H₂, CO, CO₂). The temperature of operation was ramped up to 250 °C and later on to 280 °C during the test. Argon (Ar) was used as an internal standard as the mass of N₂ is the same as of CO (m/z = 28), therefore differentiating the two with the mass spectrometer would be impossible. The reaction was carried out for 24 hours under the upper condition. Then, ¹³CO₂ was introduced in the reactor in place of the ¹²CO₂. The reactor was flushed for 2 hours with the H₂/CO/¹³CO₂ mixture, to be sure all the ¹²CO₂ is replaced. At the outlet, a cylinder is connected to capture the gases (reactants and products) at the outlet. The cylinder is then connected to another setup with a MS and GC-MS. A mass spectrometer is used to follow the ¹²CO, ¹³CO, ¹²CO₂, ¹³CO₂, ¹²CH₄ and ¹³CH₄. A GC-MS was also used to first separate the different products and then analyze them by MS. Labeled C₂, C₃ and C₄ were analyzed by this technique.

The commercial catalyst was also tested under the same condition for comparison.

IV.2. ^{13}C analysis by mass spectrometer

Figure 121 represents the concentration intensity of the $^{12}\text{CO}_2$ and $^{13}\text{CO}_2$ at the outlet of the reactor. Firstly, the level of labelled CO_2 is similar between the two catalysts and seems almost independent from the temperature. However, here the molecule of interest is the non-labeled CO_2 ($^{12}\text{CO}_2$). At 250 °C, the Fe@hollow-silicalite-1 catalyst seems to produce really little amount of no-labeled CO_2 . This could come from either the fact that WGS is still active even at this low temperature, or that, the non-labeled CO_2 was not totally replaced by $^{13}\text{CO}_2$ after the 2 hours. Nevertheless, the amount of $^{12}\text{CO}_2$ remained particularly low. The increase in temperature saw the rise of the amount of CO_2 . Indeed, data in **Chapter 4 - Study of the Fischer-Tropsch synthesis on iron-based catalysts**, the results demonstrated that for the Fe@hollow-silicalite-1 catalyst, CO_2 was being produced in reasonable amount at higher temperature. Therefore it is not surprising to observe $^{12}\text{CO}_2$ at 280 °C, as the $^{12}\text{CO}_2$ is produced in addition to the $^{13}\text{CO}_2$ from the feed.

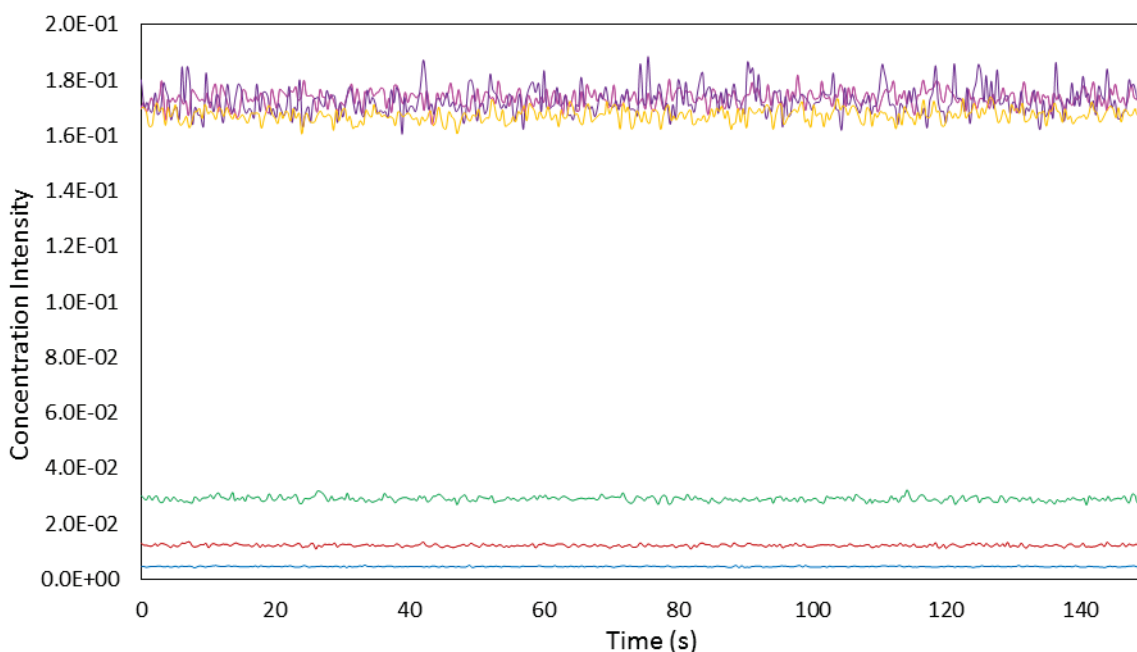


Figure 121 | MS analysis of the concentration of $^{12}\text{CO}_2$ and $^{13}\text{CO}_2$: Fe@hollow-silicalite-1 at 250 °C ($^{12}\text{CO}_2$ in blue line and $^{13}\text{CO}_2$ pink line), at 280 °C ($^{12}\text{CO}_2$ red line and $^{13}\text{CO}_2$ purple line) and the commercial catalyst at 250 °C ($^{12}\text{CO}_2$ in green line and $^{13}\text{CO}_2$ in yellow line).

The commercial catalyst gives a really high amount of non-labeled CO_2 at 250 °C. It is almost twice as for the Fe@hollow-silicalite-1 at 280 °C. Again, it was demonstrated in the previous

chapter that bulk-type catalysts, like the commercial catalyst, produce a quite important amount of CO₂.

In conclusion, the results obtained with the ¹²CO₂/¹³CO₂ is in agreement with those reported in **Chapter 4**. That is, a small amount / or no CO₂ at 250 °C and a higher amount at 280 °C for the Fe@hollow-silicalite-1 catalyst.

Figure 122 represents the concentration intensity of the ¹²CO and ¹³CO at the outlet of the reactor. Firstly, in terms of ¹²CO, the concentration intensity is less important when going from 250 °C to 280 °C. This is due to the higher conversion in ¹²CO at higher temperature. The low ¹²CO intensity for the commercial catalyst is due to its really high conversion. This observation is fully in agreement with the Fischer-Tropsch data in **Chapter 4**. Now, when looking at the ¹³CO concentration, it is clear that the amount of ¹³CO formed is really low. In the feed mixture, the ¹³CO₂ represents about 5 % of the total feed, therefore it is normal that the amount of ¹³CO observed is so low. Nevertheless, the presence of the labeled ¹³CO is proof of the R-WGS happening:

(Equation 48) Reverse-Water-gas-shift: $H_2 + CO_2 \rightleftharpoons CO + H_2O$

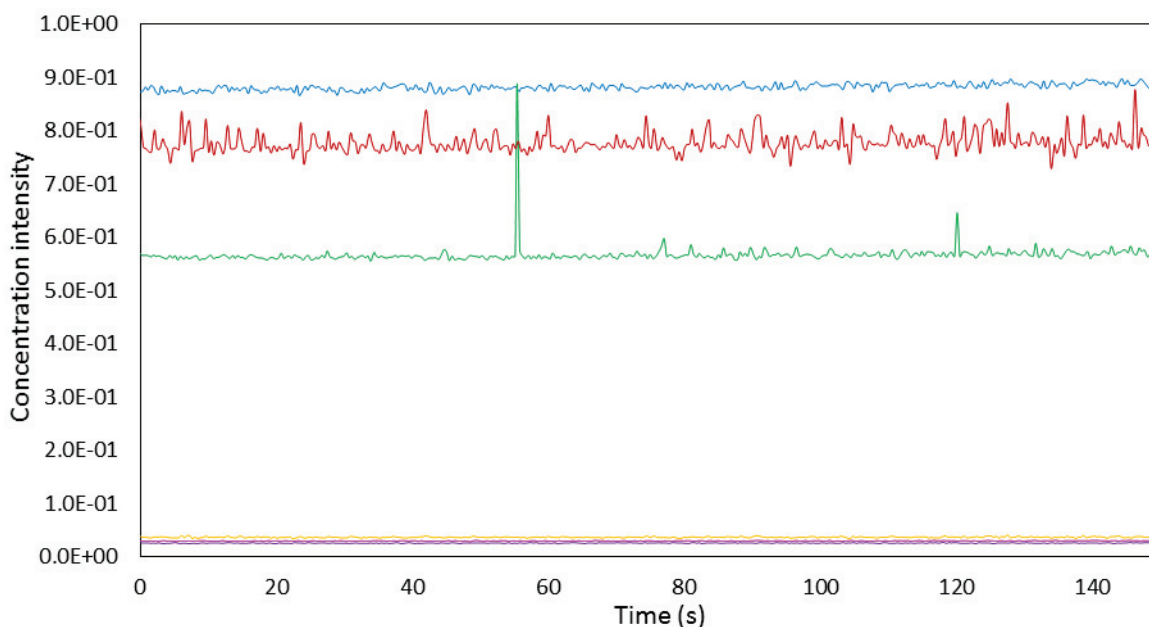


Figure 122 | MS analysis of the concentration of ¹²CO and ¹³CO: Fe@hollow-silicalite-1 at 250 °C (¹²CO in blue line and ¹³CO pink line), at 280 °C (¹²CO red line and ¹³CO purple line) and the commercial catalyst at 250 °C (¹²CO in green line and ¹³CO in yellow line).

It demonstrates that the Fe phases is WGS active, however due to the membrane presence the WGS reaction is prevented while the R-WGS is favored.

Figure 123 represents the concentration intensity of the $^{12}\text{CH}_4$ and $^{13}\text{CH}_4$ at the outlet of the reactor. Firstly, in terms of $^{13}\text{CH}_4$, the concentration intensity is more important when going from 250 °C to 280 °C. Again, as the amount of $^{13}\text{CO}_2$ converted is low the intensity of the $^{13}\text{CH}_4$ signal is particularly low too. Nevertheless, it is confirmed that some labelled C is found into CH_4 . For the non-labelled CH_4 , the figure shows a drastic increase of $^{12}\text{CH}_4$ from 250 °C to 280 °C.

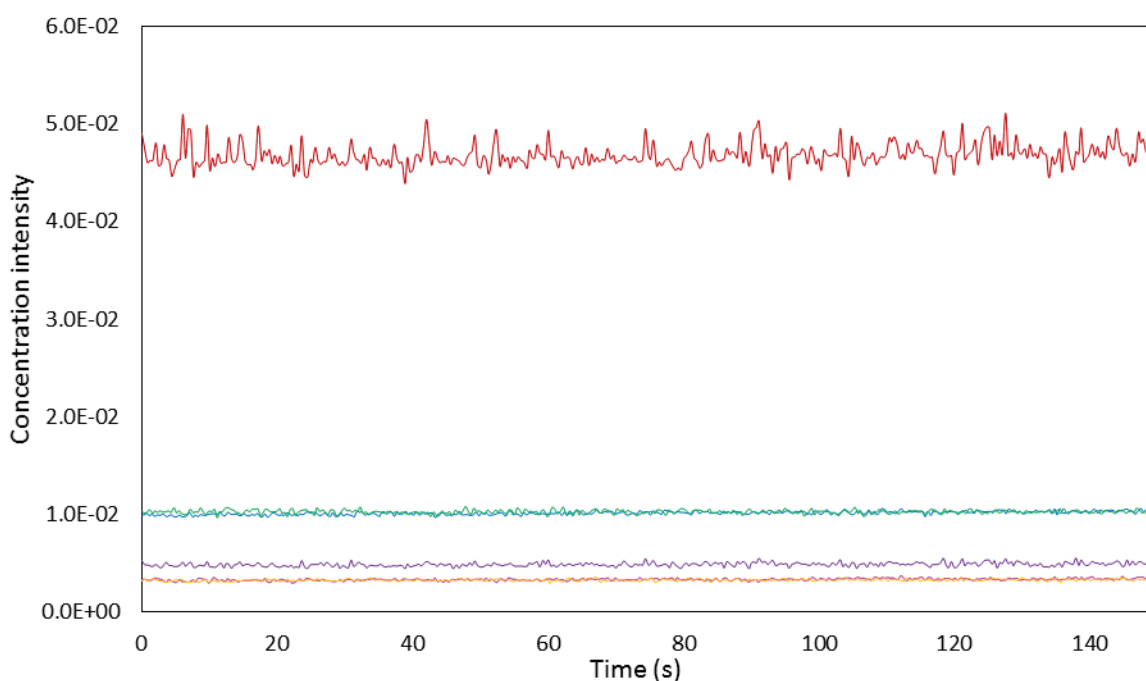


Figure 123 | MS analysis of the concentration of $^{12}\text{CH}_4$ and $^{13}\text{CH}_4$: Fe@hollow-silicalite-1 at 250 °C ($^{12}\text{CH}_4$ in blue line and $^{13}\text{CH}_4$ pink line), at 280 °C ($^{12}\text{CH}_4$ red line and $^{13}\text{CH}_4$ purple line) and the commercial catalyst at 250 °C ($^{12}\text{CH}_4$ in green line and $^{13}\text{CH}_4$ in yellow line).

The commercial catalyst, as proved earlier, produces really small amounts of $^{12}\text{CH}_4$. $^{13}\text{CH}_4$ is also observed, but in low quantity. In conclusion, labelled CH_4 is found for both catalysts, meaning that $^{13}\text{CO}_2$ is converted, even if it is in small amount, into other products.

The % of ^{13}CO , $^{13}\text{CH}_4$ and $^{12}\text{CO}_2$ is given in **Table 52**. The % was calculated by dividing the intensity signal of species ^{13}X by the sum of the intensity of ^{12}X and ^{13}X .

Table 52 | % of ^{13}CO , $^{13}\text{CH}_4$ and $^{12}\text{CO}_2$ at 250 °C and 280 °C

| | Fe@hollow-silicalite-1 | | | Commercial catalyst | | |
|--------|------------------------|------------------------|------------------------|----------------------|------------------------|------------------------|
| T (°C) | ^{13}CO (%) | $^{13}\text{CH}_4$ (%) | $^{12}\text{CO}_2$ (%) | ^{13}CO (%) | $^{13}\text{CH}_4$ (%) | $^{12}\text{CO}_2$ (%) |
| 250 | 3.3 | 25 | 2.6 | 4.3 | 24 | 14.9 |
| 280 | 4.6 | 9.8 | 6.8 | - | - | - |

What is noticeable is the high % of labelled CH_4 for both catalysts at 250 °C. At higher temperature, due to the higher conversion, it is perfectly logical that all % decrease. The large amount of labelled methane is quite unexpected. Let's imagine that $^{13}\text{CO}_2$ is converted via the R-WGS reaction to form ^{13}CO and then by the usual FTS reaction, it is transformed into $^{13}\text{CH}_4$. Then, as the ^{13}CO detected is really low, it is particularly strange to obtain such a high amount of labelled CH_4 . Therefore, by taking into account these results, it might not be wrong to say that, there is probably a direct conversion from the $^{13}\text{CO}_2$ to the $^{13}\text{CH}_4$ via the following equation:



A direct hydrogenation of the CO_2 , instead of R-WGS and then FTS, may explain the high amount of CH_4 . However, when looking in literature [164], researchers consider that the CO_2 transformed via the combination of two routes, the R-WGS and then the CO hydrogenation. Some articles mention the direct CO_2 hydrogenation route, from CO_2 to CH_4 [101].

Nevertheless, the objectives was to show that the labelled ^{13}C could be found in FTS products, which is indeed the case. Further analysis by GC-MS helped confirmed the presence (in small quantities) of labelled ^{13}C in products such as ethane, propane, propene... **(Annexe)**

In conclusion, the used of labelled $^{13}\text{CO}_2$ helped to determine if the CO_2 was really being converted during the FTS reaction. Indeed, CO_2 is being converted into mainly CH_4 , and a relatively low amount of CO , $\text{C}_2\text{-C}_4$ products. Therefore, it can be concluded that R-WGS is happening during the FTS reaction in presence of CO_2 in the feed, however a direct transformation of the CO_2 into CH_4 might need to be added to the overall equation. The iron catalyst is therefore active in the WGS reaction. The membrane does prevent the WGS reaction but does not prevent the R-WGS from happening.

Overall conclusion and perspectives

The objectives of this study was to develop a more active, selective and stable iron-based catalyst for the Fischer-Tropsch synthesis. We developed an iron nanoparticles encapsulated in hollow single crystal of silicalite-1 catalyst. An average particles size of 3.5 nm was obtained.

The developed catalyst was fully characterized by various analytical techniques and compared with other iron-based catalysts.

Extensive characterizations and Fischer-Tropsch studies on various kinds of iron catalysts helped to discern some interesting aspects that might open new pathways in rational design of iron catalyst in the near future. Indeed, all along this work, it was clear that the commercial catalyst, currently used in the industry, remains the most active and interesting catalyst from an industrial point of view. However, its poor selectivity in CO₂ makes it not the best iron-based catalyst possible. There is still room for improvement.

The iron nanoparticles encapsulated in hollow-silicalite-1 catalyst (Fe@hollow-silicalite-1), even though not as active as it was thought to be, has provided truly remarkable behavior due to the high hydrophobicity of the hollow-silicalite-1 as proven in this work. The remarkable CO₂ selectivity of this catalyst makes it of particular interest. The high hydrophobicity seems to prevent WGS from happening due to low adsorption of water inside the silicalite-1 support. Therefore, the low concentration around the iron particles seems to favor the R-WGS, or at least, the non-production of CO₂. Furthermore, at low temperature, the catalyst proved to be converting small amounts of CO₂ into mostly CH₄ and small quantities of CO, C₂ and C₃ species. Its counterpart, the well-defined nanoparticles on the surface of the silicalite-1 (Fe/hollow-silicalite-1), showed a behavior in-between the encapsulated iron nanoparticles catalyst and the commercial catalyst. That is, a really low amount of CO₂ produced and a good activity. The close proximity of the iron particles with the hydrophobic support is lowering the WGS activity of the Fe/hollow-silicalite-1 catalyst.

Unfortunately, the iron phase characterization did not help to discriminate much between all the iron catalysts, as no significant difference was observed. As a conclusion, the commercial catalyst is the best iron catalyst from an industrial point of view at this point in

time. However it would be particularly interesting to combine the performances properties of the commercial catalyst with the hydrophobic silicalite-1 properties. Indeed, having the commercial catalyst “encapsulated” inside silicalite-1 might give a really interesting catalyst to further study.

Of course, this study is far from being complete. Most observations were explained with hypothesis and are based on literature similarities.

To further develop this study, varying promoter's types and compositions may be looked at to improve catalytic properties of the iron nanoparticles encapsulated in hollow-silicalite-1 catalyst. Also, to further prove that the hydrophobicity is the main reason non-production of CO₂, silicalite-1 could be replaced by its hydrophilic counterpart, ZSM-5. Due to its hydrophilic properties, the water concentration around the iron nanoparticles should be higher, therefore WGS would be more prone to happen. One of the biggest problematic aspect in this study was the very low iron loading obtained for the newly developed catalyst. Therefore, focusing efforts on increasing the iron loading inside the Fe@hollow-silicalite-1 catalysts may help to improve the Fischer-Tropsch performances of the catalyst. Characterization of the catalyst by XRD and EXAFS would become more accurate and easier too. The increased loading would also provide some ease during catalyst upscaling as we have shown that the catalyst was having really low density.

Finally, the new information gained during this work and the various interesting aspects provided by the iron nanoparticles encapsulated in silicalite-1 catalyst, will surely help to open new pathways in rational design of iron catalysts in the near future.

Appendix

1) Mössbauer spectroscopy of FeCuK@hollow-silicalite-1 catalyst

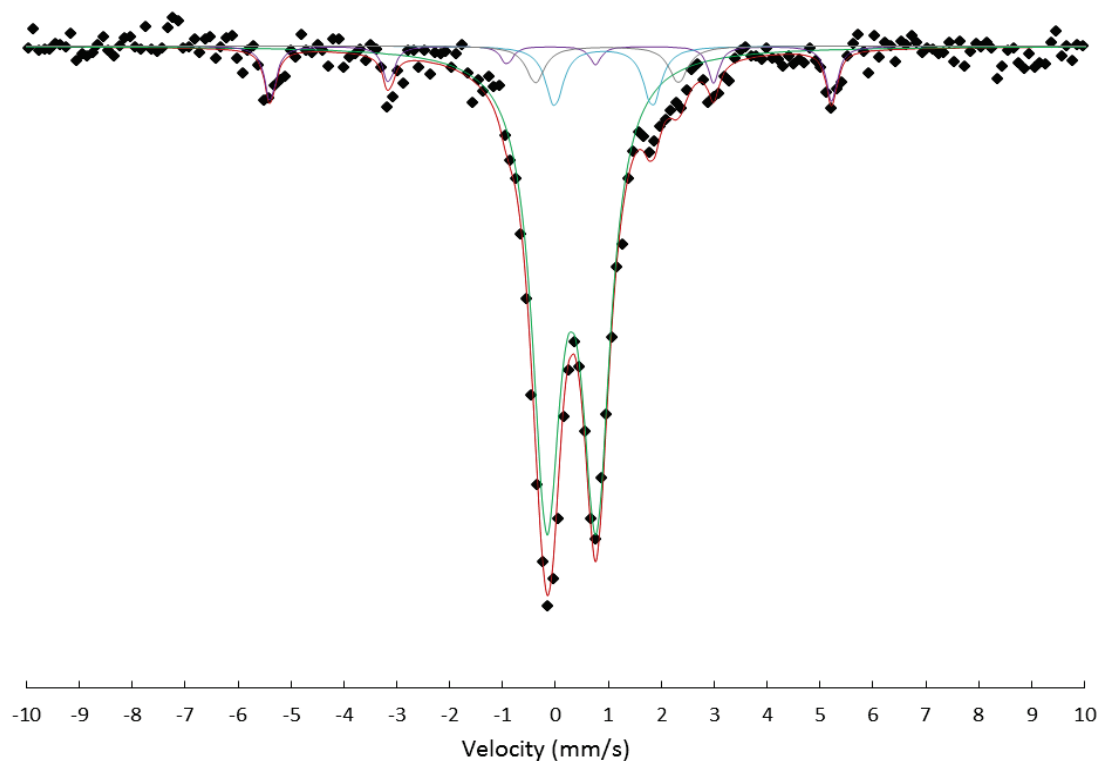


Figure 124 | ^{57}Fe Mössbauer spectrum of the fresh FeCuK@hollow-silicalite-1 catalyst after FTS: Experimental spectrum (black dot), experimental spectrum fit (red line), $\alpha\text{-Fe}$ in large particles (purple line), Fe^{3+} (green line) and Fe^{2+} (grey and blue line).

Table 53 | The Mössbauer fitted parameters for the fresh FeCuK@hollow-silicalite-1

| Sample | Splitting | IS ($\text{mm}\cdot\text{s}^{-1}$) | QS ($\text{mm}\cdot\text{s}^{-1}$) | Hyperfine field (T) | Species | Relative intensity (%) |
|-------------------------------|-----------|---|---|------------------------|--------------------|---------------------------|
| FeCuK@hollow- silicalite-1 | Doublet | 0.40 | 0.72 | - | Fe^{3+} | 64 |
| | Doublet | 1.10 | 2.48 | - | Fe^{2+} | 9 |
| | Doublet | 1.02 | 1.83 | - | Fe^{2+} | 11 |
| | Sextet | 0.05 | 0.00 | 32.8 | $\alpha\text{-Fe}$ | 16 |

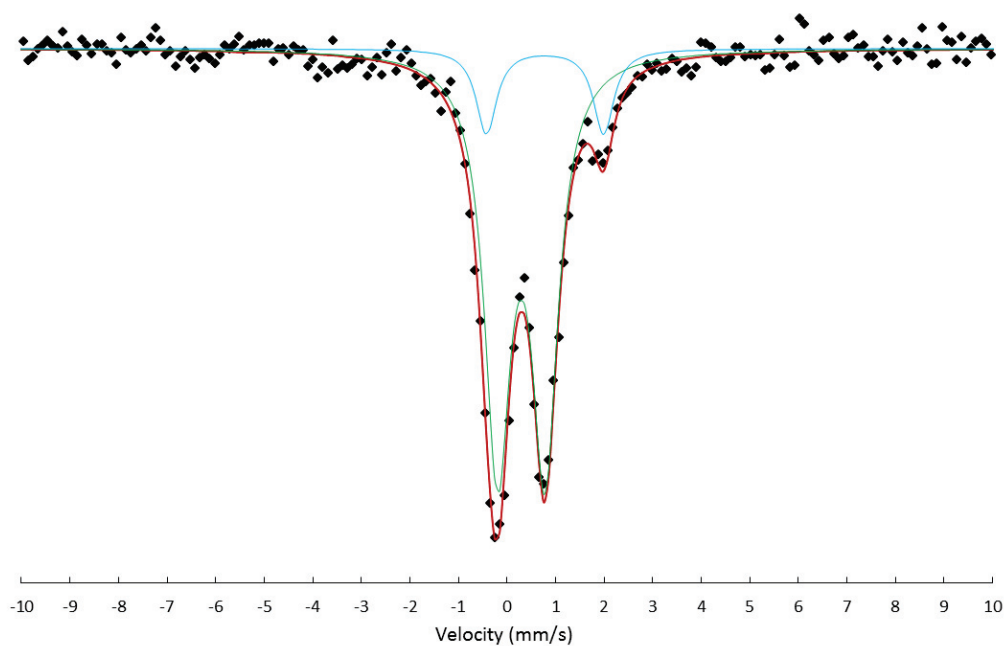


Figure 125 | ^{57}Fe Mössbauer spectrum of the spent FeCuK@hollow-silicalite-1 catalyst after FTS: Experimental spectrum (black dot), experimental spectrum fit (red line), Fe^{3+} (green line) and Fe^{2+} (blue line).

Table 54 | The Mössbauer fitted parameters for the spent FeCuK@hollow-silicalite-1

| Sample | Splitting | IS ($\text{mm}\cdot\text{s}^{-1}$) | QS ($\text{mm}\cdot\text{s}^{-1}$) | Hyperfine field (T) | Species | Relative intensity (%) |
|-------------------------------|-----------|---|---|------------------------|------------------|---------------------------|
| FeCuK@hollow- silicalite-1 | Doublet | 0.38 | 0.98 | - | Fe^{3+} | 86 |
| | Doublet | 0.88 | 2.40 | - | Fe^{2+} | 14 |

2) Olefin to paraffin ratio

Table 55 | The O/P ratio for the iron-based catalysts

| Catalysts | $\text{C}_2^-/\text{C}_2^+$ | $\text{C}_3^-/\text{C}_3^+$ | $\text{C}_4^-/\text{C}_4^+$ |
|--|-----------------------------|-----------------------------|-----------------------------|
| Fe@hollow-silicalite-1 | 0.03 | 0.5 | 0.5 |
| Fe/hollow-silicalite-1 | 0.02 | 0.1 | 0.4 |
| Fe/SiO ₂ | 0.3 | 1.2 | 1.6 |
| Commercial catalyst | 1.0 | 2.9 | 2.6 |
| Nano-structured $\alpha\text{-Fe}_2\text{O}_3$ | 1.5 | 3.1 | 2.7 |

3) Determination of the water-gas-shift reaction equilibrium

First, it would be interesting to determine if the WGS reaction is at equilibrium or not during the reaction. For that, the equilibrium constant of the reaction was calculated at different temperature following the equation of Moe J. M. [165, 166]. Moe J. M. has derived a simple equation to use empirical model to represent the equilibrium constant which is sufficiently good for design computations and is given by:

$$\text{(Equation 50)} \quad K_{\text{eq}} = \exp\left(\frac{4577.8}{T} - 4.33\right)$$

The equilibrium at different temperature is given in **Table 56** below.

Table 56 | WGS equilibrium constant

| T (°C) | Equilibrium constant (K_{eq}) |
|--------|--|
| 250 | 83.1 |
| 260 | 70.6 |
| 270 | 60.2 |
| 280 | 51.7 |

Fischer-Tropsch data on the Fe@hollow-silicalite-1 catalyst were used to determine either or not the WGS reaction is at equilibrium. A few hypothesis as to be made for the calculation.

a) If the WGS is at equilibrium

Firstly, if the **hypothesis that the WGS is at equilibrium**. The inlet data on H₂, CO and CO₂ is reported in **Table 57**.

Table 57 | Number of mol of H₂, CO, CO₂ at the inlet of the reactor

| P (bar) | H ₂ /CO/CO ₂ | T(°C) | H _{2,in} | CO _{in} | CO _{2,in} |
|---------|------------------------------------|-------|-------------------|------------------|--------------------|
| 20 | 2/1/0 | 250 | 0,2443 | 0,1222 | 0 |
| 20 | 2/1/0 | 260 | 0,2243 | 0,1122 | 0 |
| 20 | 2/1/0 | 270 | 0,2243 | 0,1122 | 0 |
| 20 | 2/1/0 | 280 | 0,2243 | 0,1122 | 0 |
| 20 | 2/0.8/0.2 | 250 | 0,4497 | 0,1801 | 0,0447 |
| 20 | 2/0.8/0.2 | 260 | 0,4497 | 0,1801 | 0,0447 |
| 20 | 2/0.8/0.2 | 270 | 0,4497 | 0,1801 | 0,0447 |
| 20 | 2/0.8/0.2 | 280 | 0,4497 | 0,1801 | 0,0447 |

As we considered that the reaction is at equilibrium, the equilibrium constant equation of Moe J. M. can help to calculate the number of mol of water at the outlet of the reactor. $H_{2,out}$, CO_{out} and $CO_{2,out}$, $CH_{4,out}$ are calculated with the GC data. The $C_{10}H_{22}$ is calculated via the least-square deviation in atom balances. The number of mol in and out of all species are respectively reported in **Table 58**.

Table 58 | Number of mol of H_2 , CO , CO_2 , CH_4 , H_2O and $C_{10}H_{22}$ at the outlet of the reactor (if WGS at equilibrium)

| P (bar) | $H_2/CO/CO_2$ | T(°C) | $H_{2,out}$ | CO_{out} | $CO_{2,out}$ | H_2O_{out} | $CH_{4,out}$ | $C_{10}H_{22, out}$ |
|---------|---------------|-------|-------------|------------|--------------|--------------|--------------|---------------------|
| 20 | 2/1/0 | 250 | 0,1882 | 0,0993 | 0,0000 | 0,0000 | 0,0033 | 0,0041 |
| 20 | 2/1/0 | 260 | 0,1628 | 0,0827 | 0,0000 | 0,0000 | 0,0050 | 0,0043 |
| 20 | 2/1/0 | 270 | 0,1535 | 0,0727 | 0,0039 | 0,0001 | 0,0088 | 0,0044 |
| 20 | 2/1/0 | 280 | 0,1317 | 0,0646 | 0,0074 | 0,0003 | 0,0099 | 0,0060 |
| 20 | 2/0.8/0.2 | 250 | 0,3508 | 0,1378 | 0,0420 | 0,0013 | 0,0050 | 0,0073 |
| 20 | 2/0.8/0.2 | 260 | 0,3379 | 0,1277 | 0,0431 | 0,0016 | 0,0073 | 0,0080 |
| 20 | 2/0.8/0.2 | 270 | 0,3064 | 0,1131 | 0,0446 | 0,0020 | 0,0123 | 0,0097 |
| 20 | 2/0.8/0.2 | 280 | 0,2860 | 0,1014 | 0,0479 | 0,0026 | 0,0171 | 0,0106 |

With these data, we can calculate the atom balance (**Table 59**) for both the inlet and outlet data. If the WGS was at equilibrium, the atom balance between the inlet and the outlet of the reactor should be verified. The atom balance is reported in **Table 59**.

Table 59 | Atom balance if the WGS was at equilibrium



| P (bar) | $H_2/CO/CO_2$ | T(°C) | H_{in} | C_{in} | O_{in} | H_{out} | C_{out} | O_{out} |
|---------|---------------|-------|----------|----------|----------|-----------|-----------|-----------|
| 20 | 2/1/0 | 250 | 0,4886 | 0,1222 | 0,1222 | 0,4790 | 0,1433 | 0,0993 |
| 20 | 2/1/0 | 260 | 0,4486 | 0,1122 | 0,1122 | 0,4396 | 0,1304 | 0,0827 |
| 20 | 2/1/0 | 270 | 0,4486 | 0,1122 | 0,1122 | 0,4400 | 0,1297 | 0,0806 |
| 20 | 2/1/0 | 280 | 0,4486 | 0,1122 | 0,1122 | 0,4346 | 0,1415 | 0,0797 |
| 20 | 2/0.8/0.2 | 250 | 0,8994 | 0,2248 | 0,2695 | 0,8845 | 0,2577 | 0,2231 |
| 20 | 2/0.8/0.2 | 260 | 0,8994 | 0,2248 | 0,2695 | 0,8843 | 0,2581 | 0,2155 |
| 20 | 2/0.8/0.2 | 270 | 0,8994 | 0,2248 | 0,2695 | 0,8801 | 0,2673 | 0,2043 |
| 20 | 2/0.8/0.2 | 280 | 0,8994 | 0,2248 | 0,2695 | 0,8779 | 0,2720 | 0,1998 |

The inlet and outlet atom do not match at all. Therefore the WGS at equilibrium hypothesis is wrong. Therefore, the WGS during the FTS reaction on the Fe@hollow-silicalite-1 catalyst is not at equilibrium. The same reasoning was applied on the commercial catalyst. The same conclusion was determined. Consequently, in both case the WGS is not at equilibrium during the FTS reaction. The next part will demonstrate the upper conclusion.


b) If the WGS is not at equilibrium

Again, the $H_{2,out}$, CO_{out} and $CO_{2,out}$, $CH_{4,out}$ are calculated with the GC data. However, as we considered that the reaction is not at equilibrium, the equilibrium constant equation of Moe J. M. cannot be used for the calculation of the number of mol of water at the outlet of the reactor. This time the H_2O and $C_{10}H_{22}$ were calculated via the least-square deviation in atom balances. The number of mol in and out of all species are respectively reported in **Table 60**.

Table 60 | Number of mol of H_2 , CO , CO_2 , CH_4 , H_2O and $C_{10}H_{22}$ at the outlet of the reactor (if WGS not at equilibrium)

| P (bar) | $H_2/CO/CO_2$ | T(°C) | $H_{2,out}$ | CO_{out} | $CO_{2,out}$ | H_2O_{out} | $CH_{4,out}$ | $C_{10}H_{22, out}$ |
|---------|---------------|-------|-------------|------------|--------------|--------------|--------------|---------------------|
| 20 | 2/1/0 | 250 | 0,1882 | 0,0993 | 0,0000 | 0,0250 | 0,0033 | 0,0022 |
| 20 | 2/1/0 | 260 | 0,1628 | 0,0827 | 0,0000 | 0,0273 | 0,0050 | 0,0022 |
| 20 | 2/1/0 | 270 | 0,1535 | 0,0727 | 0,0039 | 0,0283 | 0,0088 | 0,0023 |
| 20 | 2/1/0 | 280 | 0,1317 | 0,0646 | 0,0074 | 0,0354 | 0,0099 | 0,0033 |
| 20 | 2/0.8/0.2 | 250 | 0,3508 | 0,1378 | 0,0420 | 0,0466 | 0,0050 | 0,0039 |
| 20 | 2/0.8/0.2 | 260 | 0,3379 | 0,1277 | 0,0431 | 0,0516 | 0,0073 | 0,0042 |
| 20 | 2/0.8/0.2 | 270 | 0,3064 | 0,1131 | 0,0446 | 0,0636 | 0,0123 | 0,0051 |
| 20 | 2/0.8/0.2 | 280 | 0,2860 | 0,1014 | 0,0479 | 0,0695 | 0,0171 | 0,0055 |

With these data, we can calculate the atom balance (**Table 61**) for both the inlet and outlet data. If the WGS was at equilibrium, the atom balance between the inlet and the outlet of the reactor should be verified. The atom balance is reported in **Table 61**.

Table 61 | Atom balance if the WGS was not at equilibrium


| P (bar) | H ₂ /CO/CO ₂ | T(°C) | H _{in} | C _{in} | O _{in} | H _{out} | C _{out} | O _{out} |
|---------|------------------------------------|-------|-----------------|-----------------|-----------------|------------------|------------------|------------------|
| 20 | 2/1/0 | 250 | 0,4886 | 0,1222 | 0,1222 | 0,4876 | 0,1244 | 0,1243 |
| 20 | 2/1/0 | 260 | 0,4486 | 0,1122 | 0,1122 | 0,4490 | 0,1098 | 0,1100 |
| 20 | 2/1/0 | 270 | 0,4486 | 0,1122 | 0,1122 | 0,4496 | 0,1085 | 0,1088 |
| 20 | 2/1/0 | 280 | 0,4486 | 0,1122 | 0,1122 | 0,4466 | 0,1150 | 0,1148 |
| 20 | 2/0.8/0.2 | 250 | 0,8994 | 0,2248 | 0,2695 | 0,9000 | 0,2235 | 0,2684 |
| 20 | 2/0.8/0.2 | 260 | 0,8994 | 0,2248 | 0,2695 | 0,9014 | 0,2204 | 0,2655 |
| 20 | 2/0.8/0.2 | 270 | 0,8994 | 0,2248 | 0,2695 | 0,9012 | 0,2209 | 0,2659 |
| 20 | 2/0.8/0.2 | 280 | 0,8994 | 0,2248 | 0,2695 | 0,9008 | 0,2216 | 0,2667 |

This time, in the case of the WGS not at the equilibrium, the atom balance is verified. Therefore, one can assume that the WGS reaction is indeed not at the equilibrium during the FTS reaction in the case of the Fe@hollow-silicalite-1 catalyst. Again, the same reasoning was made for the commercial catalyst, and the same conclusion was found. In conclusion, it was proven that the Water-Gas-shift reaction is not at the equilibrium during the Fischer-Tropsch synthesis.

4) ¹³C analysis by gas chromatography coupled with mass spectrometer

Figure 126, **Figure 127** and **Figure 128**, respectively display the % of ethane, propane and propene, at 250 °C (left) and 280 °C (right). As the concentration of labelled species is really low, all labelled species for a given molecule will be counted together. **Figure 126** shows the % of labelled ethane and non-labelled ethane at the two different temperatures

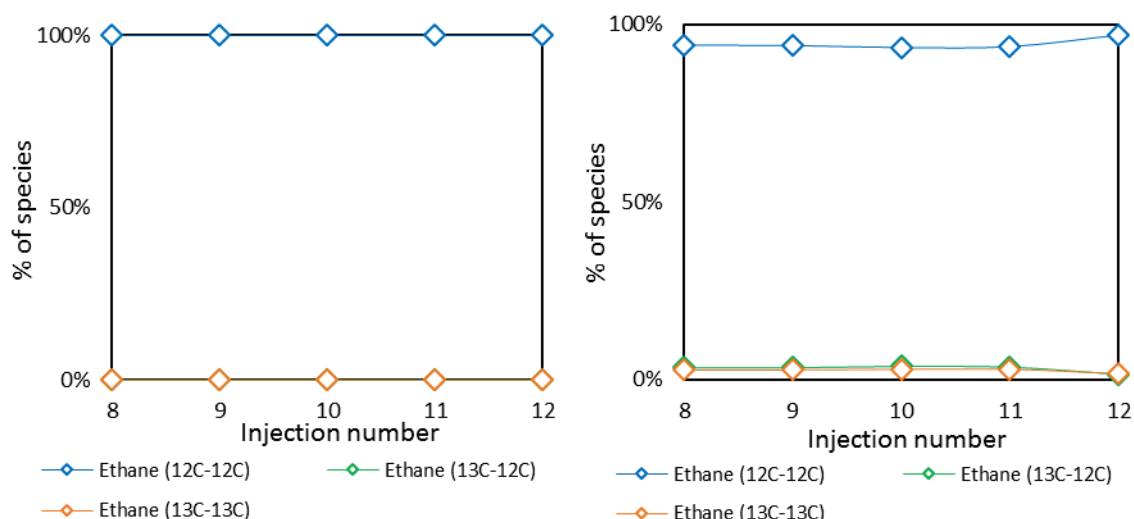


Figure 126 | GC-MS analysis of the labelled and non-labelled ethane at 250 °C (left) and 280 °C (right).

At low temperature, no labelled ethane was observed, probably due to the really low conversion of CO. However at higher temperature, labelled ethane can be observed in small quantities ($\sim 3 - 4 \%$).

For propane and propene, respectively **Figure 127** and **Figure 128**, labelled molecules can be observed in relatively low quantities. Labelled propane quantity is about $\sim 3 - 5 \%$ for both temperature whereas labelled propene is about $\sim 2 - 3 \%$.

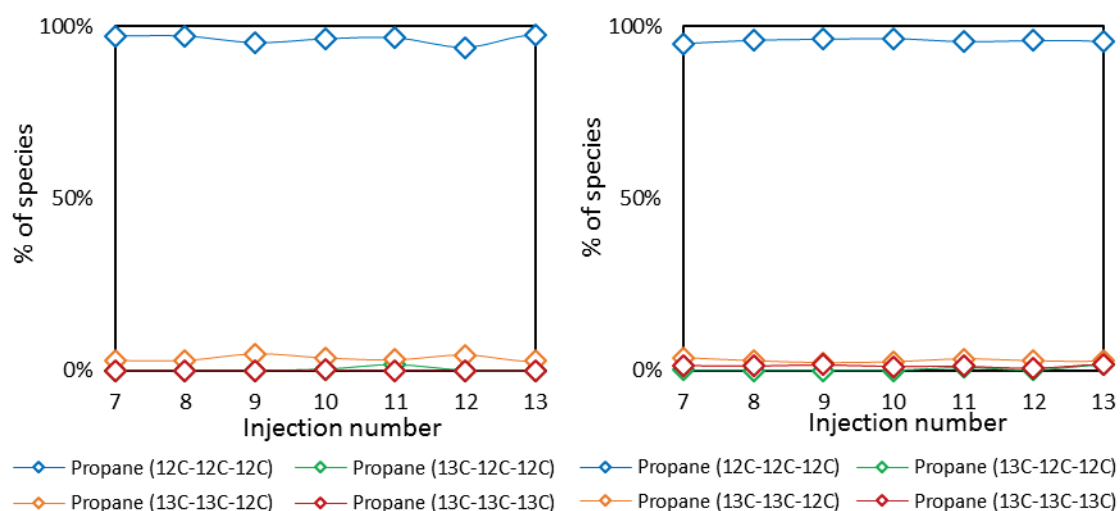


Figure 127 | GC-MS analysis of the labelled and non-labelled propane at 250 °C (left) and 280 °C (right).

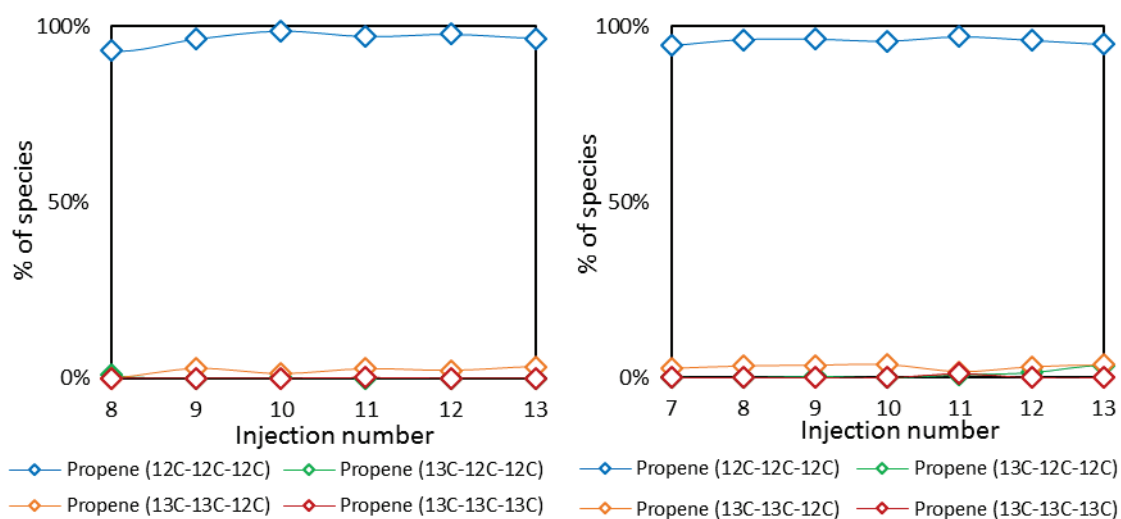


Figure 128 | GC-MS analysis of the labelled and non-labelled propene at 250 °C (left) and 280 °C (right).

Really limited amounts of labelled butane and butane could be observed. The GC-MS analysis was also applied for the commercial catalyst, the same observation could be made. No real difference could be detected between the two types of catalysts.

Bibliography

1. Ren, N. *et al.* Novel, efficient hollow zeolitically microcapsulized noble metal catalysts. *J. Catal.* **251**, 182–188 (2007).
2. FASTCARD. <https://www.sintef.no/projectweb/fastcard/>. 18–07–2016
3. Project, M. & Solutions, C. E. F. M. Annex I - 'Description of Work'. (2013).
4. Fischer, F. & Tropsch, H. Über die Herstellung synthetischer Ölgemische (Syn-thol) durch Aufbau aus Kohlenoxyd und Wasserstoff. *Brennst. Chem.* **4**, 276–285 (1923).
5. Sesderens, J. & Paul Sabatier, M. M. Nouvelles synthèses du méthane. *Chim. Org.* 4–6 (1873).
6. Casci, J. L., Lok, C. M. & Shannon, M. D. Fischer-Tropsch catalysis: The basis for an emerging industry with origins in the early 20th Century. *Catal. Today* **145**, 38–44 (2009).
7. BASF. German Patent 293. **787**, (1913).
8. BASF. US Patent 1. **850**, (1916).
9. Fischer, F. Tropsch, H. Patentschrift. (1922).
10. Schulz, H. Short history and present trends of Fischer–Tropsch synthesis. *Appl. Catal. A Gen.* **186**, 3–12 (1999).
11. de Smit, E. & Weckhuysen, B. M. The renaissance of iron-based Fischer–Tropsch synthesis: on the multifaceted catalyst deactivation behaviour. *Chem. Soc. Rev.* **37**, 2758–2781 (2008).
12. Ishihara, T., Eguchi, K. & Arai, H. Hydrogenation of carbon monoxide over SiO₂-supported FeCo, CoNi and NiFe bimetallic catalysts. *Appl. Catal.* **30**, 225–238 (1987).
13. Schulz, H. & Claeys, M. Reactions of α -olefins of different chain length added during Fischer–Tropsch synthesis on a cobalt catalyst in a slurry reactor. *Appl. Catal. A Gen.* **186**, 71–90 (1999).
14. Iglesia, E., Reyes, S. C., Madon, R. J. & Soled, S. L. Selectivity Control and Catalyst Design in the Fischer-Tropsch Synthesis: Sites, Pellets, and Reactors. *Adv. Catal.* **39**, 221–302 (1993).
15. Zhao, G., Zhang, C., Qin, S., Xiang, H. & Li, Y. Effect of interaction between potassium and structural promoters on Fischer-Tropsch performance in iron-based catalysts. *J. Mol. Catal. A Chem.* **286**, 137–142 (2008).
16. Li, S., Li, A., Krishnamoorthy, S. & Iglesia, E. Effects of Zn, Cu, and K promoters on the structure and on the reduction, carburization, and catalytic behavior of iron-based Fischer-Tropsch synthesis catalysts. *Catal. Letters* **77**, 197–205 (2001).
17. Xiong, H., Motchelaho, M. A., Moyo, M., Jewell, L. L. & Coville, N. J. Effect of Group I alkali metal promoters on Fe/CNT catalysts in Fischer-Tropsch synthesis. *Fuel* **150**, 687–696 (2015).
18. Özkara-Aydinoglu, S. *et al.* Alpha-olefin selectivity of Fe-Cu-K catalysts in Fischer-Tropsch synthesis: Effects of catalyst composition and process conditions. *Chem. Eng. J.* **181-182**, 581–589 (2012).
19. Wan, H., Wu, B., Zhang, C., Xiang, H. & Li, Y. Promotional effects of Cu and K on precipitated iron-based catalysts for Fischer-Tropsch synthesis. *J. Mol. Catal. A Chem.* **283**, 33–42 (2008).

20. Falbe, J. Fischer-Tropsch-Synthese aus Kohle. Thieme: Stuttgart (1977).
21. Zhang, Q., Kang, J. & Wang, Y. Development of Novel Catalysts for Fischer-Tropsch Synthesis: Tuning the Product Selectivity. *ChemCatChem* **2**, 1030–1058 (2010).
22. Eindhoven, T. U. & De, V. The Fischer-Tropsch synthesis : A mechanistic study using transient isotopic tracing. *Energy* (2001).
23. van der Laan, G. P. Kinetics, Selectivity and Scale Up of the Fischer-Tropsch Synthesis. *Univ. Groningen* 1–251 (1999).
24. Boerrigter, H. Economy of Biomass-to-Liquids (BTL) plants An engineering assessment. (2006).
25. de Klerk, A. Fischer–Tropsch Refining. (2011).
26. Dry, M. E. Fischer-Tropsch process. Commercial aspects. *Catal. Today* **6**, 183–206 (1990).
27. A.M. Subiranas. Combining Fischer-Tropsch Synthesis (FTS) and Hydrocarbon Reactions in one Reactor. *Dissertation, Universität Karlsruhe* (2009).
28. Botes, F. G., Niemantsverdriet, J. W. & Van De Loosdrecht, J. A comparison of cobalt and iron based slurry phase Fischer-Tropsch synthesis. *Catal. Today* **215**, 112–120 (2013).
29. Pirola, C., Bianchi, C. L., Di Michele, A., Vitali, S. & Ragaini, V. Fischer Tropsch and Water Gas Shift chemical regimes on supported iron-based catalysts at high metal loading. *Catal. Commun.* **10**, 823–827 (2009).
30. Newsome D. S. The water-gas shift reaction. *Catal. Rev. Sci. Eng.* **21**, 275–318 (1980).
31. Friedel, R. A. & Anderson, R. B. Composition of Synthetic Liquid Fuels. I. Product Distribution and Analysis of C5-C8 Paraffin Isomers From Cobalt Catalyst. *J. Am. Chem. Soc.* **72**, 2307 (1950).
32. Anderson, R. B., Friedel, R. A. & Stortch, H. H. Fischer-Tropsch Reaction Mechanism Involving Stepwise Growth of Carbon Chain. *J. Chem. Phys.* **19**, 313 (1951).
33. Khodakov, A. Y., Chu, W. & Fongarland, P. Advances in the Development of Novel Cobalt Fischer – Tropsch Catalysts for Synthesis of Long-Chain Hydrocarbons and Clean Fuels. *Chem. Rev.* **107**, 1692–1744 (2007).
34. Iglesia, E. Design, synthesis, and use of cobalt-based Fischer-Tropsch synthesis catalysts. *Appl. Catal. A Gen.* **161**, 59–78 (1997).
35. Dry, M. E. Fischer–Tropsch reactions and the environment. *Appl. Catal. A Gen.* **189**, 185–190 (1999).
36. Eliason, S. A. & Bartholomew, C. H. Reaction and Deactivation Kinetics for Fischer-Tropsch Synthesis on Unpromoted and Potassium-Promoted Iron Catalysts. *Appl. Catal. A Gen.* **186**, 229–243 (1999).
37. Morales, B. Y. F. & Weckhuysen, B. M. Promotion Effects in Co-based Fischer – Tropsch Catalysis. *Catalysis* **19**, 1–40 (2006).
38. Zhang, H. bin & Schrader, G. L. Characterization of a fused iron catalyst for Fischer-Tropsch synthesis by in situ laser Raman spectroscopy. *J. Catal.* **95**, 325–332 (1985).
39. Rethwisch, D. G. & Dumesic, J. A. Adsorptive and Catalytic Properties of Supported Metal Oxides. *J. Catal.* **101**, 35–42 (1986).
40. Lox, E. S. & Froment, G. F. Kinetics of the Fischer–Tropsch reaction on a precipitated promoted iron catalyst. 2. Kinetic modeling. *Ind. Eng. Chem. Res.* **32**, 61–70 (1993).

41. Rao, K. *et al.* Mossbauer study of iron Fischer-Tropsch catalysts during activation and synthesis. *Energy and Fuels* **10**, 546–551 (1996).
42. Rao, K. *et al.* Mossbauer-spectroscopy study of iron-based catalysts used in Fischer-Tropsch synthesis. *Top. Catal.* **2**, 71–78 (1995).
43. Cornell, R. M. & Schwertmann, U. *The Iron Oxides*, Second Edition. (2003).
44. Ding, M. *et al.* Study on reduction and carburization behaviors of iron phases for iron-based Fischer-Tropsch synthesis catalyst. *Appl. Energy* **160**, 982–989 (2014).
45. Cui, X. *et al.* Effect of pretreatment on precipitated Fe-Mo Fischer-Tropsch catalysts: Morphology, carburization, and catalytic performance. *J. Catal.* **282**, 35–46 (2011).
46. Luo, M., Hamdeh, H. & Davis, B. H. Fischer-Tropsch Synthesis. Catalyst activation of low alpha iron catalyst. *Catal. Today* **140**, 127–134 (2009).
47. Chen, W., Fan, Z., Pan, X. & Bao, X. Effect of confinement in carbon nanotubes on the activity of Fischer-Tropsch iron catalyst. *J. Am. Chem. Soc.* **130**, 9414–9419 (2008).
48. Li, S., Krishnamoorthy, S., Li, A., Meitzner, G. D. & Iglesia, E. Promoted Iron-Based Catalysts for the Fischer-Tropsch Synthesis: Design, Synthesis, Site Densities, and Catalytic Properties. *J. Catal.* **206**, 202–217 (2002).
49. Bukur, D. B., Lang, X. & Ding, Y. Pretreatment effect studies with a precipitated iron Fischer-Tropsch catalyst in a slurry reactor. **186**, 255–275 (1999).
50. Ding, M. *et al.* Study on reduction and carburization behaviors of iron phases for iron-based Fischer-Tropsch synthesis catalyst. *Appl. Energy* **160**, 982–989 (2014).
51. Shultz, J. F., Hall, W. K., Seligman, B. & Anderson, R. B. Studies of the Fischer-Tropsch Synthesis. XIV. Hagg Carbide as Catalysts. *J. Am. Chem. Soc.* **77**, 213–221 (1955).
52. D.B. Bukur, K. Okabe, M.P. Rosynek, C.P. Li, D.J. Wang, K.R.P.M. Rao, G. P. H. Activation Studies with a Precipitated Iron Catalyst for Fischer-Tropsch Synthesis: I. Characterization Studies. *J. Catal.* **155**, 353–365 (1995).
53. Niemantsverdriet, J. W. & Van der Kraan, a. M. On the Time-Dependent Behavior of Iron Catalysts in Fischer-Tropsch Synthesis. *J. Catal.* **72**, 385–388 (1981).
54. Raupp, G. B. & Delgass, W. N. Mössbauer investigation of supported Fe and FeNi catalysts. II. Carbides formed Fischer-Tropsch synthesis. *J. Catal.* **58**, 348–360 (1979).
55. Datye, A. K. The nature of the active phase in iron Fischer-Tropsch catalysts. *Stud. Surf. Sci. Catal.* **130**, 1139–1144 (2000).
56. Bezemer, G. L. *et al.* Cobalt Particle Size Effects in the Fischer-Tropsch Reaction Studied with Carbon Nanofiber Supported Catalysts. *Am. Chem. Soc.* **128**, 3956–3964 (2006).
57. van Steen, E. & Claeys, M. Fischer-Tropsch catalysts for the biomass-to-liquid process. *Chem. Eng. Technol.* **31**, 655–666 (2008).
58. den Breejen, J. P. *et al.* On the Origin of the Cobalt Particle Size Effects in Fischer-Tropsch Catalysis. *J. Am. Chem. Soc.* **131**, 7197–7203 (2009).
59. Mabaso, E. I. Nanosized Iron Crystallites for Fischer-Tropsch Synthesis. *University of Cape Town* (2012).
60. Park, J.-Y. *et al.* Alumina-supported iron oxide nanoparticles as Fischer-Tropsch catalysts: Effect

- of particle size of iron oxide. *J. Mol. Catal. A Chem.* **323**, 84–90 (2010).
61. Kang, S. H., Bae, J. W., Prasad, P. S. S. & Jun, K. W. Fischer-Tropsch synthesis using zeolite-supported iron catalysts for the production of light hydrocarbons. *Catal. Letters* **125**, 264–270 (2008).
 62. Xu, J. D. *et al.* Effect of sulfur on α -Al₂O₃-supported iron catalyst for Fischer-Tropsch synthesis. *Appl. Catal. A Gen.* **514**, 103–113 (2016).
 63. Kang, S. H. *et al.* Catalytic performance on iron-based Fischer-Tropsch catalyst in fixed-bed and bubbling fluidized-bed reactor. *Appl. Catal. B Environ.* **103**, 169–180 (2011).
 64. Baranak, M., Gürünlü, B., Sariođlan, A., Atađ, Ö. & Atakül, H. Low acidity ZSM-5 supported iron catalysts for Fischer-Tropsch synthesis. *Catal. Today* **207**, 57–64 (2013).
 65. Xing, C. *et al.* Tunable isoparaffin and olefin yields in Fischer-Tropsch synthesis achieved by a novel iron-based micro-capsule catalyst. *Catal. Today* **251**, 41–46 (2015).
 66. Santos, V. P. *et al.* Metal organic framework-mediated synthesis of highly active and stable Fischer-Tropsch catalysts. *Nat. Commun.* **6**, 6451 (2015).
 67. Torres Galvis, H. M. *et al.* Effects of sodium and sulfur on catalytic performance of supported iron catalysts for the Fischer-Tropsch synthesis of lower olefins. *J. Catal.* **303**, 22–30 (2013).
 68. Li, S., Krishnamoorthy, S., Li, A., Meitzner, G. D. & Iglesia, E. Promoted Iron-Based Catalysts for the Fischer-Tropsch Synthesis: Design, Synthesis, Site Densities, and Catalytic Properties. *J. Catal.* **206**, 202–217 (2002).
 69. Yang, Y., Xiang, H., Xu, Y., Bai, L. & Li, Y. Effect of potassium promoter on precipitated iron-manganese catalyst for Fischer-Tropsch synthesis. *Appl. Catal. A Gen.* **266**, 181–194 (2004).
 70. Li, T., Wang, H., Yang, Y., Xiang, H. & Li, Y. Effect of manganese on the catalytic performance of an iron-manganese bimetallic catalyst for light olefin synthesis. *J. Energy Chem.* **22**, 624–632 (2013).
 71. Gaube, J. & Klein, H. F. The promoter effect of alkali in Fischer-Tropsch iron and cobalt catalysts. *Appl. Catal. A Gen.* **350**, 126–132 (2008).
 72. Pendyala, V. R. R. *et al.* Selectivity control of Cu promoted iron-based Fischer-Tropsch catalyst by tuning the oxidation state of Cu to mimic K. *Appl. Catal. A Gen.* **495**, 45–53 (2015).
 73. Chonco, Z. H., Lodya, L., Claeys, M. & Van Steen, E. Copper ferrites: A model for investigating the role of copper in the dynamic iron-based Fischer-Tropsch catalyst. *J. Catal.* **308**, 363–373 (2013).
 74. Zhang, C. H. *et al.* Study of an iron-manganese Fischer-Tropsch synthesis catalyst promoted with copper. *J. Catal.* **237**, 405–415 (2006).
 75. Li, J. B. *et al.* Sodium promoter on iron-based catalyst for direct catalytic synthesis of light alkenes from syngas. *Fuel Process. Technol.* **125**, 119–124 (2014).
 76. Davis, B. H. Technology Development for Iron and Cobalt Fischer-Tropsch catalysts, Quarterly Report 2000. *Quarterly Rep.* (2000).
 77. Li, S. *et al.* Structural analysis of unpromoted Fe-based Fischer-Tropsch catalysts using X-ray absorption spectroscopy. *Appl. Catal. A Gen.* **219**, 215–222 (2001).
 78. Zhang, Y. Q., Sirimanothan, N., O'Brien, R. J., Hamdeh, H. H. & Davis, B. H. Study of deactivation of iron-based Fischer-Tropsch synthesis catalysts. *Catal. Deactiv. 2001, Proc.* **139**, 125–132

- (2001).
79. Schulz, H. Selforganization in Fischer-Tropsch synthesis with iron- and cobalt catalysts. *Catal. Today* **228**, 113–122 (2014).
 80. Bartholomew, C. H., Stoker, M. W., Mansker, L. & Datye, A. in *Studies in Surface Science and Catalysis* 265–272 (1999).
 81. Ning, W. *et al.* Phase transformation of unpromoted and promoted Fe catalysts and the formation of carbonaceous compounds during Fischer-Tropsch synthesis reaction. *Appl. Catal. A Gen.* **312**, 35–44 (2006).
 82. Gao, F., Wang, H., Qing, M., Yang, Y. & Li, Y. Controlling the phase transformations and performance of iron-based catalysts in the Fischer-Tropsch synthesis. *Chinese J. Catal.* **34**, 1312–1325 (2013).
 83. Dwyer, D. J. & Hardenbergh, J. H. The catalytic reduction of carbon monoxide over iron surfaces: A surface science investigation. *J. Catal.* **87**, 66–76 (1984).
 84. Loaiza-Gil, A., Fontal, B., Rueda, F., Mendialdua, J. & Casanova, R. On carbonaceous deposit formation in carbon monoxide hydrogenation on a natural iron catalyst. *Appl. Catal. A Gen.* **177**, 193–203 (1999).
 85. Duvenhage, D. J., Espinoza, R. L. & Coville, N. J. Fischer-Tropsch precipitated iron catalysts: Deactivation studies. *Stud. Surf. Sci. Catal.* **88**, 351–358 (1994).
 86. Duvenhage, D. J. & Coville, N. J. Deactivation of a precipitated iron Fischer-Tropsch catalyst - A pilot plant study. *Appl. Catal. A Gen.* **298**, 211–216 (2006).
 87. Hansen, T. W., Delariva, A. T., Challa, S. R. & Datye, A. K. Sintering of catalytic nanoparticles: Particle migration or ostwald ripening? *Acc. Chem. Res.* **46**, 1720–1730 (2013).
 88. Carr, C. J. A study of thermal aging of Pt/Al₂O₃ Using temperature-programmed desorption spectroscopy. *J. Catal.* **110**, 285–297 (1988).
 89. Wynblatt, P. & Gjostein, N. A. Supported metal crystallites. *Prog. Solid State Chem.* **9**, 21–58 (1975).
 90. Bartholomew, C. H. Mechanisms of catalyst deactivation. *Appl. Catal. A Gen.* **212**, 17–60 (2001).
 91. Forzatti, P. & Lietti, L. Catalyst deactivation. *Catal. Today* **52**, 165–181 (1990).
 92. Yao, Y., Hildebrandt, D., Glasser, D. & Liu, X. Fischer-Tropsch Synthesis Using H₂/CO/CO₂ Syngas Mixtures over an Iron Catalyst. *Ind. Eng. Chem. Res.* **19**, 11002–11012 (2011).
 93. James, O. O., Mesubi, A. M., Ako, T. C. & Maity, S. Increasing carbon utilization in Fischer-Tropsch synthesis using H₂-deficient or CO₂-rich syngas feeds. *Fuel Process. Technol.* **91**, 136–144 (2010).
 94. Visconti, C. G. *et al.* Fischer-Tropsch synthesis on a Co/Al₂O₃ catalyst with CO₂ containing syngas. *Appl. Catal. A Gen.* **355**, 61–68 (2009).
 95. Gnanamani, M. K., Shafer, W. D., Sparks, D. E. & Davis, B. H. Fischer-Tropsch synthesis: Effect of CO₂ containing syngas over Pt promoted Co/ γ -Al₂O₃ and K-promoted Fe catalysts. *Catal. Commun.* **12**, 936–939 (2011).
 96. Zhang, Y., Jacobs, G., Sparks, D. E., Dry, M. E. & Davis, B. H. CO and CO₂ hydrogenation study on supported cobalt Fischer-Tropsch synthesis catalysts. *Catal. Today* **71**, 411–418 (2002).

97. Riedel, T. *et al.* Comparative study of Fischer–Tropsch synthesis with H₂/CO and H₂/CO₂ syngas using Fe- and Co-based catalysts. *Appl. Catal. A Gen.* **186**, 201–213 (1999).
98. Landau, M. V., Vidruk, R. & Herskowitz, M. Sustainable production of green feed from carbon dioxide and hydrogen. *ChemSusChem* **7**, 785–794 (2014).
99. Krishnamoorthy, S., Li, A. & Iglesia, E. Pathways for CO₂ formation and conversion during Fischer-Tropsch synthesis on iron-based catalysts. *Catal. Letters* **80**, 77–86 (2002).
100. Martinelli, M. *et al.* CO₂ reactivity on Fe-Zn-Cu-K Fischer-Tropsch synthesis catalysts with different K-loadings. *Catal. Today* **228**, 77–88 (2014).
101. Riedel, T. *et al.* Fischer-Tropsch on iron with H₂/CO and H₂/CO₂ as synthesis gases: The episodes of formation of the Fischer-Tropsch regime and construction of the catalyst. *Top. Catal.* **26**, 41–54 (2003).
102. Xu, L. G., Bao, S. Q., Houpt, D. J., Lambert, S. H. & Davis, B. H. Role of CO₂ in the initiation of chain growth and alcohol formation during the Fischer-Tropsch synthesis. *Catal. Today* **36**, 347–355 (1997).
103. Chun, D. H. *et al.* Negative effects of CO₂ in the feed stream on the catalytic performance of precipitated iron-based catalysts for fischer-tropsch synthesis. *Catal. Letters* **142**, 452–459 (2012).
104. Fletcher, J. V. Mechanistic pathways of the high temperature Fischer-Tropsch synthesis Mechanistic Pathways of the High Temperature Fischer-Tropsch Synthesis. *Tech. Univ. Eindhoven* (2015).
105. He, J. J., Xu, B. L., Yoneyama, Y., Nishiyama, N. & Tsubaki, N. Designing a new kind of capsule catalyst and its application for direct synthesis of middle isoparaffins from synthesis gas. *Chem. Lett.* **34**, 148–149 (2005).
106. He, J., Liu, Z., Yoneyama, Y., Nishiyama, N. & Tsubaki, N. Multiple-functional capsule catalysts: A tailor-made confined reaction environment for the direct synthesis of middle isoparaffins from syngas. *Chem. - A Eur. J.* **12**, 8296–8304 (2006).
107. Sartipi, S., Van Dijk, J. E., Gascon, J. & Kapteijn, F. Toward bifunctional catalysts for the direct conversion of syngas to gasoline range hydrocarbons: H-ZSM-5 coated Co versus H-ZSM-5 supported Co. *Appl. Catal. A Gen.* **456**, 11–22 (2013).
108. Sartipi, S., Makkee, M., Kapteijn, F. & Gascon, J. Catalysis engineering of bifunctional solids for the one-step synthesis of liquid fuels from syngas: a review. *Catal. Sci. Technol.* **4**, 893 (2014).
109. Yang, G. *et al.* Tandem catalytic synthesis of light isoparaffin from syngas via Fischer-Tropsch synthesis by newly developed core-shell-like zeolite capsule catalysts. *Catal. Today* **215**, 29–35 (2013).
110. Wang, Y. & Tuel, A. Nanoporous zeolite single crystals: ZSM-5 nanoboxes with uniform intracrystalline hollow structures. *Microporous Mesoporous Mater.* **113**, 286–295 (2008).
111. Wang, Y., Lin, M. & Tuel, A. Hollow TS-1 crystals formed via a dissolution-recrystallization process. *Microporous Mesoporous Mater.* **102**, 80–85 (2007).
112. Ertl, G., Knözinger, H. & Weitkamp, J. *Characterization of solid catalysts. Handbook of heterogeneous catalysis* **Volume 2**, (1997).
113. Van Hardeveld, R. & Hartog, F. The statistics of surface atoms and surface sites on metal crystals. *Surf. Sci.* **15**, 189–230 (1969).

114. Li, S. Thèse de l'Université de Lyon, Metal Nanoparticles Encapsulated in Membrane-like Zeolite Single Crystals - Application to selective Catalysis. (2015).
115. Li, S. *et al.* Ultimate size control of encapsulated gold nanoparticles. *Chem. Commun. (Camb)*. **49**, 8507–8509 (2013).
116. Li, S., Tuel, A., Laprune, D., Meunier, F. & Farrusseng, D. Transition-metal nanoparticles in hollow zeolite single crystals as bifunctional and size-selective hydrogenation catalysts. *Chem. Mater.* **27**, 276–282 (2015).
117. Li, S., Boucheron, T., Tuel, A., Farrusseng, D. & Meunier, F. Size-selective hydrogenation at the subnanometer scale over platinum nanoparticles encapsulated in silicalite-1 single crystal hollow shells. *Chem. Commun. (Camb)*. **50**, 1824–1826 (2014).
118. Cheng, K. *et al.* Pore size effects in high-temperature Fischer–Tropsch synthesis over supported iron catalysts. *J. Catal.* **328**, 139–150 (2015).
119. Matter, P. H., Wang, E., Millet, J.-M. M. & Ozkan, U. S. Characterization of the Iron Phase in CN x -Based Oxygen Reduction Reaction Catalysts. *J. Phys. Chem. C* **111**, 1444–1450 (2007).
120. Herreyre, S., Gadelle, P., Moral, P. & Millet, J. M. M. Study by mössbauer spectroscopy and magnetization measurement of the evolution of iron catalysts used in the disproportionation of CO. *J. Phys. Chem. Solids* **58**, 1539–1545 (1997).
121. Audier, M., Bowen, P. & Jones, W. Electron microscopic and mössbauer study of the iron carbides θ -Fe₃C and X-Fe₅C₂ formed during the disproportionation of CO. *J. Cryst. Growth* **64**, 291–296 (1983).
122. Köhn, R. *et al.* Studies on the state of iron oxide nanoparticles in MCM-41 and MCM-48 silica materials. *Microporous Mesoporous Mater.* **63**, 125–137 (2003).
123. Galvis, H. M. T. *et al.* Supported Iron Nanoparticles as Catalysts for Sustainable Production of Lower Olefins. *Science (80-.)*. **335**, 835–838 (2012).
124. Millet, J. M. M., Knözinger, H. & Bonville, P. Characterization of iron promoter in tungstated zirconia catalysts by Mössbauer spectroscopy at very low temperatures. *J. Phys. Chem. B* **110**, 16003–16007 (2006).
125. Fierro, G., Moretti, G., Ferraris, G. & Andreozzi, G. B. A Mössbauer and structural investigation of Fe-ZSM-5 catalysts: Influence of Fe oxide nanoparticles size on the catalytic behaviour for the NO-SCR by C₃H₈. *Appl. Catal. B Environ.* **102**, 215–223 (2011).
126. Smit, E. De *et al.* Stability and Reactivity of E-X- θ Iron Carbide Catalyst Phases in Fischer - Tropsch Synthesis : Controlling μ C. *J. Am. Chem. Soc.* 14928–14941 (2010).
127. Kerdi, F., Caps, V. & Tuel, A. Mesostructured Au/C materials obtained by replication of functionalized SBA-15 silica containing highly dispersed gold nanoparticles. *Microporous Mesoporous Mater.* **140**, 89–96 (2011).
128. Zhao, D., Sun, J., Li, Q., Stucky, G. D. & Barbara, S. Morphological Control of Highly Ordered Mesoporous Silica SBA-15 Mesoporous materials are of great interest to the materials community because their pore structures as well as catalytic , adsorbed , conductive and magnetic ordered large mesoporous silica . 275–279 (2000).
129. Lupo, F. Di *et al.* Tunable Ordered Nanostructured α -Fe₂O₃ Lithium Battery Anodes by Nanocasting Technique Using SBA-15 Hard Silica Templates. *Int. J. Electrochem. Sci.* **7**, 10865–10883 (2012).

130. Jiao, F. *et al.* Ordered Mesoporous Fe₂O₃ with Crystalline Walls. *J. Am. Chem. Soc.* **128**, 5468–5474 (2006).
131. Asami, K. *et al.* Fischer-Tropsch synthesis over precipitated iron catalysts supported on carbon. *Catal. Today* **215**, 80–85 (2013).
132. Matsue, T., Yamada, Y. & Kobayashi, Y. Iron carbide nanoparticles produced by laser ablation in organic solvent. *Hyperfine Interact.* **205**, 31–35 (2012).
133. Laan, G. P. van der & Beenackers, A. A. C. M. Kinetics and Selectivity of the Fischer-Tropsch Synthesis: A Literature Review. *Catal. Rev. Sci. Eng.* **41**, 255–318 (1999).
134. Chang, J. *et al.* Kinetic modeling of Fischer-Tropsch synthesis over Fe-Cu-K-SiO₂ catalyst in slurry phase reactor. *Chem. Eng. Sci.* **62**, 4983–4991 (2007).
135. Torres Galvis, H. M. *et al.* Iron particle size effects for direct production of lower olefins from synthesis gas. *J Am Chem Soc* **134**, 16207–16215 (2012).
136. Lohitharn, N., Goodwin, J. G. & Lotero, E. Fe-based Fischer-Tropsch synthesis catalysts containing carbide-forming transition metal promoters. *J. Catal.* **255**, 104–113 (2008).
137. Zhang, K. *et al.* Adsorption of Water and Ethanol in MFI-type Zeolites Adsorption of Water and Ethanol in MFI-type Zeolites. *Langmuir* **28**, 8664–8673 (2012).
138. Özgür Yazaydin, A. & Thompson, R. W. Molecular simulation of water adsorption in silicalite: Effect of silanol groups and different cations. *Microporous Mesoporous Mater.* **123**, 169–176 (2009).
139. Eroshenko, V., Regis, R.-C., Soulard, M. & Patarin, J. Energetics : a new field of application for hydrophobic zeolites. *J. Am. Chem. Soc.* **28**, 8129–8130 (2001).
140. Hughes, Z. E., Carrington, L. A., Raiteri, P. & Gale, J. D. A computational investigation into the suitability of purely siliceous zeolites as reverse osmosis membranes. *J. Phys. Chem. C* **115**, 4063–4075 (2011).
141. Trzpit, M. *et al.* The effect of local defects on water adsorption in silicalite-1 zeolite: A joint experimental and molecular simulation study. *Langmuir* **23**, 10131–10139 (2007).
142. Cailliez, F., Stirnemann, G., Boutin, A., Demachy, I. & Fuchs, A. H. Does Water Condense in Hydrophobic Cavities ? A Molecular Simulation Study of Hydration in Heterogeneous Nanopores. *J. Phys. Chem. C* **112**, 10435–10445 (2008).
143. Hunger, B., Heuchel, M., Matysik, S., Beck, K. & Einicke, W. D. Adsorption of water on ZSM-5 zeolites. *Thermochim. Acta* **269/270**, 599–611 (1995).
144. Chezeau, J. M., Delmotte, L., Guth, J. L. & Gabelica, Z. Influence of synthesis conditions and postsynthesis treatments on the nature and quantity of structural defects in highly siliceous MFI zeolites: A high-resolution solid-state ²⁹Si NMR study. *Zeolites* **11**, 598–606 (1991).
145. Axon, S. A. & Klinowski, J. Nuclear magnetic resonance studies of the synthesis of zeolite ZSM-5 by the 'fluoride method'. *Appl. Catal. A Gen.* **111**, 29–39 (1994).
146. Gualtieri, M. L., Gualtieri, A. F. & Prudenziati, M. Seeded growth of TPA-MFI films using the fluoride route. *Microporous Mesoporous Mater.* **111**, 604–611 (2008).
147. Burel, L. & Tuel, A. Nanozeolites: New strategies for designing ultra small silicalite crystals with very few framework defects. *Microporous Mesoporous Mater.* **174**, 90–99 (2013).
148. Serrano, D. P., Calleja, G., Botas, J. A. & Gutierrez, F. J. Characterization of adsorptive and

- hydrophobic properties of silicalite-1, ZSM-5, TS-1 and Beta zeolites by TPD techniques. *Sep. Purif. Technol.* **54**, 1–9 (2007).
149. Bowen, T. C. & Vane, L. M. Ethanol, acetic acid, and water adsorption from binary and ternary liquid mixtures on high-silica zeolites. *Langmuir* **22**, 3721–3727 (2006).
150. Erdem-Şenatalar, A., Bergendahl, J. a., Giaya, A. & Thompson, R. W. Adsorption of Methyl Tertiary Butyl Ether on Hydrophobic Molecular Sieves. *Environ. Eng. Sci.* **21**, 722–729 (2004).
151. Pascual, P., Ungerer, P., Tavitian, B., Pernot, P. & Boutin, A. Development of a transferable guest-host force field for adsorption of hydrocarbons in zeolites. *Phys. Chem. Chem. Phys.* **5**, 3684–3693 (2003).
152. Corma, A. *et al.* Strategies to improve the epoxidation activity and selectivity of Ti-MCM-41. *Chem. Commun.* 2211–2212 (1998).
153. Mbaraka, I. K. & Shanks, B. H. Design of multifunctionalized mesoporous silicas for esterification of fatty acid. *J. Catal.* **229**, 365–373 (2005).
154. Blasco, T. *et al.* Direct Synthesis and Characterization of Hydrophobic Aluminum-Free Ti - Beta Zeolite. *J Phys Chem B* **5647**, 75–88 (1998).
155. Mbaraka, I. K., Radu, D. R., Lin, V. S. Y. & Shanks, B. H. Organosulfonic acid-functionalized mesoporous silicas for the esterification of fatty acid. *J. Catal.* **219**, 329–336 (2003).
156. Espinoza, R., Santamaria, J., Menendez, M., Coronas, J. & Irusta, S. 1999a 'Production of hydrocarbons'. International patent WO 1999/64380
157. Espinoza, R. *et al.* Use of membranes in Fischer-Tropsch reactors. *Stud. Surf. Sci. Catal.* **130**, 389–394 (2000).
158. Unruh, D., Rohde, M. P. & Schaub, G. Improving carbon utilization in biomass conversion to synthetic hydrocarbons via Fischer-Tropsch synthesis. *Stud. Surf. Sci. Catal.* **153**, 91–96 (2004).
159. Unruh, D., Rohde, M. P. & Schaub, G. In-situ removal of H₂O during Fischer-Tropsch synthesis - a modelling study. *DGMK - Tagungsband* **4**, 1–6 (2002).
160. Unruh, D. Fischer-Tropsch Synthese mit Synthesegasen aus Biomasse – Verbesserung der Kohlenstoffnutzung durch Anwendung eines Membranreaktors, Shaker, Aachen. (2006).
161. Rohde, M. P., Schaub, G., Khajavi, S., Jansen, J. C. & Kapteijn, F. Fischer-Tropsch synthesis with in situ H₂O removal - Directions of membrane development. *Microporous Mesoporous Mater.* **115**, 123–136 (2008).
162. Rohde, M. P., Unruh, D. & Schaub, G. Membrane Application in Fischer - Tropsch Synthesis to Enhance CO₂ Hydrogenation. *Ind. Eng. Chem. Res.* **44**, 9653–9658 (2005).
163. Rohde, M. P., Schaub, G., Vente, J. F. & van Veen, H. M. DGMK Tagungsbericht. **4**, 215 (2006).
164. Visconti, C. G. *et al.* CO₂ hydrogenation to lower olefins on a high surface area K-promoted bulk Fe-catalyst. *Appl. Catal. B Environ.* **200**, 530–542 (2017).
165. Moe J. M. Design of water-gas shift reactors. *Chem. Eng. Prog.* **58**, 33–36 (1962).
166. Smith R J, B., Loganathan, M. & Shantha, M. S. A Review of the Water Gas Shift Reaction Kinetics. *Int. J. Chem. React. Eng.* **8**, 1–32 (2010).

Joffrey Huve

© Copyright 2017